UNIVERSITÉ DU QUEBÉC À CHICOUTIMI

THÈSE PRÉSENTÉE À

L'UNIVERSITÉ DU QUÉBEC À CHICOUTIMI

COMME EXIGENCE PARTIELLE

DU DOCTORAT EN INGÉNIERIE

PAR

ZAFER KOONT

INTÉRACTION ENTRE LES PARTICULES D'ALUMINES, LES ALLIAGES D'ALUMINIUM ET

SES INCLUSIONS DURANT LA FILTRATION D'ALUMINIUM AVANT LA COULÉE

APRIL 2013

UNIVERSITY OF QUÉBEC AT CHICOUTIMI

A THESIS SUBMITTED TO

THE UNIVERSTIY OF QUEBEC AT CHICOUTIMI

IN PARTIAL FULFILLMENT OF THE REQUIREMENTS

FOR THE DEGREE OF THE DOCTOR OF PHILOSOHY

IN ENGINEERING

BY

ZAFER KOONT

INTERACTIONS BETWEEN ALUMINA PARTICLES, ALUMINUM ALLOYS, AND THEIR

INCLUSIONS DURING ALUMINUM FILTRATION BEFORE CASTING

APRIL 2013

Dedicated to mama and family

Thank you for your emotional and spiritual support...

Sevgili anneme ve tüm aileme

Sonsuz desteğinizi bir an olsun esirgemediğiniz için minnettarım...

RÉSUMÉ

Ce projet a été entrepris pour étudier les interactions entre les particules d'alumine, les alliages d'aluminium et ses inclusions sous des conditions d'écoulement de l'aluminium liquide. Le but du projet était de développer une méthode d'essai qui permet de simuler les conditions similaires à celles dans le procédé de filtration d'aluminium et d'évaluer les interactions qui ont lieu entre les différents types d'échantillons d'alumine, les alliages d'aluminium et ses inclusions. Cette méthode d'essai avait pour but de déterminer comment les différents types d'alumine se comportent durant le procédé de filtration.

Les interactions chimiques entre l'alumine, les alliages d'aluminium et ses inclusions ont été étudiées dans des conditions d'écoulement statiques et dynamique. Afin d'étudier ces interactions dans des conditions d'écoulement dynamique, la connaissance du champ de vitesse au voisinage des particules d'alumine est nécessaire. Dans ce projet, deux systèmes expérimentaux uniques qui peuvent simuler l'écoulement dans le lit du filtre industriel ont été conçus et construits. Un modèle mathématique a été développé pour prédire le champ d'écoulement autour des particules dans le système expérimental. Le modèle mathématique a été validé en comparant les prédictions avec les résultats d'un modèle physique dans lequel l'eau était utilisée comme fluide. Ensuite, le modèle mathématique a été utilisé pour effectuer des études paramétriques afin de déterminer les paramètres de design et d'opération pour le système expérimental actuel dans lequel les tests ont été faits. Cela a permis de générer un champ d'écoulement similaire à celui du filtre industriel.

Des expériences avec divers alliages d'aluminium-magnésium liquide (0, 2, 5 et 7% Mg, en poids) ont été réalisées pour des différents temps de résidence (de 6 heures à 168 heures) en utilisant les systèmes expérimentaux décrits ci-hauts. Les effets de la vitesse de l'alliage d'aluminium liquide, de la température du liquide, des propriétés physiques (porosité apparente, la rugosité de la surface, etc.) et chimiques (teneur en impuretés telles que Na_2O, SiO_2, etc.) sur le degré des réactions interfaciales entre l'alliage d'aluminium et l'alumine ont été déterminés.

Les échantillons obtenus des expériences aluminium-alumina ont été analysés à l'aide du microscope optique, du microscope électronique à balayage – la spectroscopie aux rayons X à dispersion d'énergie (MEB-EDX), du microprobe MEB, et de la diffraction des rayons X (DRX). Les résultats montrent que les réactions chimiques entre l'alpha-alumine pure à haute densité et les alliages Mg-Al liquides ne sont pas rapide; mais, la présence des impuretés (telle que Na_2O en tant que phase de bêta-alumine) et la structure poreuse de l'alumine augmentent l'étendue des réactions significativement. La phase riche en Na_2O (bêta-alumine) qui se trouve dans toutes les alumines commerciales semble être l'un des facteurs les plus importants pour les réactions spontanées avec la vapeur de magnésium, même au temps de résidence le plus court. Mg-spinelle a été trouvé comme le produit de réaction le plus important. L'analyse thermodynamique indique la même tendance.

SUMMARY

This project was undertaken to study the interactions between alumina particles, aluminum alloys, and its inclusions under liquid aluminum flow conditions. The objective was to develop a test method which can simulate the conditions similar to those in the aluminum filtration process and to evaluate the interactions taking place between various types of alumina samples, aluminum alloys, and its inclusions. With this test method, it was aimed to determine how various alumina types behave under flow conditions during the filtration process.

Chemical interactions between alumina, aluminum alloys, and its inclusions were investigated under both static and dynamic flow conditions. In order to study these interactions under dynamic flow conditions, a knowledge of the velocity field in the vicinity of the alumina particles is necessary. In this project, two unique experimental systems which can simulate the flow condition of the industrial bed were designed and built. A mathematical model was also developed to predict the flow field around the particles in the experimental system. The mathematical model was validated by comparing the predictions with the results from a physical model in which water was used as the fluid. The mathematical model was then used to conduct parametric studies to determine the design and operational parameters for the actual experimental system in which the tests were carried out. This allowed the generation of a flow field similar to that of the industrial filter.

The experiments with various liquid Mg-Al alloys (0, 2, 5, and 7 wt% Mg) were conducted for different residence times (from 6 hours to 168 hours) using the above

experimental systems. The effects of the liquid aluminum alloy velocity, the temperature of the melt, the physical (apparent porosity, surface roughness, etc.) and chemical (impurity content such as Na_2O, SiO_2 etc.) properties of alumina samples on the extent of aluminum alloy/alumina interfacial reactions were determined.

The samples obtained from aluminum-alumina experiments were analyzed by using the optical microscope, the scanning electron microscope – energy dispersive X-ray spectroscopy (SEM-EDX), the micro probe SEM, and X-ray diffraction (XRD). The results indicate that the chemical reactions between high density pure alpha-alumina and molten Mg-Al alloys are not fast; however, the presence of impurities (such as Na_2O as beta alumina phase) and the porous structure in alumina increase the extent of reactions significantly. Na_2O rich phase (beta alumina) found in all commercial alumina grades seems to be one of the most important contributors for the spontaneous reactions of Mg vapor with alumina, even at the shortest residence time. The major reaction product was found to be Mg-spinel. The thermodynamic analysis indicated the same tendency.

ACKNOWLEDGEMENTS

Last but not least, I would particularly like to thank my mom Hacire, my fiancé Melissa and my entire family for their precious support in all respects. Their unconditional love, continuous encouragement, and patience were always there when I needed it the most. I want to send my love and gratitude to my father. You are missed every day.

NOMENCLATURE

AP: apparent porosity

A_f :   time averaged blade angle

ABF: alcan deep bed filter

at %: atomic percent

Ci: initial solute concentration

Cb: bulk solute concentration

Cs: surface solute concentration

C_0:   solute concentration in particle core

C_D :   drag coefficient of cylinder.

D_d :   drag coefficient of blade.

D_p :   diameter of particle, m.

D: mass diffusion coefficient

EDS : energy dispersive X-ray spectrometry

EDX: energy dispersive X-ray

g :   acceleration of gravity, m^2/s.

gb: grain boundary

h, H : heigth

k :   rate constant (sec^{-1})

K :   kinetic energy of turbulence, m^2/s^2.

M: magnesium concentration

MMC : metal matrix composite

N :   number of blades

NA: not applicable

OES: optical emission spectroscopy

PVA: polyvinyl alcohol

r :   radius of blade revolution, m.

Re : reynolds number

rpm: rounds per minute

S :   source term , N/m^3.

sl :   solid liquid interface

SEM: scanning electron microscope

XPS: X-ray photoelectron spectroscopy

XRD: X-ray diffraction

UV: ultraviolet

u , v, w : velocity components in x, y, z directions

Vc : volume of cell, m^3.

V :   velocity vector, m/s.

x, y, z : cartesian coordinates

t: residence time, min

n, a: positive constants

T : temperature, Kelvin

wt %: weight percent

w: water

Γ_ϕ : exchange coefficient for ϕ .

ϕ :   tilt angle of blade, °.

ε :   kinetic energy dissipation, m^2/s^3.

ϕ : general variable

υ : kinematic viscosity, m^2/s.

ρ : density, kg/m^3 or g/cm^3.

ω : rotational speed, r/s.

γ: surface tension

θ : contact angle

Φs: sphericity

TABLE OF CONTENTS

LIST OF TABLES

LIST OF FIGURES

CHAPTER 1
1. INTRODUCTION

Productivity, cost reduction, and quality are indispensable requirements for today's Canadian aluminum industry in order to stay competitive in a global market. To be able to meet increasing challenges and demands on productivity and quality of aluminum, cleanliness of aluminum metal production has a great importance. The size, shape, number, and distribution of inclusions in the final or semi-final metal products are the indicators of the performance of aluminum producers and the quality of their alloys. It is obviously a great advantage to eliminate these impurities, since they reduce the fluidity of the alloy, increase the internal porosity of metal, change the mechanical properties, and deteriorate the surface quality and machinability of final or semi-final solid metal products. They can also be the source of holes or tears in the metal intended for the production of thin sheets or wires. Therefore, the filtration process of liquid aluminum alloys prior to casting has a crucial importance to fulfill cleanliness requirements of subsequent processes, in order to avoid high rejection rates and productivity losses [1-8].

1.1 Deep Bed Filtering of Molten Aluminum

Filtration process is the last possible step for the purification of molten aluminum metal prior to casting as shown in Figure 1-1. To ensure clean metal production, deep bed filters with graded tabular alumina particles are used before casting of aluminum ingots in

foundries. Liquid aluminum passes through the filter bed of superposed layers of tabular alumina particles with various sizes, and inclusions are separated from the melt.
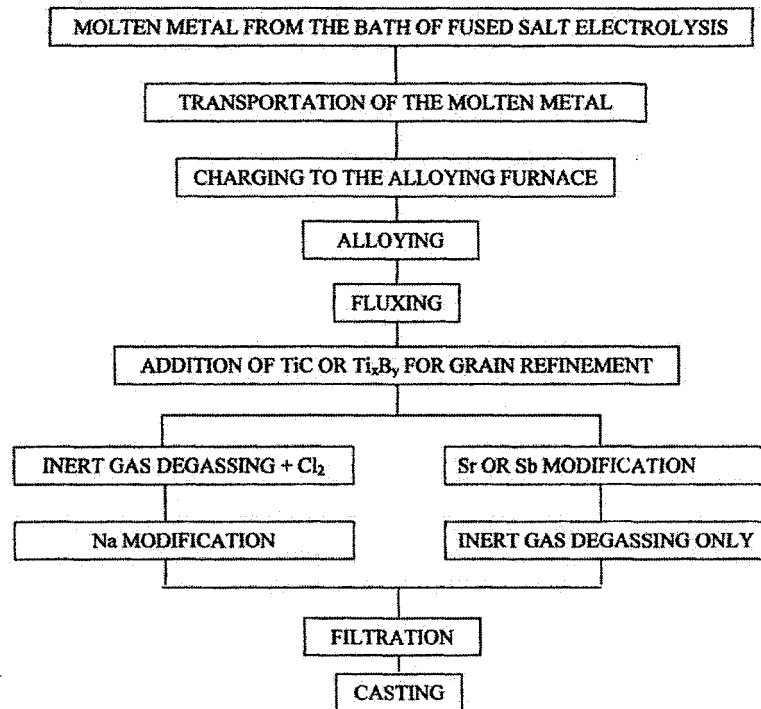
Figure 1-1: Molten Aluminum Treatment Stages Before Casting [9-10]

Deep Bed Filter is made of a steel frame associated with a refractory lining, a filtering material, an insulated lid, and heating units (Figure 1-2 and Figure 1-3). According to Clement [11], a system of liquid aluminum filtration has a steel structure is divided into two parts, a filling chamber and a filtering chamber. The first part is the space required for filling and the second part is the section where the actual filtration is carried out. The filtering chamber has an approximately height of 1.5 m and a global surface of 2.7 m^2. This section consists of layers of graded tabular alumina particles supported by ceramic grids

placed at the bottom. Alumina balls of 12-18 mm are used to prevent the crushed alumina particles (3-6 mesh gravel) from falling down through the supporting grids. They also help distribute the liquid metal uniformly over the filtering surface.
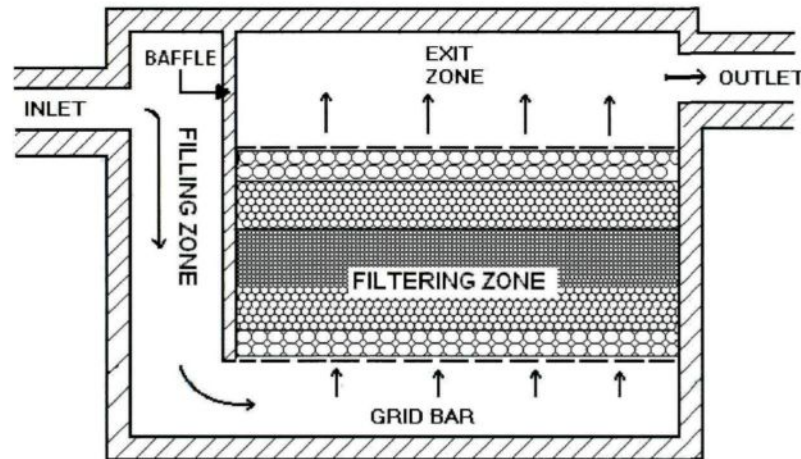
Figure 1-2: A Schematic View of a Deep Bed Filter Process Before Casting [11, 12]
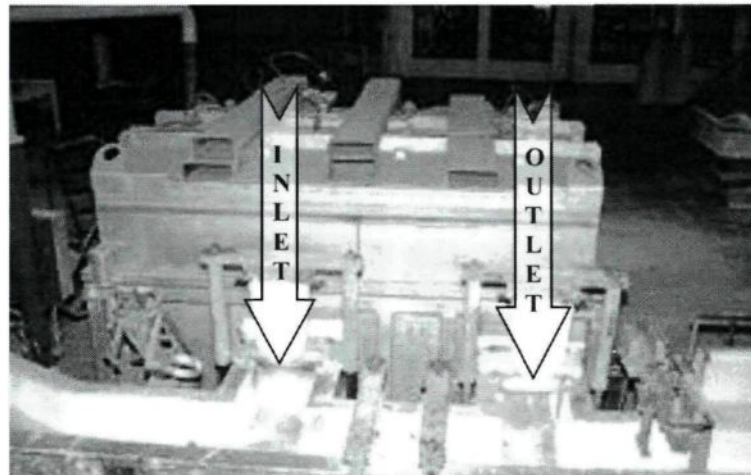
Figure 1-3: A View of a Deep Bed Filter During Molten Aluminum Filtration Process [12]

Filtration which is carried out in deep bed filters is a semi-continuous process. Each cast in the foundry lasts about 2-4 hours with a constant metal flow rate. Metal is filtered continuously prior to casting. The casting period is followed by an inter-cast period of 2-4 hours. During this period, the metal filtration stops. The driving force for filtration is generated using a gravity-pour principle.

It was reported by Clement [11] that the pore diameter in a deep filter is 100 times the filtered particle (inclusion) diameter, thus inclusions are captured by adsorption on the pore walls throughout the entire depth of the filter. The recommended filtration speed varies from 1 to 4mm/s [11]. Several thousand tons of liquid molten aluminum could be efficiently filtrated using deep bed filters.

1.2 The Statement of the Problem

An efficient filtration process requires a good quality filter media. However, the quality of bed media changes from supplier to supplier as well as from shipment to shipment coming from the same supplier. At this point, industry needs a method which can predict the efficiency of the filtration. For this, it is important to know the nature of the interactions between bed media, metal, and inclusions.

The physical simulation techniques and computer-based mathematical models [13-27] were used in aluminum industry to have a fairly good understanding of the thermal and hydrodynamic aspects of the filtration process during the last two decades. However, the experimental studies were carried out mostly with water since it is very difficult and costly

to carry out aluminum filtration studies in the laboratory. On the other hand, the mathematical models relied on empirical model parameters obtained from plant data. The physical and chemical mechanisms involved in aluminum filtration are not well known and certain discrepancies between the actual filter performance and the one predicted by the physical and mathematical models still exist. One major reason for this is that the interactions between filter media, molten aluminum, and inclusions such as reactions taking place during filter life have never been taken into account in these physical and mathematical modelling studies.

A literature search [28-72] carried out on the chemical reactions taking place at the Mg-Al alloy/alumina ceramics interface showed that there is no consensus on the interfacial reactions occurring and the resulting reaction products. The final product on aluminum/alumina interface could be either Mg-spinel ($MgAl_2O_4$), magnesia (MgO), or a mixture of both. It is evident that the interfacial reactions in all these studies are carried out under different experimental conditions (differences in aluminum alloy composition, impurity content of alumina, temperature, residence time, atmosphere control, etc.).Therefore, the final product found in each study varies. It is pointed out by researchers that not only the thermodynamics but also the kinetics of the reactions need to be considered while examining the results.

The interfacial reactions taking place between aluminum and ceramics reported in the literature are for different applications such as refractories and aluminum interface, metal matrix composites, etc.

Only a few researchers have reported the importance of dynamic conditions on the evaluation of refractory corrosion or conducted studies under dynamic conditions [59, 65-66, 73-76]. Jingguo Gao et al [65] reported that the corrosion of refractories under dynamic conditions is more severe than those observed under static conditions.

No reported studies were found in the literature on the chemical interactions of inclusions with filter media.

1.3 Objective

In this study, the objective is to investigate the interactions between alumina, liquid Al-Mg alloys, and its inclusions under both flow (dynamic) and stagnant fluid (static) conditions. The aim is to better understand the mechanism of interfacial reactions at filter media/aluminum alloy interface which is not clear in the literature.

1.4 Scope

The characterization of commercial tabular alumina particles regarding grain size, apparent porosity, chemical composition, and surface roughness properties was conducted.

Chemical interactions between alumina, aluminum alloys, and its inclusions were investigated under both static and flow conditions. In order to study these interactions under dynamic conditions, a knowledge of the velocity field in the vicinity of the alumina particles is very important. Operating a small bed filter for a long period of time is difficult and costly because metal should be melted and pumped continuously through the filter. In this project, two unique experimental systems which can simulate the flow condition of the

industrial bed were designed and built. The experiments with liquid aluminum alloys (0, 2, 5, and 7 wt% Mg addition) were conducted for various residence times (from 6 hours to 168 hours) using these experimental systems to determine the following:

- Effect of molten aluminum velocity on the extent of aluminum/alumina interfacial reactions

- Effect of impurities found in alumina (Na_2O, SiO_2, CaO, MgO) on aluminum/alumina interfacial reactions

- Effect of inclusion presence (such as MgO, $MgAl_2O_4$) at aluminum/alumina interface and its impact on interfacial reactions

Measuring the flow of molten aluminum at high temperatures is a real challenge; therefore, a replica of the experimental system was fabricated using plexiglass and glass. A visualization technique was used to measure the velocity field under different operating conditions for various design parameters of the experimental system. A parametric study was carried out, and tests were done under different conditions using the water model of the experimental system.

A mathematical model was also developed to predict the flow field around particles in the experimental system. The mathematical model was validated using the water model results. This model was then used to conduct parametric studies to identify the design and operating parameters for the actual experimental system using aluminum in which the flow field would be similar to that of the industrial filter.

The samples obtained from aluminum-alumina experiments were analyzed by using the optical microscope, the scanning electron microscope – energy dispersive X-ray spectroscopy (SEM-EDX), electron micro probe analysis and the X-ray diffraction (XRD). According to the results of these tests, reaction mechanisms were suggested.

1.5 Originality of the Study

As it is explained above, there are no reported studies in the literature on the interfacial reactions taking place between alumina (filter media), inclusions, and aluminum metal or its alloys under dynamic aluminum filtration conditions with long contact times. One of the reasons for the lack of such studies is the difficulty and cost of laboratory filtration experiments with molten aluminum.

In this study, an experimental system was designed which can be built at a reasonable cost and operate under conditions similar to those of industrial filters. This system is unique and is one of the main accomplishments of this study. It can be used not only for kinetic studies, but also studies concerning other problems related to aluminum filtration. In addition, the interfacial reactions taking place during aluminum filtration under flow conditions and the nature of the reaction products formed were studied. The results can be used to improve industrial filters.

CHAPTER 2
2. LITERATURE REVIEW

Literature review was focused on the subjects listed below:

i.   Alumina products

ii. Inclusions in molten aluminum alloys

iii. Interfacial reactions between alumina ceramics and molten aluminum alloys:

- Studies on MMC (Metal Matrix Composites);

- Studies on refractories;

- Studies on reaction kinetics of interfacial reactions.

As the filter media is made of graded tabular alumina particles, the information on alumina chemicals which have a very wide variety in the market is of importance.

In the first section of the literature survey, the production methods of alumina chemicals, especially the tabular alumina manufacturing process, were briefly reviewed in order to understand better the differences in alumina chemicals as well as the physical and chemical properties of tabular alumina.

In the second part, the studies on inclusions found in molten aluminum alloys were summarized.

In the last section, the studies found in literature on alumina ceramics/molten aluminum alloys interfacial reactions and the methods used to determine their reaction kinetics were examined.

2.1   Alumina

Aluminum oxide in various forms is used widely in our daily lives. Probably, most of the people are not aware of the presence of alumina in a wide variety of products ranging from toothpaste to spark plugs, from automobile motors and paper production to microchips of TV sets. Figure 2-1 illustrates various forms of aluminum oxide and their production starting from bauxite mine through various processing stages to a wide variety of end uses.

Figure 2-1: Specialty Alumina Production Chart [77]

2.1.1 Alumina Minerals

Aluminum is the most abundant metal and the third most abundant element in the earth's crust, though it does not occur in the metallic state because of its strong affinity for oxygen. Only a fraction of the aluminum containing raw materials is being used for the production of alumina.

Aluminum oxide (Al_2O_3, alumina, corundum) is the most widely used inorganic chemical for ceramics and is produced from bauxite mineral using the Bayer process.

Bauxite is the most important aluminum ore. It primarily contains various mixtures of hydrated aluminum oxide minerals such as gibbsite, bayerite, boehmite, and diaspore. Major impurities present in bauxite are iron oxides (as hematite, goethite or magnetite; 2-20%), titania (2-8%), and silica (0.5-10%). Other impurities can be listed as the oxides of calcium, magnesium, gallium, chromium, manganese, and phosphorus. [78-81]
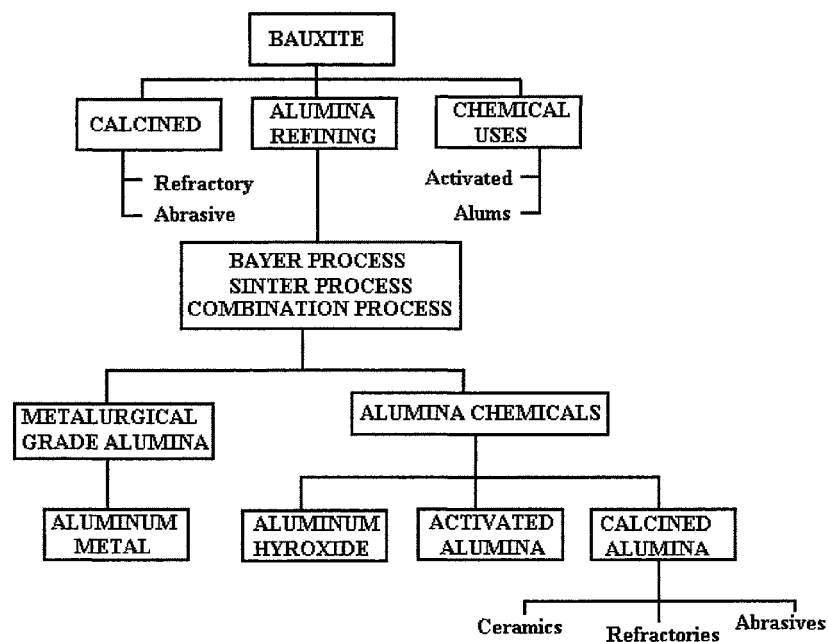
Figure 2-2: Major Outlets of Alumina [79]

Bauxites are typically classified according to their intended commercial application: metallurgical, abrasive, cement, chemical, and refractory. The bulk of world bauxite production (approximately 85%) is used as raw material for the manufacture of alumina via a wet chemical caustic leach method commonly known as the Bayer process. Subsequently, the majority of the resulting alumina produced from this refining process is in turn used as the feedstock for the production of aluminum metal by the electrolytic reduction of alumina in a molten bath of natural or synthetic cryolite (Na_3AlF_6) called the Hall-Héroult process (see Figure 2-2).

Aluminum, oxygen, and hydrogen form three crystalline compounds: Al_2O_3, $AlOOH$, and $Al(OH)_3$. Different phases of these compounds are given in Table 2-1.

Table 2-1: Comparison of Nomenclatures [78]

Mineral Name	Chemical Composition	Accepted Crystallographic Designation	Alcoa (1930)
Gibbsite	Aluminum trihydroxide	$\gamma-Al(OH)_3$	Gamma alumina trihydrate
Bayerite	Aluminum trihydroxide	$\beta-Al(OH)_3$	Beta alumina trihydrate
Nordstrandite	Aluminum trihydroxide	$Al(OH)_3$	-
Boehmite	Aluminum oxide hydroxide	$\gamma-AlOOH$	Gamma alumina monohydrate
Diaspore	Aluminum oxide hydroxide	$\alpha-AlOOH$	Alpha alumina monohydrate
Corundum	Aluminum oxide	$\alpha-Al_2O_3$	Alpha alumina

Gibbsite ($\gamma-Al(OH)_3$) occurs in huge quantities in bauxites, tropical soils, and clays. Nearly 30 million tons of gibbsite are produced each year by the Bayer process. Largest consumption of gibbsite is by the thermal decomposition to metallurgical alumina, which is electrolytically reduced to aluminum by the Hall-Heroult process.

Bayerite (β-Al(OH)$_3$) is rarely found in nature. It can be produced in several ways. It is produced commercially as a precursor for catalysts, substrates, or adsorbents which require an aluminum oxide with low sodium content.

Nordstrandite (Al(OH)$_3$) is discovered by Van Nordstrand and his coworkers in 1956. It was found in tropical soils. It has not been commercialized because its structure and properties are similar to those of gibbsite and bayerite, but its production process is more complicated compared to theirs.

Diaspore (α-AlOOH) is a major constituent of bauxites of the Mediterranean type, but also occurs in certain alumina clays and alumina rich metamorphic shales. Commercial production of diaspore has been almost abandoned because of high temperature and pressure conditions required for its formation. Gibbsite bauxites are abundant and have considerably less harsh process conditions than those of diaspore bauxites.

Boehmite (γ-AlOOH) is abundant in geologically younger bauxites. It can be synthesized by treating aluminum trihydroxides or aluminum metal hydrothermally at temperatures above 375K. Boehmite can be produced by the neutralization of aluminate solutions at around 473K. Boehmite is an industrially important precursor for activated aluminas used in the manufacture of catalysts and adsorbents.

Corundum (α-alumina) is the only thermodynamically stable form of aluminum oxide. It is one of the most important ceramic raw materials in industry. Up to 1960s, metallurgical alumina used in the Hall-Heraoult process contained high amounts of α-alumina. In today's practice, products which are only partially transformed to the stable oxide, obtained at lower calcination temperatures, are used for metallurgical purposes.

The prefix α and γ are used to designate the hexagonally packed structures and cubically packed structures, respectively [78].

2.1.2 Bayer Process

Traditionally, 90% of the aluminum hydroxide is produced from bauxite in the Bayer process which means it is the most important commercial route for the production of aluminum hydroxide. It was invented almost 100 years ago, but it is still the most economical way of manufacturing aluminum hydroxide. Consequently, the solubility of Al_2O_3 in strongly alkaline solutions has attracted much interest due to its importance for the Bayer process which is based on the reversibility of the reaction given by Eq. 2.1 between aluminum hydroxide and an alkali [80-83].

Bayer process produces a nominal 99.5% Al_2O_3 product. The alumina can be prepared in a range of grades to suit specific applications mentioned previously. The grades differ by size and shape of the crystals and the impurity content. The dominant impurity is Na_2O with a maximum concentration of around 0.5%.
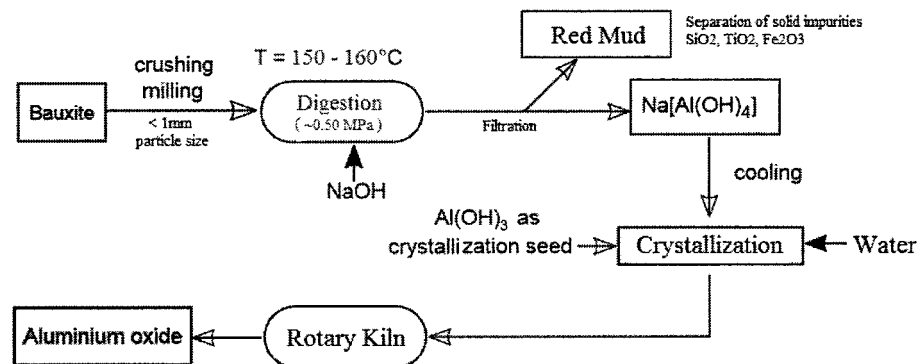
Figure 2-3: Bayer Process Flow Chart [80]

The flow chart for Bayer process is shown in Figure 2-3. The steps in this process are as follows:

Grinding: The bauxite is ground to a particle size of less than 1 mm. This is done to increase the total surface area of the particles in order to reduce the processing time for chemical reaction in the following step.

Digestion: Ground bauxite is treated with NaOH solution at 150-160°C. The system pressure is held at 0.5 MPa. The following reaction takes place and most of the hydrated alumina goes into solution as sodium aluminate [80-83]:

$$Al(OH)_3 \text{ (s)} + NaOH \text{ (aq)} \longrightarrow Na^+ \text{ (aq)} + Al(OH)_4^- \text{ (aq)} \tag{2.1}$$
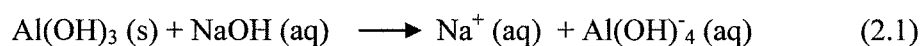
Filtration: The solid impurities such as SiO_2, TiO_2, and Fe_2O_3 cannot dissolve in NaOH solution. Therefore, they are separated by filtration.

Precipitation: After cooling, the filtered sodium alumina solution is seeded with very fine gibbsite. At lower temperature, aluminum hydroxide forms as the stable phase. Precipitation rate increases with decreasing temperature and pH. CO_2 bubbling is used to decrease pH levels.

Washing: Precipitates are filtered and then washed. This reduces the sodium content of aluminum hydroxide.

Calcination: Aluminum hydroxide is then calcined at 1100 – 1200°C to convert the hydroxide to the oxide according to the reaction given by Eq.2.2 [80-83].

$$2Al(OH)_3 \text{ (s)} \longrightarrow Al_2O_3 \text{ (s)} + H_2O \text{ (g)} \tag{2.2}$$
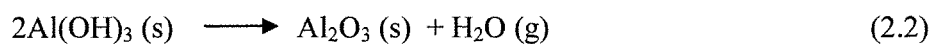
During this transformation, alumina passes though different crystalline phases as shown below:

$Al_2O_3.3H_2O \rightarrow Al_2O_3.H_2O \rightarrow \gamma\text{-}Al_2O_3 \rightarrow \delta\text{-}Al_2O_3 \rightarrow \theta\text{-}Al_2O_3 \rightarrow \alpha\text{-}Al_2O_3$
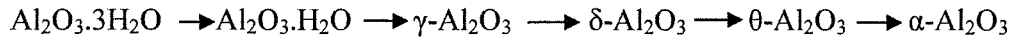
Milling: The powder produced in the previous step is milled to give the desired particle size. This product is called "calcined alumina" which has 99.5% purity, and its major impurity is Na_2O (max.0.5%). Typical composition of calcined alumina is shown in Table 2-2.

Table 2-2: Composition of Calcined Alumina [80]

	Normal Na_2O (wt%)	Low Na_2O (wt%)	Reactive (wt%)
Al_2O_3	98.9-99.7	99.5-99.8	>99.5
SiO_2	0.02-0.05	0.07-0.12	0.04-0.08
Fe_2O_3	0.04-0.05	0.04-0.06	0.01-0.02
Na_2O	0.3-0.6	<0.13	0.08

The presence of Na_2O in alumina can be unacceptable for some applications. Na+ ion is mobile in an electric field and causes degradation of electrical insulation. During high temperature processing, a sodium beta-alumina ($Na_2O.11Al_2O_3$) phase can form which leads to a reduction in density, strength, thermal shock resistance, and corrosion resistance of the final product [80, 84].

Calcined alumina is basically used in the production of metallurgical grade alumina and alumina chemicals. It was reported in the literature [79] that almost 93% of the calcined alumina output goes into metallurgical and smelter-grade alumina production. Alumina

chemicals, which consist of tabular alumina, cover the remaining 7% of the calcined alumina production.

Variations of alumina types depend on the changes in different process parameter from plant to plant, although they are produced in a similar fashion.

2.1.3 Tabular Alumina

The name "tabular" comes from its crystal shape which is in a flat tablet-like form of corundum crystals with 50 to 500 μm in size. Tabular aluminas are highly-fired, fully-shrunk recrystallized α-Al_2O_3. Structural and chemical properties of tabular aluminas are evidently different from other dense, fine-crystalline, sintered aluminas and fused aluminas. Tabular alumina was first developed by ALCOA in the late 1930's. The original process is extensively modified for over 60 years in order to have optimum product quality, economy, and consistency of production [87-90].

The production process of tabular alumina contains basic unit operations such as grinding, pelletizing, drying, sintering, and tabular crushing steps (see Figure 2-4).

CALCINED ALUMINA

```
                          ┌──────────┐        ┌──────────┐
┌──────────────┐          │ SEED BALL│        │GREEN BALL│
│  BALL MILL   │ ───────▶ │  FORMER  │ ──────▶│  FORMER  │
│(Al2O3 GRINDING)│        └──────────┘        └──────────┘
└──────────────┘                                    │
                                                    ▼
   ┌──────────┐      ┌──────────────┐        ┌──────────┐
   │   DRUM   │ ◀─── │ TABULAR BALL │        │   BALL   │
   │  MAGNET  │      │  CRUSHING    │        │  DRYER   │
   └──────────┘      └──────────────┘        └──────────┘
        │                    ▲                     │
        ▼                    │                     ▼
   ┌──────────┐              │              ┌──────────┐
   │  SCREEN  │              └──────────────│ CONVERTER│
   └──────────┘                             │(SINTERING)│
        │                                   └──────────┘
        ▼
   ┌──────────┐
   │ PACKING  │
   │ MACHINE  │
   └──────────┘
```
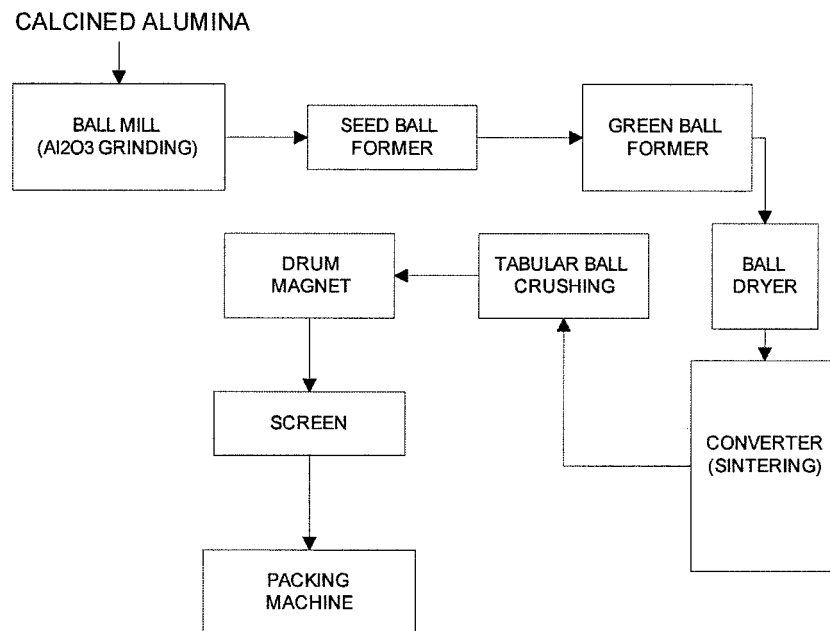
Figure 2-4: Tabular Alumina Production Flow Sheet [88]

Calcined alumina is used for tabular alumina production. Fine crystalline α-alumina feed goes through sintering and densification. It is fed into a ball mill in which dry a grinding process is performed until 100-325 mesh Bayer agglomerates are obtained.

Finely ground calcined alumina is also preferred because it can easily be shaped to balls. Green balls are produced by sequentially wetting the balls' surfaces with a fine water/binder spray. They need to have sufficient strength to avoid breakage while handling and transporting to the dryer chamber. Organic binders (starch) or H_3BO_3 is sometimes used for enhancing the green strength.

Dryer chamber which is positioned above the converter is used for sintering. By using hot exhaust gases of the converter (~500°C), nominal 15% moisture of the green balls

are removed. Thermal shock fracture is an important problem of this process; therefore, temperature should be carefully controlled. Fractured balls can impede the uniform gravity free flow through dryer since they cause channelling and non-uniform drying which further worsens the thermal shock episodes.

Sintering operation is performed using continuous Curtis converters with natural gas-air mixture or butane at sintering temperatures of 1815 to 1925°C. A discharge table controls the alumina ball flow in converter so that proper drying rates and full conversion to tabular alumina can be obtained. Flow of theoretical gas/air mixture is balanced with the alumina ball throughput. Boric acid (H_3BO_3) addition helps to reduce Na_2O content during alumina calcination at a temperature of about 1400 °C. It removes soda by volatilization as sodium borate compounds. In addition, Na_2O content and the porosity of alumina are reduced using the synergetic reaction of magnesium salt and boron compound with calcined alumina during sintering for 1-25 hours within the temperature range of about 1600° to 1900°C.

Hot sintered alumina balls are stored in cooling bins. After cooling, they go through the crushing, de-ironing, and sizing steps. Gyradisc crushers are used. After crushing, two magnetic drum separators remove the metallic iron from the crushed tabular alumina. The non-magnetic hardened alloy crushers are not eligible because of inability to remove metallic contamination by de-ironing. Graded tabular sizes are stored in the needle bins. Over-screened tabular alumina is fed back to the Gyradisc crusher for further size reduction. Different tabular alumina grades are compared in Table 2-3 [88-89].

In Japan and Europe, environmental emission control laws prevent the use of boric acid additions for soda reduction in the tabular alumina T-60 grades since 1970's. Therefore, typical T-60 tabular alumina contains 0.25 to 0.30% Na_2O. The soda level directly depends on the soda level of calcined Al_2O_3 feedstock.

Boric acid is very effective to reduce the soda level in sintered aluminas. It is reported by MacZura [45-46] that tabular alumina T-61 grade with <0.01% Na_2O is produced from 0.4-0.5% Na_2O containing calcined alumina feedstock. However, excess usage of boric acid causes channelling problems at the cooler portion of the shaft furnace because of condensation of sodium boride compounds. This might significantly increase the rejection rates.

In 1980's, ALCOA carried out an economic study on tabular alumina process, and it was reported that, even when moderate additions of boric acid is used, the rejects are in excessive amounts. Consequently, new tabular alumina grade T-64 which has a typical soda content of 0.15 to 0.20% can be produced from intermediate soda-content alumina feedstock without the use of boric acid.

Product quality of T-64 is enhanced by eliminating boron additions. This resulted in a more consistent microstructure than that of T-61 grade obtained during converter firing. Desired properties of tabular alumina which define its quality can be listed as:

- large α-Al_2O_3 crystalline structure

- high closed porosity

- low open porosity

- low water absorption

Table 2-3: Comparison of Tabular Alumina Grades [88-89]

Typical Properties (Converter discharge)	Published Data			
	ALCOA T-64	ALCOA T-60	ALCOA T-61	KAISER T-1061
Al_2O_3 (wt%)	99.7+	99.5	99.5+	99.8
SiO_2 (wt%)	0.04	0.04	0.06	0.06
Fe_2O_3 (wt%)total	0.06	-	0.06	0.03
Fe_2O_3 (wt%)acid soluble	0.01	0.02	-	-
Na_2O (wt%)	0.16	0.30	0.10	0.03
CaO(wt%)	0.04	0.05	-	-
MgO(wt%)	<0.001	-	-	-
B_2O_3(wt%)	<0.001	-	-	-
Bulk density, packed, lb/ft^3				
Converter Discharge(CD)	128		125	
Granular, -14 mesh	138		135	
Powder, -325 mesh	143		140	
Specific gravity, bulk, g/cm^3	3.50-3.65	3.6	3.40-3.60	3.40-3.56
Apparent porosity(%)	3	4.0	5	5
Water Absorption (%)	0.8	1.5	1.5	2
Specifications for shipment				
Na_2O (max) (wt%)	0.22	0.40	0.20	0.20
Apparent porosity (CD mx) (%)	7	8.0	10	10
Water Absorption (CD mx) (%)	2	4.0	4	4

If the tabular alumina is over or under fired, excessive open porosity and high water absorption rate can evidently be observed. In this case, also the grain strength values are not consistent. The open porosity problem of underfired tabular aluminas can be solved by small additions of MgO, which lowers the sintering temperature and improves the densification. Although MgO enhances the densification and lowers the porosity of alumina, it also reduces the grain size to <25 μm. The mechanical studies showed that dense and finely grained sintered aluminas have poor thermal shock resistance compared to that of the alumina with large grain size (50 to >400 μm) and lower density crystalline structure.

The physical and chemical properties of tabular alumina listed below indicate the reason for their utilisation as a refractory line raw material [90].

- High chemical purity (>99.5% Al_2O_3)

- Extreme hardness of the ultimate crystals

- Low apparent porosity (AP~3%, H_2O absorption~0.8%, 3.97 true density, 3.5 to 3.65 gr/cm^3 particle density)

- High melting point (~ 2050°C)

- Chemical inertness (no reaction with most alkalies, mineral acids except hydrofluoric and phosphoric acid)

- Relatively good thermal conductivity for ceramic materials

- Relatively good thermal conductivity

- High electrical resistivity

- Good volume stability (they are fully shrunk)

- Highly reactive surface for ceramic, chemical, and cement bonding

- Absence of microcracks and gross internal porosity

- High individual grain strength

Tabular alumina is ideal base material for the 90-100% Al_2O_3 class of high alumina brick and monolithic lining. Some of the major applications are [90] :

- Iron and steel industry: Injection lances, ladle lining, slide gate valves and nozzles, shrouds, submerged nozzle, impact pads, snorkels, tap hole mixes, torpedo lining, purging cones, well blocks, weirs, dams.

- Petrochemistry: Catalyst transfer lines in FCCU (Fluid Catalytic Cracking Unit) regenerator vessels, slide valves.

- Waste incineration furnaces

- Kiln furnaces

- Molten metal filters

2.2   Inclusions in Molten Aluminum Alloys

Inclusions in aluminum might have an adverse effect on surface appearance and severe effects on mechanical properties. They might also influence machining and forming properties of the metal.

Inclusions generally fall into two classes, exogenous and indogenous. Exogenous inclusions are imported to the molten metal stream from external sources, such as occluded particles on and within primary and secondary ingot, major alloying elements and master alloys as well as containment refractories. Indogenous inclusions form as a result of chemical reactions within the metal handling system. These inclusions are formed by oxidation and formation of aluminum carbide and halide salts.

In Table 2-4, the most common inclusion types found in unprocessed Al-Mg alloys are listed. The observed inclusion sizes in unprocessed aluminum melts change from MgO dispersoids of a few microns to Al_2O_3 films and clusters that extend to several millimeters. Most products oblige an inclusion size of less than 50 μm at concentrations in the order of several volume parts per million.

Table 2-4: Most Common Inclusions in Al-Mg Alloy System [1-6, 22]

Inclusions	Form	Chemical formula	Density (g/cm³)	Size range*
Aluminum oxide	Films or group of films Polygonal particles	Al_2O_3	3.98	t= 0.1-5 µm d= 10-1000 µm d= 0.2-30 µm
Magnesium oxide	Polygonal particles Films consisting of particles	MgO	3.58	d= 0.2-1 t= 1-8µm d= 1-100 µm
Spinel	Truncated prymidical shaped particles Thick films Lumps of particles	$MgAl_2O_4$	3.60	d= 0.1-5 µm d= 1-6 µm t=10-1000µm
Aluminum carbide	Rectangular or Hexagonal discs	Al_4C_3	2.36	d=0.5-25µm t<1 µm
Complex oxides (Na, K, Ca, Al, O)	Thick films			t≈10µm d= 50-500µm
Titanium di-boride	Clusters of hexagonal or rectangular discs	TiB_2	4.5	d=1-50 µm

* "t" is thickness and "d" is the diameter.

The studies found in the literature [6-8, 11-14] on the deep bed filtration of aluminum alloys and mechanisms of inclusion entrapment in the filter media underline the effectiveness of deep bed filters in capturing small inclusions (<20µm) due to high media surface area. In these studies, inclusion capture is considered to be the result of two sequential events:

1. Transport of an inclusion to capture sites on the filter media surface by impingement, interception, sedimentation, diffusional and hydrodynamic effects.

2. Subsequent attachment of the particles to these sites by the forces developed through pressure, chemical or Van der Waal effects.

It is stated that particulate type and size, fluid approach velocity, temperature and media characteristics are important parameters which determine the relative dominance of each force mentioned above. However, studies [18, 21, 91-93] conducted on the description of potential capture mechanisms in aqueous systems indicated that pressure/Van der Waals forces/double layer forces are responsible for particle attachment.

In literature, there is no study reported on the chemical interactions between inclusions and filter media. A number of studies on MMC was reported which dealt with the interaction between aluminum matrix and micron size reinforcement materials such as Al_2O_3, MgO, $MgAl_2O_4$, etc. These interactions are discussed in the following sections. It is important to note that the particle size of reinforcements used in MMC's are much smaller than that of the bed media or have completely different forms such as fibres. Also, almost all the studies are conducted under static (no flow) conditions and in much shorter contact times compared to those encountered during filtration.

2.3 Interfacial Reactions

Interactions of molten metals and ceramics at elevated temperatures are basically molecular interactions of solid/liquid phases. These are mostly chemically governed and strongly temperature and time dependent interactions. It is stated in literature that the chemical interactions between solid and liquid phases can be improved by increasing

wetting at the liquid/solid interface which actually corresponds to molten metal/ceramic interface in Al/Al$_2$O$_3$ system. This is achieved by either adding certain elements into the molten metal or coating the ceramic surface with a material chemically preferred by the metal [94-96].

The studies on Al-Mg alloy/alumina interfaces found in literature are either in the field of composite materials or refractories. There are also a few studies [52, 53] found on oxidation of Al-Mg alloys which also mention the possible reactions taking place along the Al-Mg alloy/alumina interfaces.

In these studies, there is no consensus among researchers on the final product of Al-Mg/Al$_2$O$_3$ interaction at elevated temperatures. It was reported that majority of the chemical reactions taking place on Al-Mg alloy/Al$_2$O$_3$ interface result in the formation of MgO (magnesia) and/or MgO.Al$_2$O$_3$ (Mg-spinel) [33,50]. It was also stated that the formation of spinel and/or magnesia phase(s) is strongly dependent on alloy compositions, alumina chemistry, the gas surrounding the ceramic substrate, experimental procedures, etc. The differences in type and composition of reaction products arise mainly from these parameters. It is also reported that sometimes thermodynamically favorable reactions between the metal and the alumina may not take place at a noticeable rate when the chemical kinetics gain importance [58-59].

2.3.1 Studies on MMC`s

The interface between reinforcement and matrix plays an important role in the mechanical properties of composites. A strong composite often requires a strong interfacial

bond to allow load to be transferred from the matrix to the fibres or particles. The strength of the interfacial bond is strongly related to the nature of interfaces. Chemical reactions between the reinforcement and matrix, the segregation of solute elements, and the formation of new phases or precipitates are often observed. Since the interfaces are crucial, many studies [28-51] have been carried out to understand the nature of the interface between matrix and reinforcements under different experimental conditions. In this part, the studies found in the literature on interfacial reactions in MMC's are reviewed.

Since the wettability between unalloyed molten Al and Al_2O_3 is not good when the temperature is below 900°C [28], different techniques have been adopted to improve the Al_2O_3 and Al matrix bonding. One of the most common methods is to alloy molten aluminum with elements such as Mg or Cu which can both strengthen the matrix and also improve the wettability of molten aluminum. When alloying elements are added into a liquid metal, the alloying element that has a higher affinity for oxygen tends to migrate to the oxygen rich interface, which is the reinforcement material surface in MMC's, in order to produce an interfacial bond.

In the literature, the possible reactions of Al_2O_3/Al-Mg alloy systems are found as follows [28-33]:

$$Mg(l) \ + \ 2Al(l) \ + \ 2O_2(g) \ = \ MgAl_2O_4(s) \tag{2.3}$$

$$Mg(l) \ + \ \tfrac{4}{3}Al_2O_3(s) \ = \ MgAl_2O_4(s) \ + \ \tfrac{2}{3}Al(l) \tag{2.4}$$

$$MgO \ (s) + \ Al_2O_3(s) = \ MgAl_2O_4(s) \tag{2.5}$$

$$Mg(l) + \tfrac{1}{3}Al_2O_3(s) \ = \ MgO(s) + \tfrac{2}{3}Al(l) \tag{2.6}$$

$$2Al(l) \ + \ \tfrac{3}{2}O_2(s) \ = \ Al_2O_3(s) \tag{2.7}$$

$$Mg(l) \ + \ \tfrac{1}{2}O_2(s) \ = \ MgO(s) \tag{2.8}$$
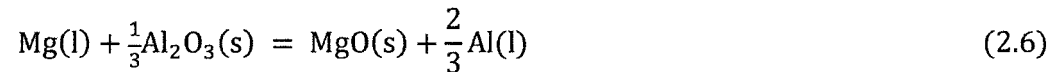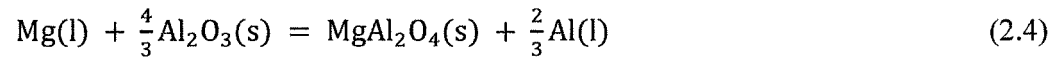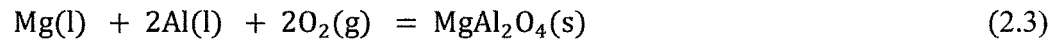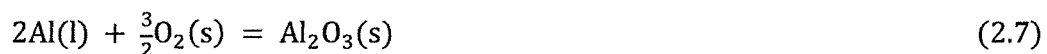
In the literature, different statements are found on the formation of spinel and/or magnesia based on the chemical reactions between Al-Mg alloys and alumina. In this section, the studies which propose chemical reactions and reaction mechanisms for Al-Mg/Al$_2$O$_3$ system are reviewed.

Levi et al.[29] studied the interfacial reactions between discontinuous polycrystalline Al$_2$O$_3$ fibres and Al- 2 to 8 wt% Mg, Al-4.5 wt% Cu and Al-4.5 wt%Cu-1 to 2 wt% Mg alloys. The effect of alloying elements on bonding of the fibres and interfacial interactions were investigated in Levi's study. The experiments were conducted using both static and vigorously agitated liquid and semi-solid alloys. The microscopic examinations showed that the addition of elements such as Mg or Cu has a great influence on attaining desired interfacial reactions which yield an increase in wetting and bonding of fibres. It was reported that the bonding was achieved through the formation of a MgAl$_2$O$_4$ (by mostly Reactions 2.3 and 2.4) or CuAl$_2$O$_4$ (spinel) layer by the reaction between fibres and Mg or Cu in the liquid Al. Electron diffraction from areas in the vicinity of the fibre showed that the presence of fine polycrystalline alpha-Al$_2$O$_3$ in the affected zone and indicated that the material at the fire edge (richest in magnesium) was MgAl$_2$O$_4$ spinel. This observation was further supported by X-ray diffractometry of fibres extracted from the composite after reaction. The reaction layer was not found to be uniform around the fibres, and this was attributed to the factors listed below:

a) The interaction between Al_2O_3 and aluminum alloy may start at localized areas and then spread laterally with simultaneous radial growth,

b) The kinetics of the reactions might be anisotropic,

c) The grinding effect of the moving primary solid particles (due to the agitation of melt) could induce severe localized erosion.

It was also pointed out by Levi et al. [29] that the reaction shown in Eq. 2.4 is thermodynamically more predominant than the reaction shown in Eq. 2.6 when Mg content is less than 4% in the temperature range from 650 to 900°C (see ΔG data for 900°C in Table 2-5). Eq.2.5 takes place in solid state; hence, it is less favorable than the other reactions. According to Levi, Eqs.2.3 and 2.4 basically determine the formation of $MgAl_2O_4$ in the system.

Table 2-5: Free Energy Changes for Possible Interfacial Reactions (ΔG in kJ/mole) [29]

Reaction	Levi [43] at 900°C			Hallstedt [55] Pure Mg at 723°C	Reac. no
	Mg concentration				
	2 wt%	4 wt%	8 wt%		
$[Mg] + 2[Al] + 2(O_2) = <MgAl_2O_4>$	-1888	-1905	-1962		2.3
$[Mg] + 4/3<Al_2O_3> = <MgAl_2O_4> +2/3[Al]$	-39	-43	-52		2.4
$<MgO>) + <Al_2O_3> = <MgAl_2O_4>$	-28	-28	-28	-47	2.5
$2[Al] + 3/2(O_2) = <Al_2O_3>$	-1388	-1391	-1401		2.7
$[Mg] + 1/2(O_2) = <MgO>$	-1016	-1018	-1024		2.8
$[Mg]+ 1/3<Al_2O_3> = <MgO> + 2/3[Al]$	-33	-46	-73	-39	2.6
$[Mg] +1/2 <SiO_2> = <MgO> + 1/2[Si]$	-	-	-	-128	2.9

Symbols: <Solid>, (Gas), [in solution]

Munitz et al.[28] investigated the interfacial reactions between Al-4 wt% Mg alloy and α-Al_2O_3 fibres at 685°C (with 30 minutes of melt agitation time). The reaction

surface investigations using Auger and electron diffraction methods indicated the presence of discrete Mg-spinel ($MgAl_2O_4$) crystals on the fibre surfaces. The thickness and coverage of the spinel was found to be varied with processing conditions.

The work done by Quigley et al. [30] also focused on interfacial reactions between Al-4 wt% Mg alloy and α-Al_2O_3 fibres (>99% pure, 15-25 μm in diameter, up to 6 mm in length) at around $720^\circ C$. Quigley's study [30] confirmed that $MgAl_2O_4$ was the main reaction product at the interface of Al_2O_3 and Al- 4%Mg alloy. It was suggested that the $MgAl_2O_4$ spinel formed by the reaction between Mg which was in molten metal solution, and both the Al_2O_3 fibre and the fine α-Al_2O_3 which resulted from oxidation of the melt. Eqs. 2.3 and 2.4 are equivalent according to Quigley et al. [30].

McLeod et al. [33] studied the kinetics of spinel growth in melts of alumina-reinforced composites using Al- 1%Mg alloys in the temperature range of $675^\circ C$ to $700^\circ C$. Stability diagrams for MgO-$MgAl_2O_4$ and $MgAl_2O_4$-Al_2O_3 equilibria were plotted by McLeod as shown in Figure 2-5. In these diagrams, Mg-spinel was shown as stable phase at $700^\circ C$ when the magnesium concentration in the melt was less than 1%. (required Mg concentration for the formation of MgO at $700^\circ C$ was shown to be higher than 1% Mg.)

Petitcorps [39] and Molins [40] worked on interfacial reactions between Al-Mg (Mg from 0.3-2.2 wt%) and Saffil Al_2O_3 fibre which contains 4 wt% SiO_2. It was reported that the reaction product is the mixture of MgO and $MgAl_2O_4$. The following chemical reactions were suggested:

$$1/2 < SiO_2 > + [Mg] = < MgO > +1/2 < Si > \qquad (2.9)$$

$$2 < SiO_2 > +[Mg] + 2[Al] = < MgAl_2O_4 > +2[Si] \qquad (2.10)$$
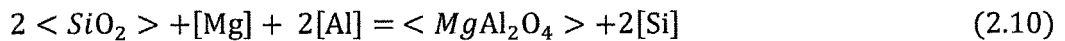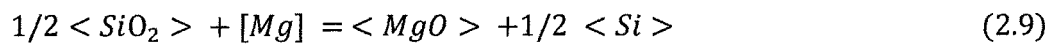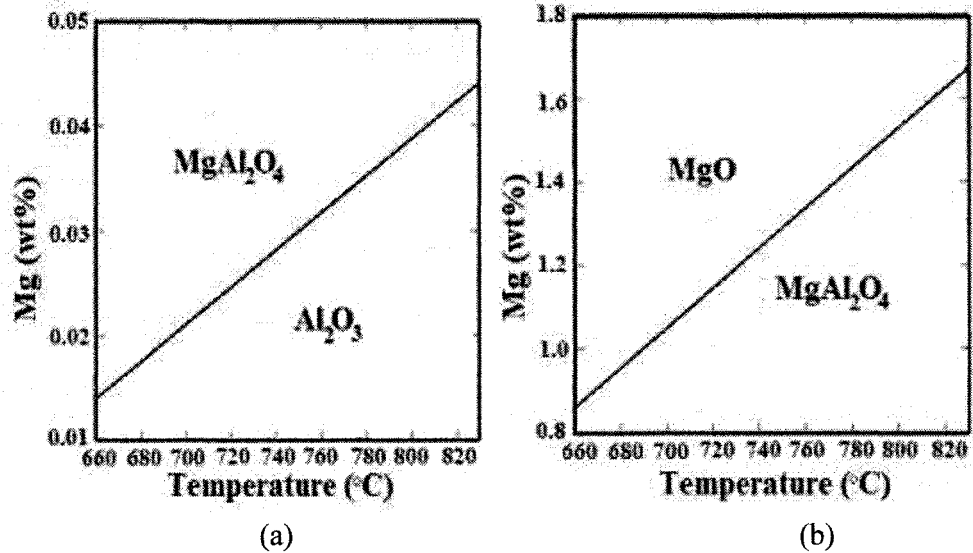
Figure 2-5: Composition / Temperature Stability Regions for (a) Al_2O_3-$MgAl_2O_4$ (b) MgO-$MgAl_2O_4$ Equilibria [33]

Hallstedt [41] also conducted reaction kinetics studies in pure Mg/Saffil (96%Al_2O_3-4% SiO_2) system at 727°C. The theoretical study on reactions in pure magnesium and saffil sytem indicated that there is a big driving force for magnesium to reduce both SiO_2 and Al_2O_3 (see Table 2-5), and the magnesium content needed to form magnesia (MgO) must be above 5 wt% at 723°C (see Figure 2-6). The experimental study showed that magnesium reduces silica (SiO_2) and frees silicon into the melt according to Eq. 2.9. Silicon then reacts with magnesium in the solution to form Mg_2Si intermetallics. TEM (Transmission Electron Microscopy) analysis of the samples confirmed the presence of Mg_2Si, and MgO was found to be the final product of magnesium and alumina interaction.
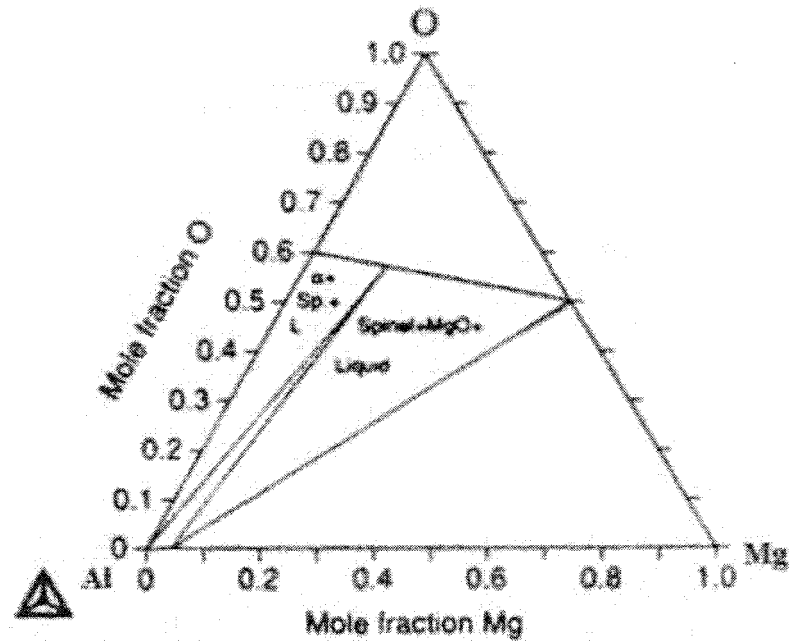
Figure 2-6: Isethermal Section at 723°C of the Al-Mg-O System [41]

(α: α-Al$_2$O$_3$; Sp.: Spinel; L: Liquid)

Karlsen et al. [44] claimed that the main oxygen source for MgO and MgAl$_2$O$_4$ formation at Al-Mg alloy/ Al$_2$O$_3$ interfaces is the trapped air bubbles by alumina particles.

Weirauch [45] reported that no reaction product observed using both optical and scanning electron microscopy methods at Al-3 wt%Mg / saffhire interface after 24 hours of contact time at 800°C. However, experiments conducted using Al-6 wt%Mg alloy by keeping the other experimental conditions constant, a mixture of spinel and α-Al$_2$O$_3$ was found at the interface. It was also reported that the interfacial reaction product in Al-3wt%Mg/MgO system was Mg-spinel under the same experimental conditions.

Vaucher and Beffort [47] claimed that, in Al$_2$O$_3$/Al-Mg alloy system, MgAl$_2$O$_4$ spinel formation is governed by the magnesium content and takes place at 4<Mg<8 wt%.

At higher contents, MgO is exclusively formed while spinel formation decreases as Mg is reduced below 4 wt% and becomes virtually non-existent under 1 wt% Mg content.

Jin and Lloyd [31, 43] investigated interfacial chemical reactions between high purity α-alumina (with major impurities 0.2 wt% Na_2O, <0.04wt%SiO_2, and <0.04wt% Fe_2O_3) and 6 different Al-Mg alloys (2, 2.7, 3, 4, 4.7, and 7 wt% Mg) for up to 120 minutes contact time at 720°C. $MgAl_2O_4$ was found as predominant reaction product for all cases even though MgO is the thermodynamically stable phase for higher magnesium concentrations. They suggested Eq.2.4 for $MgAl_2O_4$ spinel formation. The extent of spinel reaction in the different composites was assessed by dissolving the composite matrix and analyzing for the Mg concentrations in the matrices. The identification of reaction product was achieved by using SEM and TEM analyses. They found that the interfacial reaction rate decreased with the increasing Mg concentration in Al-Mg/Al_2O_3 system (Figure 2-7) when Mg wt% was above a certain value (about 2.8%) and the reaction product was still $MgAl_2O_4$ even though the Mg content was as high as 7 wt%. Lloyd et al.'s studies [31, 43] indicated that the reaction between Mg and Al_2O_3 can even take place in the solid state in 6061/Al_2O_3 composite. It should be noted that the role of aluminum formed during these reactions and its diffusion behavior have not been clearly explained in these studies.
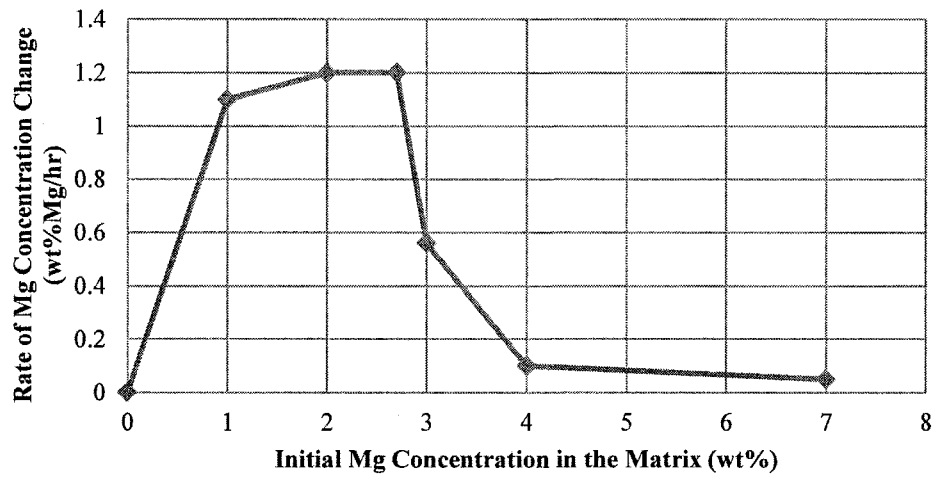
Figure 2-7: Effect of Initial Mg Concentration on the Rate of Mg Concentration Change
During Mixing [43]

Preifer [42] studied the interfacial reactions in magnesium alloy (ZE41A)/α-Al$_2$O$_3$

fibre system. It was reported in this study that a reaction layer of MgO with an average

thickness of 100 nm was found (in the temperature range from 710 to 715°C). The size of

MgO particles was within the range of 10-100 nm. It is proposed that the "seepage"

mechanism involving the infiltration of liquid magnesium through MgO crystals formed at

the initial contact of molten alloy with alumina fibres controls the growth of the reaction

zone. The first contact between magnesium in liquid aluminum and alumina grain starts the

reaction zone nucleation. MgO is formed, and then it grows on the edges of the alumina

grains. MgO nucleation occurs further into the original alumina grains as molten Mg seeps

in between already nucleated and growing MgO grains. It reacts with Al$_2$O$_3$ at the pre-

existing reaction zone/ Al$_2$O$_3$ interface. This seepage process continues until the MgO

grains close to the matrix/reaction zone interface are grown to be large enough to close off

the seepage spaces between these grains or until the molten metal is solidified. This mechanism can explain the formation of the limited thickness of the reaction zone.

In the study conducted by Zhong [46], SEM and TEM (Transmission Electron Microscopy) analyses showed that MgO is the main reaction product in α-Al_2O_3 particles/5083 aluminum alloy (Al-4.1 wt % Mg) system (in as-cast or in remelted composites). Eq. 2.6 was suggested as the main reaction which accounts for the formation of MgO. It was stated that the kinetics is controlled by the seepage of Mg and the release of Al(l) along the newly formed spinel and MgO boundaries. The reaction rate in this system was found to be very low compared to the formation of $MgAl_2O_4$ because of the large volume expansion occurring during the MgO formation. This narrows the diffusion channels between the newly formed crystals. Another factor contributing to the low reaction rate observed is the relatively low Mg diffusivity in MgO crystal.

The interfacial reactions between α-Al_2O_3 fibres (~13μm) and 5083 Al-Mg alloys (4.1 wt% Mg) during the fabrication of composite by composcasting and subsequent remelting at 800°C for 0.5-4 hours was also studied by Zhong and L'Esperance et al. [46]. The main reaction product was found to be fine MgO crystals (5-20 nm) for the as-cast and remelted composites (the residence time ~½ hour). The reaction zone width was about 50-80 nm in as-cast composites, and 100-150 nm in composites held at 800°C for 0.5 hour. It was observed that after remelting at 800°C for 4 hours, layers of large $MgAl_2O_4$ crystals with approximately 1.5 μm thickness replaced previously formed MgO layer (see Figure 2-8). This phenomenon was attributed to the decreasing Mg content in the matrix metal by the author.
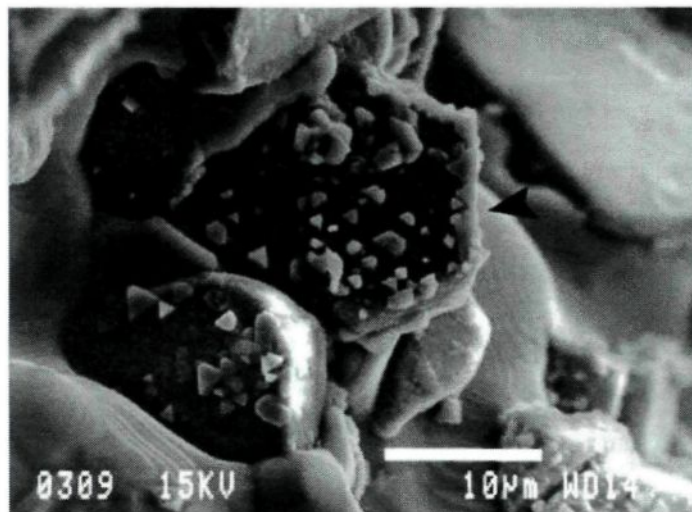
Figure 2-8: Scanning Electron Microscope Images Showing MgAl$_2$O$_4$ Crystals on the Surfaces of the Al$_2$O$_3$ Particles (Composite Remelted at 800°C for 4 hours) [46]

According to Pai et al. [36], MgO was the only reaction product at the interface of 4.5-12wt%Mg-Al alloys and 80 μm diameter Al$_2$O$_3$ particles at 720-790°C. The wetting and bonding characteristics of sapphire (alpha-alumina) with Al-0.94%Mg alloy under 5x10^{-5} torr vacuum at 727°C also showed the presence of MgO at the surface of alumina particles. Varying degrees of magnesium presence was found on alumina particles by electron microprobe investigation, and the X-ray diffraction of the composites confirmed the presence of MgO on alumina particles. The previously mentioned Eq. 2.6 was also suggested by Pai for the MgO formation.

The studies [52, 53] on oxidation of Al-Mg alloys conclude that magnesium increases the oxidation potential of Al-Mg alloys because of its high affinity for oxygen. The analysis of the oxides formed on the surface shows strong evidence of extensive magnesia and spinel formation.

Cappleman and Clyne [38] did not find any interfacial reaction products at σ-Al_2O_3 fibre/9.5-11 wt%Mg-Al alloy interface. The contact time of fibres and molten aluminum alloy was kept very short during the fabrication of composites by using the infiltration method.

From this literature review, it is evident that the interfacial reactions are associated with different fabrication conditions, alloy compositions or the purity of reinforcing materials. Since the thermodynamic calculations cannot always match with the experimental results due to the effect of reaction kinetics, experimental studies need to be carried out under the conditions similar to those of the industrial application of interest.

2.3.2 Studies on Refractories

In aluminum industry, refractory materials are used in almost every step of the production lines, from the alumina calciners and the primary production electrolytic cells, and to the cast house furnaces and other metal handing equipment. Aluminum confinement refractory materials used in aluminum cast house furnaces serve for the following purposes:

    i.   minimize heat losses

    ii.   protect the underlying insulation materials from molten metal

    iii.   protect the steel casing from high temperatures and molten metal

Severe corrosion conditions at and below the metal line are present in aluminum confinement units [54-57]. The chemical corrosion and deterioration of aluminum cast house furnaces are related to the reactions taking place between refractories and penetrating

molten metal. The deterioration of the refractory lining is governed by molten metal properties, refractory material properties, and the mineralogy of the reaction products.

Table 2-6 shows the electrochemical/electromotive series of the metals [58]. All metals will reduce oxides below themselves in the table. For instance, calcium will react with any other oxide present in the table. As it can be seen clearly from this table, the refractories containing silica, sodium, and iron or minerals of these elements will be attacked and deteriorated as a result of exposure to aluminum metal. Presence of alloying elements such as Mg and Ca will result in chemical attack on the refractory materials due the reducing nature of these materials.

Studies found in the literature on the corrosion of refractories generally deal with the aluminosilicate refractory behavior in Al-Mg alloys [54-66, 70-72].

Alumino silicate refractory corrosion by Al-Mg alloys was studied by Steinke and Stett [97]. They outlined the following phenomena which contribute to the refractory attack.

-   Vapor transport and deposition of metals in refractory pores

-   Reduction of refractory oxides (such as silica) with the deposited metals

-   Reaction of simple oxides to form complex oxides of greater volume (e.g. mullite),

-   Increased liquid metal penetration due to enhanced wetting of the altered solid surfaces.

Table 2-6: Electrochemical Series of Metals at 1027°C and Their Stability in Decreasing Order [58]

Metal	Oxide	Free Energy per mole Oxygen, kJ/mole
Ca	CaO	-499
Mg	MgO	-458
Zr	ZrO_2	-428
Al	Al_2O_3	-420
Ti	TiO_2	-354
Si	SiO_2	-335
Na	Na_2O	-236
Fe	Fe_2O_3	-162

Refractories are often corroded by molten aluminum alloys containing magnesium. Magnesium is a strong reducing agent which actively participates in the conversion reactions. As an example, it reacts with aluminum oxide and forms spinel phase. Eq. 2.4 and 2.10 are suggested for the spinel formation mentioned above [54, 59, 62, 66].

Spinel formation reactions with Eq. 2.4 is accompanied by a volume the expansion of ~17 vol% and might result in refractory material spalling and/or crack formation, promoting increase in molten metal penetration (Molar volume of SiO_2=27.25 cm^3, Al_2O_3=26.33 cm^3, $MgAl_2O_4$=39.7 cm^3) [59, 62, 66].

Allaire [54] studied the corrosion mechanisms of aluminosilicate refractory exposed to Al-5 wt%Mg alloys at 850°C and 1150°C for the residence time of four days under static conditions. In this study, the loss of magnesium due to oxidation is compensated by daily additions of 40 g of this metal into the molten aluminum alloy. It was reported that an initial layer of spinel forms at the refractory/molten metal interface. The suggested reactions for spinel formation were given as Eq. 2.4 and Eq. 2.10. The second reaction was reported as the most probable one, thermodynamically the most favorable.
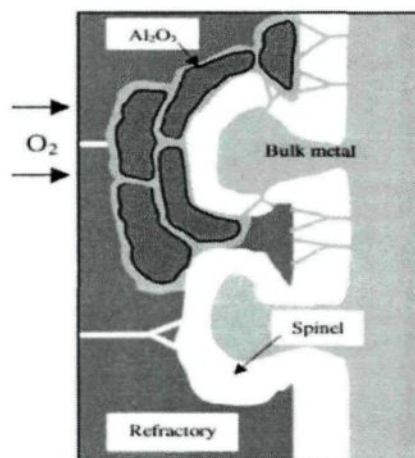
Figure 2-9: A Schematic View of a Refractory with Inward Corundum Growth [54]

It was reported by Allaire [54] as well as other researchers [59, 62] that Eq.2.10 mentioned above is accompanied by a volume change (~26 vol% decrease), which allows the formation of microchannels and further metal penetration into the refractory (see Figure 2-9).

This leads to further spinel formation in the refractory. Eventually, magnesium present in the metal depletes; and aluminum penetrates through the microchannels, and starts reducing silica according to Eq. 2.11 shown below forming corundum.

$$2Al(l) + \frac{3}{2}SiO_2(s) = Al_2O_3(s) + \frac{3}{2}Si(l) \qquad (2.11)$$
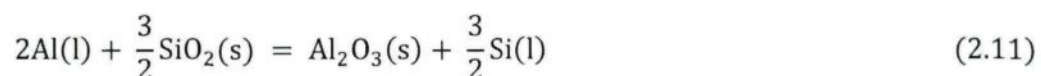
The effect of magnesium content on inward corundum formation was not found to be as significant as the effect of temperature. At high temperatures, the kinetics of silica reduction rate was higher (volume decrease was higher); therefore, metal penetration was

accepted as the corrosion rate controlling process. Eq. 2.11 results in ~35% volume decrease. Less severe corrosion in the presence of magnesium was attributed to the presence of spinel layer that reduces the metal penetration rate because of positive volume change according to Eq. 2.4 [54, 59, 62].

The corrosion kinetics of aluminosilicate refractories by Al-5wt% Mg alloy was studied by Gao et al. [65] under both static and dynamic conditions. The before mentioned Eq.2.11 was suggested by Gao for the corrosion of refractory at 850°C. Immersion test was used for the static corrosion test in which samples were submerged into molten metal and left in the crucible for four days. In the dynamic corrosion tests, a special experimental set-up seen in Figure 2-10 was built, and the sample was rotated at different rpm values while it was submerged in the molten aluminum for up to four days. It was observed that corrosion under dynamic conditions is more severe than it is under static conditions.
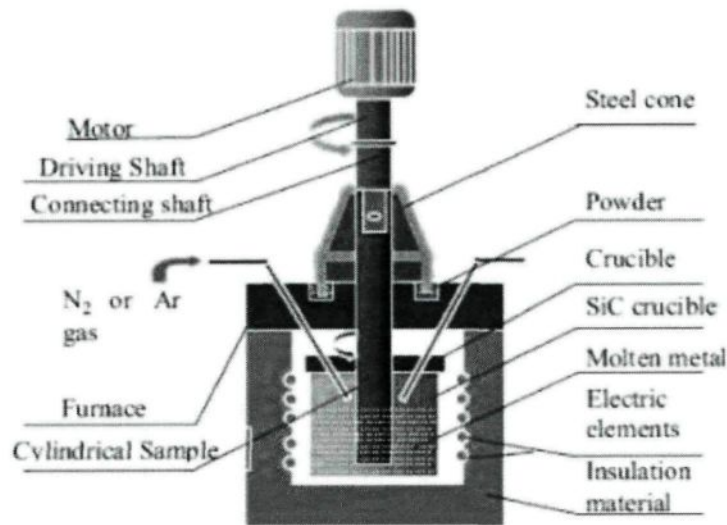
Figure 2-10: Experimental Set-up for Dynamic Corrosion Testing [65]

Other researchers [70-72] who studied the corrosion of aluminosilicate refractories by molten aluminum also discussed the impact of impurities such as iron oxide and sodium oxide on the corrosion resistance of refractories. It is reported in these studies that Na_2O is one of the most important impurity in alumina. It causes the formation of beta-alumina ($Na_2O.11Al_2O_3$ or $NaAl_{11}O_{17}$) at ~1300°C during either calcination or high temperature sintering process according to Eq. 2.12.

$$Na_2O + 11Al_2O_3 = Na_2O.11Al_2O_3 \text{ (β-alumina)} = 2NaAl_{11}O_{17} \qquad (2.12)$$
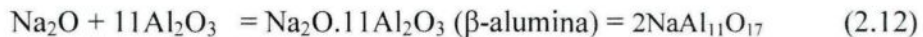
Beta-alumina is an active phase in a refractory exposed to liquid aluminum. Its presence decreases thermal shock resistance and inertness of the refractory. The researchers agree that sodium escapes in vapor phase from the refractory as shown in Eq. 2.13. It is also mentioned by Yurkov [70] and Allaire [71] that the sodium is oxidized again via either direct oxidation (>10^{-19} atm P_{02}), or reduction of other impurities such as SiO_2, etc. (<10^{-19} atm P_{02}). However, the authors did not support the following reaction with thermodynamic data which seems to have positive ΔG^o value (Table 5-18).

$$6NaAl_{11}O_{17} \text{ (β-alumina)} + 2 Al \longrightarrow 6Na \text{ (vapor)} + 34Al_2O_3 \qquad (2.13)$$

Baspinar [72] identified the sodium rich phase observed on the sample surface after the sodium vapor escaped from beta-alumina when refractory and molten aluminum alloy were in contact. He reported that the sodium vapor reacted with the binder of the refractory

which was rich in SiO_2. The needle-like structure observed on the sample surface (shown in Figure 2-11) was investigated with SEM-EDX analysis and the major elements in this structure were found to be Al, O, Na, and some Si as shown in Figure 2-12.
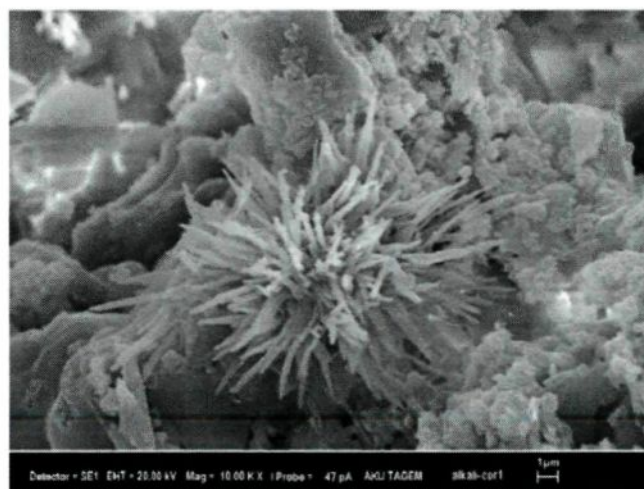
Figure 2-11: Needle like Structure Phase Developed after Sodium Vapor and Refractory Binder Interaction in Baspinar's Study [72]
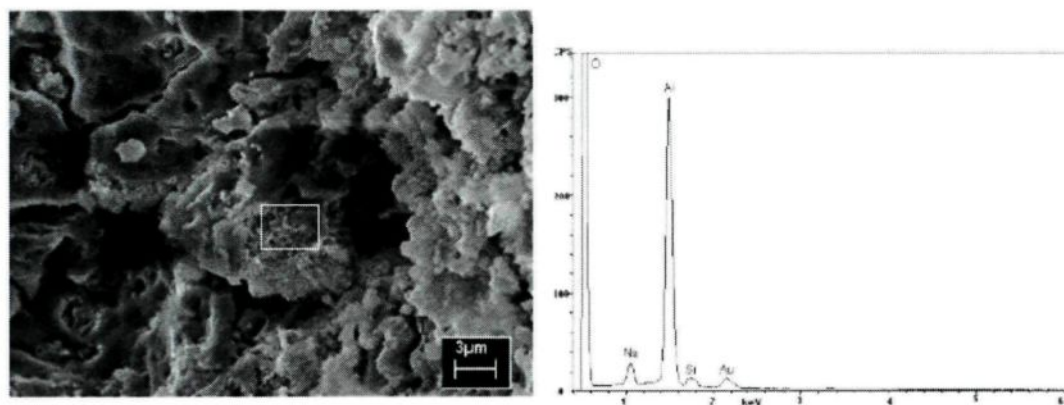
Figure 2-12: EDX Analysis Results for Needle-like Structure of the Reaction Product Formed at Refractory/Aluminum Alloy Interface [72]

The present work was conducted in conjunction with the study done by Ergin [9, 10] on the wettability of filter media by aluminum alloys during aluminum filtration. Ergin studied the wetting characteristics of different tabular alumina particles (~1.2 mm in diameter) with Al-Mg alloys using infiltration method. In this method, the molten Al- 6.9 wt% Mg alloy at 730°C was pushed through the closely-packed alumina bed which was placed in a vertical tube furnace. The TEM studies conducted on samples which were left in the furnace for extended periods of contact times ranging from one to three days under static conditions. The TEM analysis results showed that the phase found at the metal/ceramic interface was Mg-spinel (see Figure 2-13 and 2-14). No magnesia presence was observed.
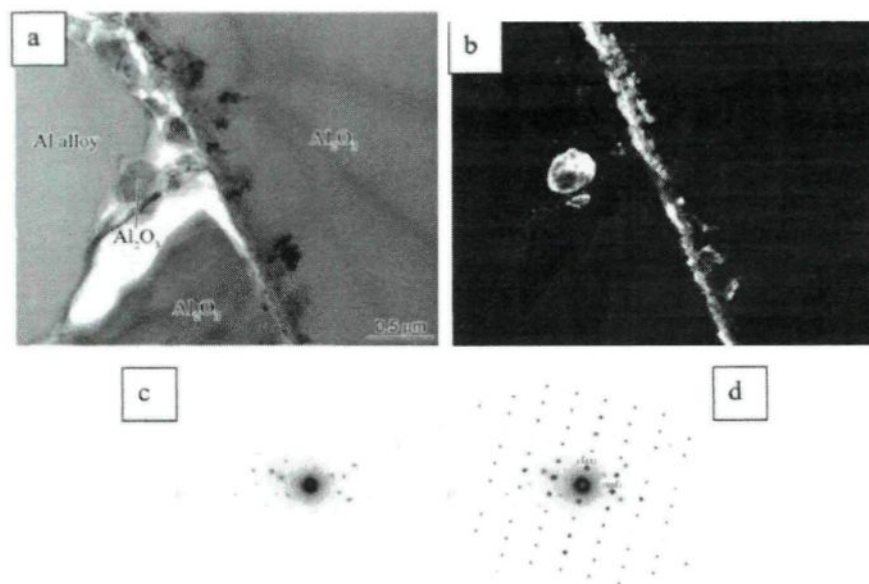
Figure 2-13: (a) Bright-field Image, (b) Dark-field Image in a Spinel Reflection, and (c) Selected Area Diffraction Pattern from Spinel (d) [211] Pattern for Spinel Superimposed on the Diffraction Pattern [9, 10]
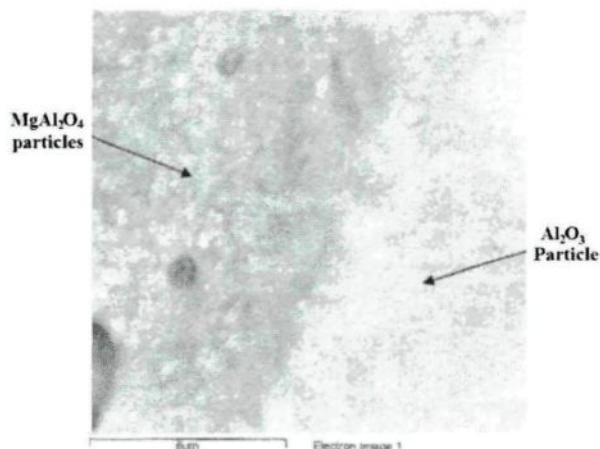
Figure 2-14: Image of Micron and Sub-micron Size Spinel Particulates Detected on Alumina Particles [9,10]

2.3.3 Studies on Reaction Kinetics

Ceramic/metal interfaces are present in a great number of industrial applications such as ceramic/metal composites, refractories, ceramic/metal seals, and so forth. Understanding the formation and evolution of such interfaces is therefore essential for the better design and optimization of these applications. In some cases, the thermodynamics of the reactions is not enough to explain what really happens physically. Sometimes, thermodynamically less favorable reaction might take place as oppose to a more favorable one which might have very slow kinetics. At this point, kinetics of reactions plays a major role.

In order for aluminum metal to attack ceramic surface, following two conditions must be fulfilled:

1. Ceramic material must be reducible by molten aluminum metal,

2. Molten aluminum metal must be in contact with the ceramic material.

In literature, it is stated that the chemical interactions between solid and liquid phases can improve significantly the wetting on the liquid/solid interface, e.g. metal/ceramic interfaces. This phenomenon is called chemical wetting, and it is promoted by either introducing certain alloying elements into the metal [66-69,94-96] or coating the substrate surface with a substance chemically preferred by the metal [43,69]. When alloying elements are added into a liquid metal, the alloying element that has a higher affinity for oxygen than the base metal tends to migrate to the oxygen rich interface and form an interfacial bond through chemical interactions. Upon the reaction between the alloying element and the substrate, a continuous layer of solid, which is better wetted by the metal with respect to the original substrate, is created. The creation of this additional layer might result in an increase in the surface energy (decrease in surface tension) and/or decrease in the metal/ceramic interfacial tension value.

Thermo-chemical properties of the materials which were discussed in the previous section play an important role in the first condition mentioned above, and the second condition is linked to the reaction kinetics. Wetting characteristics of the materials have an important impact on reaction kinetics. The general condition for wetting is that the interfacial energy of the grain boundary (γ_{gb}) balances with the interfacial energy of the solid-liquid interface (γ_{sl}). The relationship between these energies and the wetting angle (θ) is shown by the equation [9]:

$$\gamma_{sl} = 2\gamma_{gb}.\cos(\theta/2) \tag{2.14}$$

System is considered wettable when the contact angle (θ) between aluminum metal and ceramic material is less than $90°$. Although the contact angle is always greater than $90°$

for the system under consideration [9,10], molten Al-Mg alloys wet (have smaller contact angles) alumina based ceramics more than pure Al [58].

The presence of impurities in the ceramic material such as alkalis (Na_2O, K_2O, etc.), can affect the reaction kinetics through "parasitic" reactions causing volume expansion and cracking of the ceramic surface [58].

Levi et al. [29] studied the reaction kinetics between α-alumina fibres and vigorously agitated molten Al- (2, 4, and 8 wt %) Mg alloys at 600-640°C. The presence of $MgAl_2O_4$ at the metal /ceramic interface was confirmed by the SEM and TEM analyses. Experimental results showed that the alumina fibres that were exposed to the same conditions display very large differences in the thickness of the "apparent interaction zone". It was observed that the fibres which did not show an appreciable interaction zone were still bonded to the matrix, indicating that the surface reactions responsible for wetting are not necessarily those associated with the formation of the "apparent interaction zone". Data for the average maximum thickness of the apparent interaction zone was plotted as shown in Figure 2-15. The change in the interaction zone thickness with the residence time was represented with a parabolic growth (Equation 2.15):

$$\text{Apparent interaction zone thickness} = a.t^n \qquad (2.15)$$

where t is the residence time and a and n are positive constants. It was underlined by Levi [29] that the irregular shapes of the interactions zones made it difficult to assign a unique value for the thickness in a particular sample; therefore the data shown in Figure 2-15 represent only the general trends. However, it can also show the possibility of differences

in the interaction mechanisms and products between the lower and higher magnesium

content alloys (see Table 2-7).

Table 2-7: "n" Value for Different Magnesium Concentrations [29]

Mg wt %	n value
2	0.57
4	0.59
8	0.38
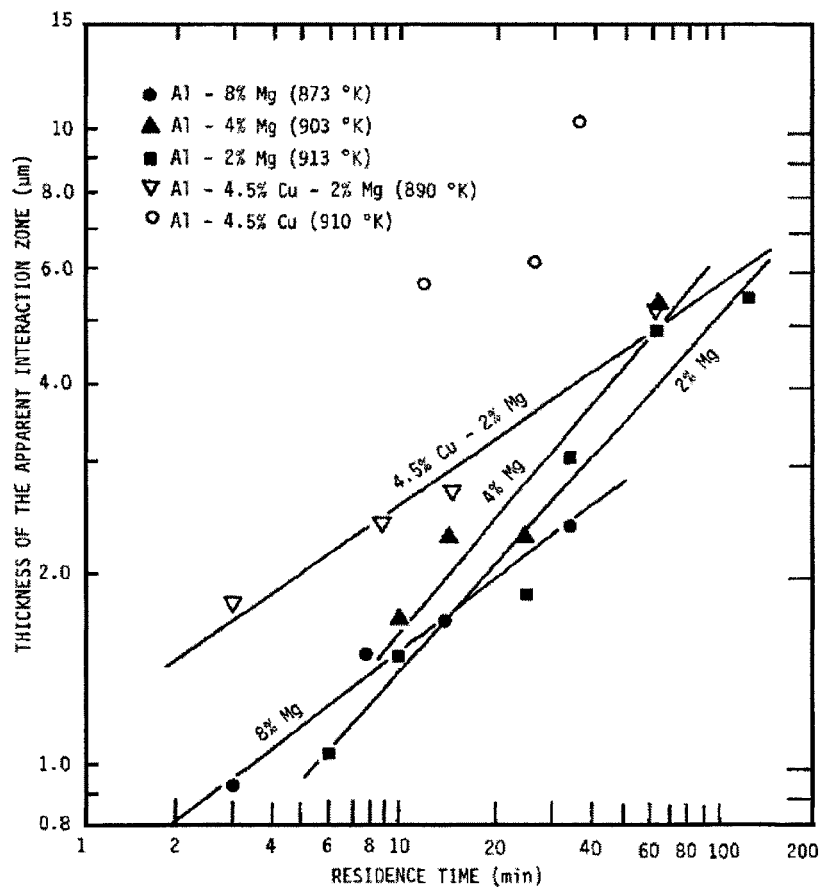
Figure 2-15: Apparent Interaction Zone Thickness vs. Residence Time [29]

Kinetics of spinel growth in Al- 1% Mg alloy/alumina composite system in the temperature range of 975 to 1073K was studied by McLeod [33]. Molten composite was alloyed with 1 wt% Mg. Melt was stirred in air continuously to avoid particle settling during the experiments. Determining the magnesium loss with time in the matrix metal was the target of the trial. Disc samples were taken from the melt and quenched at specified intervals. The amount of magnesium in the matrix alloy was measured by first dissolving the matrix (from a 2g portion of the disc sample) using aqua regia. This solution cannot dissolve Al_2O_3 and $MgAl_2O_4$. The level of magnesium was calculated from ICP measurements of the Mg to Al ratio in the leached solution. Magnesium concentration vs. time data was plotted in Figure 2-16.
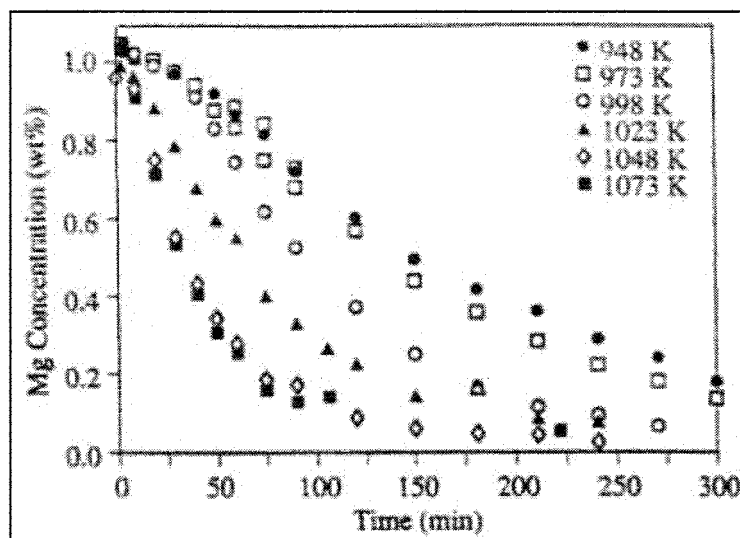
Figure 2-16: Loss of Mg Resulting from Spinel Formation for Alumina in Super Purity Aluminum-1 wt% Mg [33]

The extent of the reaction at any time t was defined by McLeod as shown:

$$\propto (t) = \frac{M_O - M(t)}{M_O - M_e} \qquad (2.16)$$

where M_O is the initial Mg concentration at t=0, M(t) is the Mg concentration at time t, and M_e is the equilibrium Mg concentration. Avrami-Erofev equation shown below (Equation 2.17) was found to be applicable for the solid phase decomposition reactions in the ~0.05<α<0.9 range. It was found that the presented data fitted best to the first order equation (n=1) [33].

$$-\ln(1-\propto) = k(t - t_0)^n \qquad (2.17)$$

The rate constant "k" fits an Arrhenius-type relationship; therefore, k was taken as :

$$k = 50 \exp\left(\frac{-103000}{RT}\right) \qquad (s^{-1}) \qquad (2.18)$$

The combination of Equations 2.16, 2.17, and 2.18 yields a formula for the weight percent of magnesium as a function of time, t in seconds, and temperature, T in Kelvin as shown in Equation 2.19 [33].

$$M = 0.03 + (M_0 - 0.03).\exp[\ 50 \exp((\frac{-103,000}{RT})\ (t_0 - t)] \qquad (2.19)$$

As discussed partially on page 41, Gao et al. [65] investigated the corrosion kinetics of aluminosilicate refractories by molten Al-5 wt% Mg under both static and dynamic flow

conditions using experimental set-up shown in Figure 2-10. In static flow experiments, refractory samples were left in the molten aluminum at 850°C for different time periods (24, 31, 47, 62, 72, and 79 hours). After the experiment, the collected samples were cut from the cross-section (Figure 2-17) and following formula (Equation 2.20) was suggested as a measure of the extent of the corrosion for each sample.

$$Corrosion\ depth = (corrosion\ area)/(perimeter\ of\ sample) \qquad (2.20)$$

The corrosion depth was found to be directly related with square root of time which was illustrated in Figure 2-18. It was reported by Gao et al. [65] that the linear correlation obtained from this figure appears to be an indication of diffusion process-governed corrosion mechanism in this system.
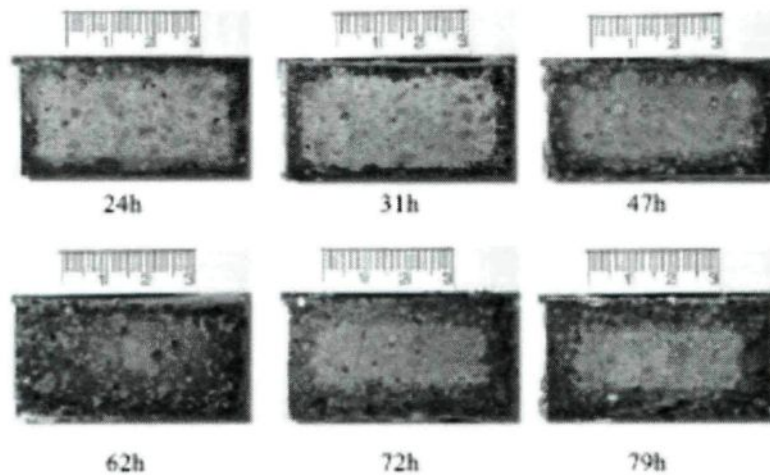
Figure 2-17: Cross-section of Refractory Samples after Different Times of Corrosion [65]
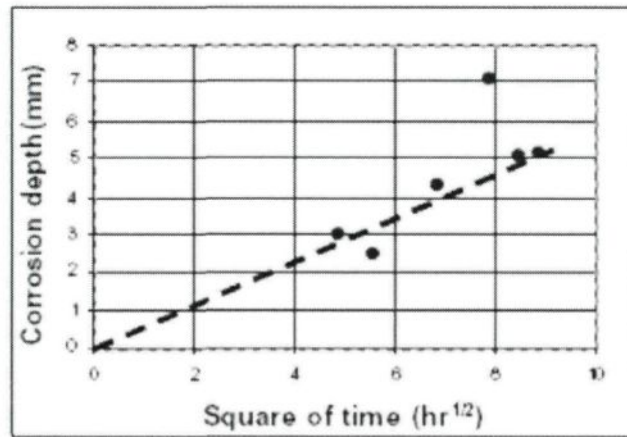
Figure 2-18: Increase in Average Corrosion Depth with Time [65]

Wetting and corrosion in the Al-Mg-Si-O systems were studied by Weirauch et al. [80] under dynamic conditions. A rotating cylinder technique was used to test the corrosion behavior of refractories in molten Al-Mg alloys at 800°C under argon gas. The tests of disc-shaped refractory samples in molten aluminum alloys were conducted using a similar experimental set-up shown in Figure 2-10.

Cochran [74] stated that the rotating cylinder technique for testing samples under dynamic conditions allows a full description of the fluid flow. The combination of equations governing the fluid flow with those for chemical diffusion (diffusion followed by a reaction) results in a complete characterization of the process known as convective diffusion. The equation shown below, proposed by Levich [75] describes mass transport under the conditions of forced convection. The rate of change in height of the disk, dH/dt, which is rotated about its axis in the liquid, is related to mass diffusion coefficient, [D], kinematic viscosity, [υ], the angular velocity of the disk, [ω], and composition gradient indicating the level of solute saturation (C_i: initial, C_b: bulk) by an equation of the form :

$$\frac{dH}{dt} = 0.62\,[D]^{2/3}\,[\upsilon]^{-1/6}[\omega]^{1/2}(C_i - C_b) \tag{2.21}$$

Weirouch et al. [66] also studied the refractory corrosion under metal flow condition using the rotating cylinder technique. The forced convection results were combined with wetting experiments to provide a complete description of the refractory degradation mechanisms. It was stated that the liquid-phase transport due to forced-convection did not affect the attack of the refractory. The attack initially proceeds by a diffusion-controlled, reduction reaction where the front advances in a nearly linear form. Channels develop within the coherent reaction product layer causing an increase in the rate of attack (Figure 2-19).
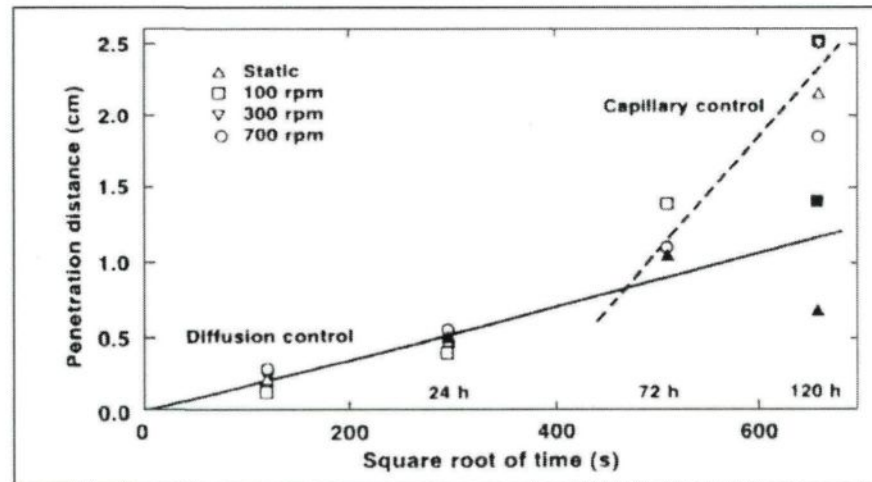
Figure 2-19: Attack of Silica Brick by Al-5.5 wt%Mg Alloy at 800°C in Argon (Solid symbols refer to as-received brick surfaces while open symbols are cut surfaces) [66]

The transport processes might be involved in the refractory attack in addition to the interfacial chemical reaction. Reactants must be brought from the bulk alloy through a

liquid boundary layer, δ, to the refractory/metal interface. In order to sustain the reaction, the reactants must then be transported through the developing reaction layer to the interface with the fresh silica refractory. The overall process of refractory attack is outlined in Figure 2-20. At this point, Weirouch et al. [66] state that transport within the liquid phase does not affect the overall rate of reaction under the conditions used in his study.

Transport through the reaction layer is aided by the porous nature of the reaction product. The conversion of two moles of silica to one mole of spinel (Eq. 2.10) results in 27% reduction in volume and crack formations in the structure. This kind of structure is conductive to rapid transport (due to formed cracks and cavities), and the rate is controlled by the interfacial reaction as stated also by Laidler-1965.
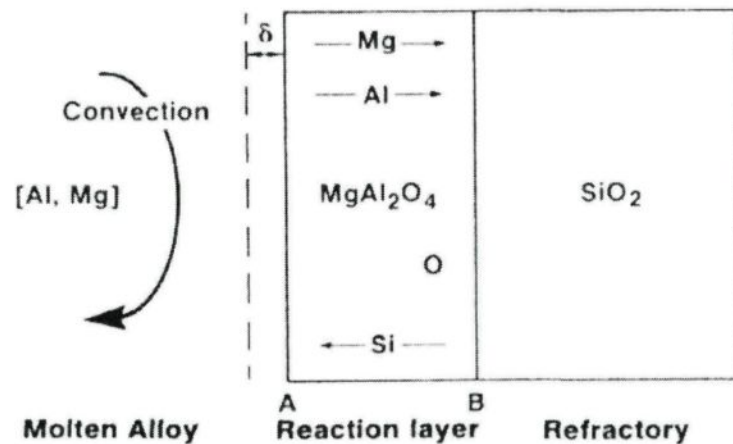
Figure 2-20: Schematic Outline of the Refractory Corrosion Mechanism [66]

Brondyke [76] observed that the attack of alumina-silica refractories by aluminum in static immersion and cup tests. It was said that the wetting was a necessary first step

followed by the diffusion of aluminum and silicon through the product layer to the reaction front. It was proposed that the capillary movement of the corrosive liquid might be the rate controlling step in refractory corrosion.

As it can be seen from the review of the literature given above, there are a few studies carried out under dynamic conditions, and most of them are related to refractory corrosion. There are no studies, to our knowledge, on the interactions between alumina, aluminum and inclusions under dynamic conditions similar to those encountered during filtration.

CHAPTER 3
3. EXPERIMENTAL SET-UP AND PROCEDURE

3.1 Experimental System Design

An experimental study carried out during this project focused on the interactions of molten aluminum alloys with alumina ceramics and inclusions under dynamic conditions. The knowledge of molten metal velocity in the vicinity of alumina particles at elevated temperatures (680-750°C) was the key factor in this project in order to investigate the reaction kinetics at molten metal/alumina ceramics interface in the presence of flow; therefore, one of the most challenging parts of the experimental study was to determine the most suitable experimental system design which can basically fulfill the following purposes:

1. To create a uniform molten metal flow similar to the one in industrial filters in the section of the experimental system where the alumina samples are placed in order to study the interactions under flow conditions,

2. To control the metal velocity and temperature in the sample holder section of the experimental set-up (around samples),

3. To have an easy-to-use and robust enough system to conduct several experiments in molten metal at elevated temperatures (690-750°C) for durations ranging from one hour to one week.

A literature search was conducted to find out the system designs utilized under dynamic conditions. A few studies [65-66] were found in literature used for studying refractory corrosion under molten metal flow conditions. In these systems, the experimental set-up

design was simply composed of a rotating sample submerged into molten metal with the rotation controlled by an electrical motor (see Figure 3-1). The samples tested were generally laboratory made refractory carrots (cylindrical refractory rods ~10-15 cm in length, ~2.5-3.5 cm in diameter) which were bigger compared to the size of tabular alumina samples (~3-6 mm in diameter) to be tested in the current study; therefore, the above experimental system design was not found suitable for this study.
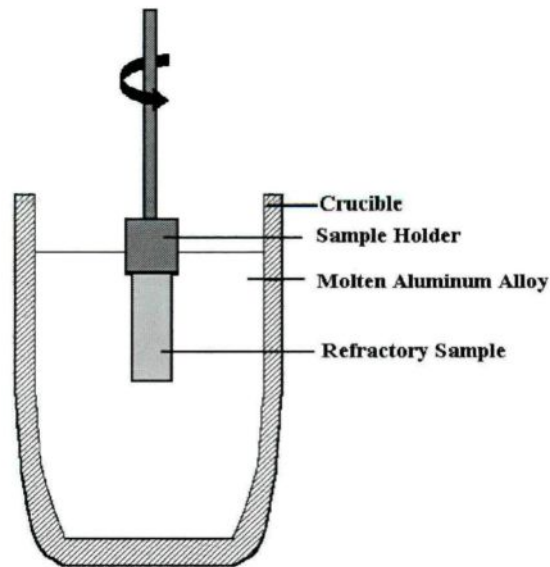
Figure 3-1: Experimental Set-up for Dynamic Refractory Corrosion Studies [66]

A number of experimental systems (shown in Appendix 1 in chronological order) were designed, fabricated, and tested in the laboratory during the early phase of the study. Carrying out the experiments with molten aluminum under flow conditions was a real challenge. The aim of the experimental study was to simulate the real molten aluminum filtration operation conditions when alumina bed was subjected to liquid metal flow. Based on the results of these preliminary experiments, two experimental systems were chosen for

use in this study to meet the above objectives. In the next section, these two systems are described in detail.

3.1.1 Experimental System-I (with Mixer Motion)

Here, the latest design of the system is presented. The evolution of the design is described in Appendix 1. The experimental system-I design (Figure 3-2) consists of two main parts. The first part is cylindrical crucible (Canadian Thermix-40BB SiC) which has approximately a 15kg liquid aluminum holding capacity. The crucible is placed into the Pyradia^{TM} resistance melting furnace. The second part is composed of a mixer and a sample holder which is to be submerged into the cylindrical crucible filled with molten aluminum at elevated temperatures. The 63 mm diameter mixer has 4 blades which are tilted $37.5°$. The bottom part of the holder has a compartment in which one layer of alumina particles were placed. This part represented a filter section which had a large number of holes at the bottom and the top plates. These holes allow the liquid metal to circulate within the crucible and keep the alumina particles inside at all times. Metal circulation is created by the mixer motion which pushes the molten metal downward through diffuser plates and creates a molten metal flow in the sample holder section. The diffuser plates act as a distributor which redirects the metal flow towards the filter section and creats a vertical uniform flow.

Components of Set-up

1. Electrical Motor
2. Counter
3. Mixer
4. Liquid Aluminum
5. Filter Section
6. Diffuser Plate-1
7. Diffuser Plate-2
8. Crucible
9. Pyradia Melting Furnace
10. Heating elements
11. CO₂ gas
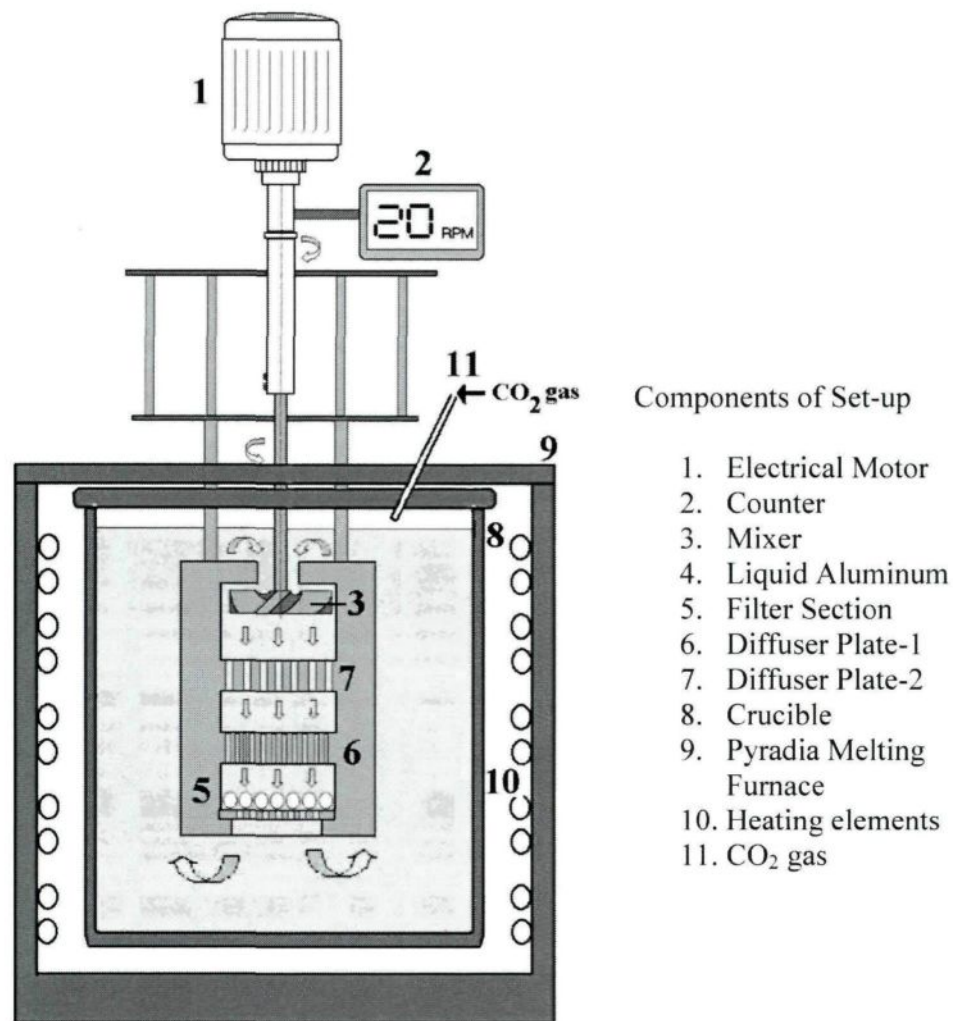
Figure 3-2: A Schematic View of the Experimental System-I

The cylindrical body of the experimental system and the mixer were fabricated using high quality graphite (high density graphite-pressurized at high temperature). Stainless steel rods (8mm diameter) were used to hang the cylindrical body to the carrier (Figures 3-2, 3-3, and 3-4) which allowed the system to move up and down. These rods were insulated using high density and high purity alumina hollow cylinder. The mixer shaft

is also made up of high density alumina rod (8 mm diameter). Different designs of sample holder section (bottom plate) were tested using high quality graphite (Appendix 1). The design shown in Figure 3-5.a was determined as the most convenient one in terms of sample collection and sample cleanliness issues. Commercial alumina samples were placed onto high purity and high density alumina slots which provided alumina sample position stability (samples rest on the alumina slots and do not fall into the crucible), high degree of cleanliness (no contact with graphite), and convenience for sample collection after experiments (See Figure 3-5.c).
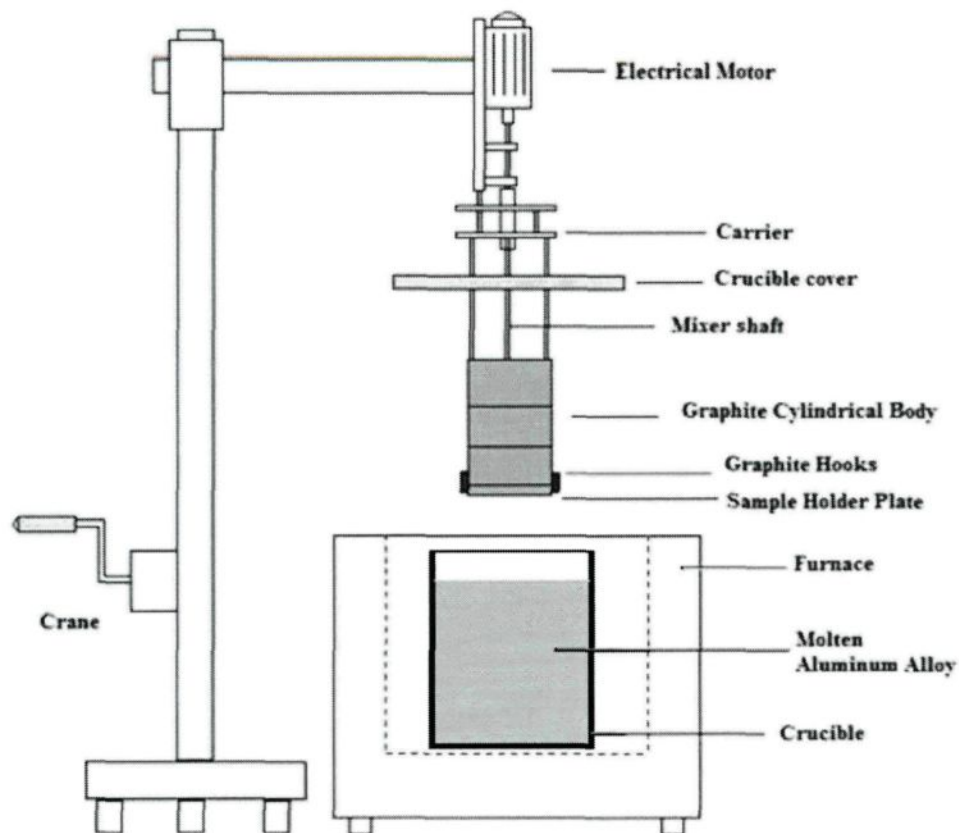
Figure 3-3: Experimental Assembly for System-I
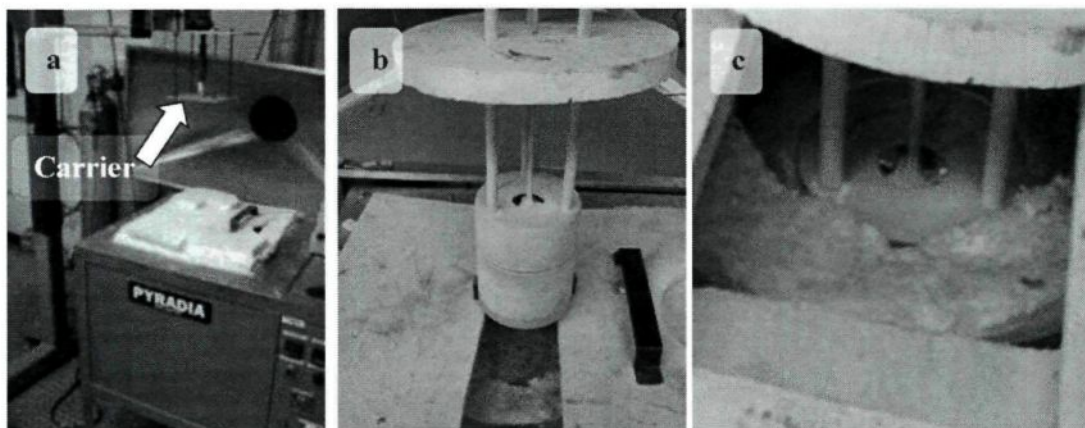
Figure 3-4: Experimental System-1 (a) Pyradia^{TM} Resistance Melting Furnace, (b) Cylindrical Body Before Being Submerged, (b) Cylindrical Body Partially Submerged into Molten Aluminum.

Molten metal velocity and flow profile around alumina samples are necessary for the investigation of aluminum alloy/alumina interactions. A numerical model of the experimental system (See Chapter 4 for details) was used to determine the velocity profiles around alumina samples. After the validation of the numerical model results using a water model, the experiments with molten aluminum commenced.
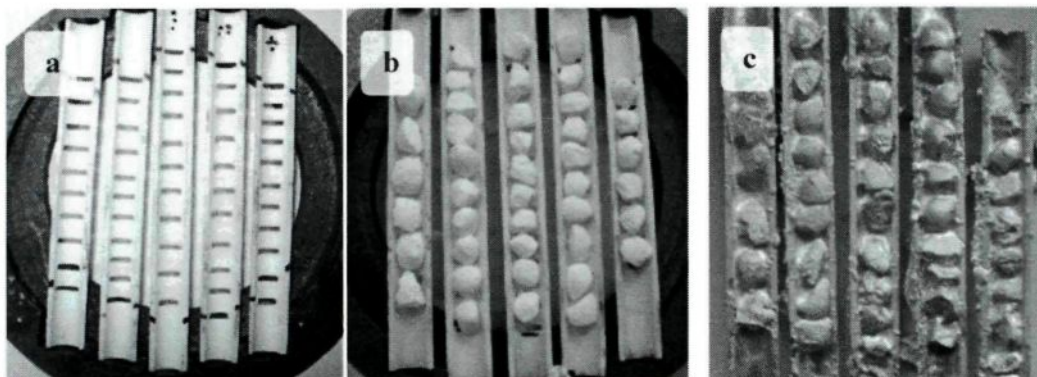
Figure 3-5: Sample Holder Plate Design (a) Without Alumina Samples, (b)with Alumina Samples Before Experiment, and (c) Appearance of the Samples After Experiment.

A detailed experimental procedure can be found in Section 3.5.

3.1.2 Experimental System-II (with a Rotating Disc)

Experimental System-II is made of two main parts. The first part is a cylindrical crucible with a liquid aluminum holding capacity of 15kg (same as the one used in the experimental system-I) placed in the Pyradia melting furnace (shown in Figure 3-4). The second part is a 70mm diameter, ~12mm thickness graphite disc which is connected to a rod from its center and submerged into the crucible containing molten aluminum alloy. Samples to be tested were placed at a certain distance from the center of the disc. The disc was rotated in the molten metal with a constant rotational speed corresponding to the target metal flow velocities (1.8 and 3.6mm/s) around samples placed on the disc.

The experimental apparatus assembly is shown in Figures 3-6 and 3-7. High-density graphite was used to fabricate the disc for the experiments conducted with molten aluminum. The rod at the center of the disc was made of high density alumina (~8 mm diameter).

For experiments longer than three days, an additional sample holder disc or discs was/were placed on the alumina rod so that a larger number of samples could be tested in a certain period of time. In this project, both alumina tablets prepared in the laboratory as well as commercial tabular alumina particles were tested. Figure 3-6 shows the one-layer experimental set-up used for alumina tablet tests. Grooves of 2 mm depth and 10 mm width, placed at 5 cm and 2.5 cm distance from the center of the graphite disc, held the

alumina samples gently and prevented samples from falling into the crucible. Figure 3-7 presents a multi-layer set-up.
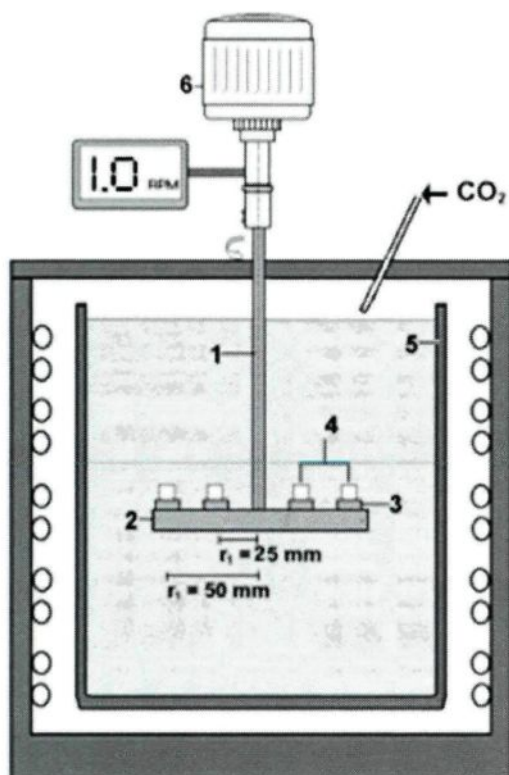
Components of set-up:

1. Alumina shaft
2. High Density Graphite Disc
3. Sample holder-Alumina or high density graphite
4. Alumina samples
5. SiC cylindrical crucible
6. Electrical Motor

Figure 3-6: A Schematic View of the Rotating Disc Type Experimental System

Experiments with tabular alumina particles required the utilization of a slightly different disc design (Figure 3-8b) than the one used for the alumina tablet tests (Figure 3-8a). This design had multiple layers, and each layer had four sample holder cells which could hold up to seven +4.87-6.35 mm tabular alumina particles. Sample holder cells were made up of high purity and high density alumina. They were fabricated by cutting 16mm diameter alumina hollow tubes into half. These cells were placed 2.5cm and 5cm away

from the center of the alumina shaft which was rotated at ~0.67 rpm (approximately 1 rotation per ~90 seconds). This configuration allowed the tests to be carried out with two different metal velocities (1.8mm/s and 3.6mm/s) at the same time. Multi-layer system made possible to conduct full length experiments and take samples at intermittent times without interrupting the experiment.

The preliminary experimental results using multi-layer experimental setup showed that the alumina particles placed in different levels had similar affected zone thicknesses. It was also verified that under similar experimental conditions, the experimental systems I and II provided very similar results.
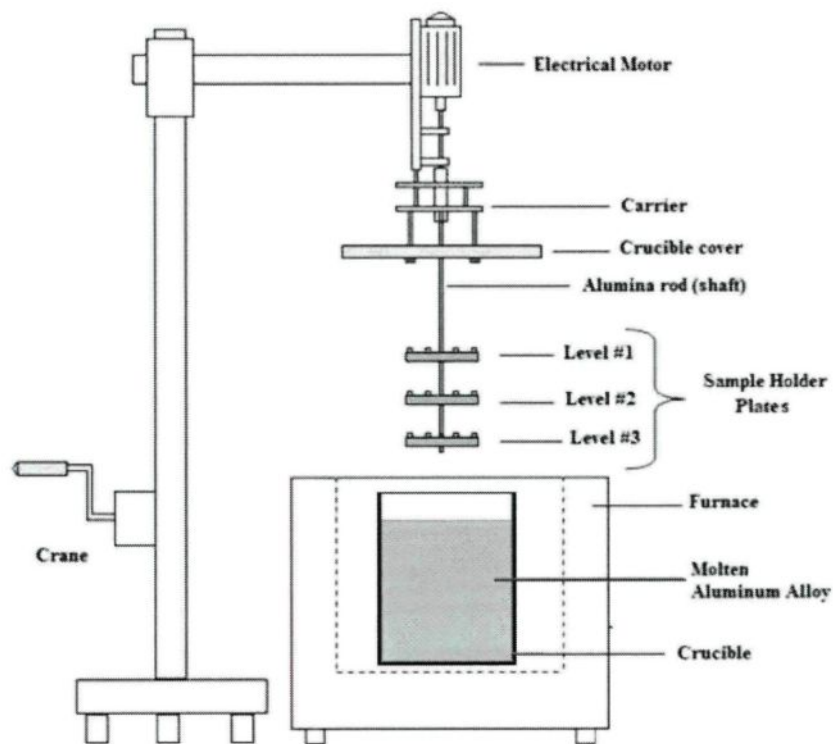
Figure 3-7: Experimental Assembly for System-II
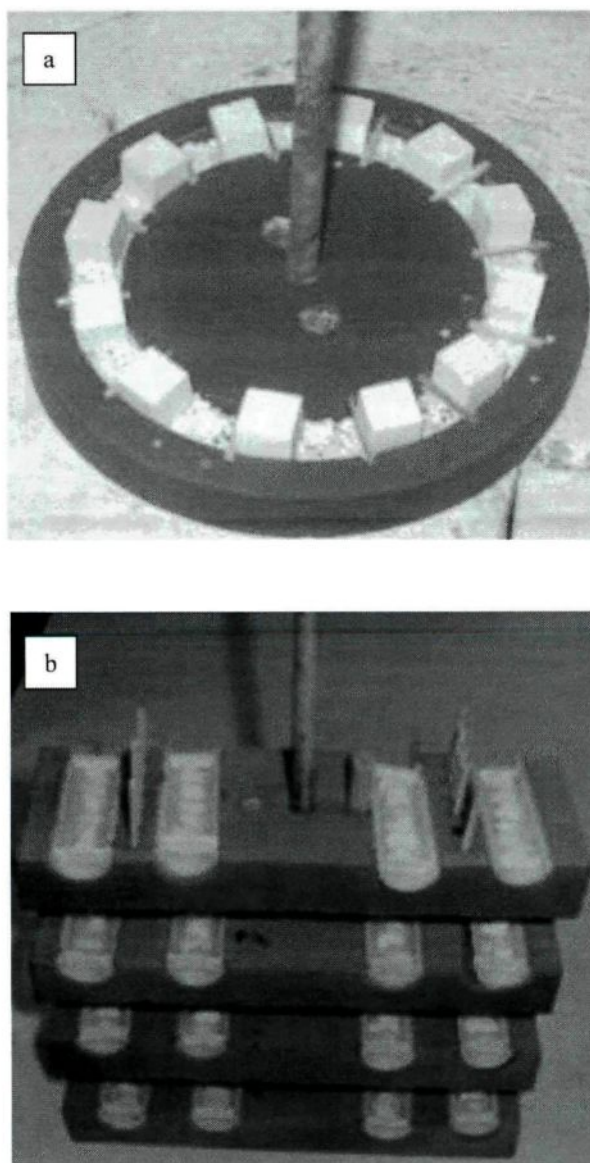
Figure 3-8: Experimental System Design #2 (a) Alumina Tablet Experiments with A Single Layer Disc, (b) Tabular Alumina Particle Experiments with Multiple-Layer Rotating Discs.

A detailed experimental procedure can be found in Section 3.5.

3.2 Parameters of the Experimental Study

The experimental study was conducted to determine the effects of different parameters on the extent of reactions between alumina samples and molten aluminum alloys as well as inclusions. These are shown in Table 3-1 below.

Table 3-1: Parameters to Be Studied in the Experimental Study

	Parameters	
1	Aluminum alloys	2, 5, and 7% Mg-Al alloys
2	Commercial tabular alumina particles	Alcoa, Aluchem, Alufin, Naigai
3	Laboratory made alumina tablets	-Reference Alumina (Alcoa T64) - High Na_2O - High SiO_2 - High MgO
4	Liquid metal velocities	- Static (0 mm/s) - Dynamic - 1.8 mm/s - Dynamic - 3.6mm/s
5	Liquid metal temperature	- 690°C - 715°C - 750°C
6	Commercial tabular alumina particle size	+4.35-6.37 mm
7	Inclusion sources	MgO, $MgAl_2O_4$

3.2.1 Aluminum Alloy Preparation

Industrial grade pure aluminum (0% Mg) and aluminum alloys with three different magnesium concentrations (2, 5, and 7%Mg) were used in the experimental study. The alloys were prepared using RTA-P1020 industrial grade pure aluminum ingots and PMG-90 pure magnesium ingots from Norsk Hydro Magnesium (Table 3-2).

Table 3-2: Chemical Compositions of Industrial Grade Pure Al and Pure Mg Metals

Elements	%wt	Elements	%wt
Al	99.79	Mg	99.90
Si	0.06	Al	0.006
Fe	0.14	Cu	<0.001
Cu	<0.01	Fe	0.032
Mn	<0.01	Mn	0.002
Zn	<0.01	Na	0.0006
Ti	0.003	P	0.0021

The alloy preparation procedure can be summarized as:

• Aluminum and magnesium ingots were cut to a proper size using bi-metal band saw.

• Oil and dirt on both magnesium and aluminum pieces were removed using alcohol.

• The amount of aluminum and magnesium needed for the desired alloy type, shown in Table 3-3, was weighed.

• Aluminum pieces needed for the alloy were placed in the SiC-crucible and Pyradia™ resistance melting furnace at 250°C for at least two hours.

• The furnace temperature was increased 250°C every two hours until the metal temperature reached ~730°C.

Table 3-3: Amount of Al and Mg Metals Required for Alloy Preparations

%Mg in Alloy	Pure Mg, (g)	Pure Al, (g)	Total weight, (g)
0	0	12000	12000
~2.0	255	11745	12000
~5.0	632	11368	12000
~7.0	885	11115	12000

- Magnesium pieces were left in the drying furnace at least half an hour before adding them into pure molten aluminum for alloying.

- The yield of magnesium alloying was found to be ~95%. Table 3-3 was based on this calculation.

- Magnesium pieces were placed in the preheated graphite plunger using an aluminum foil which helped keep small magnesium pieces together inside the plunger.

- When the liquid metal temperature reached 730°C, the plunger was submerged into pure liquid aluminum metal slowly and waved carefully without getting the head of plunger out of the metal surface (to avoid oxidation).

- Plunger was removed after a couple of minutes.

- The furnace temperature was then set to the desired experimental temperature.

- When the alloy temperature reached the desired temperature, a sample for a chemistry analysis with the optical emission spectroscopy was taken.

3.2.2 Commercial Granular Alumina Particles

Four different commercial types of tabular alumina particles (Naigai, Aluchem, Alcoa, and Alufin) which are the most common deep bed filter media materials were tested in the experiments. A study on the chemical and physical characterization of the particles was conducted before the experiments with molten aluminum started (see Section 3.4 for detailed information).

The size of the alumina particles used in the filter media in industrial filtration operations changes between 1.5 to 18 mm. The particles are placed in the insulated deep bed filter steel box, layer by layer, in different sizes. The reports and studies found in the literature indicate that the filtration of aluminum is carried out more efficiently at the layer where the small particles (1.5-3 mm and 3-6 mm) are found. The bigger particles such as 12-18 mm are used in the filter box for supporting the small particle layers, therefore, the particle size for the present project was chosen as +4.87-6.35 mm. All above commercial alumina grades were tested with this criterion.

In order to determine the effect of particle size on the reaction kinetics at the alumina/aluminum alloys interface, a couple of experiments were also conducted using 1.5-3.0 mm size particles of Alcoa T64 with 5%Mg-Aluminum alloy.

The physical properties such as percent apparent porosity, bulk density, porosity size and distribution throughout the particle cross-section, α-alumina grain size, and surface roughness (r_a) were also investigated for each alumina type.

The apparent porosity % and bulk density measurements were done using the "Standard Test Method for Apparent Porosity, Liquid Absorption, Apparent Specific Gravity, and Bulk Density of Refractory Shapes by Vacuum Pressure" which is explained in detail at Section 3.3.

The porosity size and distribution and α-alumina grain size measurements were performed using ceramography methods which involve basically grinding, polishing, and etching steps of the mounted ceramic materials. These steps are explained in Section 3.3.

Surface roughness measurements of the particles were done using the ADE MicroXam-3D non-contact profilometer at UQAC. The details of the profilometer specifications can be found in section 3.3 as well.

3.2.3 Laboratory Made Alumina Tablets

Tabular alumina (α-Al_2O_3) is the only thermodynamically stable form of aluminum oxide. It is one of the most important ceramic raw material in industry as discussed in Chapter 2. Tabular alumina has ~98% purity and the other constituents of alumina which are considered as impurities are Na_2O, SiO_2, CaO, Fe_2O_3, TiO_2, MgO, etc. The effects of the impurities such as Na_2O, SiO_2, and MgO (present in alumina) on aluminum/alumina affected zone thickness which evolves during the filtration process were also investigated during this study.

The alumina particles used in hot metal tests during the first part of the study did not permit the determination of a detailed analysis of the effects of these impurities on the aluminum/alumina affected zone. This was due to the differences in their chemical compositions as well as their physical properties such as % porosity, shape and dimensions, grain size, etc.

Alumina tablets with different impurity contents and similar physical properties were manufactured in the laboratory so that the effect of different components present in alumina on aluminum/alumina reactions can be investigated exclusively.

3.2.4 Tablet Preparation Procedure

Alcoa T-64 grade ground tabular alumina of 20μm particle size and 0.5μm RTA RAC45B calcined alumina powders with 99% purity were used for tablet preparation in the laboratory. The ingredients added into the alumina powder mixture are listed in Table 3-4 below. The general tabular alumina purity value of 98% was respected during the preparation of the test samples.

Table 3-4: List of the Ingredients Used in the Alumina Tablet Preparation

Ingredients	%Purity	Particle Size	Supplier
Alcoa T64-tabular alumina	99%	20 μm	Alcoa Chemicals
RTA RAC45B-Calcined	99%	0.5-1.5 μm	RTA Chemicals
Silica (SiO₂)	99.9%	1-5 μm	Atlantic Equipment Engineers
Soda ash (Na₂CO₃)	99%	1-5 μm	Ecole Polytechnique-CIREP
Magnesium oxide (MgO)	99.8%	1-5 μm	Atlantic Equipment Engineers

A 50-ton capacity hydraulic press and the steel mould shown in Figure 3-9 were used for pressing the tablets. Polyvinyl alcohol (PVA) of 5% wt and alumina mixture were blended until PVA was distributed in the mixture homogenously. PVA is a binder which forms bridges between flocculated alumina grains. It was used to plastisize the alumina powder and to increase the green strength of the tablet after pressing and the drying process. PVA (Poly vinyl alcohol) is completely burnt off during the sintering of the alumina.

(a)   (b)
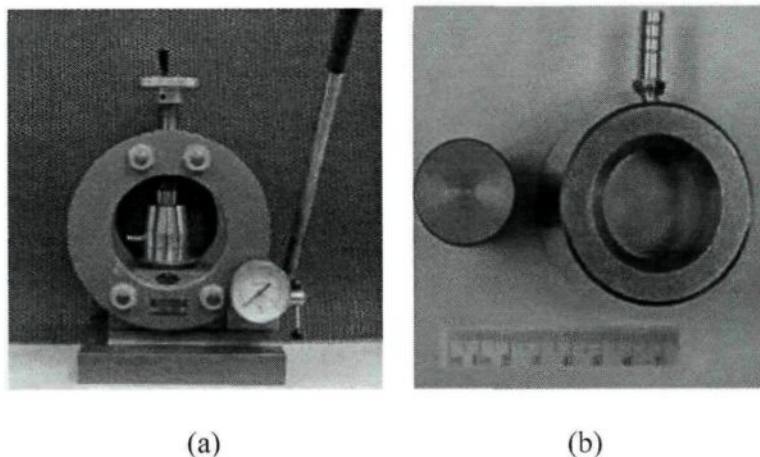
Figure 3-9: (a) The 50 Ton-Capacity Hydraulic Press, and (b) 32 mm ø Steel Mould.

The powder-PVA mixture was then weighed (~20 g for each sample) and cast into the steel mould and pressed under a load of 30 tons in order to form cylindrical samples (discs) of 32 mm diameter and 10 mm thickness.

The pressed tablets were piled in two rows onto a refractory plate filled with 0.5-1mm diameter high purity tabular alumina gravels to prevent the contact of sample tablets with the refractory plate so that possible contamination of the tablets could be avoided. The samples were left in the drying furnace for overnight at 120°C.

The next step was sintering the tablets at the RTA Arvida Research Center laboratory using a high temperature Blue-M, atmosphere controlled furnace. Appearance of the tablets before and after sintering can be seen in Figure 3-10. Argon gas was blown into the furnace in order to protect the heating elements from oxidizing.

- The heating and cooling rate of the furnace was set to 3°C/min.

- The tablets were heated up to 1600°C and left at this temperature for 5 hours. Sintering process temperature and time data can be seen in Figure 3-11.

- Very few tablets (<5%) showed internal cracks after the sintering process.

- The apparent porosity level of the tablets was found to be ~15%.

- The quality of the tablets was found reasonable.

Cuisson#1
BEFORE

Cuisson#1
AFTER SINTERING at 1600°C
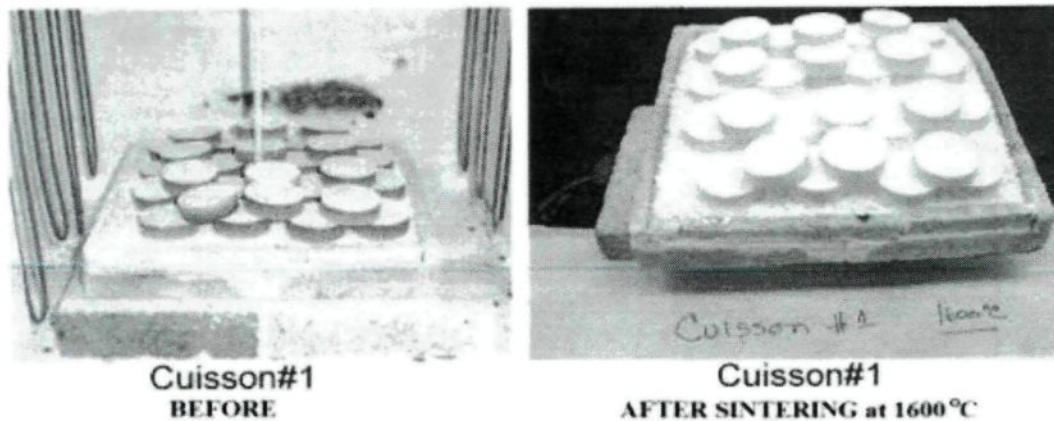
Figure 3-10: The Appearance of the Tablets Before and After Sintering at 1600°C
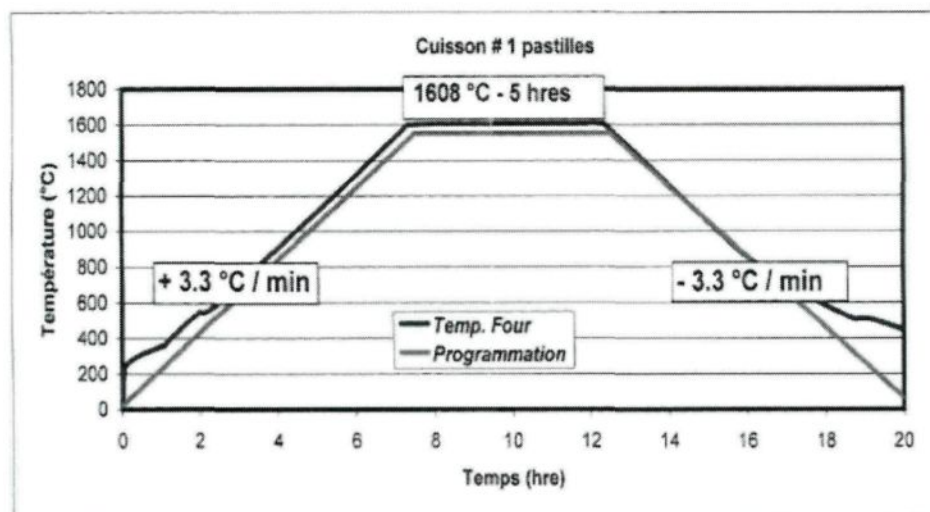
Figure 3-11: The Temperature Profile of the Sintering Furnace During Sintering Process

After sintering, the samples were cut into 10x10x10 mm cubes using a diamond saw as shown in Figure 3-12.
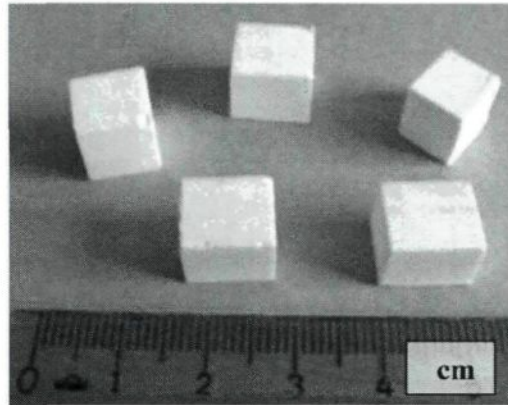
Figure 3-12: Alumina Tablets Ready for Experiments with Molten Aluminum Alloys

3.2.5   Liquid Metal Velocity

The plant data shown below was used to calculate the molten aluminum alloy velocity [12].

- Nominal metal flow rate : 850 kg/minute (0.363 m^3/minute)
- Increased metal flow rate : 1100 kg/minute (0.469 m^3/minute)
- Density of liquid aluminum (ρ_{Al}:2345 kg/m^3)
- Area : ~ 4 m^2

According to the data given above, the liquid alloy velocity is between 1.50 to 1.95mm/s. This information was used to design an experimental system which can operate in this molten metal velocity range.

The major part of the experimental study was conducted using 1.8mm/s. The effect of velocity was also tested using 3.6mm/s and 0.0mm/s (static) molten metal velocities (see Table 3-5).

Table 3-5: Molten Aluminum Alloy Velocities Used in the Experimental Study

Molten Metal Velocity, mm/s	Description
0.00	Static experiments
1.80	Average molten metal velocity
3.60	Two times higher than the average velocity

3.2.6 Liquid Metal Temperature

The molten metal casting temperature in the plant is between 680 to 720°C. The major part of the experimental study was conducted at 715°C, but also temperatures listed below in Table 3-6 were used in the experimental study to determine the effect of temperature on reaction rates.

Table 3-6: Molten Aluminum Alloy Temperatures Used in the Experimental Study

Molten Metal Temperature, °C	Description
690	Used to determine the reaction rates at low temperature
715	Average aluminum alloy filtration temperature
750	Used to determine the reaction rates at high temperature

3.2.7 Inclusion Study

One of the purposes of the experimental study was to determine the interactions of inclusions with alumina (tablets) and aluminum under flow condition. The most common inclusion types in deep bed filters were identified as MgO, Mg-spinel ($MgAl_2O_4$) films or clusters of films from the literature.

To investigate the interactions of inclusions (listed in Table 3-7), alumina and aluminum, 3 mm diameter hole was drilled onto the alumina tablet. A piece of inclusion source was placed in this hole as shown in Figure 3-13. MgO was in particle form; therefore; they were placed in the hole on the alumina tablet easily. On the other hand, the Mg-spinel was in powder form and was mixed with a small amount of PVA to make a paste form of Mg-spinel. The hole on the alumina tablet was filled with this paste, and it was well-dried before being tested in the experiments with molten metal.

Table 3-7: Inclusion Sources Used in the Experimental Study

Inclusion Type	Description
MgO	97.2%purity, 1-9 mm diameter balls-Baymag 30
Mg-spinel	99.8% purity-1-5 micron powder- Atlantic Equip.Engineers
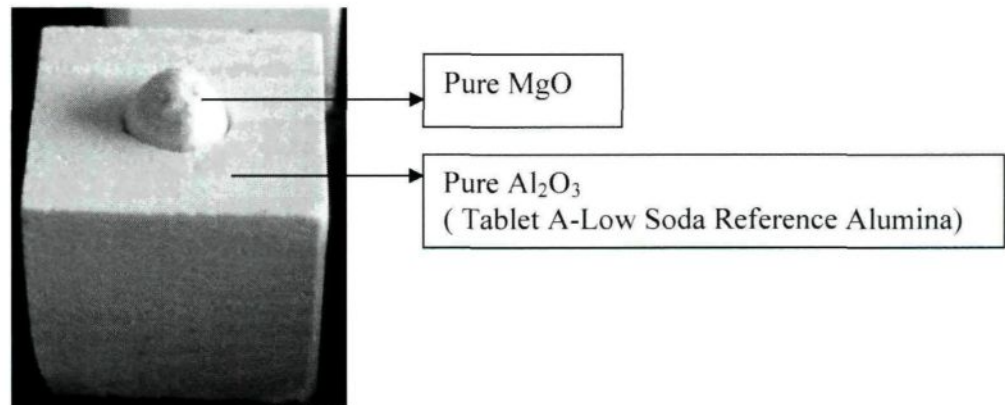
Figure 3-13: Inclusion Study Using Alumina Tablets and Pure MgO Balls

3.3 Physical Characterization of Alumina Samples

3.3.1 Apparent Porosity

Apparent porosity is one of the primary properties of ceramic materials. This property of ceramic is widely used in the evaluation and comparison of product quality and as part of the criteria for selection and use of ceramic products in a variety of industrial applications.

The apparent porosity measurements of different alumina particles and laboratory-made tablets were carried out using the "Standard Test Method for Apparent Porosity, Liquid Absorption, Apparent Specific Gravity, and Bulk Density of Refractory Shapes by Vacuum Pressure" (ASTM C830-93 -Reapproved 1998). This test method is applicable to all refractory samples (volume ~400 cm^3) except those that chemically react with both water and mineral spirits. The test method requires a weighing scale with a precision of 0.1 g. On the other hand, the alumina samples have quite smaller volumes (volume ~0.1-1 cm^3) compared to the refractory samples mentioned earlier in this test method; therefore, an analytical balance with a 0.1 mg accuracy was used in order to have a high degree of precision for alumina samples.

Procedure:

1. Determination of Dry Weight, D: Dry the test specimens to constant weight by heating to 105 to 110°C for an hour and determine the dry weight, D, in grams to the nearest 0.1 mg.

2. Saturation: Place the test specimens in a suitable vacuum pressure vessel which was closed, secured, and evacuated to an absolute pressure of not more than 1.9 in Hg

(6.4 kPa). Hold at this pressure for 30 minutes. Allow the water to enter the vessel while maintaining the vacuum for 5 minutes. Then close the vacuum line, and leave the samples in the water for 20 minutes. Saturated specimens are now ready for weighing.

3. <u>Determination of Suspended Weight, S:</u> Determine the weight, S, of each test specimen in grams to the nearest 0.1 mg after saturation and while suspended in liquid. This weighing is usually accomplished by suspending the specimen in a loop or halter of 0.643 mm diameter copper wire hung from one arm of the balance. The balance was previously counter-balanced with the wire in place and immersed in liquid to the same depth as is used when the refractory specimens are in place.

4. <u>Determination of Saturated Weight, W:</u> After determining the suspended weight, blot each specimen lightly with a moistened smooth linen or cotton cloth to remove all drops of liquid from the surface, and determine the saturated weight, W, in grams to the nearest 0.1 mg by weighing in air.

5. <u>Calculation of apparent porosity, P:</u> The apparent porosity expresses (in %) the relationship of the volume of open pores in the test specimen to its total volume.

$$\text{Volume of Pores, cm}^3 = (W-D)/\rho_w \qquad (3.1)$$

$$\text{Total Volume, cm}^3 = (W-S)/\rho_w \qquad (3.2)$$

$$P, \% = [(W-D)/(W-S)] \times 100 \qquad (3.3)$$

Where $\rho_w = 1$ g/cm^3 is the density of water

3.3.2 Grain Size Measurements

The grain size measurements of the ceramic materials can be carried out using either thermal or chemical etching methods.

The thermal etching method requires leaving the polished ceramic samples about 20 minutes in a high temperature furnace which is set to 150°C below the sintering temperature of the ceramic material. This set-temperature is around 1750-1800°C for commercial grade tabular aluminas since their sintering temperature is over 1900°C. High temperature requirement did not allow the utilisation of this method in the present study.

The chemical etching was found to be more suitable method to pursue. Two methods can be used for etching. First one is to use 85% phosphoric acid which is an extremely dangerous material. The second one is to find a chemical which can react with grain boundaries and reveal them. Magnesium alloyed molten aluminum metal which was used in the hot metal experiments of the present study is one of the best candidates for this type of chemical etching. Magnesium diffuses into the pores and also to grain boundaries of alumina gravel. If the alumina gravels are overexposed to molten Mg-Aluminum until magnesium reaches the core of the gravels, then the grain boundaries become visible after polishing the samples. The following procedure was developed to measure the grain size of the commercial grade alumina gravels.

- Seven alumina gravel samples from four different suppliers were kept in 5%Mg-Al molten alloy at 715°C for 10 days.

- Samples were prepared for metallographic investigation as explained in section 3.5.

- Observations after sample preparation showed that the alumina samples subjected to magnesium diffusion for a long time turned to grayish-black color, and grain boundaries were clearly visible in some portions of the alumina structures (see Figure 3-14).

- The grain size measurements were performed at these sections of the samples using the image analysis manually.
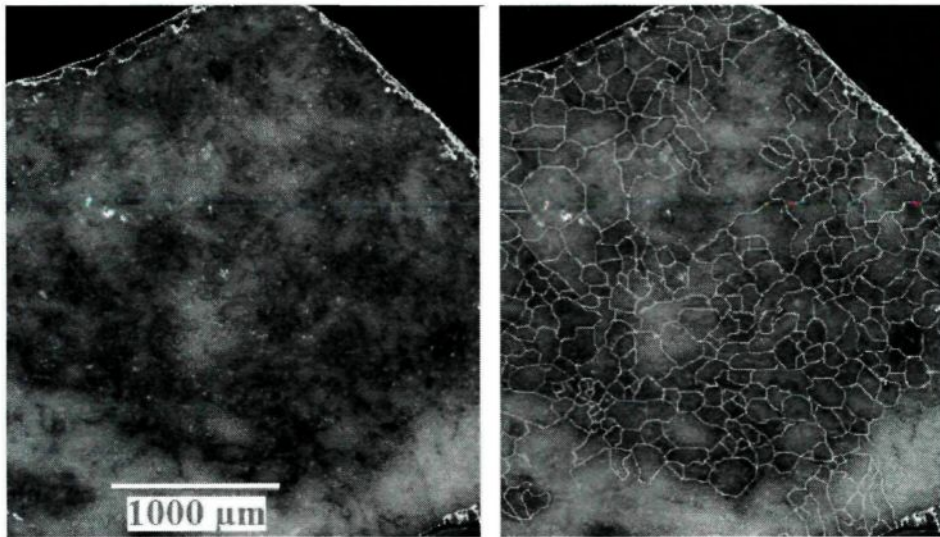
Figure 3-14: Revealed Grain Boundaries of Commercial Grade Alumina Gravel (Aluchem)

3.3.3 Surface Roughness Analysis

The surface roughness measurements were done using the MicroXAM non-contact 3D surface profilometer which is able to measures roughness, finish and texture of surfaces ranging from highly polished surfaces in optics, wafers, and disk media to rough surfaces such as rolled steel and aluminum, paper, plastics, and ceramics. It can characterize 3D microstructures such as those of micro-electronic mechanical systems (MEMs).

3.4 Chemical Characterization of Alumina Samples

Four different commercial type tabular alumina particles which are the most common deep bed filter media materials were tested in the experiments. A study on the chemical and physical characterization of the particles was conducted before starting the experiments. X-ray fluorescence analysis of the alumina particles shown in Table 3-8 were performed by the COREM chemical analysis and characterization laboratory.

Five types of laboratory-made alumina tablets were tested in the experiments. The X-ray fluorescence analysis of the sintered laboratory-made alumina tablets shown in Table 3-9 were also performed by the COREM chemical analysis and characterization laboratory located in Quebec City, Canada.

Table 3-8: X-ray Fluorescence Analysis of Tabular Alumina Samples

Sample	%Al_2O_3	%Na_2O	%SiO_2	%MgO	%Fe_2O_3	%TiO_2	%K_2O
Naigai	98.3	0.250	0.040	<0.10	<0.01	0.010	< 0.01
Alufin	97.7	0.080	0.050	<0.10	0.050	0.26	0.01
Aluchem	98.0	0.170	0.050	<0.10	0.020	0.01	0.01
Alcoa-T64	98.6	0.240	0.050	<0.10	0.060	0.01	<0.01

Table 3-9: X-ray Fluorescent Analysis of Alumina Tablet Samples.

	Sample	%Al_2O_3	%Na_2O	%SiO_2	%MgO	%Fe_2O_3	%K_2O
Tablet A	High Purity Al_2O_3	98.7	0.050	0.10	<0.10		
Tablet B	High Na_2O	98.1	0.330	0.07	<0.10	0.080	0.01
Tablet C	High Silica	98.1	0.020	0.64	<0.10	0.230	<0.01
Tablet D	High MgO	98.0	0.090	0.10	0.53	0.080	0.010

3.5   Experimental Procedure

The experimental procedure used for both System-I and System-II can be summarized as follows.

1. Liquid aluminum alloy was prepared as explained in the previous section.

2. The experimental system was placed into the reheating furnace at $120^{\circ}C$ for 60 minutes.

3. Then, for System-I:

    a. The cylindrical graphite body was attached onto the carrier using steel bolts.

    b. The sample holder plate with alumina samples (shown in Figure 3-4) was pinned to the bottom of the set-up using graphite hooks.

    c. The mixer shaft was connected to the electrical motor shaft that has an adjustable speed from 0 to 100 rpm.

4. For System-II, the disc or discs were placed onto the alumina shaft which was then connected to the electrical motor shaft that has an adjustable speed as mentioned above.

5. Then, the system was ready to be submerged into liquid aluminum (see Figure 3-2).

6. The graphite body of the experimental set-up was lowered very slowly using the crane system until the bottom of the set-up is just above the molten metal.

7. CO_2 gas (>99% pure) was blown with a volumetric flow of 2-3cm^3/min right onto the liquid metal surface. This gas was used both to protect the graphite parts of the experimental set-up and to avoid excessive oxidation of aluminum alloy.

8. Using refractory materials, the openings at the furnace top were closed so that the heat loss could be reduced to a minimum.

9. Furnace temperature was set 30-40°C higher than the target temperature in order to compensate for the heat loss that occurs when the experimental set-up at low temperature was submerged into molten aluminum.

10. The graphite body was submerged into molten aluminum slowly (~1cm depth / min).

11. The bolts of the stainless steel rods connected to the carrier were checked and tightened often. Due to higher thermal expansion of steel (compared to graphite and alumina insulation materials), molten aluminum might infiltrate into the joint openings between steel and insulation materials. This might cause the whole and/or partial loss of the experimental system parts.

12. Hot metal temperature was measured after the whole system was submerged into the molten metal.

13. Mixer speed set-up: Once the metal temperature reached the target, the mixer speed was set, and the switch was turned on to start the experiment. For experiments with:

   a. System-I: The mixer speeds were set according to Table 3-10 which shows the corresponding molten metal velocities in the filter section for different mixer speeds.

   b. System-II: The position where samples had to be placed on the disc and its rotational speed were set according to Table 3-11 shown below.

Table 3-10: The Mixer Speed vs. Molten Metal Velocities [Chapter 5]

Mixer speed, RPM	Velocity, mm/s
0	0.00
15	1.50
20	1.80
25	3.20
26	~3.60

Table 3-11: Molten Metal Velocity Calculations for Samples Placed on Rotating Disc

Alumina Sample Distance from Disc Center, mm	Time/turn, s	Disc Speed, rpm	Average Velocity, mm/s
25	90	0.67	~1.80
25	45	1.33	~3.60
50	90	0.66	~3.60

14. In experiments which required stagnant molten metal (no fluid flow-static experiments), mixer was run only 5 minutes at 20 rpm with System-I and 1 rpm with System-II at the beginning of the test in order to make sure that the alumina samples were in contact with liquid aluminum. After five minutes of fluid flow around particles, the mixer was turned off until the end of the test.

15. Magnesium metal in the aluminum alloy has a higher partial vapour pressure than aluminum. It tends to evaporate and form oxides at the metal surface. Therefore, magnesium metal was added everyday into molten metal after cleaning the oxides formed at the metal surface.

    a. System-I: The amount of magnesium metal to be added into the molten aluminum alloy was determined as 10, 15, 20 g/day for 2, 5, and 7%Mg-Al

alloy, respectively, based on the experimental results obtained during preliminary experiments.

b. <u>System-II</u>: The magnesium loss in the experiments which were conducted using System-II was not as high as the one observed with System-I due to slower speed of the mixer rotation. In these experiments 5 g of magnesium metal was added daily.

16. Sample collection: When the experiment was finished,

a. <u>System-I</u>: The whole set-up was taken out of the liquid metal, the hooks of the sample holder plate were dismantled, and the plate was placed on a refractory for sample collection. Using a pincer, the slots containing alumina samples inside are taken out of the sample holder plate grooves and left to cool down on a warm refractory brick.

b. <u>System-II</u>: The alumina samples were collected intermittently according to the experimental schedule. The sample collection for rotating disc(s) was as follows:

i. Metal surface was cleaned using a spatula.

ii. The rotating disc was ascended in the crucible using the adjustable carrier (crane) until it was right below the molten metal surface.

iii. The disc motion was not paused. The sample positions were determined using velocity patterns of samples while the disc rotated.

iv. Using a pincer, samples were removed from the disc and placed onto a warm refractory to cool down.

v. The set-up was then lowered to its original depth and the experiment continued.

17. The samples taken out were ready for metallographic preparation.

3.6 Ceramographic Sample Preparation

Metallographic investigation of the test samples was the one of the most important parts of this study since the affected zone of alumina particles and aluminum metal was the main focus of the project.

As it is mentioned earlier in the experimental study part, all tests were carried out using only one layer of alumina particles or tablets placed into the filter section or on a rotating disc. At the end of the experiments, alumina samples were partially or fully covered by aluminum metal (see Figure 3-15).

The alumina samples were placed on the bottom piece of the plastic mould carefully, ensuring that the metal flow direction was parallel to the surface to be cut and polished in order to have a cross-sectional view of the alumina-aluminum interface parallel to the metal flow direction. In Figure 3-16, a schematic description of the sample preparation is presented. It was necessary to start the metallographic preparation as soon as the samples were cold enough to be mounted into epoxy. As mounting material, 24 hour curing time ANAMET 233-L Epoxy resin-hardener kit, and as castable mounting mould, ANAMET CMMC-150 38 mm diameter, two piece of plastic mould were used.

After sample was placed into the mounting mould, epoxy resin and epoxy hardener mixture was poured. Mould was then placed into a desiccator with a vacuum line connected

for removing the entrapped air bubbles in the sample and resin-hardener mixture. This made epoxy sounder which is an indispensable quality for subsequent grinding and polishing processes.
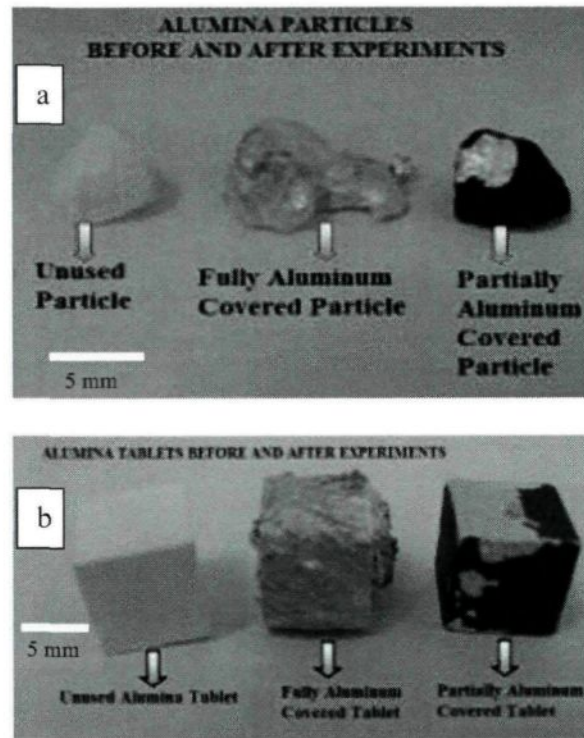
Figure 3-15: Appearance of (a) Alumina Particles, and (b) Lab-Made Alumina Tablets Before and After Tests
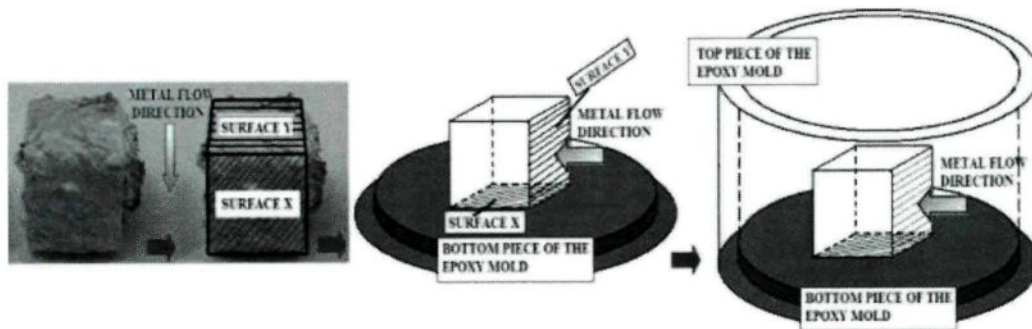
Figure 3-16: A Schematic Description of Sample Preparation

The surface to be polished is shown schematically in Figure 3-17 as Z Plane. Struers Unitom-2 (Figure 3-18) cut-off machine was used for removing ~5 mm material from the mounted alumina sample. This device was operated using 26EXO type diamond cut-off wheel for cutting samples which contained alumina ceramics.

Several grinding and polishing recipes were tried using conventional grinding and polishing techniques in order to obtain the best image quality of alumina\aluminum interface for optical microscope or SEM investigations. Many of these trials ended up with failure due to fuzzy images at the interface. The blur image roundness occurs due to high abrasion rate of aluminum metal at the alumina\aluminum interface. Alumina particles are hard and rigid, whereas aluminum metal has a soft and sticky character compared to alumina particles; therefore, aluminum metal abrasion rate was higher than that of alumina. The test samples contained almost 90% alumina particles or tablets, and 10% aluminum metal (see Figure 3-19 below). When conventional grinding process with SiC type abrasive papers and/or Al_2O_3 type abrasive plates was employed, long grinding residence time was required to get a flat surface because of hard alumina particles.
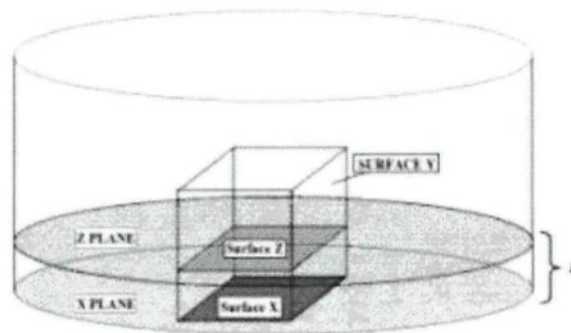
Figure 3-17: A Schematic Description of the Cutting of Mounted Sample
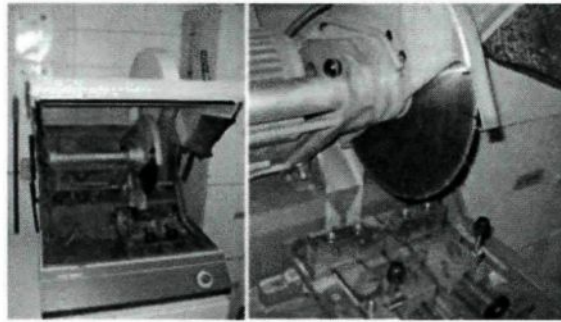
Figure 3-18: Struers Unitom-2 Cut-off Machine and 26EXO Type Diamond Disc
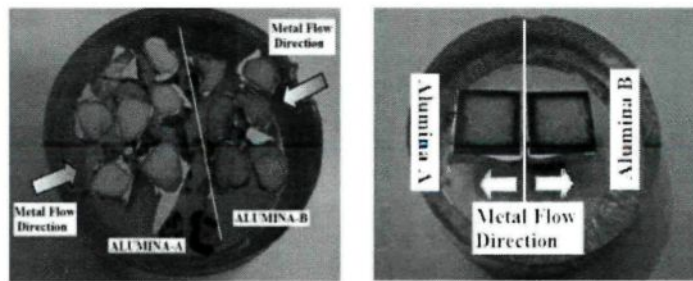
Figure 3-19: View of Samples After Polishing

Table 3-12: Sample Preparation Procedure

Grinding					
Platen	**Cooler**	**Force/ samples [lb]**	**Rotation [RPM]**	**Duration**	**Plate and Sample Holder Rotation Directions**
Diamond pad (Buehler)	Water	9	300	2 min.	Same
Polishing					
Polishing Cloth	**Polishing Suspension**	**Polishing Extender**	**Force/sample [lb]**	**Rotation [RPM]**	**Duration**	**Direction**
MD Largo (Buehler)	9μ, diamond Metadi	-	6.7	150	7 min.	Same
Textmet 1000 (Buehler)	3μ diamond paste	Metadi Fluid	5.6	150	6.5 min.	Same
OP CHEM (Buehler)	0.05μ Colloidal Silica	water	5.6	150	2min.	Opposite

A metallographic sample preparation procedure (Table 3-12) was developed with the assistance of Aluminum Technology Centre (ATC) Metallography Laboratory.

- A short, high-pressure, grinding step using a diamond plate (220 μm grit) overcame the roundness problem.

- The water-based 9 μm diamond was employed as the first step of polishing. The polishing trials using oil based diamond suspension left a greyish-black hue on white alumina particles and it was impossible to remove this hue without going back to the grinding step. The porous structure of alumina did not permit to the use of oil-based diamond suspensions at this step.

- As the last step of polishing process before using colloidal silica, 3 μm diamond paste with TextMet1000 polishing cloth was used. The same greyish black hue (diamond paste accumulation in alumina pores) was observed on alumina particles when the polishing cloth TextMet1000 was overused. The over-usage of polishing cloth should be avoided to prevent the contamination of test samples.

- Same metallographic sample preparation method was used for both alumina particle and tablet samples.

3.7   Analysis of Metallographic Samples

3.7.1   Optical Microscopy and Image Analysis

The optical microscopy analyses were conducted using the Nikon Eclipse ME600 upright optical microscope with 3-axis motorized stage controller Model ST100 equipped with Clemex Image Analyzer and Sony Digital Color Camera shown in Figure 3-20 below.

After the samples were polished, the first investigation was always made with the optical microscope. Both micro and macro digital images of the samples were taken by using the optical microscope, macro image set-up table, and Sonny digital camera with a suitable lens for this purpose. These images were analyzed using the image analyzer to determine the average affected zone thickness for each sample.
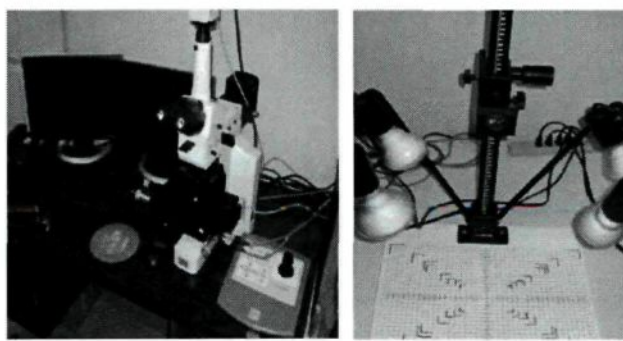
Figure 3-20: Nikon Upright Optical Microscope and its Accessories

An example of an optical microscope image can be seen in Figure 3-21. Under the optical microscope, the reaction zone has a distinctive yellow-goldish color at alumina/aluminum interface as shown in Figure 3-21. The appearance of the affected zone was observed in dark (blackish) color at the macro image in Figure 3-22.
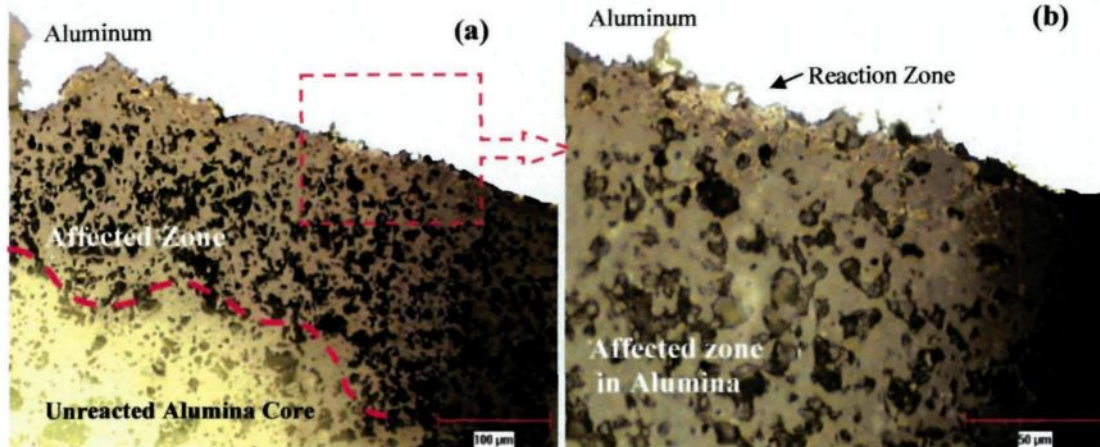
Figure 3-21: View of an Alumina/Aluminum Interface after an Experiment

The sizes of samples were relatively large to use microscope digital images for the reaction zone area measurements; therefore, digital macro images were used for this purpose as shown in Figure 3-22. The image analysis software (CLEMEX Vision^{TM}, Version 3.0) was used for color threshold analysis. It separated the different zones with different colors found on the sample surface. The color thresholds used in this analysis were adjusted carefully using the exact reaction and affected area layer thicknesses determined by the optical microscopy analyses.

Figure 3-22: Macro Images of Aluchem type Alumina After Three Day Experiment

The red color in Figure 3-23 represents the black/gray affected zone where magnesium diffusion took place on alumina particle. The green part is basically the white unaffected alumina zone.

Figure 3-23: Analysis of the Alumina Gravel Samples After Experiments

The reaction zone on alumina particles were not only on the alumina particle surface/aluminum interface. Most of the particles showed intergranular reactions. The most common method to determine the extent of the reaction zone in refractories was found in the literature [65] which uses the following equation:

$$Average\ affected\ zone\ thickness, (x) = \frac{Area\ of\ the\ affected\ zone, (s)}{Perimeter\ of\ the\ particle, (p)} \quad (3.4)$$

3.7.2 SEM-EDS Analysis

Part of scanning electron microscopy tests was conducted in the Electron Microscope Laboratory of the Aluminum Technology Center of the National Research Council of Canada in Saguenay. A field-emission-gun Leo 1525 FEGSEM equipped with an Oxford Instrument INCA 300 thin-window energy-dispersive X-ray (EDS) system

Figure 3-21: View of an Alumina/Aluminum Interface after an Experiment

The sizes of samples were relatively large to use microscope digital images for the reaction zone area measurements; therefore, digital macro images were used for this purpose as shown in Figure 3-22. The image analysis software (CLEMEX Vision™, Version 3.0) was used for color threshold analysis. It separated the different zones with different colors found on the sample surface. The color thresholds used in this analysis were adjusted carefully using the exact reaction and affected area layer thicknesses determined by the optical microscopy analyses.

Figure 3-22: Macro Images of Aluchem type Alumina After Three Day Experiment

The red color in Figure 3-23 represents the black/gray affected zone where magnesium diffusion took place on alumina particle. The green part is basically the white unaffected alumina zone.

Figure 3-23: Analysis of the Alumina Gravel Samples After Experiments

The reaction zone on alumina particles were not only on the alumina particle surface/aluminum interface. Most of the particles showed intergranular reactions. The most common method to determine the extent of the reaction zone in refractories was found in the literature [65] which uses the following equation:

$$Average\ affected\ zone\ thickness, (x) = \frac{Area\ of\ the\ affected\ zone, (s)}{Perimeter\ of\ the\ particle, (p)} \quad (3.4)$$

3.7.2 SEM-EDS Analysis

Part of scanning electron microscopy tests was conducted in the Electron Microscope Laboratory of the Aluminum Technology Center of the National Research Council of Canada in Saguenay. A field-emission-gun Leo 1525 FEGSEM equipped with an Oxford Instrument INCA 300 thin-window energy-dispersive X-ray (EDS) system

analyzer was used to analyze the samples. The operating voltage was 20kV. EDS examination were performed using 30 or 60 urn aperture diameters, which gave a probe size of approximately 20-25nm. EDS chemical maps with pixel resolution of 512x512 were acquired without automatic drift correction. Additional analyses were carried out at the Materials Technology Laboratories of the University of Sherbrook.

In order to facilitate the SEM analysis, a method was developed based on making use of different fluorescence characteristics of magnesia and spinel under the ultra-violet (UV) light. According to this method, in a dark room, long wave UV-light was applied onto the polished samples by using a portable UV light source (Model UVGL-25, Mineralight® Lamp, multi band 254/366 nm), and the sites where the spinel was formed were determined. The vicinities of the fluorescent regions were marked by using a diamond tipped pencil (Agilent, catalog no: 420-1000) so that the spinel formation sites could be rapidly identified during the SEM analysis.

A couple of samples were analyzed at the Laval University in Quebec City using SEM microprobe analysis-Jeol.

3.7.3 XPS Analysis - ArcelorMittal Dofasco R&D Laboratory

X-ray Photoelectron Spectroscopy (XPS) PHI Quatera *SXM*™ (ULVAC-PHI INC.), also known as Electron Spectroscopy for Chemical Analysis (ESCA), is a surface analysis technique that provides the chemical state and the surface quantity by irradiating mono-energetic X-rays and measuring the energy of photoelectrons emitted from the sample surface. *Quantera SXM*™ is an XPS Microprobe which provides a scanning X-ray beam of

9 - 200 μm in diameter. XPS is equipped with high performance thin film analysis capabilities.

The XPS analyses of the samples were conducted at ArcelorMittal Dofasco Research and Development Center in Hamilton. The operational conditions of the XPS analyses are shown in Table 3-13. The aluminum skin on alumina samples as shown in Figure 3-15a were peeled off to analyze both the blackened alumina surface and the bottom of the peeled aluminum metal assuming that some of the interfacial reaction product is ripped and left on both sides while peeling off the aluminum skin.

Table 3-13: Operational Conditions of XPS Analyses

Pass Energy	224.00 eV
Take off angle	45^0
Beam size	100 μm

3.8 List of Experiments

The list of experiments conducted using the commercial alumina grades, lab-made alumina tablets, and alumina tablets with inclusion sources are summarized in Table 3-14, 3-15, 3-16, and 3-17, respectively.

Table 3-14: Experimental Parameters for the Experiments with Commercial Tabular Alumina Grades (+4.80-6.35 mm) using Experimental System I

Exp. no	Parameters				Tabular Alumina Grades			
	Holding Time (day)	% Mg Conc.	Mixer Speed (rpm)	Molten Metal Temp. (°C)	Naigai	Aluchem	Alcoa-T64	Alufin
1	1	0	20	715	√	√	√	√
2	3	0	20	715	√	√	√	√
3	5	0	20	715	√	√	√	√
4	1	5	20	715	√	√	√	√
5	3	5	20	715	√	√	√	√
6	5	5	20	715	√	√	√	√
7	1	5	0	715	√	√	√	√
8	3	5	0	715	√	√	√	√
9	5	5	0	715	√		√	√
10	1	7	20	715	√	√	√	√
11	3	7	20	715	√	√	√	√
12	5	7	20	715	√	√	√	√
13	1	2	20	715	√	√	√	√
14	3	2	20	715	√	√	√	√
15	5	2	20	715	√	√	√	√

Table 3-15: Summary of Experiments Conducted for Testing Commercial Alumina Gravels (+4.80-6.35 mm) Using Experimental System II

Exp. no	%Mg conc.	Disc Rot. Speed, rpm	Temp., °C	Holding Time	Commercial Alumina Gravels			
					Alcoa T64	Naigai	Aluchem	Alufin
1	5%	0.67	715	6, 12 hours	√	√	√	√
2	5%	0.67	715	6, 12 hours	√	√	√	√
3	5%	0.67	715	1, 3, 5, 7 days	√	√	√	√
4	5%	0.67	715	1, 3, 5, 7 days	√	√	√	√
5	5%	0	715	1, 3, 5, 7 days	√	√	√	√
6	5%	0	715	1, 3, 5, 7 days	√	√	√	√
7	5%	0.67	750	1, 3, 5, 7 days	√	√	√	√
8	5%	0.67	750	1, 3, 5, 7 days	√			
9	2%	0.67	715	6, 12 hours	√	√	√	√
10	2%	0.67	715	6, 12 hours	√	√	√	√
11	2%	0.67	715	1, 3, 5, 7 days	√	√	√	√
12	2%	0.67	715	1, 3, 5, 7 days	√	√	√	√
13	7%	0.67	715	6, 12 hours	√	√	√	√
14	7%	0.67	715	6, 12 hours	√	√	√	√
15	7%	0.67	715	1, 3, 5, 7 days	√	√	√	√
16	7%	0.67	715	1, 3, 5, 7 days	√	√	√	√

Table 3-16: Experiments Conducted with Lab-made Alumina Tablets Using Exp. System II

Exp. no	%Mg Conc.	Disc Rot. Speed, rpm	Temp., °C	Lab Made Alumina Tablets			
				A - T64	B-Na₂O	C-SiO₂	D-MgO
1	5%	0.67	715	√	√	√	√
2	5%	0.67	715	√	√	√	√
3	5%	0	715	√			
4	5%	0	715	√			
5	5%	0.67	750	√			
6	5%	0.67	750	√			

Holding time: 6, 12, 24, 48 hours

Table 3-17: List of Experiments Conducted for Testing Lab-made Alumina
Tablets/inclusion Sources using Experimental System II

Experiment no	%Mg concentration	Disc Rotational Speed, rpm	Temperature, ^{0}C	Inclusion Source	
				MgO	Spinel
1	5%	0.67	715	√	√
2	5%	0.67	715	√	√
3	2%	0.67	715	√	√
4	7%	0.67	715	√	√

Holding time: 6, 12, 24, 48 hours

CHAPTER 4

4. PHYSICAL AND NUMERICAL MODELING OF EXPERIMENTAL SYSTEM-I USING WATER

In order to investigate the interaction of alumina particles and aluminum alloys under flow conditions, the flow around the particles should be known. It is very difficult to measure the flow in molten aluminum which is at high temperature (700-750°C). Therefore, water experiments were carried out to measure the velocities using the design of the experimental system-I. Water is a practical replacement for aluminum during hydrodynamic studies because water at 25°C and aluminum at 700°C have similar kinematic viscosities (dynamic viscosity / density), 1.005×10^{-06} m^2/s and 1.300×10^{-06} m^2/s, respectively.

Existing 3D, one-phase steady-state model [105-106] was modified for the experimental set-up geometry (experimental system I) using CFX4$^{\text{TM}}$ commercial code. A parametric study was carried out to predict the flow field for different operating conditions and design parameters. The conditions yielding uniform flow in the vicinity of the particles placed in the sample holder section of the experimental system were identified. The predictions of the model were compared with the velocities experimentally measured using water. This comparison validated the model. The validated model can be used for different purposes. In this study, it was used to calculate the flow field for different experimental system designs until the uniform flow field was obtained in the filter section of the system.

It was also used to predict the velocities around the particles during the experiments with aluminum simply by changing the properties of water with those of aluminum.

4.1 Objectives

The objectives of this part were to:

1. To modify the mathematical model to simulate the experimental system,

2. To carry out the simulations for the same conditions used in the visualization study and to compare the simulation results with the experimental ones, and

3. To conduct a parametric study to find the optimum design and operational variables which would give a flow field similar to the actual bed filter using aluminum.

4.2 System

The evolution of the design of experimental system -I is elaborated in Appendix 1 and the latest design is also given in Chapter 4. The earliest design had a crucible with 9 kg capacity, and the design of the top part was different (see Figure 3-2, Figures 4.1-4.2) than that of the latest one with 15 kg capacity. Modified experimental set-up geometry used in the model is shown in Figure 4-3.

It was previously mentioned that the molten metal velocity profile in the sample holder (filter) section of the experimental system was necessary for the investigation of reaction kinetics at the aluminum/alumina interface. It is very difficult to measure the flow in molten aluminum which is at high temperatures (700-750°C). Therefore, a replica of the experimental system described above was fabricated using glass and Plexiglas as shown in Figure 4-4 below so that the interior of the system was visible. The water experiments were

carried out to measure the velocities in the system. This was done by adding fluorescent tracer or graphite powder-water solution into the water and recording the experiments with a digital high speed camera. With this technique, it was possible to measure the velocities by studying the video clip frame by frame using a computer. Then, it was possible to calculate the velocities in aluminum from the flow similarity principal (constant Reynolds number). The water model results were used to validate the mathematical model.

Parts of experimental system:

1. Electrical motor
2. Rotational speed indicator
3. Mixer
4. Cylinder wall
5. Top plate
6. Filter
7. Molten aluminum
8. Crucible
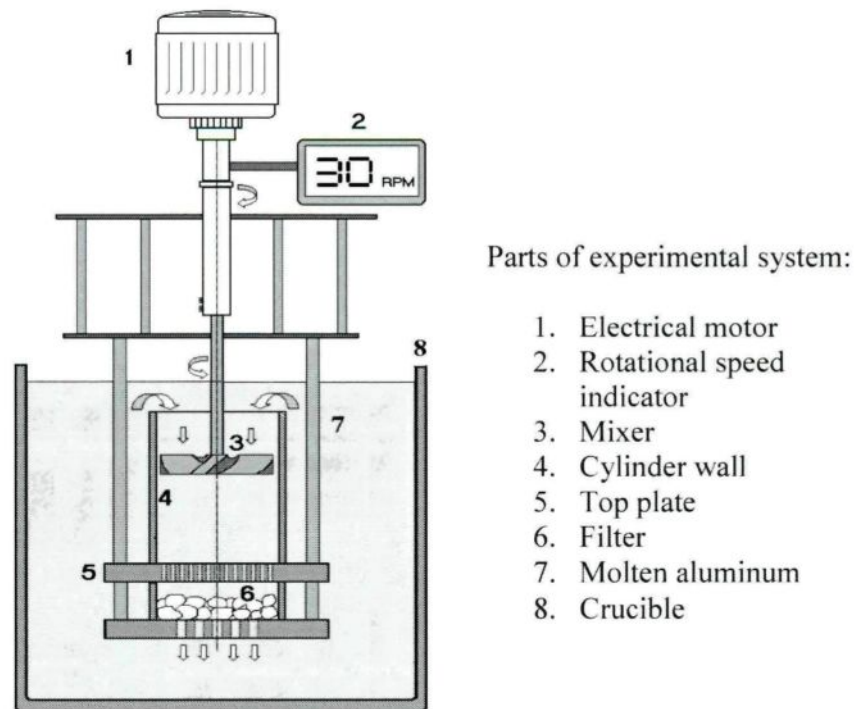
Figure 4-1: A Schematic Description of the Experimental System-I: Early Design
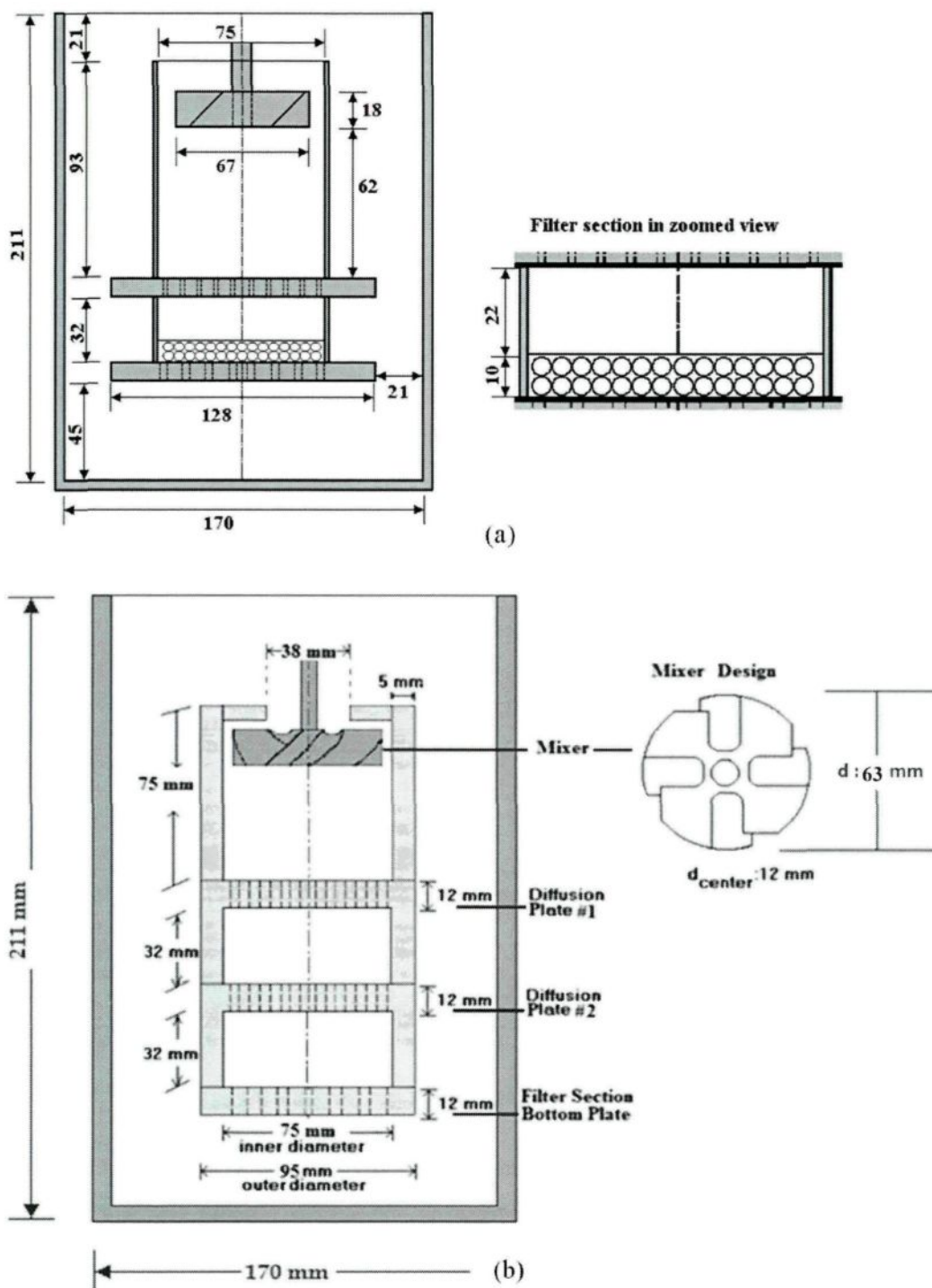
Figure 4-2: Technical Drawings of the Experimental System-I: (a) Early and (b) Recent Designs
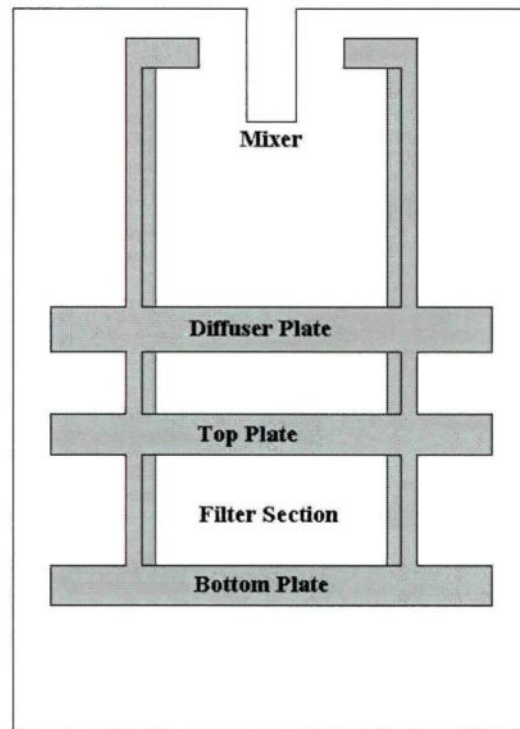
Figure 4-3: The Modified Experimental Set-Up Geometry Used in the Model
(Recent Design)
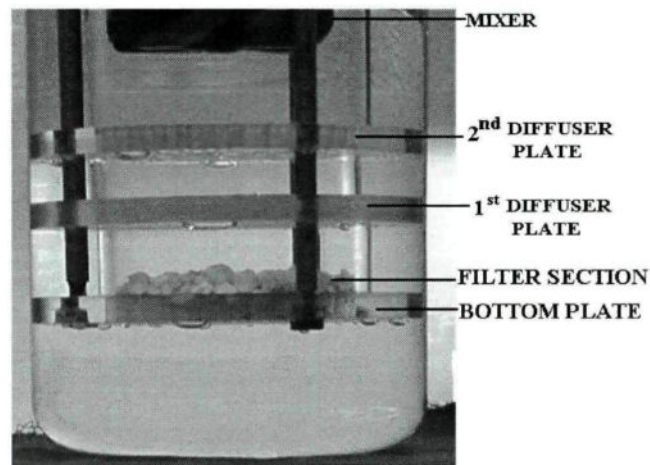
Figure 4-4: General View of the Water Model of the Experimental Set-Up

4.3 Model

The momentum transfer equations and k-ε turbulence model equations are used for solving the flow. The general form of the conservation equation is

$$\frac{\partial \rho \cdot \phi}{\partial t} + div \ (\vec{U} \cdot \rho \cdot \phi) - div \ (\Gamma_\phi \cdot grad \ \phi) = S_\phi \qquad (4.1)$$

where ϕ represents the variable to be solved such as velocity components (u, v, w), mass fractions, turbulent kinetic energy or turbulent dissipation. Γ_ϕ and S_ϕ are the exchange coefficient and the source term respectively. The source term represents any body force acting on the system such as pressure, gravity, buoyancy. $\vec{U}$ is the velocity vector, and ρ is the liquid density. In the model, the source term was used to represent the mixer motion. The pressure drop in a porous media of the filter section is calculated using the Ergun equation.

4.3.1 Source terms for the mixer motion

A source term which representing the force exerted on the cell volume by the momentum transfer from the blades of the mixer to the liquid phase is incorporated into the model. The source term components for a tilted blade are shown as follows [18]:

$$S_U = \frac{1}{2} \rho \left[(\omega.r.\cos\phi|u \ )^2 - u^2 \right] \cdot C_d \cdot n \cdot \overline{A}_f \qquad (4.2)$$

$$S_r = \frac{1}{2} \rho \left[(\omega.r.\sin\phi|v \ )^2 - v^2 \right] \cdot C_d \cdot n \cdot \overline{A}_f \qquad (4.3)$$

$$S_W = \frac{1}{2} \rho \left[(\omega.r.\cos\phi|w \ )^2 - w^2 \right] \cdot C_d \cdot n \cdot \overline{A}_f \qquad (4.4)$$

S_u, S_v, S_w terms represent the source terms applied in x, y and z directions, respectively. ϕ is the blade angle, ρ is the density of liquid, C_d is the drag coefficient for a flat blade, A_f and n are the time-averaged blade and the area number of blades, respectively. A_f is defined in Equation 4.5 where Vc is the volume of a given cell.

$$\overline{A}_f = \frac{V_c}{2\pi r} \tag{4.5}$$

4.3.2 Porous Media Resistance

The pressure drop in a porous media is given by the Ergun equation shown below [107]:

$$\frac{dP}{dL} = \left[\frac{150\,\mu}{\phi_s^2\,d_P^2} \frac{(1-\varepsilon)^2}{\varepsilon^3} + \frac{1.75\,\rho}{\phi_s\,d_P} \frac{(1-\varepsilon)}{\varepsilon^3} |U| \right] \cdot \vec{U} \tag{4.6}$$

In the above equation dP is the pressure drop. μ, ρ, and Φ_s are the fluid viscosity, fluid density and the sphericity of the bed particles. d_p id the bed particle diameter and $\Phi_p.d_p$ is the equivalent diameter of spherical particles. The Equation 4.6 can be written as:

$$\frac{dP}{dL} = -R.\vec{U} \tag{4.7}$$

Where R is the term given in the parenthesis in Equation 4.6.

4.3.3 Boundary Conditions

The top surface of the system was assumed flat and frictionless. In the model, a symmetry-plane boundary condition is used to represent the surface.

4.3.4 Summary of Main Assumptions

1. The turbulence is represented by the k-ε model.

2. The motion of the mixer is represented as a source term in the momentum equation.

4.3.5 Parametric Study

The objective of the parametric study was to optimize the operating conditions and the design of the experimental system to obtain a uniform flow pattern in the filter section. The parameters studied are:

1) Additional diffuser plates (system design)

2) Rotational speed of the mixer

3) The distance between the mixer and the top plate of filter section

4) Mixer diameter

5) Number of mixer blades and blade angle

6) Particle size

4.3.6 Solution technique

In this model, equations were solved by using the CFX4^{TM} commercial code which has a multi-block option for the representation of complex geometries. It uses finite-volume method.

The model consists of 39 blocks which are shown in Figure 4-5. The total number of cells is 68 625 in the model. The body-fitted Cartesian coordinates were used in the model; however, the actual geometry of the system is cylindrical. The cartesian system

caused small differences in shape with respect to the actual system. In Figures 4-6a and 4-6b, the top and bottom plates of the sample holder with several holes (similar to the actual system) are shown. Figure 4-6c presents the additional diffuser system. In the mathematical model, the ratio of void sections to solid sections were kept similar to that of the experimental system; therefore, the differences between the actual plate and its representation in the model were assumed negligible. Although some deformed cells were present within the interior blocks, the steady-state solution converged, and it required only 120 iterations and 45 minutes of computational time on SUN ULTRA-1.
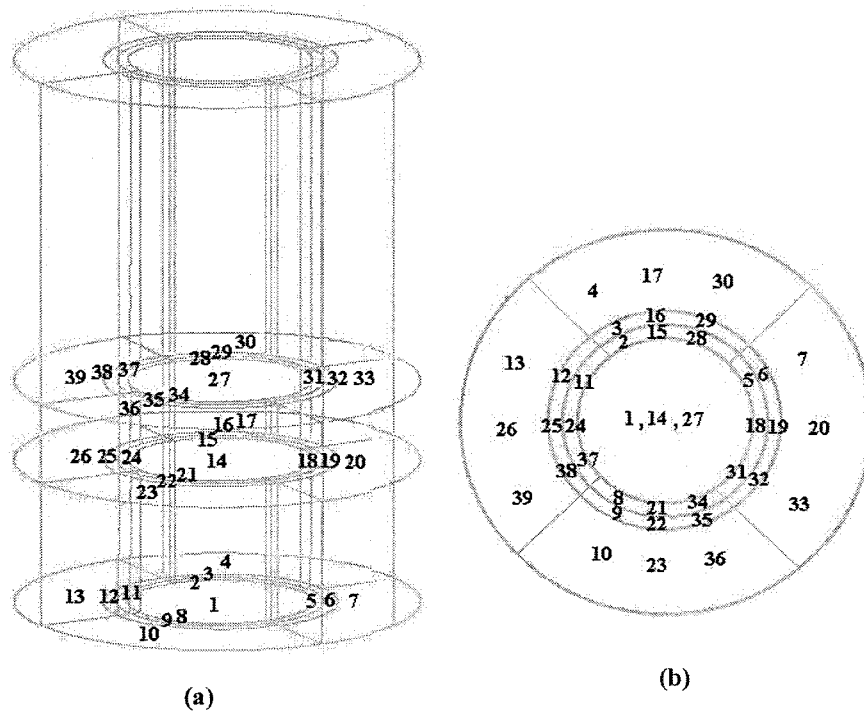
Figure 4-5: Block Configuration of the Model (a) Overall View, (b) Top View
(Numbers indicate the block numbers)
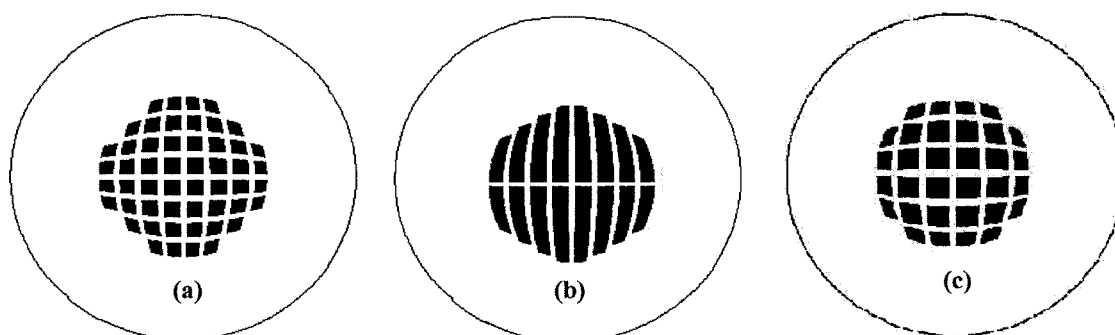
Figure 4-6: Mathematical Model Representations of (a) Top Plate (with 41% porosity), (b) Bottom Plate (48% porosity), and (c) Additional Diffuser Plate (38% porosity)

CHAPTER 5

5. RESULTS AND DISCUSSION

5.1   Physical and Mathematical Modeling Results Using Water

A 3D, one-phase steady-state model was modified for the experimental set-up geometry using the CFX4^{TM} commercial code. A parametric study was carried out to predict the flow field for different operating conditions and design parameters. In this section, the results of this study is presented and discussed. A physical water model (experimental system) was used to validate the mathematical model results. Once validated, the mathematical model can be used to predict the flow field when aluminum is used instead of water. Eleven different cases were examined in the parametric study using the mathematical model. The cases are summarized in Table 5-1.

5.1.1   System Design Simulations

In the first part of the study (from Case 1 to Case 6), the effect of the rotational speed on the uniformity of the flow was studied. All other system parameters such as mixer diameter, mixer height, mixer blade angle, number of blades, and particle size were kept constant (see Table 5-1). Table 5-2 summarizes the results of these simulations.

The mathematical model was run in steady-state mode. The model predictions were compared with experimental measurements in order to validate the mathematical model results. The simulation results are presented in Appendix 2.

Table 5-1: System Variable with Respect to the Cases in the Study.

	Rot. speed (rpm)	Mixer d (mm)	Distance between mixer and top plate (mm)	Blade Angle (°)	Number of Blades	Particle diameter (mm)	Top cover (Y/N)	Simple Buffer (Y/N)	Conical buffer (Y/N)	Dif. Plate (Y/N)
Case 1	15 30	67	62	45	4	9	No	No	No	No
Case 2	15 30	67	62	45	4	9	Yes	No	No	No
Case 3	15 30	67	62	45	4	9	Yes	Yes	No	No
Case 4	15 30	67	62	45	4	9	Yes	No	Yes	No
Case 5*	15 20 25 30	67	62	45	4	9	Yes	No	No	Yes
Case 6**	15 20 25 30	67	62	45	4	9	Yes	No	No	Yes
Case 7	20	63 59 54	62	45	4	9	Yes	No	No	Yes
Case 8	20	67	62	37.5 45 60	4	9	Yes	No	No	Yes
Case 9	20	67	44 56 62 82	45	4	9	Yes	No	No	Yes
Case 10	20	67	62	45	2 4 8	9	Yes	No	No	Yes
Case 11	20	67	62	45	4	3 6 9 12 18	Yes	No	No	Yes

*: Diffuser plates are 18 mm apart from each other.

**: Diffuser plates are 30 mm apart from each other.

In Case 1, the simulations were carried out using the experimental system shown in Figures 4-1 and 4-2a in Chapter 4. The results of the simulations are presented in Figure A2-1 in Appendix 2. The average velocity in the filter section was calculated as 1.75 mm/s and 4.90 mm/s for the rotational speeds of 15 and 30 RPM, respectively. It can be seen in Figure A2-1 that the flow in the filter section was not uniform. The objective was to obtain a filter section with uniform vertical flow passing through the particles as it is the case in an industrial filter.

It was noticed that the flow created by the impeller was not uniform in the "filter section". The fluid was pushed downwards by the blades, but the majority of the flow was re-directed upwards/bounced back after hitting the diffuser plate. Only a small portion of the flow entered the filter section resulting in low velocities. The flow re-circulation observed in this section is due to the effect of the mixer. The velocity in the filter section (Chapter 4 in Figure 4-1) could not be increased, even if the rotational mixer speed was doubled (see Appendix 2, Figure A2-1.b). A cover was placed over the top for enhance the pressure distribution and flow in the filter section (see Case2). This increased the velocities in the filter section, but a small improvement was detected in the flow uniformity (see Appendix 2, Figure A2-2). The model predictions showed that the velocity imposed by the mixer is lowest just below the shaft, and it increases along the mixer blades reaching to maximum at the blade tip as expected. The same trend was also observed during water experiments.

High liquid velocities were predicted at the wall-side of the section above the filter section. In order to prevent their effect on the velocity profile in the filter section, a simple

circular baffle (~40 mm Ø) and a conical buffer (~40 mm lower in diameter at the bottom and ~62 mm greater in diameter at the top) were added between the mixer and the top plate to reduce the effect of the high velocities in the filter section. The results are presented in Figures A2-3 and A2-4 respectively (Cases 3 and 4). An improvement was detected in the system but there were still non-uniform regions in the central part of the filter section.

Table 5-2: Model Results for System Design Simulations

Case #	Rotational speed (rpm)	Average velocity (mm/s)	Uniform fluid flow (Yes/No)
Case 1	15	1.75	N
	30	4.90	N
Case 2	15	1.85	N
	30	5.20	N
Case 3	15	0.65	N
	30	2.2	N
Case 4	15	0.80	N
	30	2.35	N
Case 5	15	1.2	Y
	20	1.9	Y
	25	2.7	Y
	30	3.50	Y
Case 6	15	1.15	Y
	20	1.8	Y
	25	2.53	Y
	30	3.20	Y

In order to visualize the flow field in the physical model, a fluorescent tracer and a black colored paint (very fine graphite powder mixed with water) were tested. The paint was denser than the water. However, when it was further diluted with water, it allowed better visualization of the flow field compared to the fluorescent tracer. In Figure A2-5 (a) and (b) , the comparison of flow fields between experimental and mathematical model

results are presented for Case 4 and 30 rpm rotational mixer speed. Recirculation and irregular fluid flow in the system can be seen in both cases.

In Case 5, the diffuser plate with 38% porosity shown in Figure 4-6(c) was placed 18 mm above the top plate of the filter section. The simulations were performed for 15, 20, 25, and 30 rpm rotational speeds. This improved the velocity profile in the filter section as can be seen in Figure A2-6 in Appendix 2. The directional non-uniformity of the flow in the filter section was almost eliminated, but the velocity was not uniform in the system. Especially, the wall-side velocities of the filter section were still higher than those of the central part. In Figure A2-7 (a) and (b), the comparison of flow fields between experimental and mathematical model results are presented for Case 5 and 30 rpm rotational mixer speed. The flow field in the experimental system was found to be similar to that of the mathematical model result. The re-circulation zone above the filter section can be observed in both experimental results and model predictions.

It was observed experimentally that the effect of the high velocities induced by the tip of the blades can be reduced by increasing the distance between two diffuser plates. The distance between two plates was increased from 18 to 30 mm for Case 6. The results are shown in Figure A2-8. This configuration gave a uniform flow with desired average velocities in the filter section. The high velocities at the bottom of this section correspond to the region with the particles. The particle bed was represented using a porous region in the mathematical model. The presence of particles reduces the available space for the fluid flow. The fluid passes through the pores at a higher velocity as expected.

The experiments with the water system were carried out using the same system configuration as that of Case 5 and Case 6. The average velocities measured in the filter section are presented in Table 5-2 and 5-3. Figure 5-1 compares the experimental and mathematical model results. As it can be seen from this figure, the agreement between the model and the experiments is good at low average velocities, which is the region of interest. Increasing average velocity increases the discrepancy between the predictions of the model and the experimental results. This could be due to the experimental measurements. When the mixer speed is low, it is easier to follow the tracer passing thorough the filter section and near the walls. Uniform fluid flow was obtained with the system design used in Case 6. The different mixer rotational speeds showed that lower rotational speeds (15 and 20 RPM) have more uniform fluid flow than the higher speeds. Case 6 with rotational speed of 20 rpm was taken as the base case.

Table 5-3: Physical and Mathematical Model Results - Average Liquid Velocities (mm/s)

	Mixer Rotational Speed			
	15 RPM	20 RPM	25 RPM	30 RPM
Case 5-Simulation	1.2	1.9	2.7	3.5
Case 5-Experiment	1.35	2.14	3.13	4.46
Case 6-Simulation	1.15	1.8	2.53	3.2
Case 6-Experiment	1.28	1.9	3.1	4.73
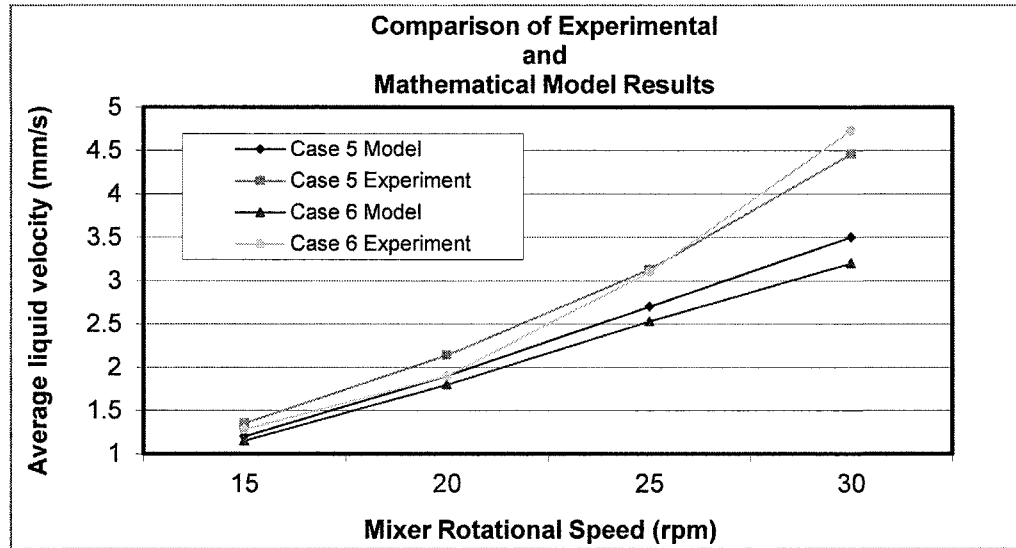
Figure 5-1: Experimental and Mathematical Model Results for Cases 5 and 6

5.1.2 Parametric Study

A parametric study was carried out with water. Five cases (from Case 7 to 11) are studied (base case is Case 6). The purpose was to investigate the effects of different parameters on the flow. The rotational speed was kept constant at 20 RPM which gives the desired liquid velocity (~1.8-1.9 mm/s) in the filter section. The results of the parametric study were summarized in Table 5-4.

5.1.2.1 Mixer Diameter (Case 7)

The simulations were performed using four different mixer diameters (67 mm -base case, 63 mm, 59 mm, 54 mm). The results of these simulations are shown in Figure A2-9 for the filter section. Decreasing the mixer diameter decreased the average velocity but increased the central velocities giving more uniform flow. In addition, decreasing the mixer

diameter reduced the high velocities at the wall-side. This could be due to the fact that the mixer was very close to the wall. Decreasing its size slightly relieved this constriction. The 4mm reduction from the base case (67 mm) regulated the velocities in the filter section, but 8mm reduction of diameter size decreased the liquid velocities at the wall-sides. 63mm mixer diameter was chosen and utilized during all Al experiments.

5.1.2.2 Mixer Blade Angle (Case 8)

The simulations were carried out for the 37.5°, 45° (base case) and 60° blade angles for Case 8. The uniformity of the flow with 37.5° angle blade was better than those of the others. In this case, the difference between the maximum and minimum liquid velocities was decreased and average velocity was increased. Increasing the angle to 60° caused a decrease in both the maximum and minimum liquid velocities compared to the base case. The flow pattern was uniform in this case, too. The results of the simulations are presented in Figure A2-10. 37.5 ° angle was chosen for use during the Al experiments.

5.1.2.3 Mixer Height (Case 9)

Four different distances between the mixer and the top plate of the filter section were used in the simulations (44, 56, 62 -base case, 82 mm from the top plate of the filter section) for Case 9. It was seen that increasing the distance between the mixer and the top plate of the filter section increased the liquid velocities in the filter section. The main reason for this result is the presence of the diffuser plate between the mixer and the top plate of the filter section. Decreasing the distance between the mixer and the diffuser plate

reduces the effect of the mixer because flow created by the mixer blades is deflected by the diffuser plate in the upward direction. Results are shown in Figure A2-11. A mixer height of 44mm was used in the experimental study.

5.1.2.4 Number of Mixer Blades (Case 10)

The simulations were performed for mixers which have 2, 4 (base case) and 8 blades. The results showed that increasing blade numbers increases the liquid velocity in the filter section, but the flow uniformity does not change. Figure A2-12 shows the flow pattern predicted. The mixer with four blades was found to be the most suitable for experimental system.

5.1.2.5 Particle Size in Filter Section (Case 11)

The simulations were carried out using the four different particle sizes (see Case 11) to study the effect of the particle size on the flow pattern in the filter section. These are 3, 6, 12, and 18 mm diameter particles in addition to 9 mm used in the base case.

Increasing the particle size decreased the resistance of the filter section, therefore the velocities slightly increased. A clear relation was not observed between the particle size and the fluid flow uniformity. The simulation results are shown in Figure A2-13. In the experimental study, it was decided to use 3-6 mm size particle which is in use in commercial filtration process.

Table 5-4 : Parametric Study Results (Rotational Speed = 20rpm)

	Mixer diameter (mm)	Mixer blade angle (°)	Mixer height (mm)	# of blades	Particle diameter (mm)	Maximum liquid velocity (mm/s)	Minimum liquid velocity (mm/s)	Average velocity (mm/s)
Case 6 base case	67	45	62	4*	9	2.40	1.40	1.80
Case 7	**67**	45	62	4*	9	2.20	1.40	1.80
	63*	45	62	4*	9	2.10	1.45	1.70
	59	45	62	4*	9	2.00	1.40	1.60
	54	45	62	4*	9	1.65	1.20	1.50
Case 8	67	**37.5***	62	4*	9	2.10	1.50	1.90
	67	**45**	62	4*	9	2.20	1.40	1.80
	67	**60**	62	4*	9	1.60	1.10	1.50
Case 9	67	45	**44***	4*	9	1.00	0.80	0.90
	67	45	**56**	4*	9	1.70	1.20	1.60
	67	45	**82**	4*	9	>2.00	1.60	1.90
Case 10	67	45	62	**2**	9	1.40	1.20	1.30
	67	45	62	**8**	9	3.00	1.70	2.30
Case 11	67	45	62	4*	**3***	1.40	1.00	1.30
	67	45	62	4*	**6***	2.20	1.50	1.60
	67	45	62	4*	**12**	2.40	1.60	1.75
	67	45	62	4*	**18**	2.60	1.70	2.10

*: preferred to use in the experiments.

5.2 Physical Characterization of Alumina Samples

5.2.1 Apparent Porosity Measurements

Apparent porosity is one of the most critical parameters of the study. The measurement procedure was explained in Section 3.3 of Chapter 3. The open porosity values of lab-made alumina tablets and commercial granular tabular alumina types are shown in Figures 5-2 and 5-3 and Tables 5-5 and 5-6.

Table 5-5 : Apparent Porosity Measurements of Lab-Made Alumina Tablets

	Batch 1	Batch 2	Batch 3	Batch 4	Average %Apparent Porosity	St. Dev.
Tablet A-Reference Tablet Alumina (Alcoa T64)	13.6	15.15	16.3	15.8	15.21	1.17
Tablet B- High Soda (0.33% Na$_2$O)	17.8	15.7	16.4	16.1	16.50	0.91
Tablet C – High Silica (0.64% SiO$_2$)	16.18	16.25	15.1	14.4	15.48	0.89
Tablet D – High MgO (0.53% MgO)	15.95	14.94	17.35	17.8	16.51	1.31

Chemical analysis results of these tablets can be found in Table 3-9 in Chapter 3.
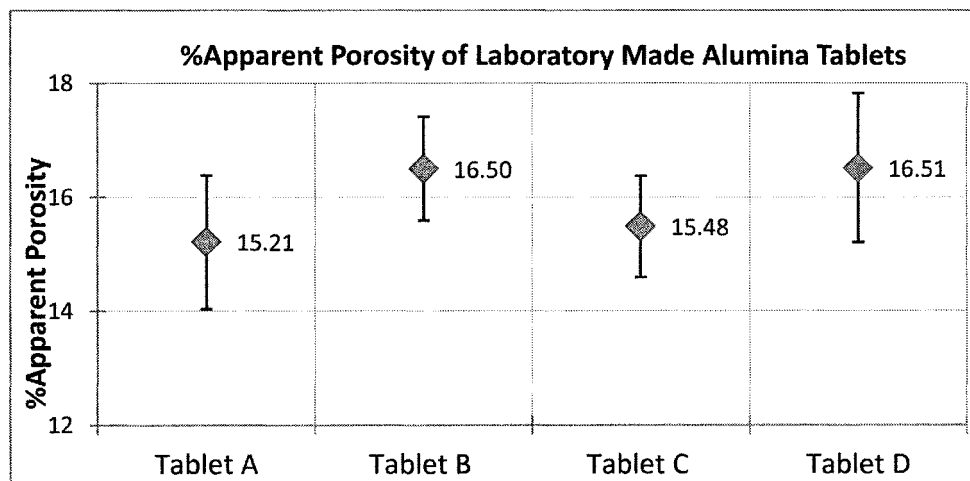
Figure 5-2: Apparent Porosity (Open) Measurements of Lab-made Alumina Tablets

Table 5-6: Apparent Porosity Measurements of Commercial Alumina Types

	Batch 1	Batch 2	Batch 3	Batch 4	Average %Apparent Porosity	ST DEV
Alufin	8.66	5.44	7.88	8.35	7.58	1.46
Naigai	4.89	6.3	7.06	8.53	6.70	1.52
Alcoa T64	2.92	4.92	3.50	3.45	3.70	0.86
Aluchem	5.42	2.5	3.08	3.64	3.66	1.26
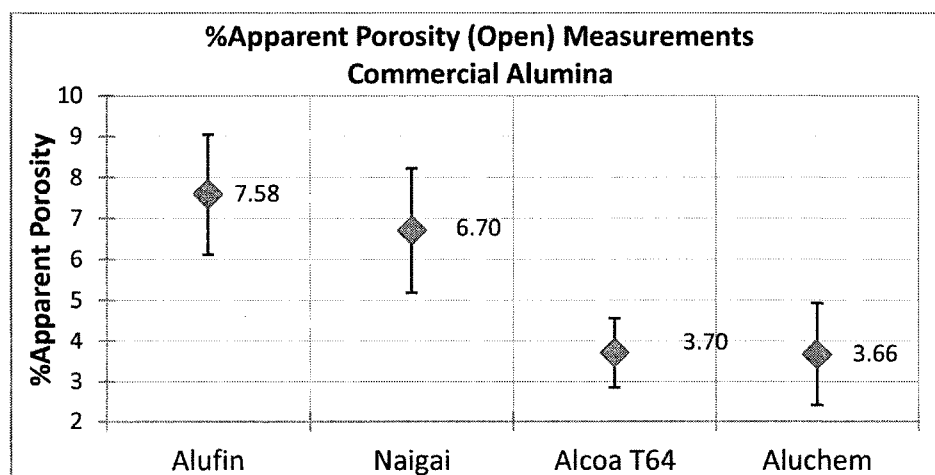
Figure 5-3: Apparent Porosity (Open) Measurements of Commercial Tabular Alumina

As it can be seen in Figures 5-2 and 5-3 and Tables 5-5 and 5-6, the variation in apparent porosity of different commercial alumina types is higher compared to that of alumina made in the laboratory. One of the major reasons for the preparation of lab-made alumina was to reduce the variations in apparent porosity values seen in commercial alumina types. These results show that lab-made alumina tablets have consistent structures, less variation in apparent porosity values although their values are higher than those of the commercial alumina grades.

5.2.2 Grain Size Measurements

Grain size measurements were conducted as described in Section 3.3.2 of Chapter

3. The results are summarized in Figure 5-4 for commercial tabular alumina grades. Alcoa

T64 and Aluchem have similarly large grain sizes while Alufin and Naigai have smaller

grains.
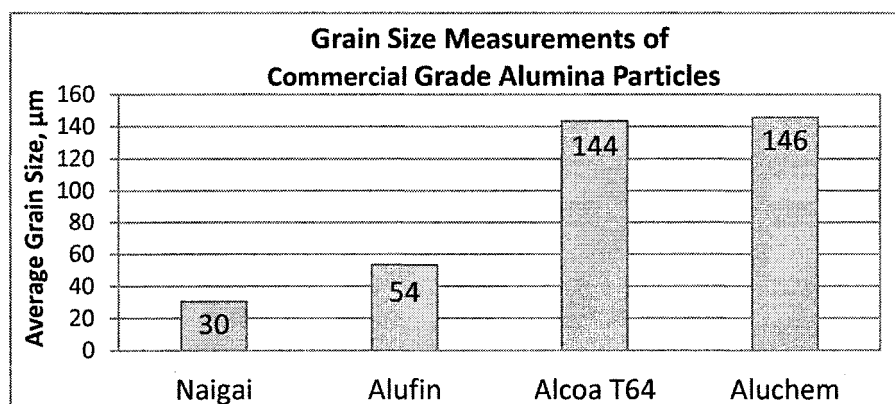
Figure 5-4: Grain Size Measurements of Commercial Tabular Alumina Particles

Laboratory-made alumina tablet grain size could not be measured, because of their

relatively higher porosity level.

5.3 Experiments using Molten Aluminum Alloys

5.3.1 Determining Mg Loss in Experiments with Molten Aluminum

Magnesium has a high vapor pressure; consequently, it evaporates from the melt. It

also oxidizes very quickly when it is in contact with oxygen at the temperatures 690-750°C

at which the experiments were conducted. Because of the long duration of the experiments

(from 6 to 168 hours) carried out during the present study, the magnesium concentration in

the molten aluminum alloys had to be strictly controlled. For this purpose, a number of preliminary experiments were conducted to determine the loss of magnesium in the melt for three different aluminum alloys (2, 5, and 7%Mg-Al alloys) at 715 °C. The experimental system I was used in these preliminary tests with a mixer speed of 20 rpm. Samples for optical emission spectroscopy (OES) analysis were taken before and after each test. The duration of the tests was kept constant at 120 hours (5 days). Samples were analyzed at Cegep de Chicoutimi, Metallurgy Department, in La Baie Campus. Results are shown in Table 5-7 below.

Table 5-7: Magnesium Loss during Experiments Conducted at 715 °C (Experimental System I using CO_2 gas)

Trial	Target Mg %	Duration, hour	Mg % Before	Mg % After	Weight of Molten Alloy, g	Mg loss, g
1	2.00	120	2.05	1.82	11000	25
2	5.00	120	4.98	4.63	11000	39
3	7.00	120	7.12	6.67	11000	50

Table 5-8: The Effect of Daily Magnesium Additions on Final Mg% in the Molten Aluminum Alloys (Experimental System I using CO_2 gas)

Trial	Target Mg%	Duration, day	magnesium addition, g	%Mg before	%Mg after	%difference from target
1	2.00	5	5	1.98	2.12	6.06
		3	5	2.06	2.16	8.15
2	5.00	5	8	4.98	5.13	2.60
		3	8	5.07	5.17	3.40
3	7.00	5	10	6.92	7.10	1.45
		3	10	6.80	7.08	1.13

Based on the results shown above, 5 , 8, 10 g of magnesium metal were added daily into 2%, 5%, and 7%Mg-Al alloys, respectively, in order to keep the magnesium concentration in a reasonable range during experiments. Table 5-8 shows the results of optical emission spectroscopy (OES) analysis of the samples which were taken from the experiments during which the daily additions of magnesium metal were made. These results showed that the final magnesium concentration in 5% and 7%Mg-Al alloy was very close to the target concentration. The 2%Mg-Al alloy results were about 8% higher than the target concentration, therefore, the daily amount of magnesium metal added for 2%Mg-Al alloy was decreased to 4 g /day for ~11000 g of melt.

The molten metal flow velocity on the top surface of the crucible in the Experimental System II was much weaker than the one visually observed in Experimental System I, due to the slower rotational speed of the mixer shaft which is actually 1-3 rpm. The effect of the mixer rotational velocity on surface flows generated in the crucible was already studied previously using the mathematical model (see the results in Appendix 2, Figure A2-14). The observations made during experiments with molten aluminum alloys showed that decreasing metal circulation in the crucible decreases the amount of dross/oxides volume in the melt generated during experiments. It was decided to make the same amount of additions suggested previously every second day instead of daily in order not to alloy more than needed. This decreased the amount of magnesium addition into the melt by 50%. Initially, the final magnesium concentration was less than 6% different from the target concentration; therefore the procedure was standardized for all the experiments

conducted using the System II. Table 5.9 shows the OES analysis results for three samples collected from the experiments conducted using Experimental System II.

Table 5-9: The Effect of Magnesium Additions on final Mg% in the Molten Aluminum Alloys (Experimental System II)

Trial	Target Mg wt%	Duration, hour	Mg addition, g/2days	Mg wt% before	Mg wt% after	%difference from target
1	2.00	120	4	1.99	2.05	2.50
2	5.00	120	8	5.06	5.27	5.40
3	7.00	120	10	7.08	7.21	3.00

5.3.2 Minimization of Aluminum Alloy Oxidation

At the beginning of the study, a research grade argon gas was used for surface protection in order to avoid the oxidation of aluminum alloy during long duration experiments. Although the argon flow was increased up to 100 cm^3/min, no benefit of the surface protection by argon gas was observed in these experiments. Therefore, an alternative cover gas was sought.

The literature survey indicated the advantages of using CO_2 gas in magnesium containing alloys. A number of experiments with 5% Mg-Al alloy at 710°C were conducted using 99% pure Praxair CO_2 gas. CO_2 flow rate was kept at 10-15 cm^3/min levels during these tests. Carbon dioxide gas was found to be very effective compared to argon gas in terms of its ability to impede the dross formation rate even during the experiments longer than three days. The greatest advantage of CO_2 compared to argon gas is its molar weight which is 44 g/mole. It is heavier than air (29 g/mole); eventually, it acts like a blanket on the metal surface and prevents its contact with air.

The stability of the system in terms of oxide formation, fluid flow dynamics, magnesium loss in the melt, etc. was verified during these trials. Finally, the use of CO_2 gas in the experiments was optimized and the flow rate was decreased to 3 cm^3/min (see the Appendix 1 for details).

5.3.3 Effect of Aluminum Alloy Mg content on Affected Zone for Different Commercial Grade Alumina Particles

Deep bed filtration is a semi-continuous process. The filtration period (liquid metal flow-dynamic) is followed by a holding period (static liquid metal condition) and this is repeated periodically during the filter life.

The alumina particles were analyzed before the experiments (before contact with the liquid aluminum alloy). This analysis showed that the commercial alumina grades have different structures such as porosity distribution as shown in Figure 5-5 (Darker zones are the higher porosity areas. More examples can be seen in Appendix 4.) It was also observed that the porosity differed from one particle to another. Some of the particles showed more porous structure in the outer shell than in their core as seen in Figure 5-5.

After each experiment, photographs of alumina particles which were in contact with Mg-Al alloy were taken as shown in Figure 5-6. These particles displayed a darker region (affected zone) close to the surface. Formation of this layer was attributed to metallic vapors, such as magnesium, coming from the metal bath and diffusing through the porosity network. It was stated that the reactions between some phases (such as Na beta-alumina discussed in Sections 5.4.3 and 5.4.4) and metallic vapors result in the color change in these

zones. No color change in alumina particles was observed when experiments were conducted using pure aluminum.

(a)

(b)
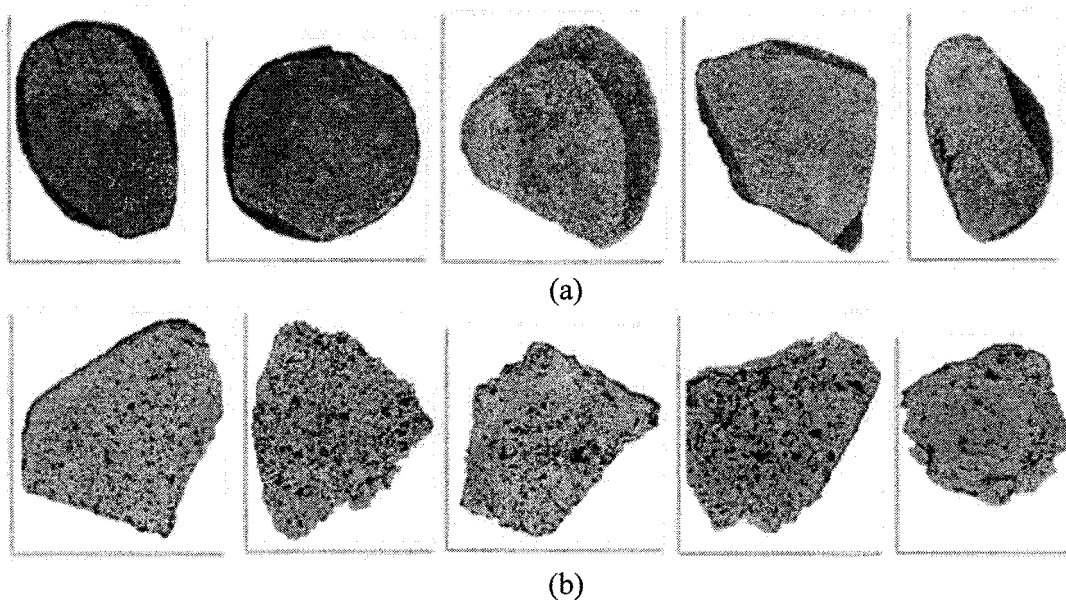
Figure 5-5: Optical Microscope Images of Unused Commercial Alumina Particles (a) Naigai, (b) Aluchem (~5mm Diameter Particles)

(a)

(b)
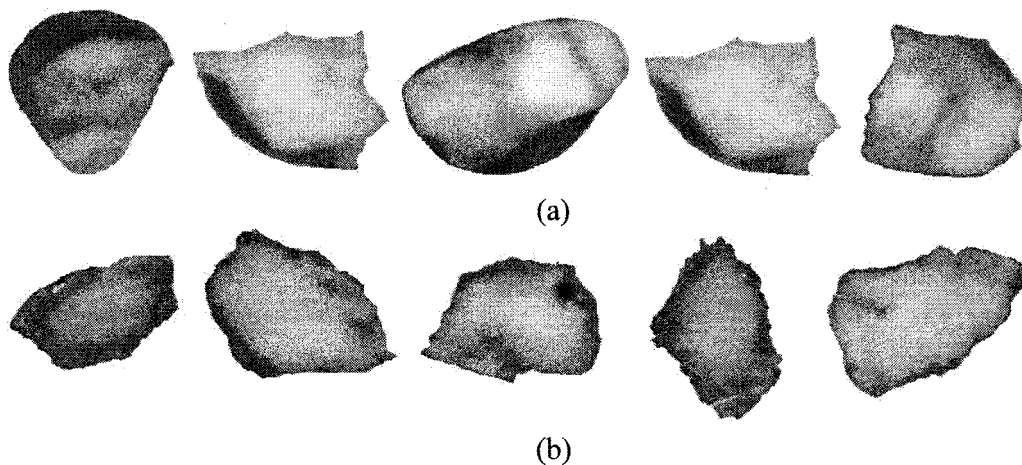
Figure 5-6: Cross-sectional Appearance of Commercial Alumina Grades After Experiments with Liquid Mg-Al Alloys (a) Naigai, (b) Aluchem. (~5mm Diameter Particles)

Commercial grade pure (Alcan P-1020) aluminum alloy and its alloys with 2%, 5%, and 7%Mg at 715°C were used for testing the effect of Mg content on the extent of affected zone at alumina/aluminum interface.

Table 5-10: Summary of Experiment Results for Various %Mg-Al Alloys (1.8mm/s flow velocity at 715°C)

	2%Mg-Al Alloy		5%Mg-Al Alloy		7%Mg-Al Alloy	
	Slope	R^2	Slope	R^2	Slope	R^2
Alufin	0.008	0.86	0.012	0.98	0.049	0.83
Naigai	0.011	0.83	0.014	0.84	0.058	0.85
Alcoa T64	0.004	0.70	0.006	0.91	0.009	0.75
Aluchem	0.005	0.93	0.007	0.73	0.012	0.29

All commercial grade tabular alumina experiments showed that increasing magnesium content in aluminum alloy increases the affected zone thickness. The experiments using commercially pure aluminum (P1020) did not show any affected zone and any reactions on the sample surface. This means that the magnesium diffusion from molten aluminum alloy through alumina particle is the main reason for the reaction/affected zone observations on samples.

The experimental results indicated that the thickness of the affected zone increases with increasing contact time, almost linearly as shown in Figures from 5-7 to 5-10. Table 5-10 summarizes the slopes and the R^2 (correlation coefficients) values of affected zone thickness vs. contact time curves for the experiments. The linear correlation of Mg content and contact time seems to be more obvious when 2 and 5%Mg-Al alloys were used. On the other hand, the 7%Mg-Al alloy experiment results showed lower R^2 values with linear correlation. It appeared that polynomial type trend fitted much better in the majority of

cases for 7%Mg-Al alloy experimental results which are shown as dashed trend lines in the figures. This means that the affected zone formation mechanism may be slightly different when alumina is in contact with an alloy containing 7%Mg compared to those of the lower Mg content alloys. In this group, the affected zone thickness increases fast in first couple of days. This rate slows down in the later stages of the experiments. The reasons for this phenomenon will be elaborated in the metallographic investigation section 5.4.

Figures with error bars can be found in Appendix 3.

Figure 5-7: Effect of Mg content on the Affected Zone Thickness for Alufin Tabular Alumina Particles (1.8mm/s Flow Velocity at 715 °C)

Figure 5-8: Effect of Mg content on the Affected Zone Thickness for Naigai Tabular Alumina Particles (1.8mm/s Flow Velocity at 715°C)

Figure 5-9: Effect of Mg content on the Affected Zone Thickness for Alcoa T64 Tabular Alumina Particles (1.8mm/s Flow Velocity at 715°C)

Figure 5-10: Effect of Mg content on the Affected Zone Thickness for Aluchem Tabular Alumina Particles (1.8mm/s Flow Velocity at 715°C)

5.3.4 Effect of Molten Metal Velocity on Affected Zone Thickness for Different Commercial Grade Alumina Particles

Investigation of the effect of molten metal velocity on affected zone/reaction zone is one of the most important purposes of this study. Numerous experiments were conducted to simulate the velocities which are found in the filtration process.

Table 5.11: Summary of Results for Various Molten Aluminum Velocities (5%Mg-Al Alloy at 715°C)

	Static 0.0 mm/s		Dynamic 1.8mm/s		Dynamic 3.6mm/s	
	Slope	R^2	Slope	R^2	Slope	R^2
Alufin	0.005	0.95	0.012	0.98	0.019	0.96
Naigai	0.006	0.99	0.014	0.83	0.018	0.88
Alcoa T64	0.001	0.86	0.006	0.91	0.008	0.88
Aluchem	0.002	0.92	0.0066	0.73	0.0071	0.90

Table 5-11 and Figures 5-11, 5-12, 5-13, and 5-14 summarize the results of the velocity effect on affected zone for four different types of commercial tabular alumina. The velocity experiments were conducted using 5%Mg-Al alloy. The results show that increasing molten metal velocity around particles increases the extent of the affected zone. The smallest affected zone thicknesses were obtained when the experiments were conducted under no-flow condition (static). The relation between the metal velocity and increase in the affected zone thickness seems to be linear for most of the cases. Figures with error bars can be found in Appendix 3.
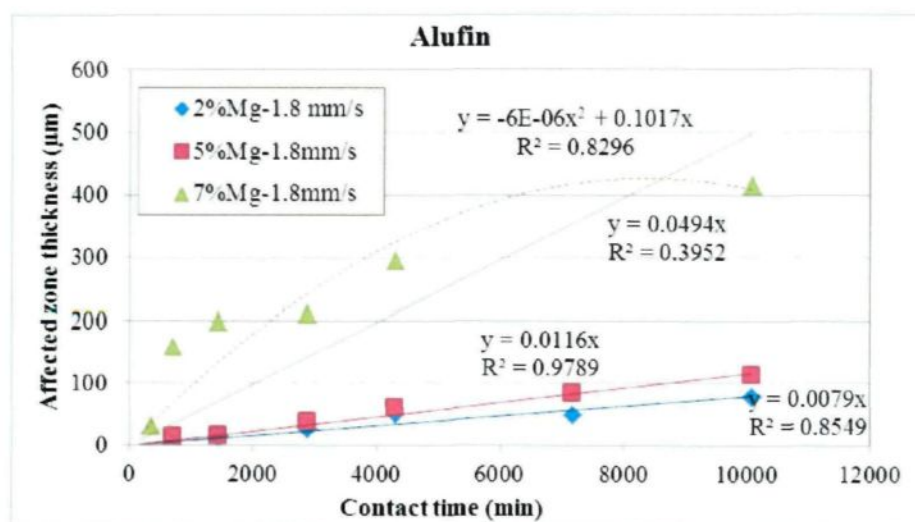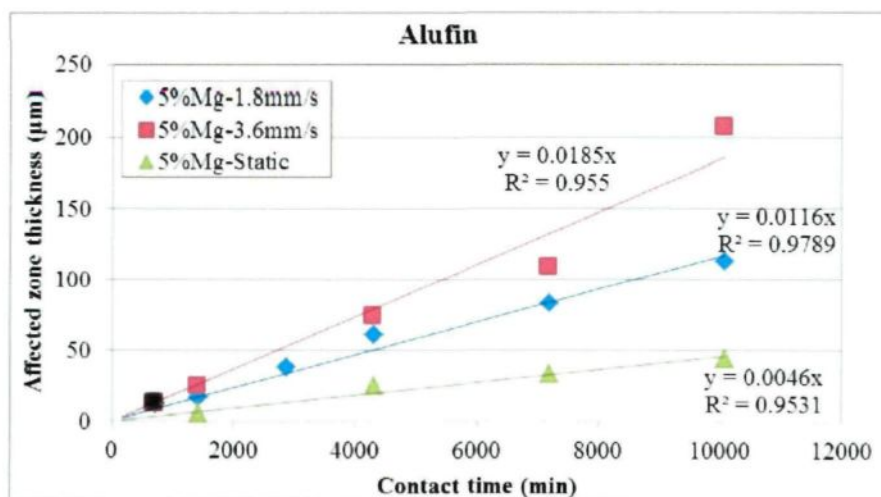

Figure 5-11: Effect of Velocity on the Affected Zone Thickness for Alufin Tabular Alumina Particles (5%Mg-Al alloy at 715°C)
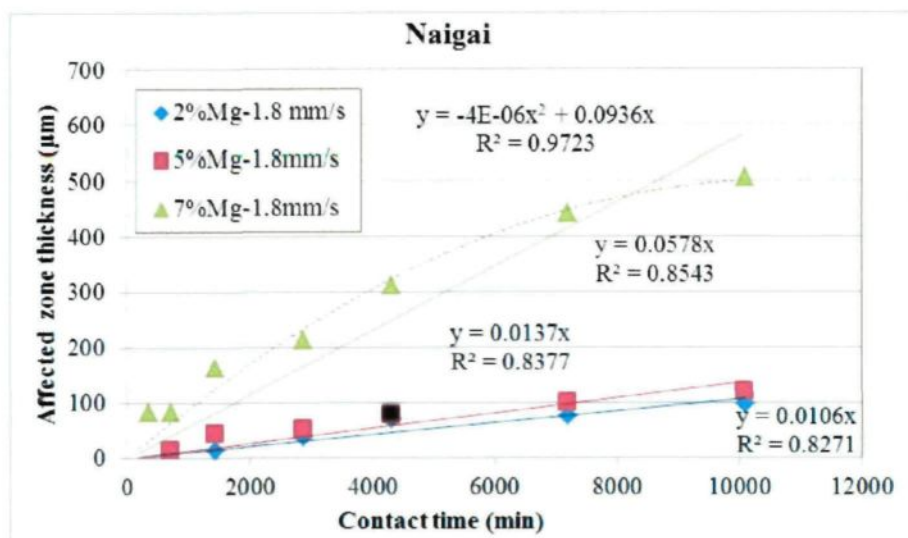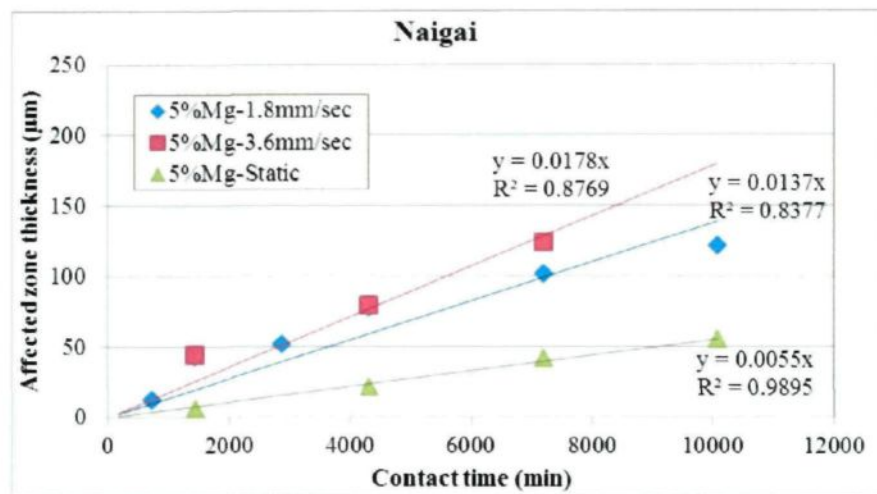
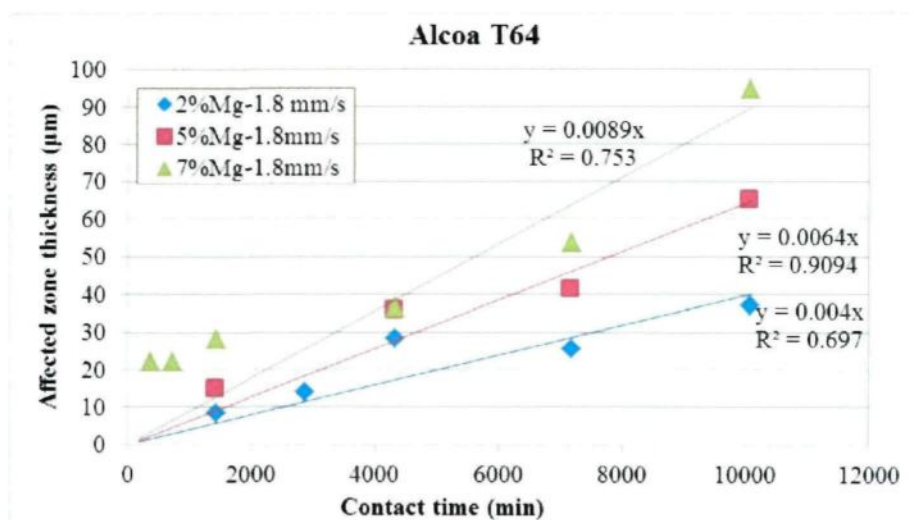Figure 5-12: Effect of Velocity on the Affected Zone Thickness for Naigai Tabular Alumina Particles (5%Mg-Al alloy at 715°C)
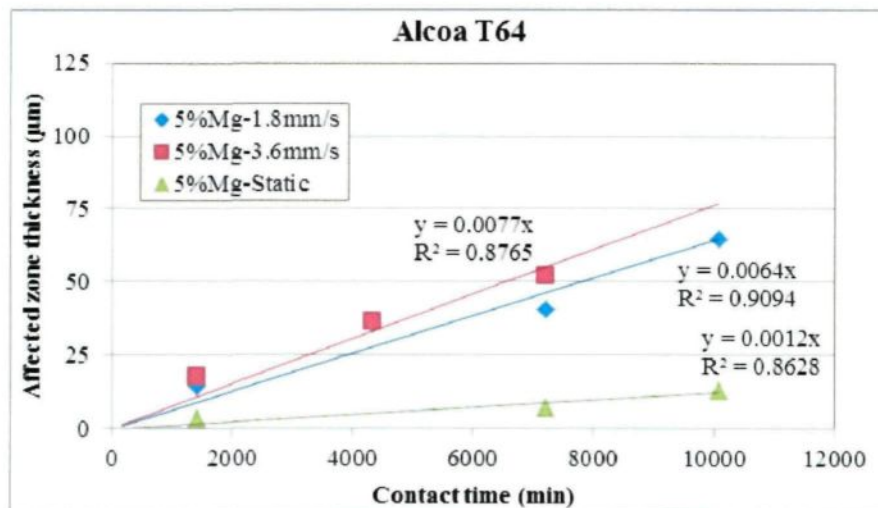
Figure 5-13: Effect of Velocity on the Affected Zone Thickness for Alcoa T64 Tabular Alumina Particles (5%Mg-Al alloy at 715°C)
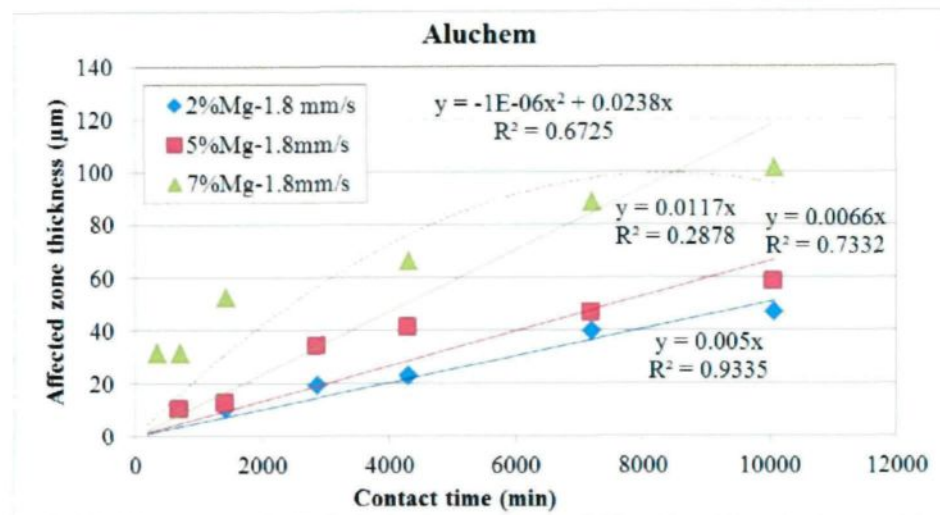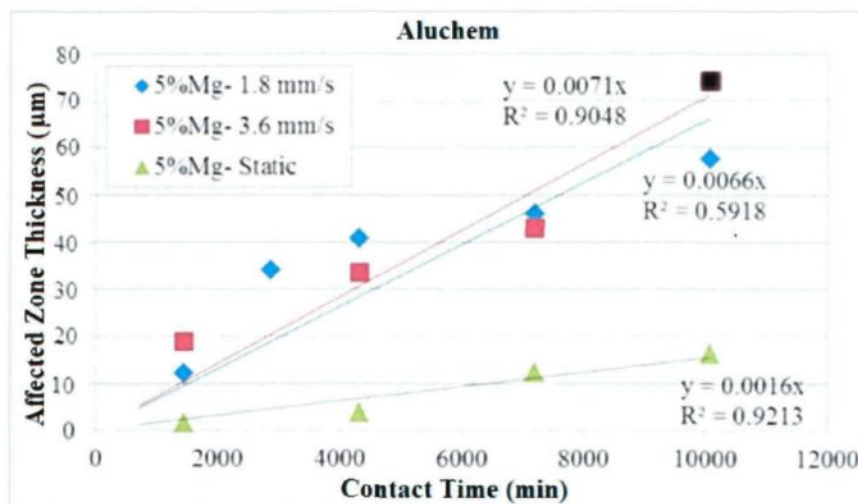
Figure 5-14: Effect of Velocity on the Affected Zone Thickness for Aluchem Tabular Alumina Particles (5%Mg-Al alloy at 715°C)

5.3.5 Effect of Commercial Grade Alumina Type on Affected Zone Thickness

The experiments were carried out with four different alumina types using aluminum alloys containing 2%, 5%, and 7% Mg. Figures 5-15, 5-16, and 5-17 present the effect of the alumina type on the affected zone thickness. In these experiments, it is quite obvious that the alumina particles can be grouped into two regarding the extent of their affected zone. These groups are:

1. Particles with thicker affected zone (Naigai and Alufin)

2. Particles which thinner affected zone (Aluchem and Alcoa T64).
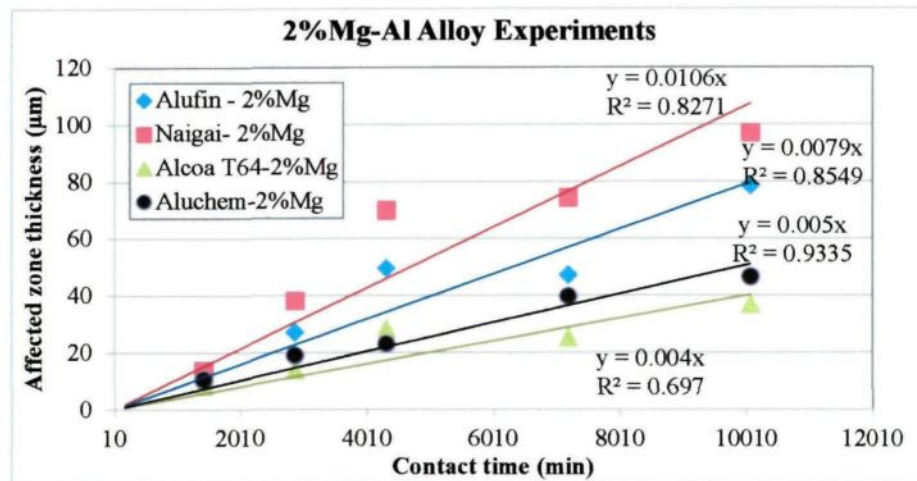
Figure 5-15: Effect of Alumina Type on the Affected Zone Thickness Using 2%Mg-Al Alloy (at 715°C Using 1.8mm/s Flow Velocity)
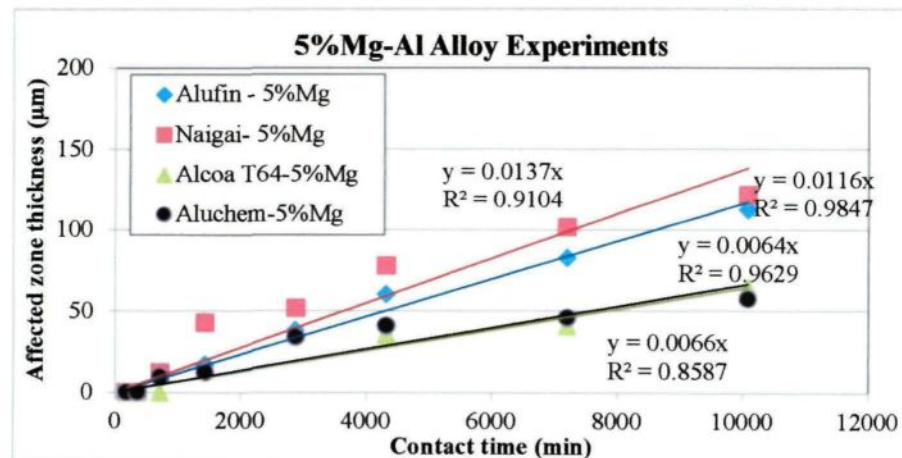
Figure 5-16: Effect of Alumina Type on the Affected Zone Thickness Using 5%Mg-Al Alloy (at 715°C Using 1.8mm/s Flow Velocity)
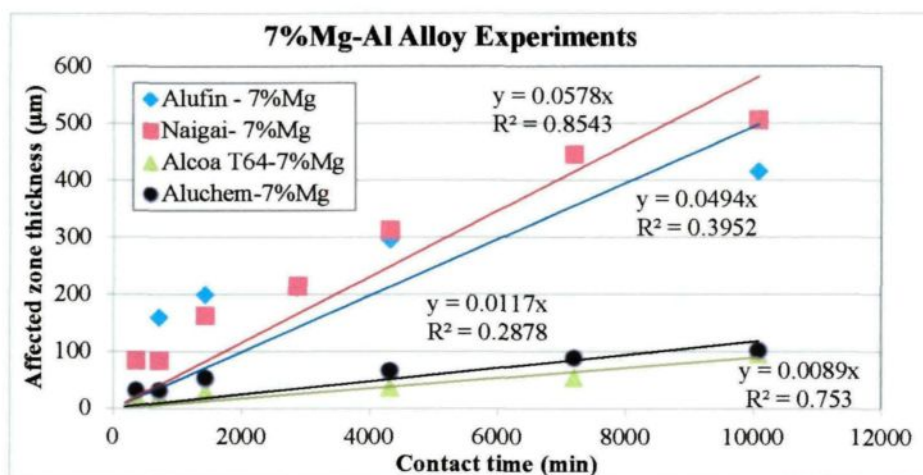
Figure 5-17: Effect of Alumina Type on the Affected Zone Thickness Using 7%Mg-Al Alloy (at 715°C Using 1.8mm/s Flow Velocity)

Figures with error bars can be found in Appendix 3.

5.3.6 Effect of Apparent Porosity on Affected Zone Thickness for Different Commercial Grade Alumina Particles

The difference in affected zone thickness for these two commercial alumina groups mentioned in the previous section aligns quite well with the differences in their major physical properties such as apparent porosity (open porosity) and grain size.

As it can be seen from Figure 5-18, the alumina types with high apparent (open) porosities such as Alufin and Naigai have thicker affected zones. This was observed in all experiments. Naturally, magnesium diffusion is expected to increase with increasing porosity.
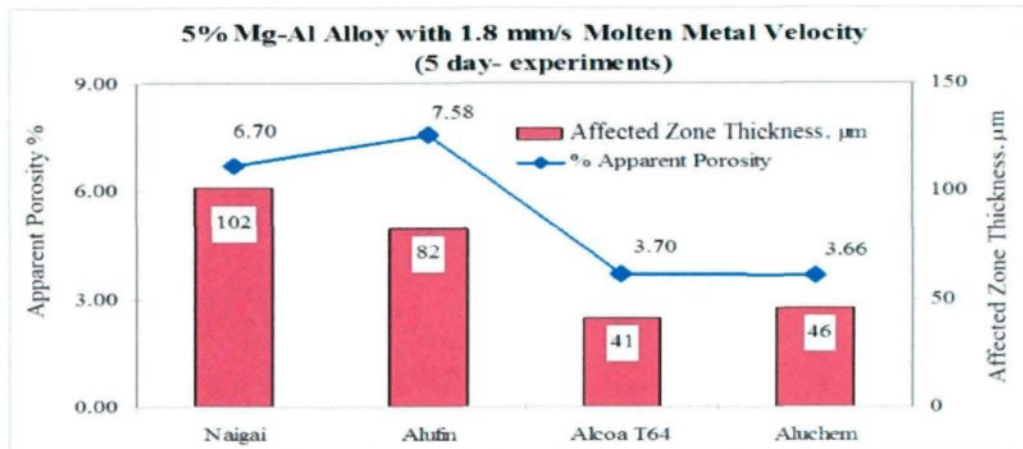
Figure 5-18: Average Apparent Porosity and Affected Zone Thickness Relation
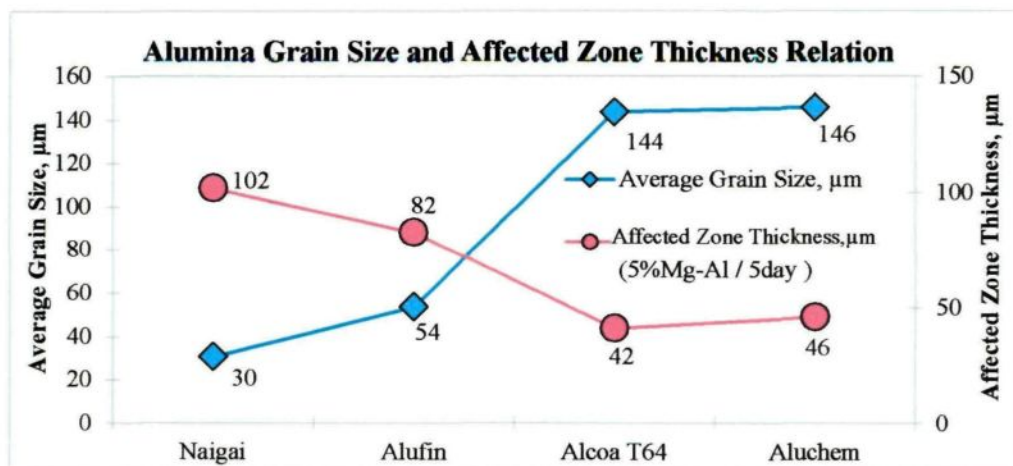
Figure 5-19: Grain Size and Affected Zone Thickness Relation

Other important observation of the current study is the correlation between grain sizes and the affected zone thickness. The alumina types with higher apparent porosity also had smaller grain size values as presented in section 5.2.2. Smaller grain size alumina types showed the highest affected zone thickness as shown in Figure 5-19. The metallographic

investigation results which are discussed in detail in Section 5.4 indicate the presence of inter-granular reactions in all commercial alumina types. High porosity of these aluminas facilitates the diffusion of Mg near the grain boundaries. Grain boundaries are the locations where most of the impurities are found. Smaller grains in the structure result in larger grain boundary areas where the reaction between alumina and Mg takes place.

5.3.7 Effect of Temperature on Affected Zone Thickness for Different Commercial Grade Alumina Particles

The temperature effect on the affected zone thickness was studied at 715°C, and 750°C for all commercial alumina types. In addition, Alcoa type alumina was also tested using 690°C. The experiments were conducted only with 5%Mg-Al alloy in this part of the study. The results are shown in Figures from 5-20 to 5-23 and summarized in Table 5-12. As it was expected, higher affected zone thicknesses were observed in all cases when the temperature of molten aluminum was increased since diffusivity increases with increasing temperature.

Table 5-12: Summary of Results for Various Molten Aluminum Temperatures

	690°C		715°C		750°C	
	Slope	R^2	Slope	R^2	Slope	R^2
Alufin			0.012	0.98	0.022	0.70
Naigai			0.014	0.84	0.017	0.52
Alcoa T64	0.003	0.13	0.006	0.91	0.099	0.97
Aluchem			0.007	0.73	0.098	0.98
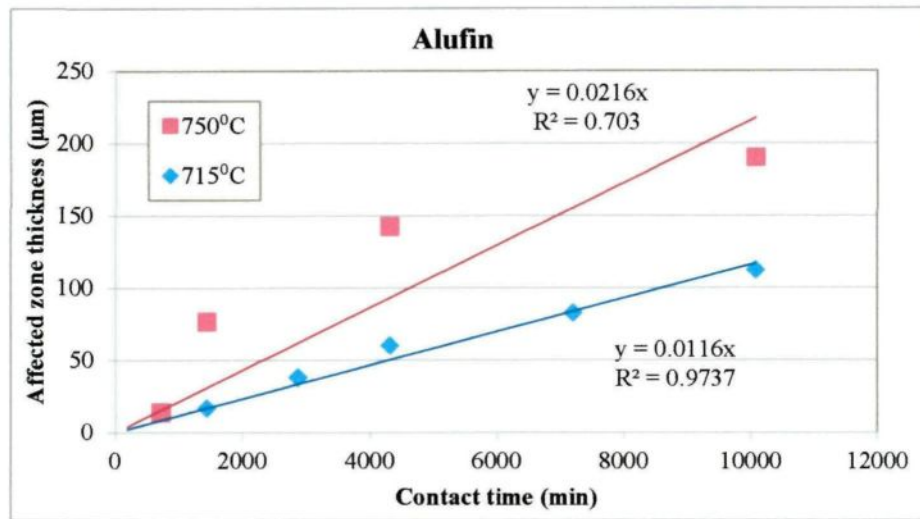
Figure 5-20: Effect of Temperature on Affected Zone Thickness – Alufin (Experiments with 5%Mg-Al Alloy – 1.8mm/s Metal Velocity)
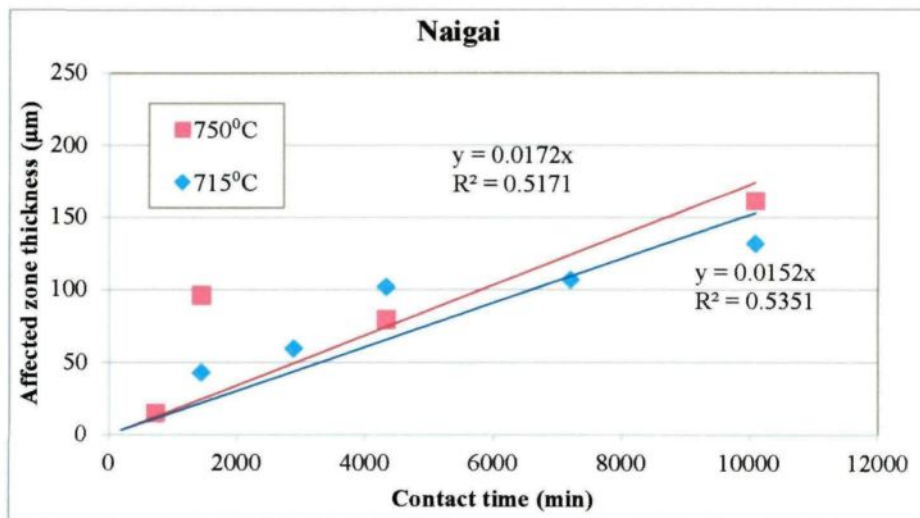
Figure 5-21: Effect of Temperature on Affected Zone Thickness – Naigai (Experiments with 5%Mg-Al Alloy – 1.8mm/s Metal Velocity)
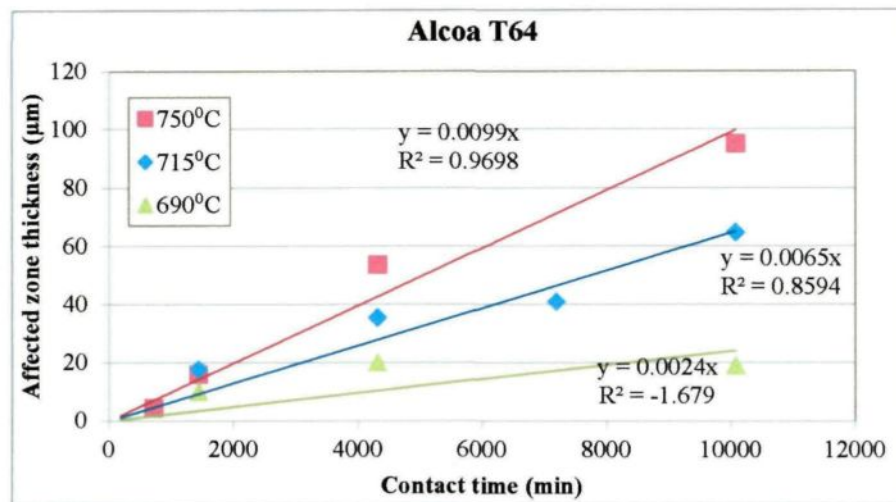
Figure 5-22: Effect of Temperature on Affected Zone Thickness – Alcoa T64 (Experiments with 5%Mg-Al Alloy – 1.8mm/s Metal Velocity)
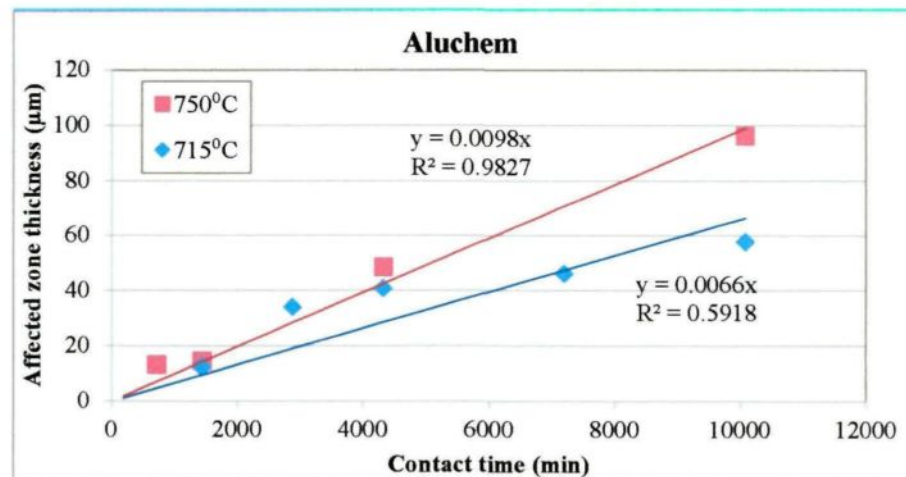
Figure 5-23: Effect of Temperature on Affected Zone Thickness – Aluchem (Experiments with 5%Mg-Al Alloy – 1.8mm/s Metal Velocity)

Figures with error bars can be found in Appendix 3.

5.3.8   Effect of Commercial Grade Alumina Particle Surface Roughness Values on Affected Zone Thickness

The roughness measurement results presented in Figure 5-24 indicate that average roughness height values (Ra) for commercial grade alumina particles roughly change between 7.0 and 8.3 microns. It's not possible to derive any correlation between Ra value and affected zone thickness from the results. The roughness of the laboratory-made alumina tablets was approximately the same.

Roughness does not seem to be an important factor in this study since they are similar for all commercial alumina types and did not vary for the laboratory-made tablets.
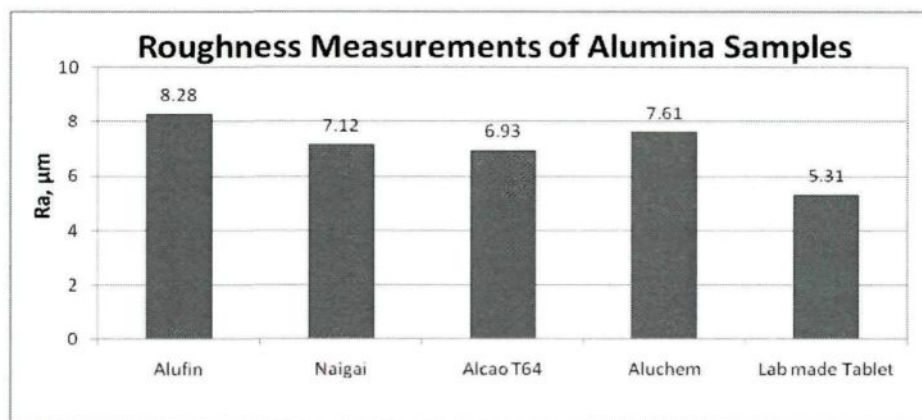
Figure 5-24: Alumina Surface Roughness Measurement Results

5.3.9   Effect of Impurities on Affected Zone Thickness for Different Commercial Grade Alumina Particles

As discussed in Chapter 3, commercial alumina grades contain various impurities such as Na_2O, SiO_2, MgO, Fe_2O_3, TiO_2, etc. in various concentrations. Only chemical

impurity content and the affected zone thickness do not show a strong correlation, because the physical aspects of alumina such as percent open porosity have a strong influence on the affected zone thickness and are not constant for all commercial grades. Table 5-13 summarizes the total major impurity (Na_2O + SiO_2) contents and the affected zone thicknesses observed in this study.

Table 5-13: Total Impurity Content of Commercial Grade Alumina

	Impurity % (Na_2O + SiO_2)	% Porosity	Affected Zone Thickness*, µm
Naigai	0.29	6.7	101.6
Alufin	0.13	7.6	82.4
Alcoa T64	0.29	3.7	40.9
Aluchem	0.22	3.7	45.9

* Experiments with 5%Mg-Al Alloy, 1.8mm/s metal velocity, 5 day duration.

5.3.10 Effect of Temperature and Various Impurities on Affected Zone Thickness – Laboratory-Made Alumina Tablets

The laboratory-made alumina tablets were also used to investigate the alumina/aluminum interactions (most likely the effects of magnesium diffusion). One of the reasons for using laboratory-made alumina in these experiments was to eliminate variation originating from physical or chemical properties of alumina structure which was observed in commercial grades. The other reason was to produce custom made alumina with desired composition (such as high Na_2O, SiO_2, and MgO) so that the effect of impurities on alumina/aluminum interaction could be determined (Figure 5-25). The chemical compositions of these alumina samples can be found in Section 3.4 in Chapter 3.
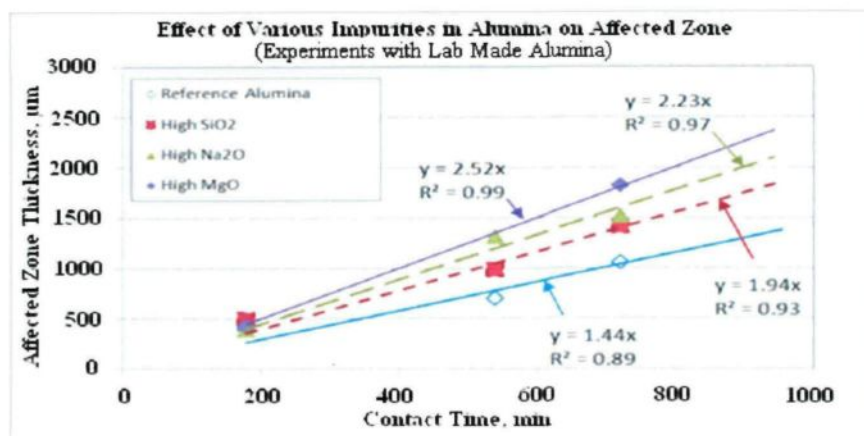
Figure 5-25: Effect of Impurities in Alumina on Affected Zone Thickness (5%Mg-Al Alloy, 1.8mm/s Flow Velocity, Experimental System II)
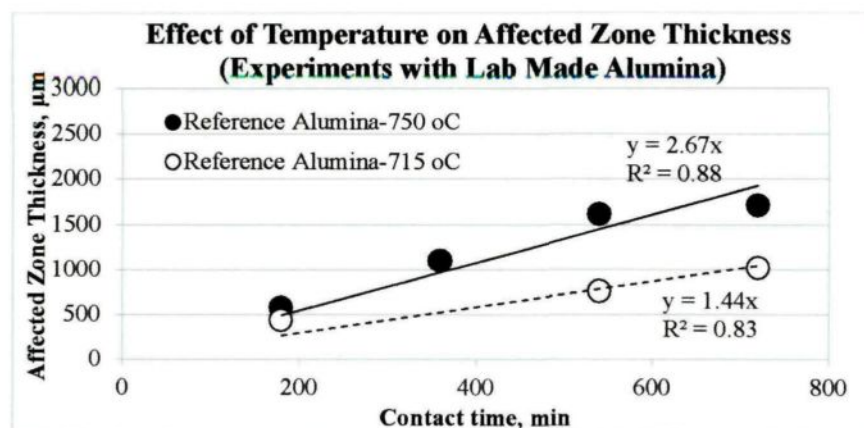
Figure 5-26: Effect of Molten Aluminum Temperature on Affected Zone Thickness (5%Mg-Al Alloy, 1.8mm/s Flow Velocity, Experimental System II)

The aim was to produce alumina tablets with low open porosity levels (4-7%) similar to commercial particles. Alumina production with lower open porosity levels requires high sintering temperatures (>2000°C). Unfortunately the sintering furnace capability used in this study was not more than 1600°C which provided only ~15% open porosity levels for lab-made alumina tablets. Nevertheless, the experiments were pursued

using these tablets, because it was believed that these experiments can still serve for some of the previously purposes and the results show the trends comparatively.

The reference laboratory-made alumina (Alcoa T64- with no extra impurity addition) was also tested in 5%Mg-Al alloy at 715°C and 750°C as shown in Figure 5-26. Results show that increasing liquid metal temperature increases the magnesium diffusion through the core of the alumina tablets resulting in thicker affected zone formation.

The slope of the lines obtained with lab made alumina in Figure 5-26 are roughly 100-200 times greater compared to the slopes obtained with commercial alumina grades. This underlines one more time that the porosity is an important contributor in to the affected zone thickness which basically allows magnesium to diffuse through the core and to react with the components present in alumina.

5.3.11 Comparison of Experimental System-I (Mixer) and System-II (Disc) Results

As it was explained in the Chapter 3 on experimental set-up and procedure, experiments were conducted using two different systems (Experimental system-I with mixer motion and system-II with rotating disc). The details about the experimental set-ups used in these experiments can be found in Chapter 3.

The results shown in Figure 5-27 compare the affected zone thickness observed for Alcoa T64 grade alumina using these two experimental systems. The experiments were conducted using three different magnesium contents (2%, 5%, and 7% wt) at 715°C liquid aluminum temperature under dynamic conditions (~1.80 mm/s flow velocity).

System-I results are in good agreement with the ones obtained using System-II as can be seen in Figure 5-27.
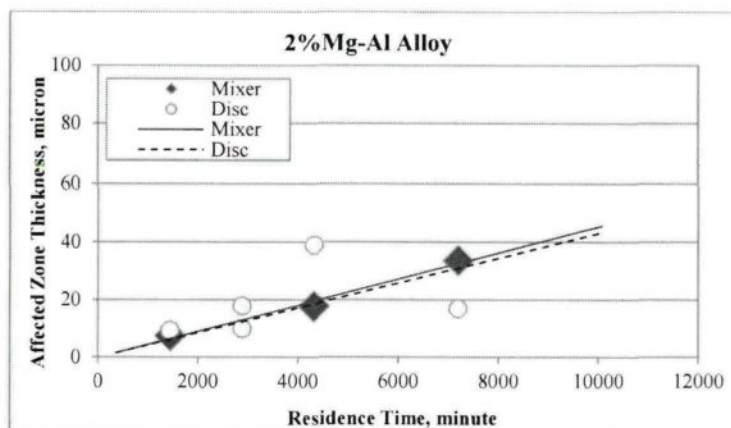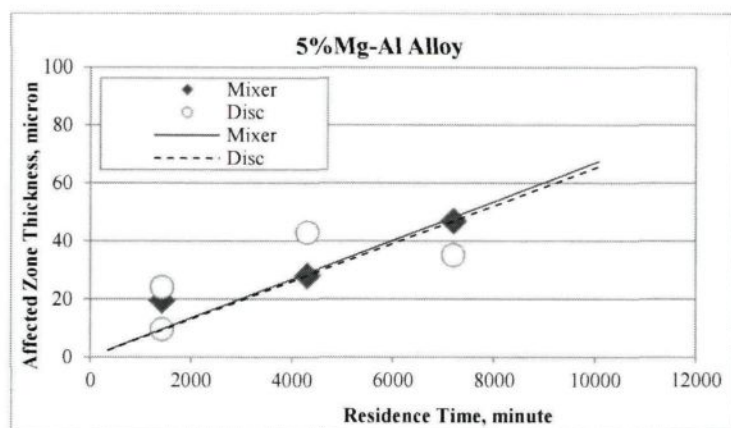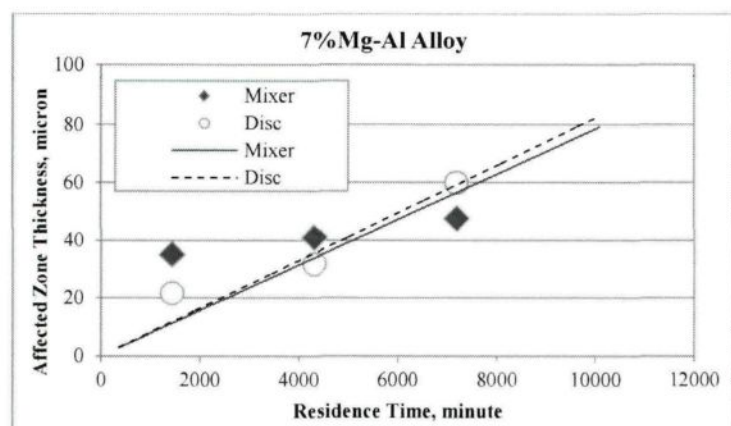
Figure 5-27: Results of Alcoa T64 -Dynamic Experiments with 1.8mm/s with (a) 2%Mg, (b) 5%Mg, (c) 7%Mg-Al Alloy

5.3.12 Comparison of Experimental System-II Top and Bottom Disc Results (Effect of Aluminostatic Pressure on Affected Zone Thickness)

Experimental system-II has multiple discs on a rotating rod as explained in Chapter 3. The following study was conducted to determine if there is any difference in affected zone thickness on alumina samples due to the difference in positions of top and bottom discs. In the experiments, top and bottom discs are located approximately 5 and 25 cm below the metal surface level, respectively.

A 24-hour experiment which was described schematically in Figure 5-28 was conducted using 5%Mg-Al alloy at 715°C. lab –made alumina tablets were used in this test. Three tablets from each disc were recovered at the end of the experiment. Metallographic investigation results were summarized in Figure 5-29.

The affected zone thickness measurements shown in Figure 5-29 indicated that the effect of the disc position on affected zone thickness of alumina samples are negligible for top and bottom discs. The difference in average affected zone thickness was found to be less than 5%.
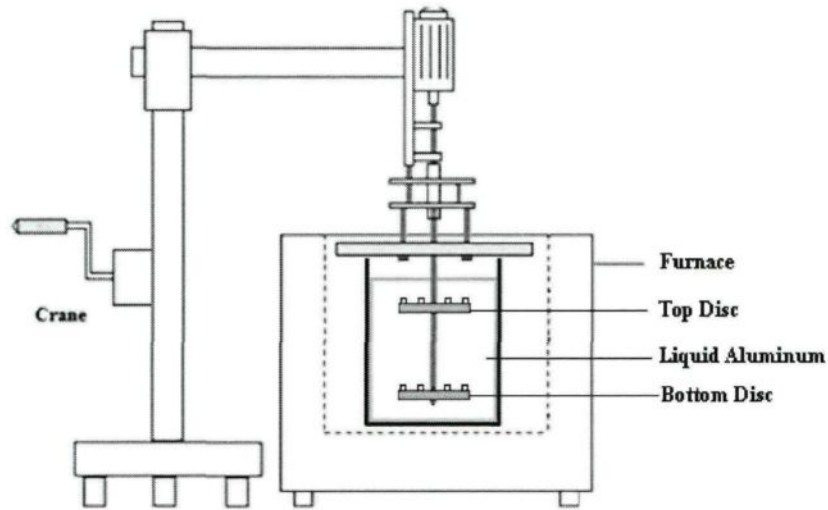
Figure 5-28: A Schematic Description of Experimental System-II : Positions of Top and Bottom Discs
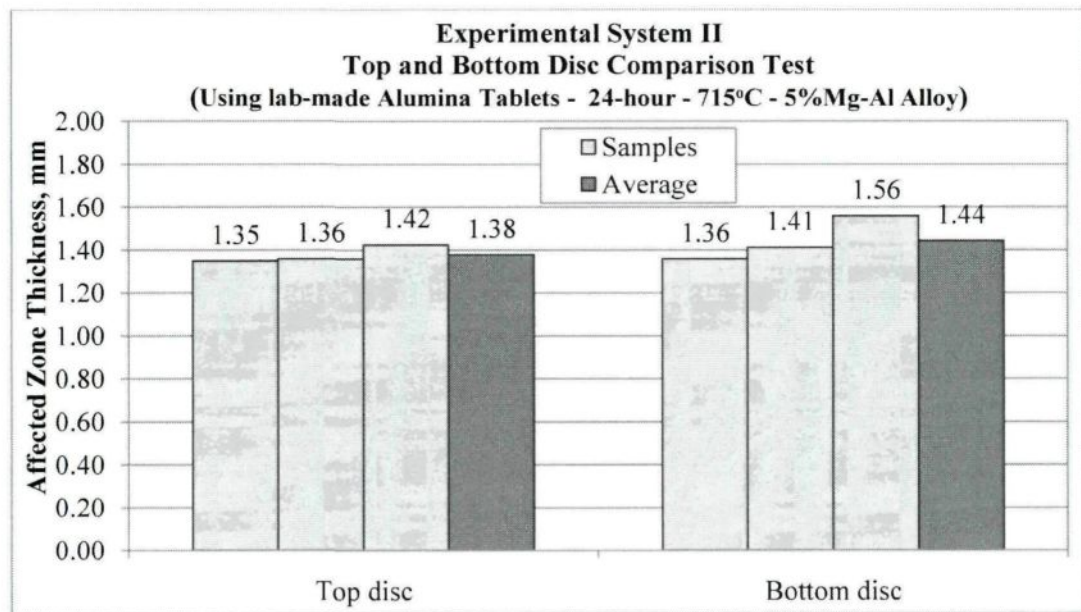
Figure 5-29: Experimental System-II: Comparison of Results for Top and Bottom Discs

5.4   Metallographic Study

A metallographic study including surface analysis methods such as optical microscopy, SEM-EDX, SEM-Microprobe, and XPS-Photoelectron microprobe was conducted to identify the reaction products observed at the aluminum alloy/alumina, and alumina/inclusion interfaces.

5.4.1   Metallographic Investigations of Commercial Alumina Particles Before Contact with Al-Mg Alloys

First, the commercial alumina particles were investigated in unused (raw) state. The purpose of this study was to determine the structural differences of various commercial alumina types. Figure 5-30 show the general appearance of the commercial alumina particles "as received" under microscope (see Figures A4-1 to A4-4 in Appendix 4 for more examples). The dark areas seen in these images are the pores of the alumina particles. These images were analyzed using the image analysis method to determine the internal structure (average pore size and number of pores per particle) of each particle, and the variations in the internal structure characteristics of each commercial alumina group.   The results are summarized in Figure 5-31.
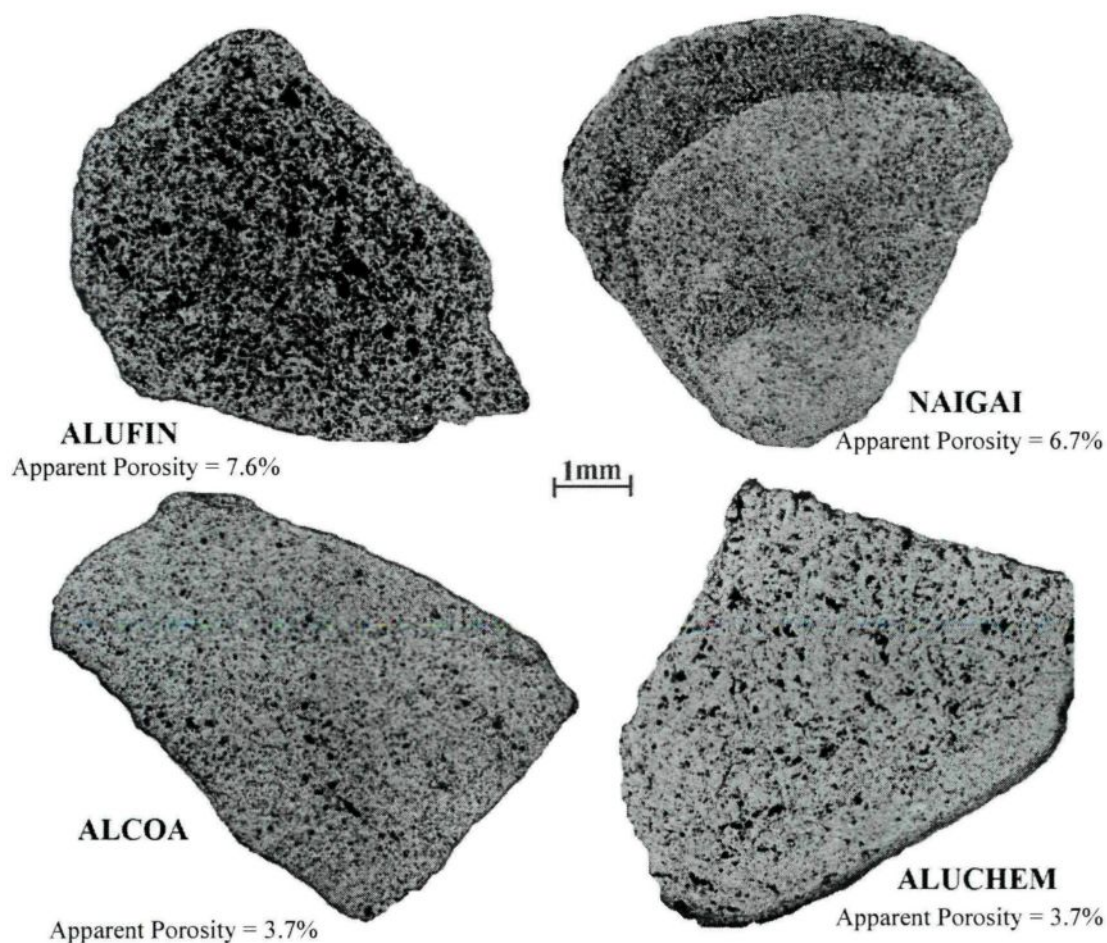
Figure 5-30: Typical Appearance of Various Commercial Alumina Types in Raw State

Based on the results shown in Figure 5-31, Alufin has the largest pore size and the second highest number of pores per mm^2 after Naigai. Visual observations also indicated that Alufin and Naigai have higher porosity. Naigai type alumina has the most inhomogeneous pore distribution observed among all commercial alumina types. The dark color band seen around the perimeter of particles is the high porosity zone. The core of the

particle is generally denser than the outer side. Naigai particles have the smallest pore size, and the highest number of pores.

Alcoa and Aluchem show very similar characteristics. They both have the lowest number of pores, and the distribution of pores seems to be more homogeneous in all groups. The size of the pores is relatively larger in Aluchem compared to that of Alcoa.
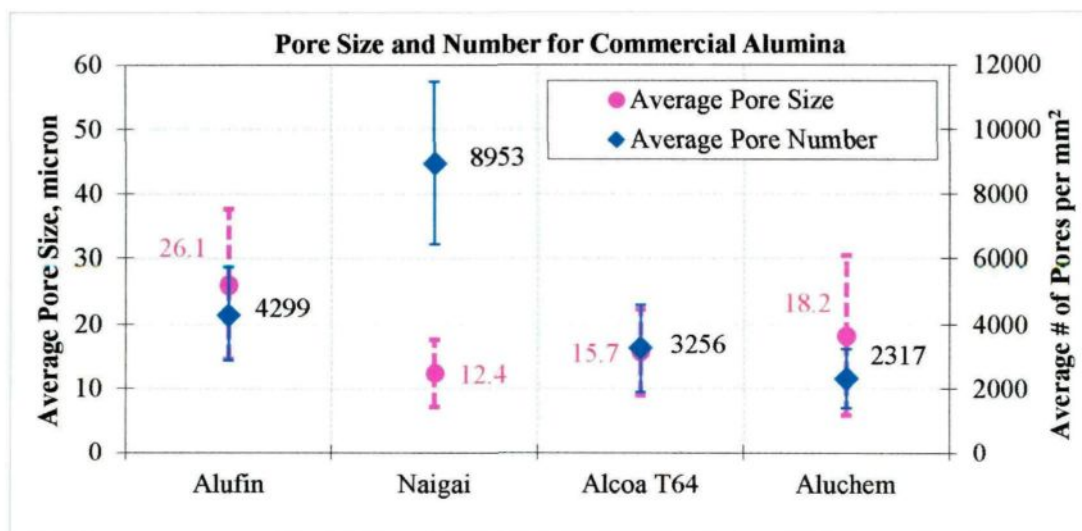
Figure 5-31: Pore Size and Pore Number/mm^2 Measurements using Metallographic Investigation for Commercial Alumina Particles

5.4.2 SEM Analysis Results of Commercial Alumina Particles after Contact with Al-Mg Alloys

In order to facilitate the SEM analysis, in addition to the conventional metallographic investigation using optical microscope, a method was developed making use of different fluorescence characteristics of magnesia and spinel under UV light. It was

found in the literature that some minerals such as magnesite [$MgCO_3$], Mg-spinel [$MgAl_2O_4$], chondrodite [$(Mg,Fe)_5(SiO_4)_2(F,OH,O)_2$], forsterite [$Mg_2SiO_4$] showed fluorescent behavior under UV light [9]. Ergin at al [9,10] also stated that some magnesium containing minerals other than spinel in the form of carbonates or hydrates of magnesium show fluorescent behavior; however, these are not expected to be found at the aluminum/alumina interface of the samples in the current study. The fluorescent sites under UV light found on current studies' samples are expected to be Mg-spinel. All polished samples obtained in this study were examined under UV light in a dark room as shown in Figure 5-32, and possible spinel sites were marked before SEM analysis. It should be noted that this method is helpful to locate spinel particulates.
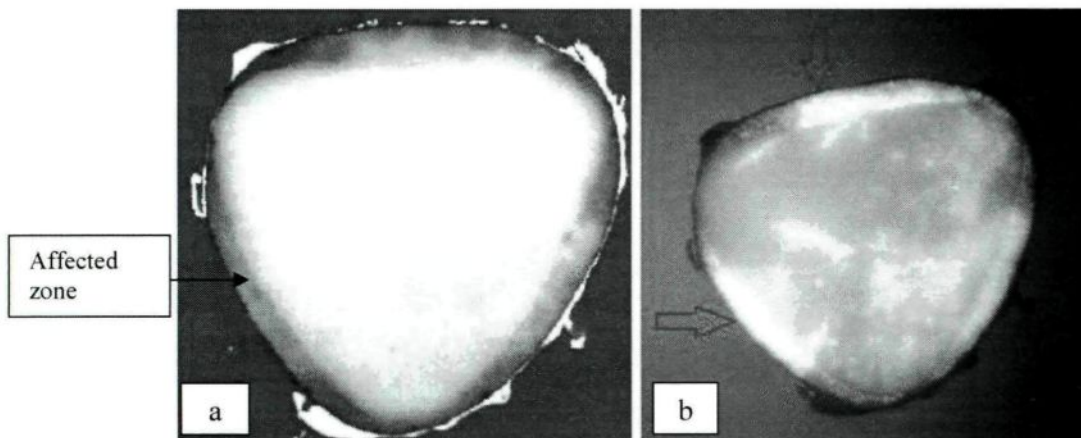
Figure 5-32: Appearance of Alumina Samples Under (a) Day Light, (b) UV Light

Table 5-14: Stoichiometric Values of Pure Phases [72, 103, 104]

	Mg		Al		O		Na	
	Wt %	at.* %	Wt %	at. %	Wt %	at. %	Wt %	at. %
MgSpinel ($MgAl_2O_4$)	17	14	38	29	54	57	-	-
Magnesia (MgO)	60	50		-	40	50		-
Alpha (α) Alumina ($α-Al_2O_3$)	-	-	53	40	47	60	-	-
Beta-Alumina Phases $NaAl_9O_{14}$			49.6	37.5	45.7	58.3	4.7	4.2
$Na_2O.11Al_2O_3$ ($NaAl_{11}O_{17}$)	-	-	50.2	38	46	59	3.8	3.2
$MgO.11Al_2O_3$	2.1	1.8	51	39	42	58	-	-

*at. % : Atomic %

Theoretically, if EDX (energy dispersive X-ray spectroscopy) or WDS (wave dispersive X-ray spectroscopy) quant analysis is conducted on a pure spinel or magnesia samples, respectively, Al-Mg-O or Mg-O should correspond to their stoichiometric amounts. Then, the presence of spinel and magnesia can easily be determined by comparing the percentages of different elements found in alumina in a specific region with these values. The stoichiometric percentages (atomic% and weight %) of Mg, Al, and Na in spinel, magnesia, α-alumina and β-alumina are given in Table 5-14 above.

The thickness of reaction zone changes from a couple of hundred nanometers to a couple of hundred micrometers. Magnesium diffusion through an alumina particle causes a discoloured region at the interface. A reaction zone formation at the surface starts and this penetrates into the interior of the particle. The extent of degradation (due to reaction) on the alumina particle surface increases with increasing time. The thickness of this reaction zone

may change depending on the magnesium content, temperature, impurities in alumina, etc. This thickness is not the affected zone thickness shown in Figure 5-32 as the discolored gray zone. This zone is where the reaction is occurring at the interface. The affected zone covers larger area where the magnesium diffusion is visible as a greyish/black hue.

Whenever the size of the reaction zone/product was too small, the back scattered electrons carried the information coming not only from that tiny particulates, but also from the matrix material (layer existing underneath the detected particulates which are quite likely alumina in this study). This resulted in the measurement of varying Mg atomic% values (from 5% to 21%) for reaction products which made the phase identification process difficult and confusing, even though these particulates have similar appearances under microscope. Some of the analyses were repeated using a microprobe and XPS to make sure similar results were obtained, and the reaction product was identified as Mg-spinel. These results were also in agreement with those of Ergin [9,10]. He analyzed the Mg-aluminum alloy/alumina interface of sessile-drops formed during the wetting experiments using TEM, and the interfacial reaction product was identified as Mg-spinel.

5.4.3   Na-rich Phase Observed in the Commercial Alumina Particle

Metallographic investigations revealed the presence of a second phase, a Na-rich phase in alumina other than α-Al_2O_3 phase. Other elements found in this phase were Si and Ca, but their concentrations were generally 1/10th of Na concentration. This phase was found to be a strong contributor to the degradation of alumina in the presence of magnesium in

liquid aluminum. This phase is usually found in the vicinity of α-Al₂O₃ grain boundaries. It has a relatively darker appearance compared to the matrix α-Al₂O₃ phase.

The electron microscope image and semi-quantitative EDX point analysis shown in Figures 5-33 and 5-34 indicate that major elements found in Na-rich alumina phase were O, Al, and Na, respectively. The individual measurements showed that Na concentration varies between 2.2 to 3.5 atomic % while the contents of O and Al are in the ranges of 62-70 atomic % and 27-35 atomic %, respectively, as seen in the analysis below and also in similar analyses (Table 5-17) conducted using other particles.

Chemical Composition-Spectrum 1

Element	Weight %	Atomic %
O K	49.35	61.99
Na K	2.76	2.41
Al K	47.39	35.29
Si K	0.27	0.19
Ca K	0.23	0.12
Totals	100	100
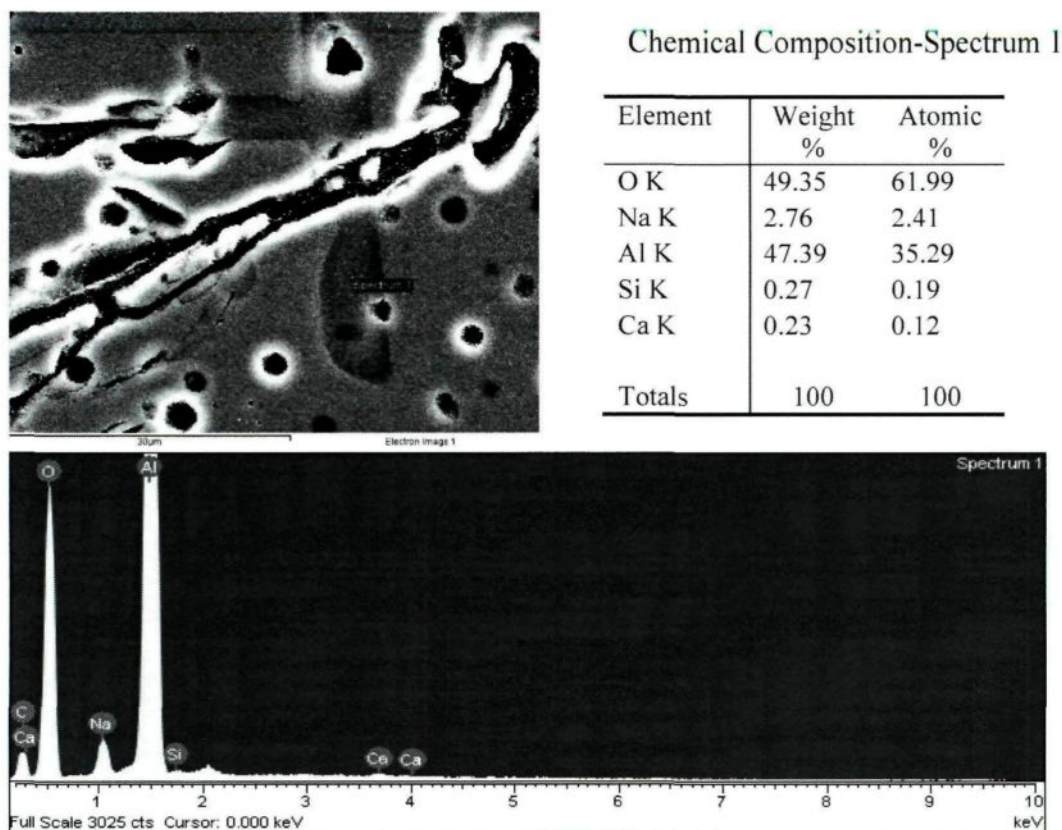
Figure 5-33: Na-rich Phase in Alcoa T64 Particle (SEM-EDX Analysis Results)
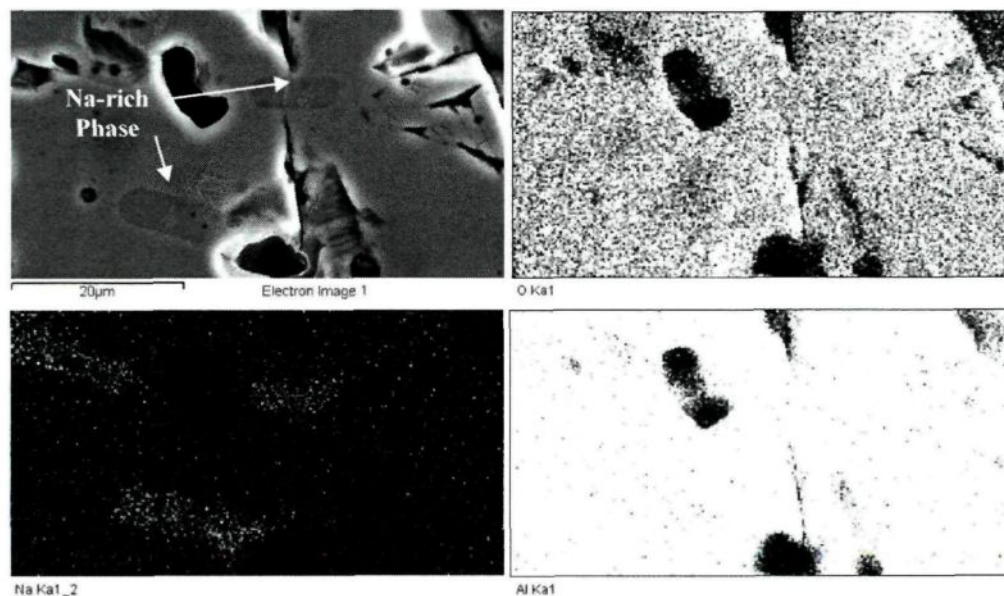
Figure 5-34: SEM Mapping Study with Na-rich Phase in Naigai Particle

In the NaAlO$_2$-Al$_2$O$_3$ phase diagram published by Thanh [98], Na-rich phase observed in the commercial alumina microstructure is identified as Na$_2$O.11Al$_2$O$_3$ (or NaAl$_{11}$O$_{17}$) based on the Na$_2$O content of the commercial alumina discussed in Chapter 3 (0.17-0.25 Na$_2$O wt.% shown in Table 3-8). The phase Na$_2$O.11Al$_2$O$_3$ is generally called β-Al$_2$O$_3$ (beta alumina) in the literature. However, the beta alumina is described as NaAl$_9$O$_{14}$ in the Na$_2$O-Al$_2$O$_3$ phase diagram in Figure 5-35 obtained with a thermodynamic analysis software called FACT (Facility for the Analysis of the Chemical Thermodynamics), developed by Ecole Polytechnique and McGill University. The latter beta alumina definition was used in the proposed reactions in the following sections.

In the stoichiometric $NaAl_9O_{14}$ beta-alumina phase, O, Al, and Na concentrations are 58.3, 38.5, 4.2 atomic %, respectively, as shown in Table 5-14. Na-rich alumina phase was observed on all commercial alumina particles tested in this study.

Tabular alpha alumina is produced by sintering calcined alumina at ~2000°C. The presence of Na_2O in alpha-alumina as an impurity causes beta-alumina formation at high temperature sintering. It was reported in the literature that [72] the presence of beta alumina in tabular alpha-alumina structure can result in the deterioration of the structural strength at high temperatures due to the differences in thermal expansion behavior of alpha-and beta-alumina. It also decreases the chemical inertness of alpha-alumina phase.
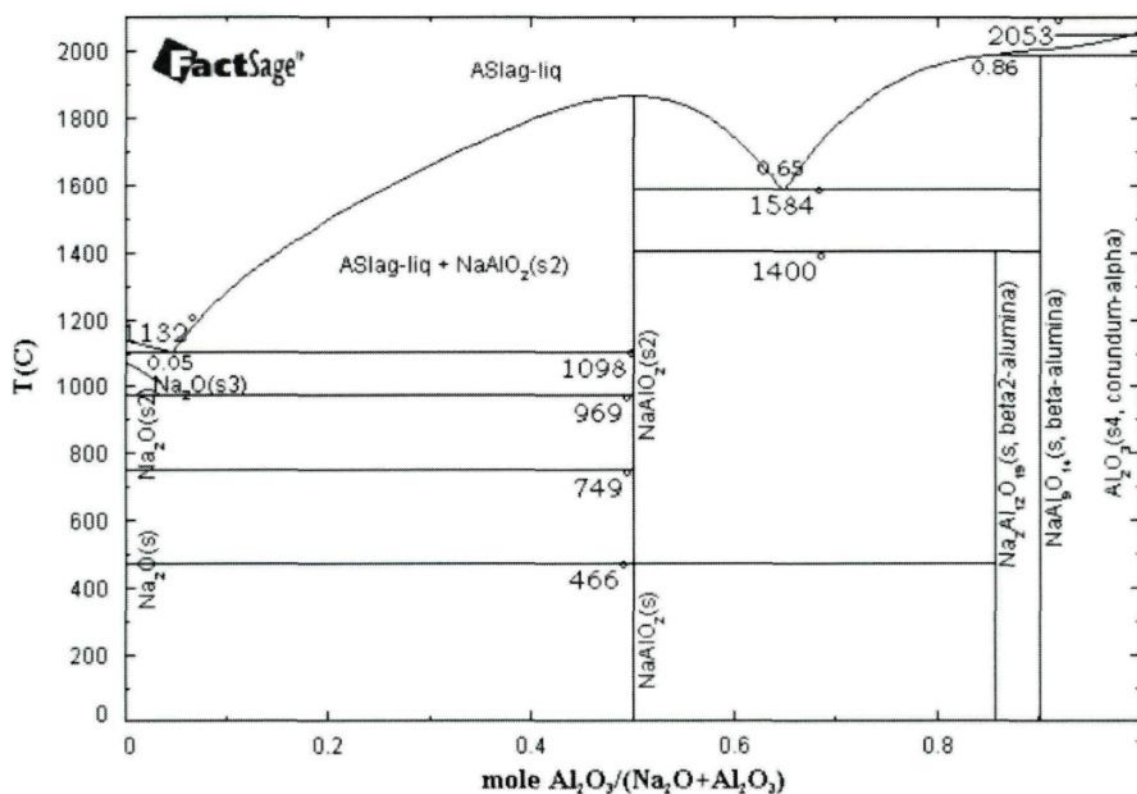
Figure 5-35: Na_2O– Al_2O_3 Phase Diagram - FactSage [103]

5.4.4 Metallographic Investigations on Commercial Alumina/Aluminum Alloy Interface

Several experiments were conducted to investigate the alumina/aluminum interfacial reactions. The results of these investigations showed that two different reaction mechanisms cause the degradation of alumina.

1. Inter-granular reactions taking place in Na-rich alumina phase

2. Surface reactions taking place at alumina/aluminum interface

5.4.4.1 Inter-granular Reactions

Tabular alumina is made of ~98% α-Al_2O_3 which is one of the most chemically stable materials when it is in contact with molten aluminum. Its weakest points are ~2% impurity content, 3-5% apparent porosity level, and relative low resistance to Mg vapor attack. Actually, the first mechanism (inter-granular reaction taking place in Na-rich alumina phase) mentioned above is driven by magnesium diffusion through grain boundaries, pores, Na-rich phase, and existing cracks in the particle structure.

The magnesium diffusion makes the appearance of alumina darker (gray/black). Beta-alumina phase seems to be affected by the magnesium diffusion more rapidly than alpha-alumina grains, which are very dense and chemically inert even after 7-day duration experiments.

The reactions first take place where impurities, especially Na-rich alumina phase, are found in the structure. Na-rich alumina can be observed as a slightly darker phase using the optical microscope as shown in Figure 5-36. This phase cannot be distinguished from the matrix phase on unused polished alumina surface, but it becomes apparent even after a

couple of hours contact time with Mg-Al molten alloy. It seems that the color change in alumina occurs mainly due to the presence of this phase which gets darker following the magnesium diffusion. The electron microscope mapping analysis shown in Figure 5-37 indicates that this dark phase observed in grain boundary is very rich in Na, Mg, Al, and O elements. This analysis clearly indicates the magnesium diffusion occurring in grain boundary and the presence of Na-rich alumina phase as can be seen in Figure 5-37. The yellowish/gold color zones (Pt 1 along the grain boundary, Pt 2, and some in Pt 3) in Na-rich alumina phase are the locations where the reaction products are found.

Figure 5-36: Inter-granular Reactions in Na-rich Regions (7%Mg, 715°C, 12-hour Contact Time, Alcoa T64)

Chemical compositions of three points shown in Figure 5-36 were analyzed using EDX. The results are summarized in Tables 5-15, 5-16, and 5-17, respectively. It is quite

couple of hours contact time with Mg-Al molten alloy. It seems that the color change in alumina occurs mainly due to the presence of this phase which gets darker following the magnesium diffusion. The electron microscope mapping analysis shown in Figure 5-37 indicates that this dark phase observed in grain boundary is very rich in Na, Mg, Al, and O elements. This analysis clearly indicates the magnesium diffusion occurring in grain boundary and the presence of Na-rich alumina phase as can be seen in Figure 5-37. The yellowish/gold color zones (Pt 1 along the grain boundary, Pt 2, and some in Pt 3) in Na-rich alumina phase are the locations where the reaction products are found.

Figure 5-36: Inter-granular Reactions in Na-rich Regions (7%Mg, 715°C, 12-hour Contact Time, Alcoa T64)

Chemical compositions of three points shown in Figure 5-36 were analyzed using EDX. The results are summarized in Tables 5-15, 5-16, and 5-17, respectively. It is quite

obvious that from first point to third point (from the alumina/aluminum interface to the interior of alumina on the grain boundary), magnesium content is decreasing from 21 atomic % to 0.39 atomic %, and Na content is increasing from zero to 2.22 atomic %, respectively. The reaction zone where the highest Mg content is found has yellowish color appearance in optical microscope image. The analysis in Table 5-15 indicates the typical Mg-spinel atomic % values based on data given in Table 5-14.

Figure 5-37: SEM Mapping Study on Sample Shown in Figure 5.36 (7%Mg, 715°C, 12-hour Contact Time, Alcoa T64)

Table 5-15: Quantitative Analysis of Point 1: Reaction Site 1 Shown in Figure 5-36

Element	App Conc.	Intensity Corrn.	Weight%	Weight% Sigma	Atomic%
O K	9161.64	1.3838	52.06	0.27	63.71
Mg K	2616.71	1.0934	18.82	0.19	15.16
Al K	3697.01	0.9983	29.12	0.23	21.13
Totals			100.00		100.00

Table 5-16: Quantitative Analysis of Point 2: Reaction Site 2 Shown in Figure 5-36

Element	App Conc.	Intensity Corrn.	Weight%	Weight% Sigma	Atomic%
O K	12990.33	1.3772	53.23	0.16	65.13
Na K	239.01	1.4128	0.95	0.06	0.81
Mg K	2005.98	1.0884	10.40	0.10	8.37
Al K	6432.44	1.0252	35.41	0.15	25.69
Totals			100.00		100.00

Table 5-17: Quantitative Analysis of Point 3: Reaction Site 3 Shown in Figure 5-36

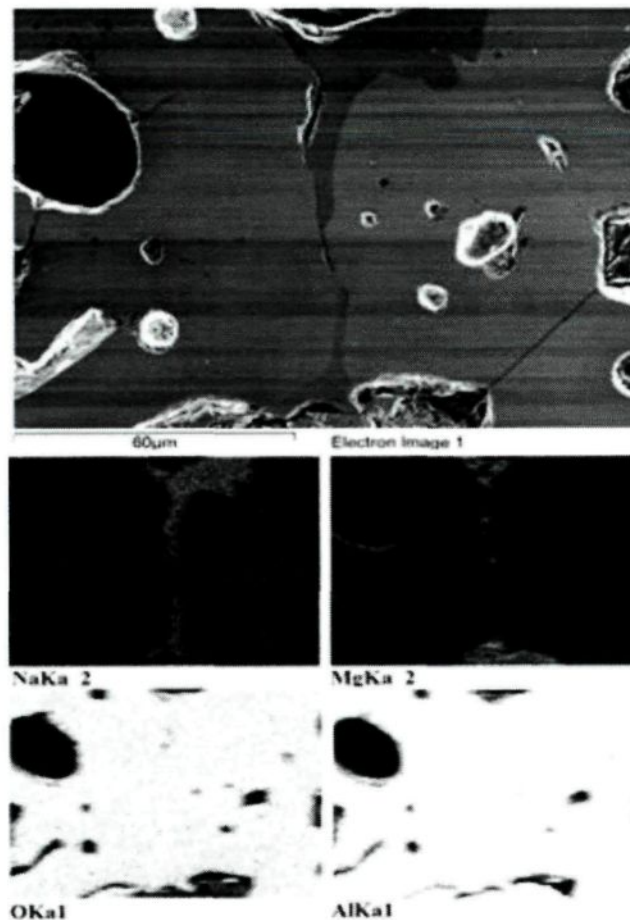| Element	App Conc.	Intensity Corrn.	Weight%	Weight% Sigma	Atomic%
O K	15768.50	1.3937	58.76	0.13	70.35
Na K	709.43	1.3822	2.67	0.05	2.22
Mg K	100.52	1.0652	0.49	0.04	0.39
Al K	7670.14	1.0460	38.08	0.12	27.04
Totals			100.00		100.00

EDX analyses conducted on Point 2 and Point 3 shown in Figure 5-36 indicate only a partial conversion of Na-rich alumina phase into Mg-spinel structure because the Mg content is only ~8.4 at.% and 0.39 at.%, respectively , at these points.

This analyses underline that Na depletes in Na-rich phase while Mg diffuses through. Magnesium reacts with Na-rich phase, and sodium (Na) appears to leave the structure. Equation 5-1 and 5-2 are the two possible reactions between magnesium and Na-rich alumina phase. Based on the EDX analysis results, Mg spinel ($MgAl_2O4$) is the reaction product; therefore, Equation 5-1 which suggests the depletion of Na from solid

phase and the formation of aluminum metal and Mg-spinel seems to be the most reasonable explanation of this phenomenon. The yellowish gold color areas observed in the reaction zone are the places where Mg-spinel and aluminum metal formation occurs.

$$\frac{2}{7} NaAl_9O_{14}(s) + Mg(vapor) \rightarrow MgAl_2O_4(s) + \frac{4}{7} Al(l) + \frac{2}{7} Na \ (vapor) \qquad (5.1)$$

$$\frac{1}{14} NaAl_9O_{14}(s) + Mg(vapor) \rightarrow MgO(s) + \frac{9}{14} Al(l) + \frac{1}{14} Na \ (vapor) \qquad (5.2)$$
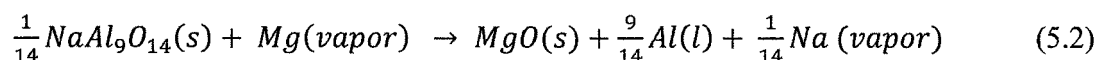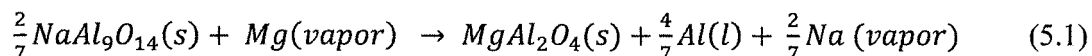
According to FACT (Facility for the Analysis of the Chemical Thermodynamics) analysis shown in Section 5.5, Table 5-18, $\Delta G°$ value for Equation 5.1 is -89 kJ which is slightly lower than that of Equation 5.2 (-82 kJ) at 1000 K. This means that Mg-spinel formation is thermodynamically favored as opposed to MgO formation.

The mechanism and the reaction product observed in grain boundaries and Na-rich alumina zone did not show any changes when different Mg-Al alloys were used in the experiments. In Appendix 4, more results showing $MgAl_2O_4$ formation in Na-rich phase and grain boundaries can be found on various samples (Figures from A4-5 to A4-10, Table A4-1).

5.4.4.2 Surface Reactions

5.4.4.2.1 Reactions in Na-Beta Alumina Phase

Tabular alumina particles are usually produced in 12-18mm diameter size in ball form. After sintering, these balls are crushed and sieved in order to obtain various particle sizes. The particle size in deep bed filters varies between 2 to 18 mm, and the majority of

particles used in the current study were between 4.87-6.35 mm. Because of the crushing process, Na-rich alumina phase sometimes happens to appear on the particle surface, which promotes surface reactions at the alumina particle/liquid aluminum interface.

Alcoa particle shown in Figure 5-38 and 5-39 is an ideal example to demonstrate the structural changes occurring in the alumina due to Mg diffusion. Both figures clearly demonstrate the reacted and affected areas at alumina/aluminum interface on a cross-section of the sample. EDX analyses were conducted on the reacted and the affected areas. Major elements that exist in these areas were found to be O, Al, Mg, and Na. The reacted areas where alumina structural changes occur show higher Mg and lower Na peaks compared to those of the affected zone. It seems that Mg diffusion trough the particle depletes Na content. The same reaction mechanisms explained in the previous section by Equation 5.1 are valid for the surface reactions taking place in the Na-rich zone. The crack/void formation due to the reaction suggested in Equation 5.1 can be observed clearly in Figure 5-38.
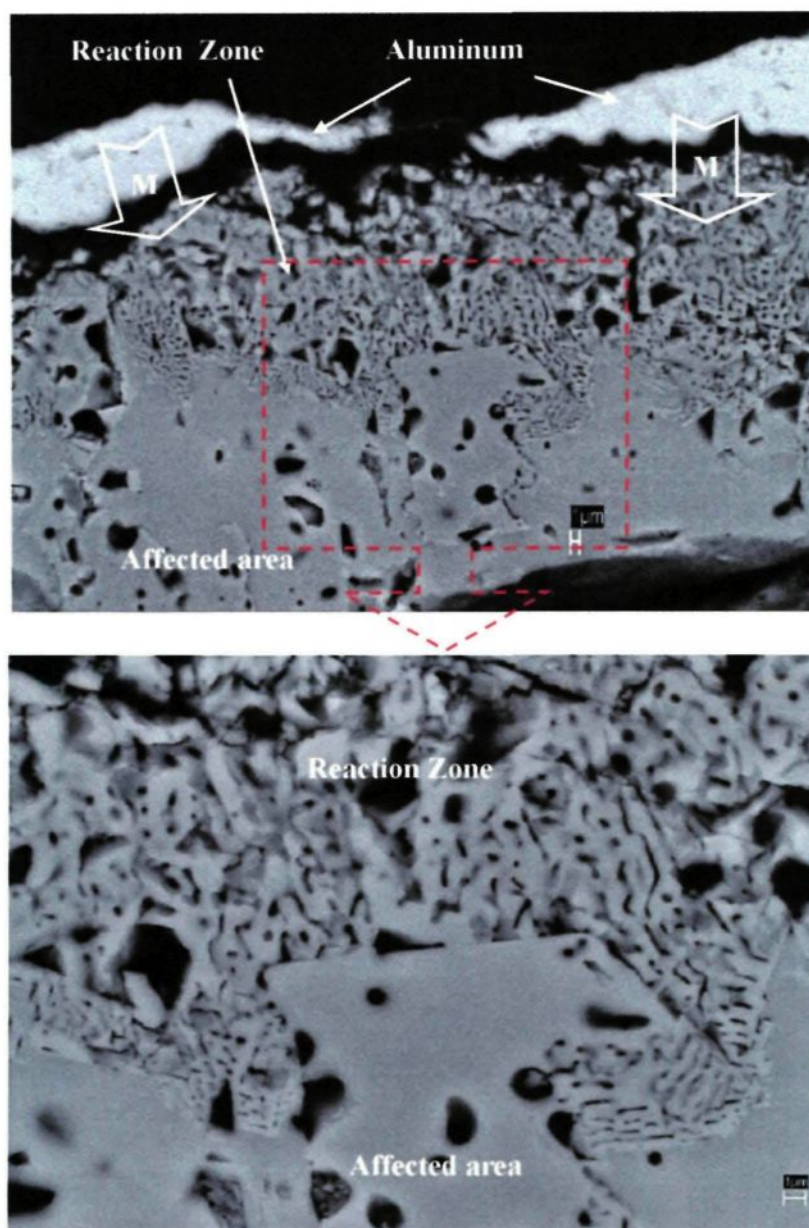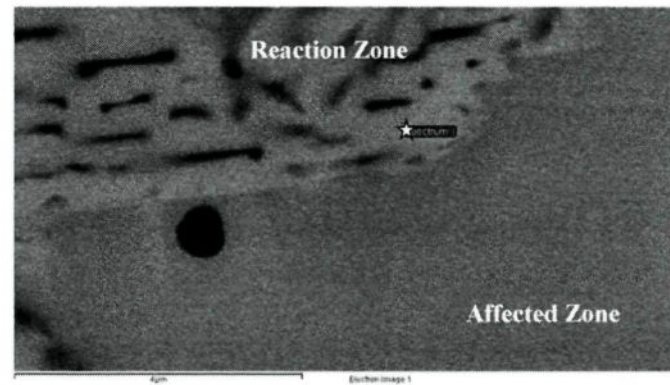
Figure 5-38: SEM Image Showing Surface Reaction Zone on Alcoa Particle (Cross-section-
5%Mg, 715°C, 72-hour Contact Time)
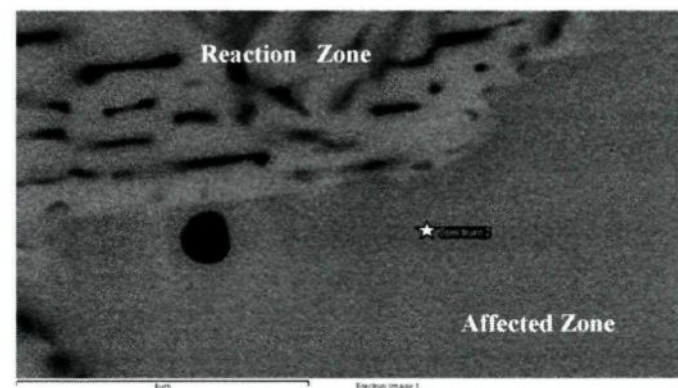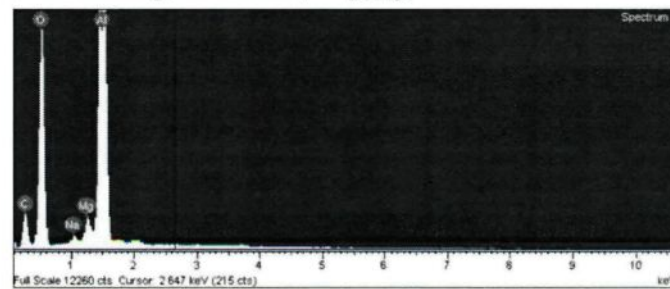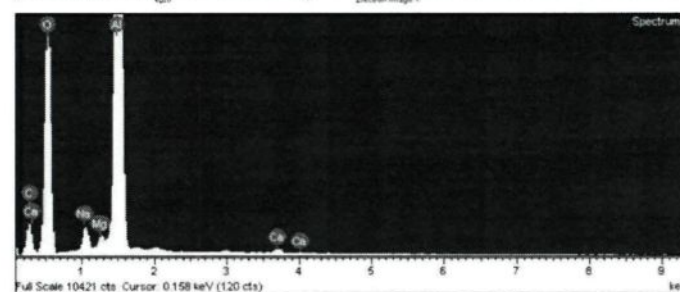
Figure 5-39: SEM-EDX Analyses at (a) Reaction Zone, (b)Affected Zone on Alcoa T64
Particle (Dynamic Experiment with 1.8 mm/s- 5%Mg, 715°C, 72-hour Contact Time)

5.4.4.2.2 Scanning of Peeled-off Alumina Surface

After the experiments, the alumina particles generally have a thin layer of aluminum skin left on their surface. Aluminum skin samples from the surface of the alumina particles were peeled-off carefully. Skin samples (Alcoa T64) taken intermittently during dynamic experiment (at 1.8mm/s velocity) with 5%Mg-Al alloy at 715°C were examined by SEM-EDX. The contact times for these samples were 3, 12, 24, and 48 hours.

Figure 5-40 shows the SEM image of a typical commercial alumina surface at high magnification before the experiments. The surface of alumina is covered by powder like fine grains. SEM-EDX analyses conducted on these fine grains showed that they are aluminum oxide. These images will be used to compare the changes occurring on the alumina surface when it is in contact with liquid aluminum.

Figure 5-40: SEM Image of Unused Commercial Alumina Particle (a) 500x, (b) 2500x

The peeled-off alumina (after contacting with Mg-Al alloy) looks black/gray in most of the cases (see Figure 3-15 in Chapter 3). A couple of peeled-off alumina particles were investigated using the X-ray diffraction (XRD) which is a quantitative method to identify the reaction products. The black/gray surface was scraped off using a dremel and a diamond tip to have some powder for the XRD analysis. The results showed that the major content of the 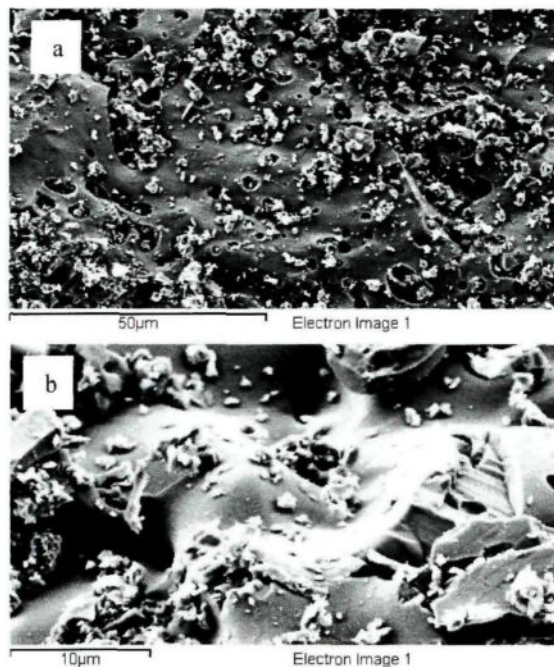powder taken from alumina surface was rhombohedral alumina (see Figure A4-11 in Appendix 4). It's believed that the XRD method did not work for the identification of the reaction product in this case, because the reaction product layer is too thin. During the sample preparation for the XRD test while trying to remove a reaction product layer, a thick layer of matrix phase (Al_2O_3) must have been scraped-off of the particle surface.

Figure 5-41 shows the surface of a sample which was in contact with liquid aluminum under flow conditions for 3 hours. Compared to the initial surface image, the needle-like structure observed (as shown in Figure 5-41.a) was the major difference. The literature survey [72] indicated that the needle-like structure forms due to the interaction of Na vapour and oxides. This observation confirms the relationship between the magnesium diffusion and the Na-beta alumina suggested earlier in Equation 5.1. The detection of sodium leaving the alumina seems to be a tangible proof of the suggested mechanism.

The regions, where EDX analyses are conducted, are indicated in Figure 5-41.c. The first analysis showed that the micro grains existing on virgin alumina starts to convert into discrete Mg-spinel crystals when contacted with liquid aluminum (Figure 5-41.e). The

second analysis indicates the presence of Na and the initiation of surface reactions (Figure 5-41.f).

Figure 5-41: EDX Analysis Results of Non-polished Alcoa T64 Particle Surface After 3h of Contact Time at Various Magnifications (a-d), 5%Mg-Al Alloy-1.8mm/s metal velocity-715°C and EDX Point Analysis Results for (e) Discrete Crystal, and (f) α-Alumina Surface Shown in (c).
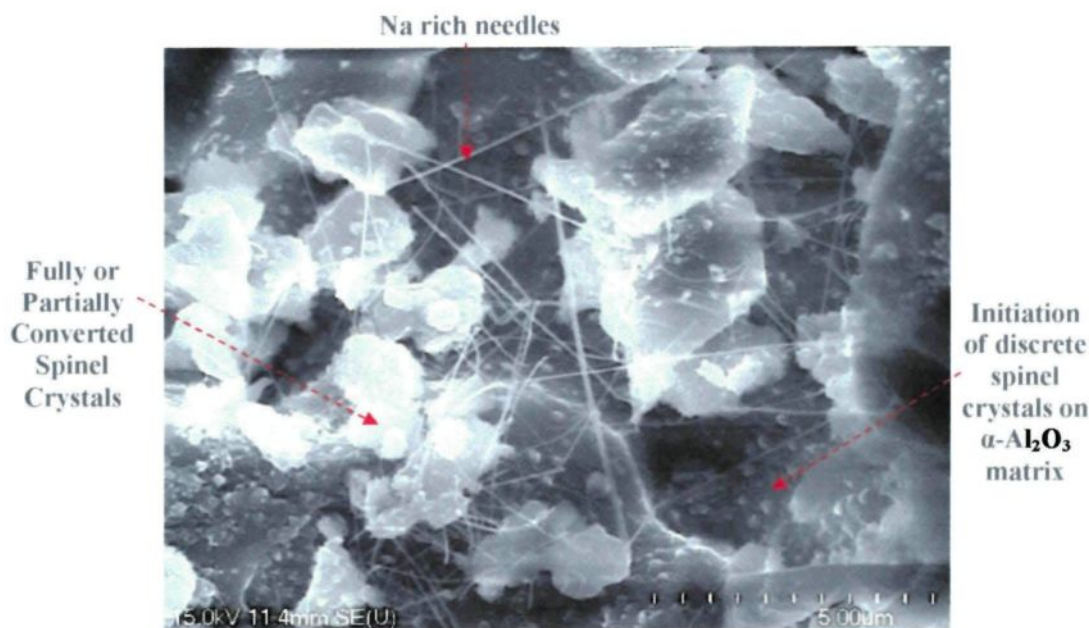
Figure 5-42: SEM Image of Non-polished Alcoa T64 Particle Surface After 12-hour Contact Time (5%Mg-Al Alloy-1.8mm/s Metal Velocity-715°C)

Figure 5-42 shows the particle surface after 12 hours of interaction with aluminum alloy under flow conditions. The tangled needle like Na rich phase and the fully or partially converted spinel crystals are found on alumina surface. Alpha-alumina seems to have rougher surface due to the initiation of discrete spinel crystals.

The particle surface after 24 hours of contact time was examined first visually. A dark spot on the peeled off particle surface was found interesting. The following SEM scan showed that the dark spot actually looks different than the rest of the alumina surface (Figure 5-43.a). It was found by SEM analysis that this crater like dark surface surrounded by a dashed line contains high levels of Na_2O. A quant analysis on the Na rich area indicates ~35 at.% Na in Figure A4-12.a in Appendix 4. This is the highest Na level

observed in the alumina analyses of this study. It must be one of the highest levels of Na_2O containing alumina-phase shown in the Na_2O-Al_2O_3 phase diagram earlier. An optical microscopy image of a similar spot (found on another alumina sample) can be seen from its cross-sectional view in Figure A4-12.b in Appendix 4.

The images in Figure 5-43.c and 5-43.d demonstrate the structural differences between the Na rich and normal zones on the particle surface. Na rich zone shows a needle-like fused structure. On the other hand, the normal surface has discrete crystals and some needle like structure on alpha-alumina. The normal surface was further investigated using higher magnifications (see Figures 5-43.e and 5-43.f) to have a better understanding of the structure and the surface reaction mechanism. The SEM image in Figure 5-43.e shows the appearance of a typical Mg-spinel discrete crystal formed on alpha alumina. Figure 5-43.f is an example of Na rich needle like bushy structure. It seems that this bushy structure also contains discrete spinel crystals. The EDX analysis conducted (Figure A4-13 in Appendix 4) on circled area detected 15 at.% magnesium. Another possibility is the conversion of the bushy structured oxide into Mg-spinel with continuous magnesium diffusion from the alloy.

Figure 5-44 shows the SEM images taken on alumina surface which was in contact with the liquid aluminum alloy for 48 hours. The overall alumina surface seems to be less affected compared to the other samples investigated earlier. The higher magnification surface examination resulted in a very interesting finding. The discrete Mg-spinel crystal showed Na-rich needle-like arms which seems to keep the crystal attached alpha-alumina

surface (Figure 5-44.b). The result of EDX analysis can be seen in Figure A4-14 in Appendix 4.
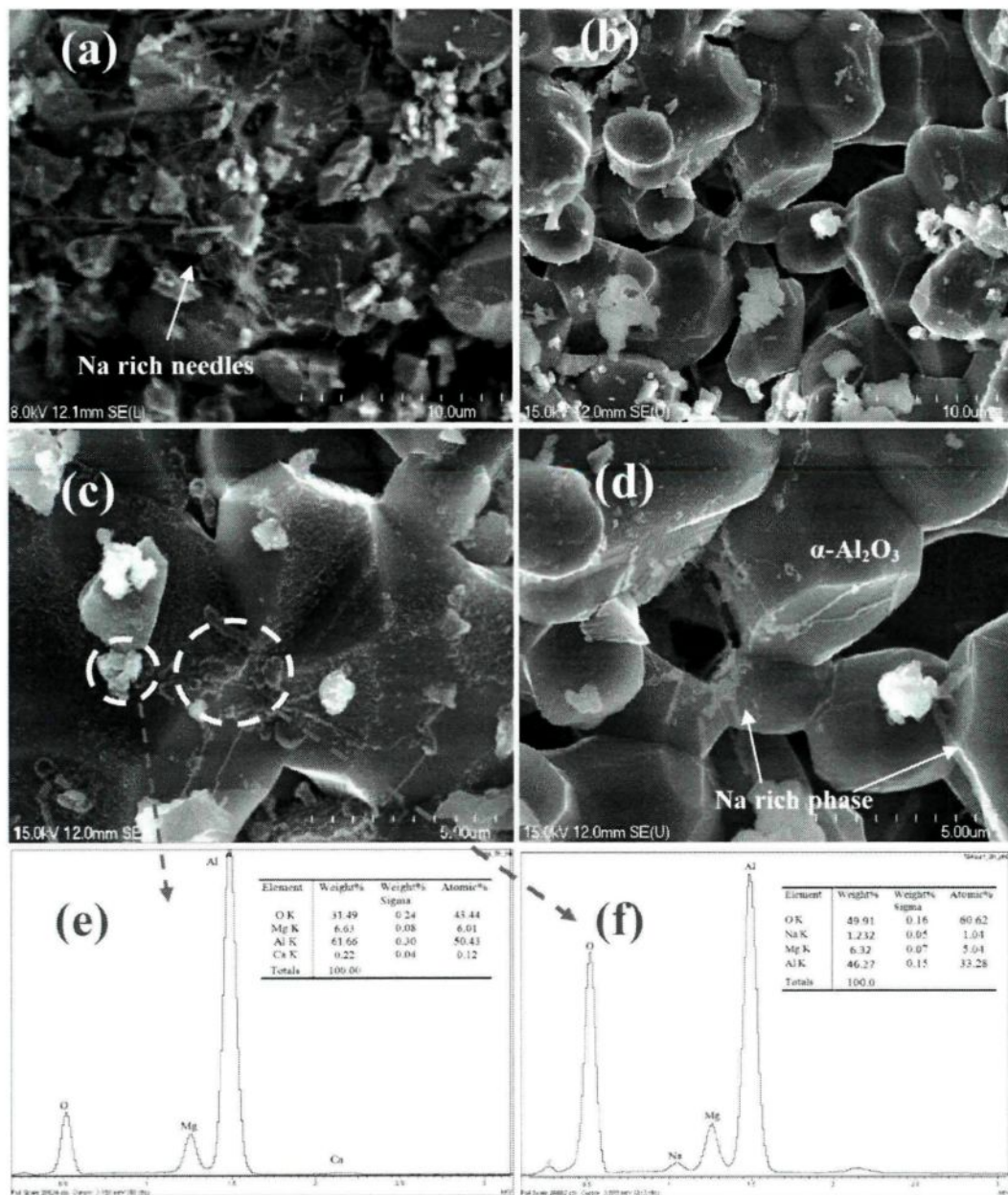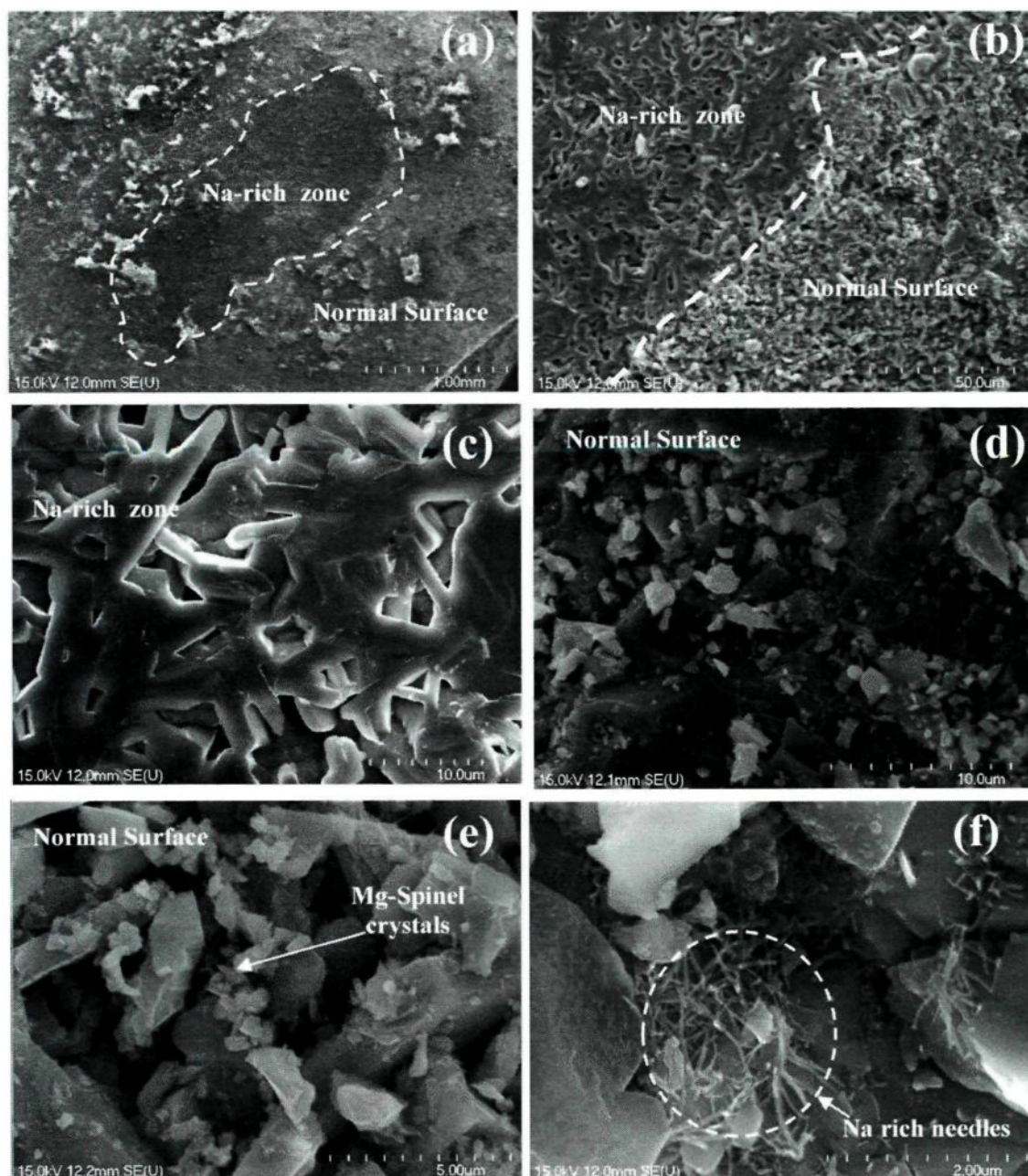

Figure 5-43: SEM Images of Non-Polished Alcoa T64 Particle Surface After 24-hour Contact Time at Various Magnifications (a-f) (5%Mg-Al Alloy-1.8mm/s Metal Velocity-715°C)
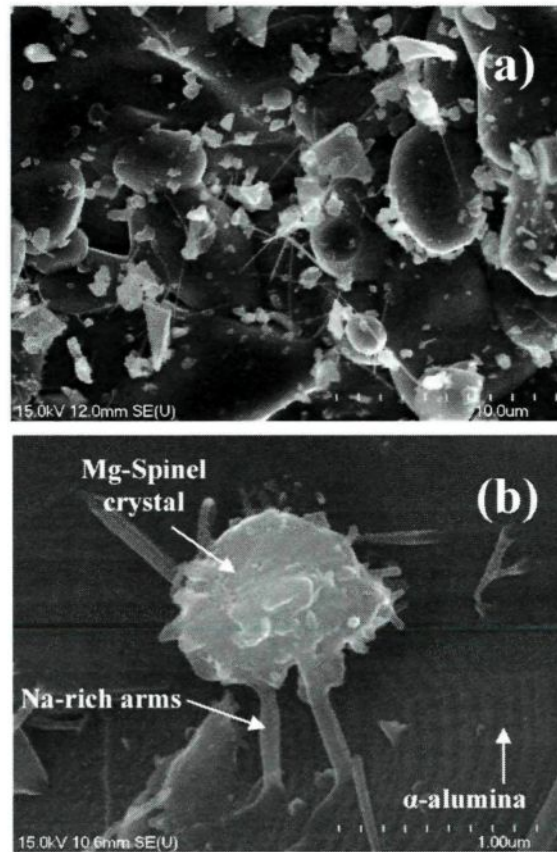
Figure 5-44: SEM Images of Non-polished Alcoa T64 Particle Surface After 48-hour Contact Time at Various Magnifications (a) Mg-spinel Crystals and Na-rich Needle-like Structures on Alumina Particle Surface, (b) Single Mg-spinel Crystal with Na-rich Arms Attached on Alumina Particle (5%Mg-Al Alloy-1.8mm/s metal velocity-715°C)

5.4.4.2.3 Degradation of Alumina Structure due to Surface Reactions

Alumina surface degrades as the reactions take place, and this can be seen from the appearance and growth of reaction zone.

Surface reactions in the Na-rich alumina zone, to a greater extent, can be seen on another Alcoa samples shown in the images in Figures 5-45 and 5-46. In these samples, a large Na-rich (2-3 Na at.%) alumina phase was found on the particle surface. Samples were taken at various contact times from the experiments conducted using 5%Mg-Al alloy. In

mapping study shown in Figure 5-46, magnesium diffusion though the alumina particle, and the presence of Na in the alumina structure can be clearly seen.
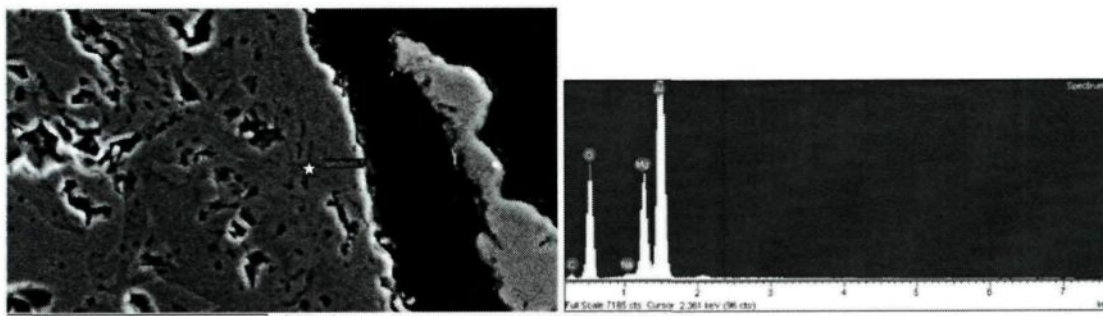
Figure 5-45: SEM EDX Point Analysis at Aluminum/Alumina Interface Reaction Zone - Alcoa Particle (5%Mg, 715°C, 96-hour Contact Time, Alcoa)
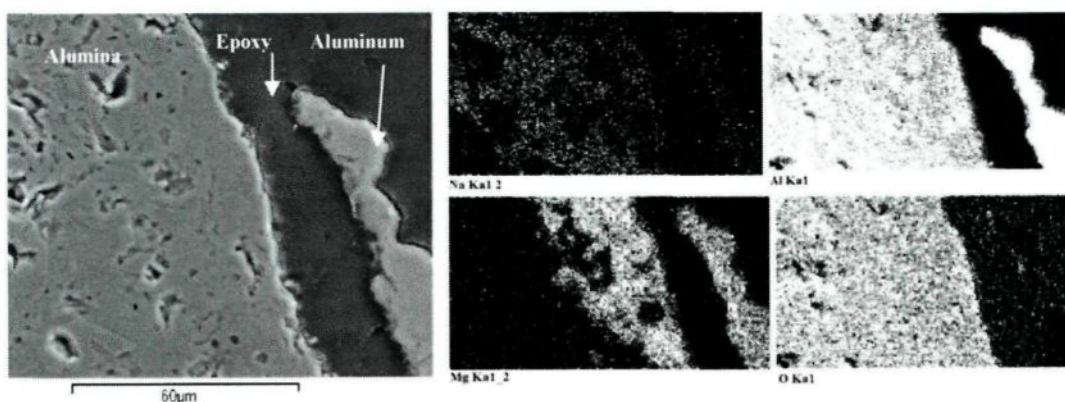
Figure 5-46: SEM Mapping Study at Aluminum/Alumina interface -Alcoa Particle shown in Figure 5-45 (5%Mg, 715°C, 96-hour Contact Time)

The presence of Mg-spinel and aluminum metal in the interior of particle are shown clearly in Figures 5-47 and 5-48. There seems to be two possible reasons for this phenomenon. It's either the result of a reaction or the infiltration of molten metal through cracks and pores.

As shown earlier in Figure 5-38, the cracks/cavities forms due to the reduction of Na-rich alumina phase by magnesium. These cracks might be filled with Mg-spinel and aluminum metal as a result of Equation 5.1.

The presence of aluminum metal inside an alumina particle can also be interpreted as a result of aluminum infiltration into alumina pores; but the aluminum infiltration does not seem to occur before the degradation of alumina structure reaches a certain extent. The presence of aluminum inside the pores was observed in the particle even though the wetting between alumina and liquid aluminum on the particle surface was not good. Without good wetting, the aluminum infiltration through the pores is not a phenomenon expected to occur. However, the samples were investigated from a cross-sectional view which can only show 2 dimensional images. There may be other areas on the alumina/aluminum interface with better wetting and greater reaction zones, which allow metal infiltration through the pores. It's also possible that both mechanisms, aluminum infiltration through the pores and aluminum metal formation as a result of Reaction 5.1, might be taking place simultaneously.
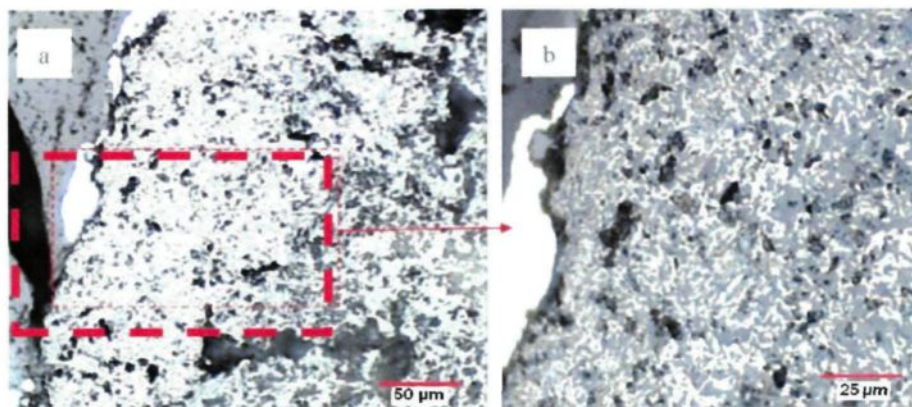
Figure 5-47: Appearance of a Large Reaction Zone at Alcoa Particle / 5%Mg-Al Alloy
Interface (a) 100x, (b) 200x Magnification Under Optical Microscope (2mm
Particle,715°C, 3-day 1.8mm/s Dynamic Experiment)
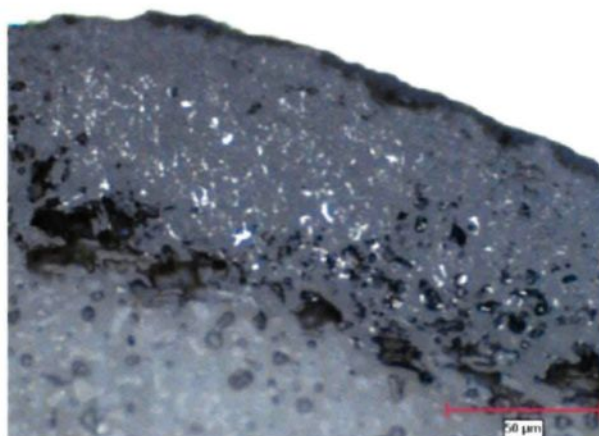
Figure 5-48: Presence of Aluminum Metal in Cavities within the Alcoa T64 Reaction Zone

The extent of this phenomenon depends on the size and the location of the Na-rich

alumina phase. Sometimes, it is observed on a large surface area as shown in Figure 5-49,

or a localized area on the particle surface as shown in Figure 5-50. The surface degradation

phenomenon is shown in Figure 5-49 using images which were taken at various stages of

degradation. The images shown in Figure 5-50 summarize the stages of the degradation mechanism.
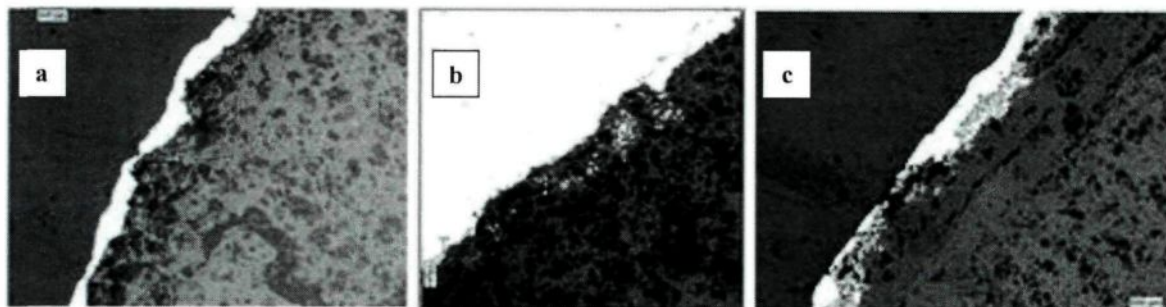
Figure 5-49: Dynamic Experiments using Alcoa T64 Type-5mm Particle Alumina with 5%Mg-Al Alloy After (a) 1st Day, (b) 2nd Days, (c)3rd Days at 715°C

Figure 5-49 shows Alcoa T64 alumina particle/5%Mg-Al alloy interface images taken from a set of dynamic experiments (1.8mm/s liquid aluminum flow around particles) at various contact times (1, 2, and 3 days). It is obvious that the magnesium diffusion through alumina particle causes a discoloured region at the interface at first. Aluminum and Mg-spinel formation in the interior of the particle starts the second day, and the extent of degradation on the alumina particle surface increases as shown in Figure 5-49.c. The thickness of this reaction zone may change depending on the magnesium content, temperature, impurities in alumina, etc. This thickness is not the affected zone thickness mentioned in the previous sections. This is showing the thickness of the zone where reaction is occurring at the interface. The affected zone covers a larger area where the magnesium diffusion is visible as a greyish/black hue.

The depletion of Na from beta-alumina due to Mg diffusion through the particle causes cavity/void formations as discussed in Section 5.4.4.2.1. Localized surface

degradation also starts with the magnesium diffusion as shown in Figure 5-50.a and 5-50.b. Further magnesium diffusion into these areas promotes $MgAl_2O_4$ and liquid Al formation and/or aluminum infiltration through pores and cavities as shown in Figures 5-50.c and 5-50.d. This is followed by further aluminum infiltration into these reaction zones. This increases the extent of surface degradation as shown in Figure 5-50.e and 5-50.f. Under flow conditions, the liquid aluminum washes out the degraded areas and leaves a big cavity on the particle surface. This phenomenon likely causes inclusion generation in liquid aluminum with time. In some cases, the degradation occurs even underneath the particle surface as shown in Figure A4-15 in Appendix 4.
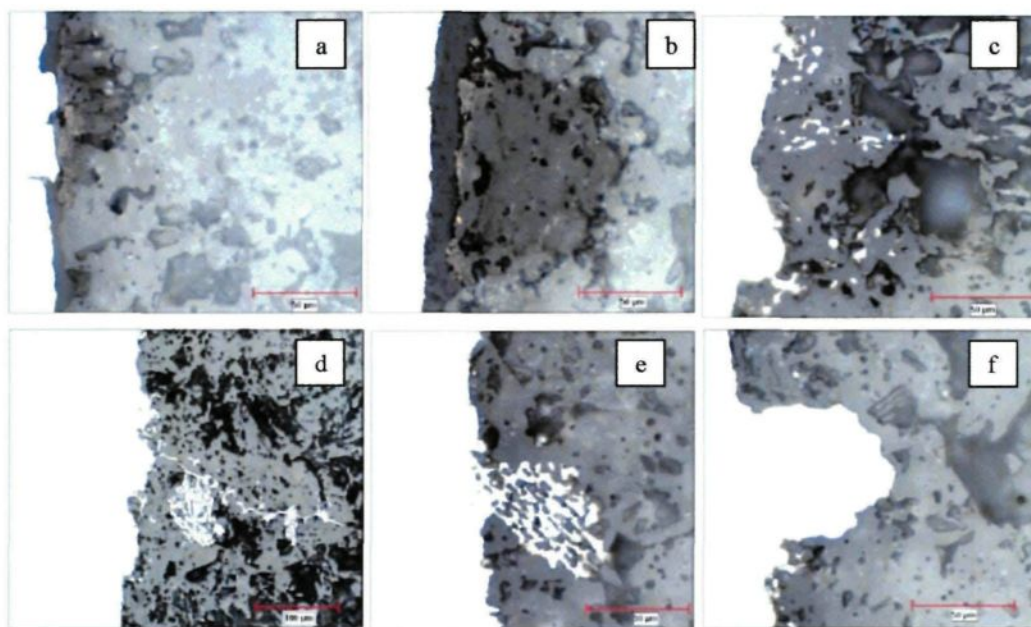

Figure 5-50: Stages of Localized Alumina Surface Degradation (a) Initiation of Degradation, (b) Magnesium Diffusion Through Particle, (c) Initiation of Aluminum Infiltration, (d), (e) and (f) Increased Aluminum Infiltration and Accelerated Degradation (Dynamic Experiments -Alcoa T64 Type-5mm Particle with 5%Mg-Al Alloy at 715°C)

There is no doubt that the degradation in alumina structure can affect the filtration process negatively depending on the percentage of eroded alumina particles in the filter. In this study, most of the degradations were found in localized areas in 10-20 % of the particles.

Experimental study observations showed that the extent of degradation may vary depending on the contact time, the magnesium content in liquid aluminum, the area of Na rich alumina zone, the liquid metal velocity around the particle, and the open porosity level of the structure.

5.4.4.2.4 Surface Reactions at Alpha-Alumina/Aluminum Alloy Interface

The other surface reaction observed in this study is an oxide film formation in the vicinity of the aluminum/alumina interface as shown in Figure 5-51. This formation took place regardless of the magnesium content in liquid aluminum, but the thickness of the oxide film and its integrity/strength seemed to be affected by the magnesium content.

-7%Mg-Al Alloy
-715 °C
-72-hour contact time
-Alcoa T64

(a)

40 μm

-5%Mg-Al Alloy
-715 °C
-24-hour contact time
-Alcoa T64

(b)

40 μm

-2%Mg-Al Alloy
-715 °C
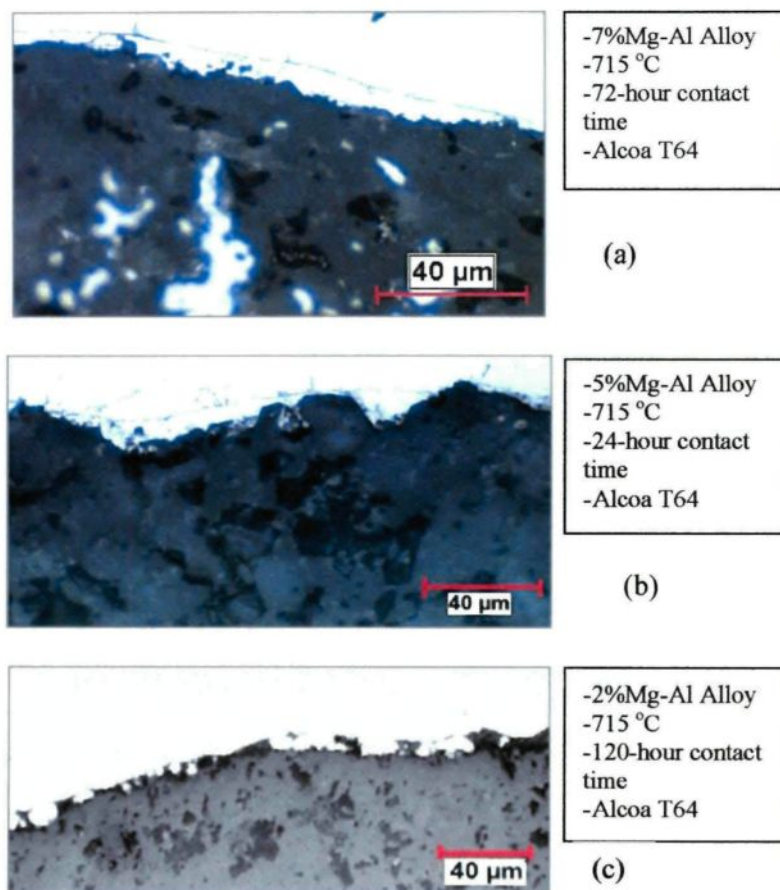-120-hour contact time
-Alcoa T64

40 μm   (c)

Figure 5-51: Oxide Film Formation with (a) 7%Mg, (b) 5%Mg, and (c) 2% Mg-Al Alloy
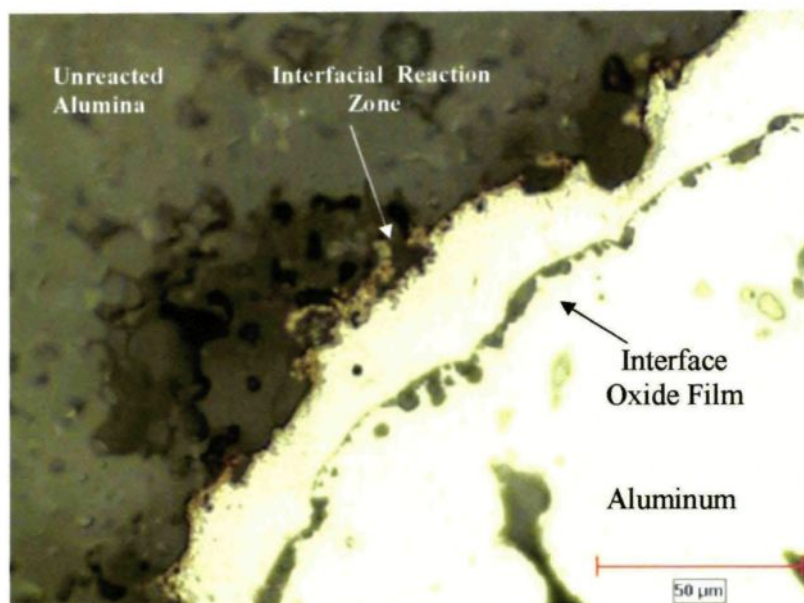
Figure 5-52: Surface Reaction and Oxide Film Formation at Alumina/7%Mg-Al Alloy Interface Alcoa T64

The oxide film looked like a chain made of tiny oxide beads when higher magnesium content alloys were used as shown in Figures 5-52, 5-53, and 5-54. The EDX and SEM analyses shown in Figures 5-53 and 5-54 indicated that these oxide beads are tiny grains of Al_2O_3 at the early stages of the experiment. Magnesium in aluminum alloy converted these tiny Al_2O_3 grains into $MgAl_2O_4$ with time. Figure 5-54.c shows both partially and fully converted fine grains from Al_2O_3 to $MgAl_2O_4$ in the oxide film.

It appears that the first interaction of liquid aluminum alloy with the powder-like fine grains of alumina which exist on the alumina surface creates the oxide film. In micro scale, liquid aluminum also supposedly has a very thin oxide layer on the surface due to the presence of oxygen in the semi-controlled environment. When liquid aluminum first gets in contact with the alumina surface, which is covered with micron size powder-like alumina

grains, a very thin layer of oxide film wraps the alumina surface. The reaction of liquid aluminum and these powder-like alumina grains may result in the oxide film formation which covers the alumina surface like a semi-transparent blanket.
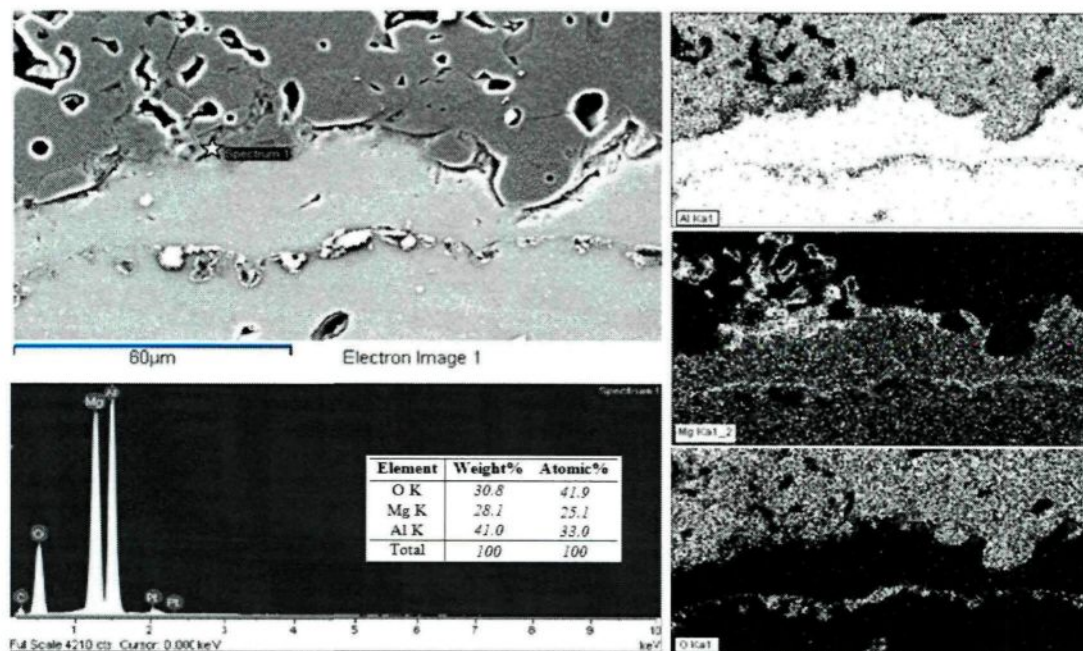

Figure 5-53: Surface Reaction and Oxide Film Formation at Alumina Alcoa T64/7%Mg-Al Alloy Interface (120-hour Contact Time)
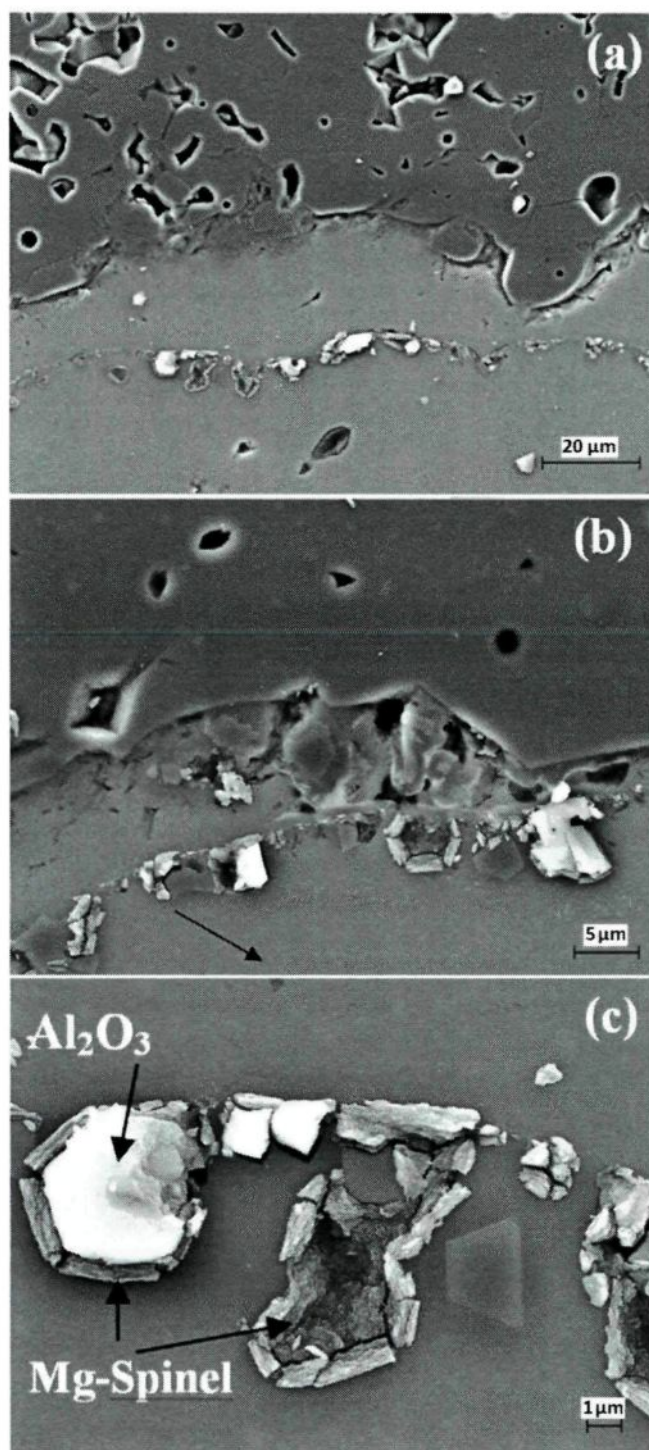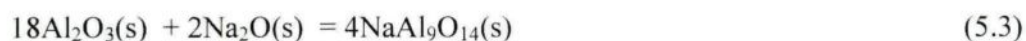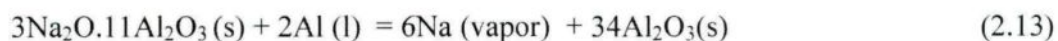
Figure 5-54: SEM Images of the Oxide Film at the Alumina T64/Aluminum Interface at Various Magnifications (7%Mg-Al, at 715°C)

Another hypothesis for oxide film formation was found in the literature [70], which claims that the following reactions shown in Equation 2.12 and 2.13 take place at the molten metal and refractory interface, and the result is the oxide film formation. Na enters molten aluminum from both refractories and cryolite during electrolysis. Partly dissolved sodium in aluminum metal increases the chemical activity of the melt. It is easily oxidized by air. It contacts aluminum oxide present on the surface of the melt and forms beta-alumina. Beta-alumina formation equation in Equation 5.3, obtained with FACT SAGE (Facility for the Analysis of Chemical Thermodynamics) Thermodynamic Analysis Software is slightly different than the one shown in Equations 2.12 and 2.13. Yurkov [70] claims that this oxide layer exists as a thin film on the metal surface. It covers the refractory surface upon metal's contacts with it. Further interaction of beta-alumina in the thin film with molten aluminum results in formation of porous Al_2O_3 film (Equation 2.13). However, Yurkov [70] does not support Equation 2.13 with the thermodynamic data which seem to have a positive ΔG° value at 1000 K. Thermodynamic data is shown in Section 5.5.

$$11Al_2O_3(s) \ + \ Na_2O\,(s) = \ Na_2O.\,11Al_2O_3\,(s) \tag{2.12}$$

$$3Na_2O.11Al_2O_3\,(s) + 2Al\,(l) = 6Na\,(vapor) + 34Al_2O_3(s) \tag{2.13}$$

$$18Al_2O_3(s) + 2Na_2O(s) = 4NaAl_9O_{14}(s) \tag{5.3}$$

Oxide film is an important observation, but it should be noted that the oxide film was not found on every alumina tested in this study. Some particles were partially covered and some did not have any oxide film at all. This observation indicates that the

integrity/strength of the oxide film might be the function of Mg content of the melt (which determines the thickness and the type of oxide film on liquid the aluminum surface), surface conditions of alumina, thickness of oxide film, and more importantly the liquid metal flow conditions around alumina particles. This statement is supported by the experimental results. More frequent oxide film formation was observed on samples during static experiments and on the bottom side of the samples in dynamic experiments where the liquid metal flow cannot reach easily. Based on the experimental results, both the largest affected zone and oxide film thickness values were observed with 7 wt% Mg alloys. This means that the integrity/strength of oxide film weakens or becomes more permeable with increasing oxide film thickness.

The extent of aluminum/alumina interaction is correlated with the consistency of oxide film which may act like a barrier for magnesium diffusion through particle. This phenomenon may explain why some alumina particles showed a limited affected zone thickness or color change (magnesium diffusion through it) even after the 7-day dynamic experiments. The EDX analysis results conducted on surface reaction sites at the aluminum/alumina interface indicated the presence of ~25 at.% magnesium as shown in Figure 5-55. The mapping study clearly showed that the magnesium is very rich at the interface, but its diffusion to the interior of the particle is limited.

SEM images shown in Figure 5-56 were taken from an alumina sample after 72-hour contact time during the dynamic experiments with 5 wt% Mg-Al alloy. The aluminum skin on the alumina sample was partially peeled off, and the top of the alumina, and bottom of the aluminum skin surfaces were investigated using SEM and XPS. The SEM analysis

showed the presence of discrete Mg-spinel crystals at the alumina/aluminum interface. The XPS analysis results shown in Appendix 4 (Figure A4-16 and A4-17) conducted on similar samples confirmed that the reaction product is Mg-spinel.
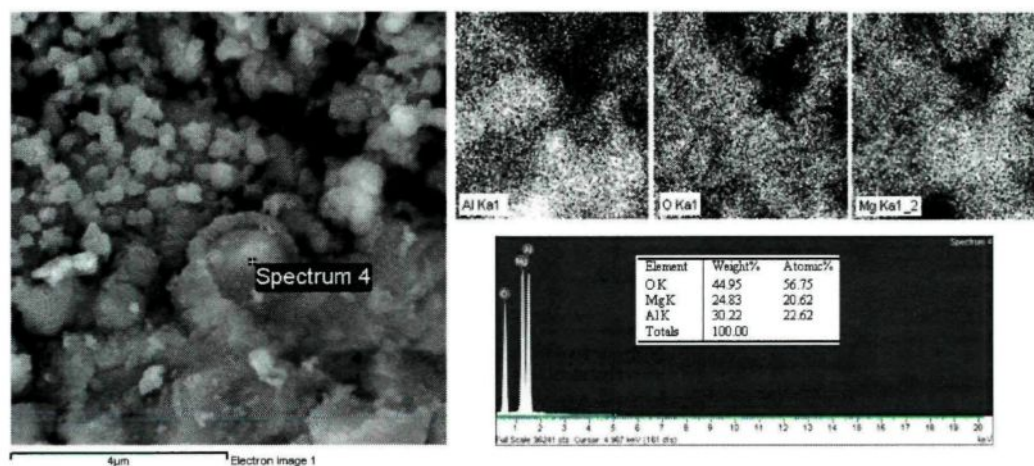
Figure 5-55: Mg-spinel Crystals on Peeled Surface of Naigai Alumina (Static Experiment Using 7%Mg-Al Alloy, 3 Day of Contact Time, at 715°C)
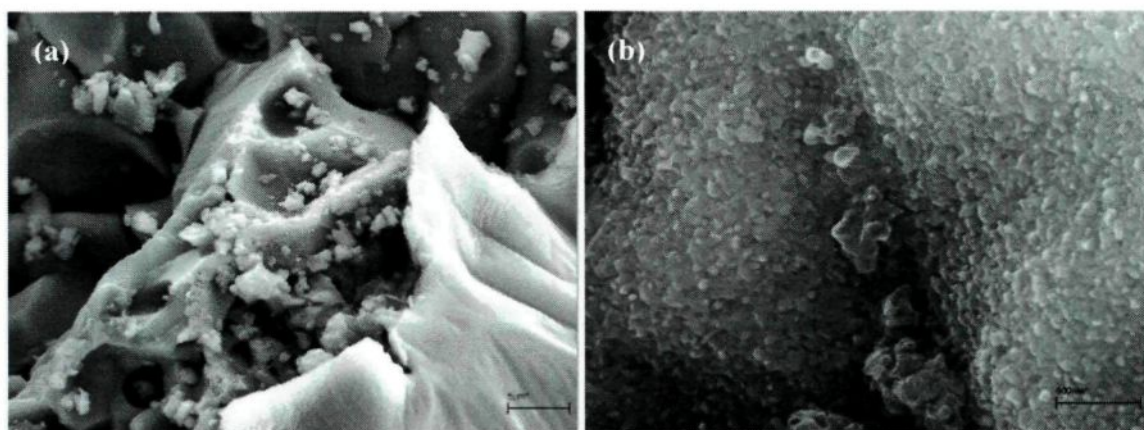

Figure 5-56: Mg-Spinel Crystals on Peeled off (a) Aluchem Surface after 3 Day Experiment with 5%Mg-Al Alloy (b) Bottom Part of Aluminum Skin

A peeled-off sample from the surface of alumina which was in contact with 7%Mg-aluminum alloy during a static experiment (Figure 5-55) was investigated, and typical Mg-

spinel crystals were found on the alumina surface. The formation of these crystals seems to occur when Mg-Al alloy contacts with the above alumina powder-like particles and alpha-alumina. Conversion of small alumina powders into $MgAl_2O_4$ crystals is expected to take place much faster than the reaction taking place between alpha-alumina and aluminum alloy because of its higher specific surface area. The appearance of this interfacial reaction can be seen from the cross-sectional view as a yellowish layer at the particle/aluminum interface in Figure 5-57 (on another sample which was tested using 2%Mg-Al alloy for 7 days).
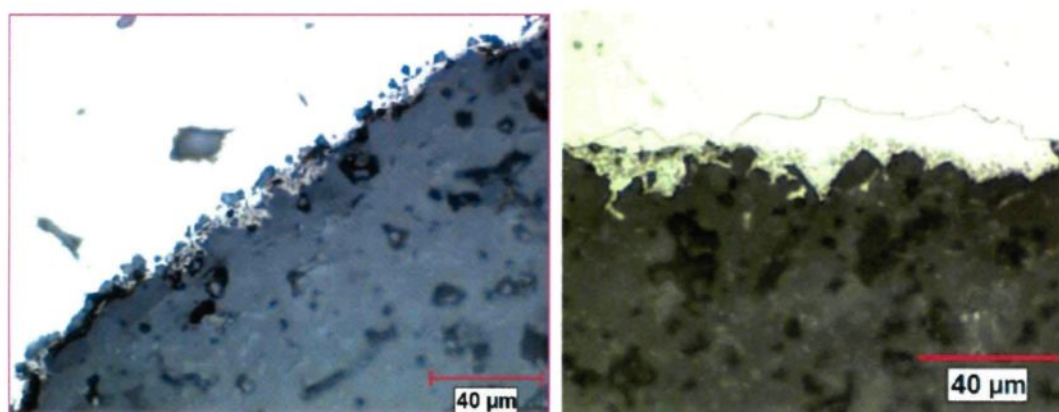
Figure 5-57: Interface Reactions using 2%Mg-Al alloy at 715°C (a) Alcoa T64-7day Dynamic Experiment, (b) Naigai-2day Dynamic Experiment

The oxide film and the discrete Mg-spinel crystal formation observations are in line with the results of Jin et al.'s [31] MMC study except with one difference. This study was conducted under conditions similar to the current one. In Jin et al.'s study, Mg-spinel formation observations was strongly correlated with the magnesium content in aluminum alloy. They claim that the formation of Mg-spinel crystals is favorable when the

magnesium concentration is less than 3% in liquid aluminum, and the Mg-spinel crystal formation was almost non-existant or negligible when 7%Mg-Al alloy was used. However, in this study, the magnesium spinel and oxide film formations were observed regardless of the magnesium content and the alumina type. Only their extent was different.

Optical microscope, SEM, and XPS investigations conducted on other samples can be found in Appendix 4 in Figures from A4-18 to A4.24.

5.4.4.3   Metallographic Examination of Actual Deep Bed Filter Samples

Industrial deep bed filter media samples were also investigated in order to compare the results with those of the current study. The media used in the deep bed filter was provided by Rio Tinto Alcan Laterrier Plant. The operating conditions of the filter were as follows:

- 3-6 mm Alcoa T64 type alumina particles were used in the filter.
- The filter was in use for 7 days semi-continuously.
- Various aluminum alloys were filtered during its life.
- Operation temperature was kept between $690^{\circ}C$ and $715^{\circ}C$.
- CO_2 gas was used to prevent oxidation of aluminum alloys continuously.
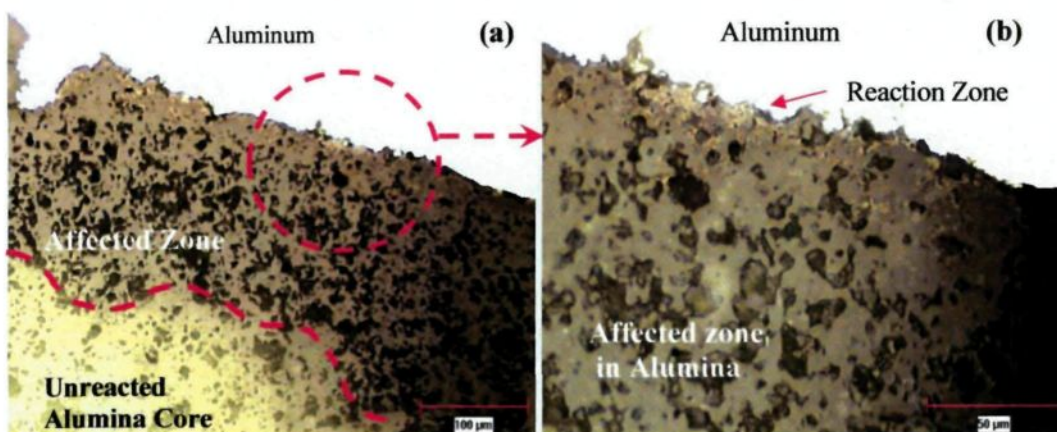
Figure 5-58: Appearance of Industrial Filter Media (Alumina)/Aluminum Interface

Metallographic investigation results of the filter media were found to be very similar to those of the experiments conducted in the laboratory. The appearance of an alumina/aluminum interface on typical industrial filter media is shown in Figure 5-58. The affected zone thickness of the actual media seemed to be between 50 to 100 microns which aligns well with the experimental results found for Alcoa T64 alumina (~60 micron) with 5%Mg-Al alloy, 7-day experiments under flow conditions in the current study as shown in Figure 5-16.

Aluminum/alumina interface on the actual filter media was also analyzed using SEM-EDX. In Figure 5-59, the morphology of the phase observed at the interface seemed to be Mg-spinel discrete crystals. Magnesium content at reaction zones were changing from 7 to 12 at.% on this sample which also matches with the experimental results discussed previously (Table 5-15 and Table 5-16). A SEM line scan was conducted on ABF industrial filter media alumina/aluminum interface as shown in Figure 5-60 This analysis showed that

magnesium concentration peaks at the interface. Na also exists in the alumina used as filter media in the industrial filter.
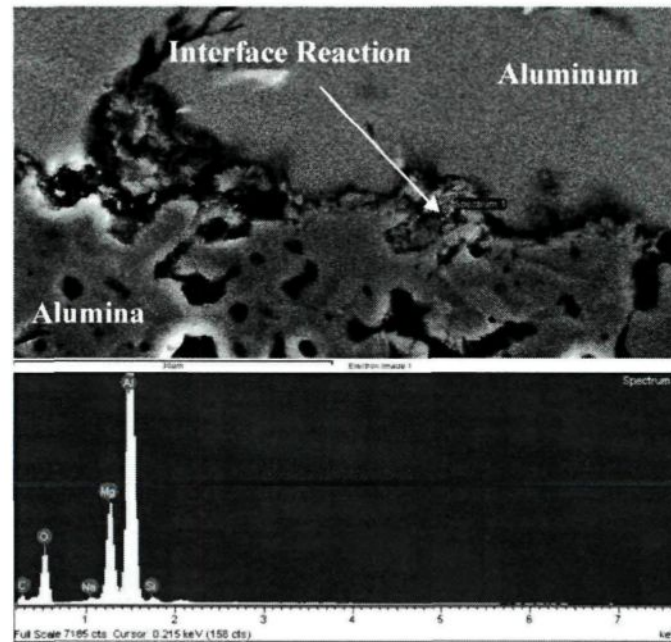

Figure 5-59: EDX Analysis of Interface Reaction Zone on Actual Filter Media
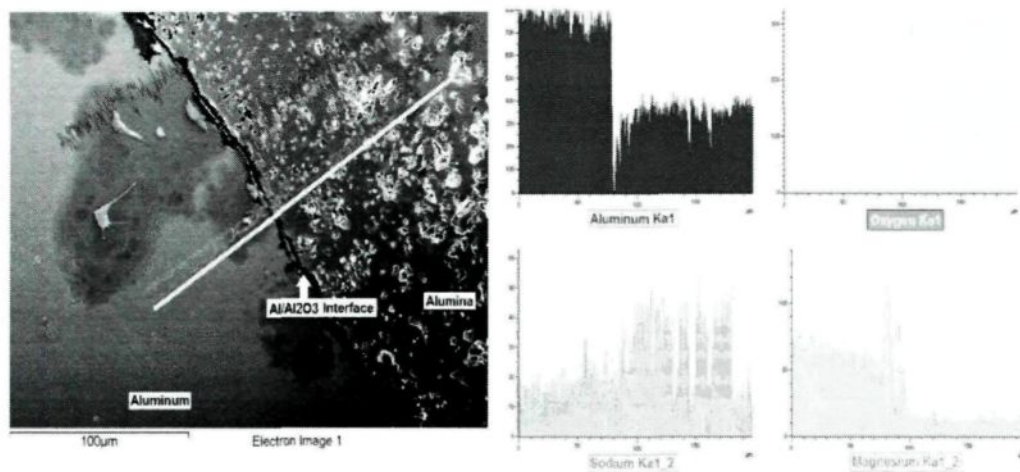
Figure 5-60: SEM Line Scan Investigation Conducted on Alumina Used in Industrial Filter

The type of reactions found on actual filter media was very similar to the ones detected in the current experimental study as well. The surface reactions at the alumina/aluminum interface (presence of discrete Mg-spinel crystals), magnesium diffusion through pores and inter-granular reactions/degradations, internal Mg-spinel formation and aluminum metal generation in Na-rich zones (beta-alumina) in alumina, and the presence of oxide film formation at the interface were the common observations which were also found from the investigations carried out on the samples of the current study (Figure 5-61).

Figure 5-61: Appearance of (a), (b) and (c) Affected and Reaction Zone, (d) Localized Oxide Film at the Alumina/Aluminum Interface on Actual Filter Media

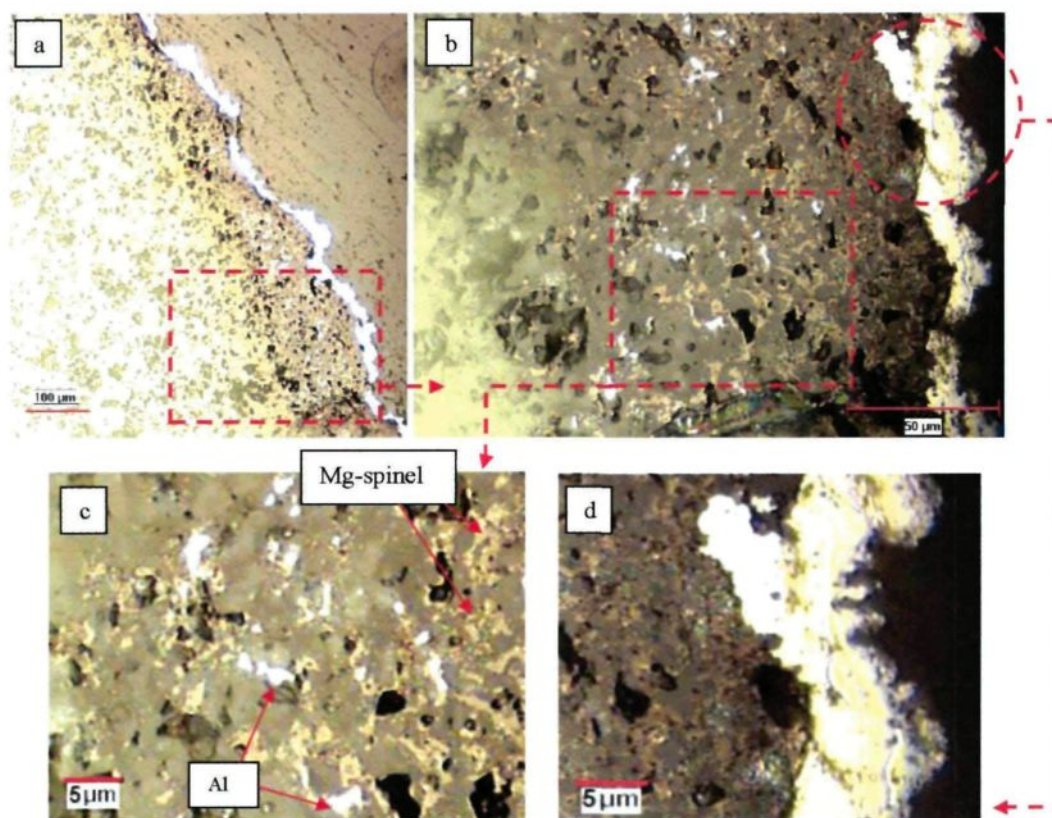### 5.4.5   Metallographic Examinations of Laboratory-Made Tablets

The experiments with laboratory-made alumina tablets are summarized in the two parts. Alumina tablets with and without impurities such as Na_2O, SiO_2, and MgO were tested to determine the effect of impurity levels on the affected zone thickness, and the results were presented in Section 5.3.10.   In this section, the results of metallographic examinations are presented.

5.4.5.1   Metallographic Examinations of Laboratory-Made Tablets used to Study the Effect of Impurities on the Affected Zone Thickness

The appearance of reference alumina tablets (Alcoa T64 with no impurities) during the dynamic experiments (1.8mm/s) with liquid aluminum alloy at various contact times is shown in Figure 5-62. The thickness of the reaction zone at the tablet surface (from intersection as shown in Figure 5-63) was much higher compared to that of the reaction zone observed on commercial particles. As it was mentioned previously, the tablets tested in these experiments had ~15% apparent porosity because of the lower sintering temperature of approximately $1600^{\circ}C$ compared to the commercial tabular alumina sintering temperature which is slightly lower than the tabular alumina melting point of ~$2000^{\circ}C$. Higher sintering temperature generally provides coarser tabular alumina grains, denser structure, and lower porosity. Laboratory-made tablets were manufactured using 20-µm size tabular alumina powder. Because the actual tablet sintering temperature was relatively lower, it did not seem to have a huge impact on the final grain size of the alumina tablets. This means that the grain size of alumina tablets is nearly equal to the size of

alumina powder particles or slightly coarser. These grains were bound to each other with the solidification of binder PVA at elevated temperature. The diffusion of magnesium through the pores of the laboratory-made tablets was found to be much faster compared to those of the commercial alumina granules. This is attributed to the higher apparent porosity (~15% open porosity) and lower grain size of tablets (~20μm, which is roughly equal to the alumina powder size used to make these tablets). The easy access of magnesium from surface to tablet core increased the conversion rate of alumina grains and the impurities found among these grains into Mg-spinel crystals. The reaction product was found to be Mg-spinel for all cases as shown in Figure 5-64 regardless of the impurity type mentioned in Chapter 3 (Table 3-9). The appearance of tablets containing various types of impurity after contact with molten alloy is shown in Figure 5-65.
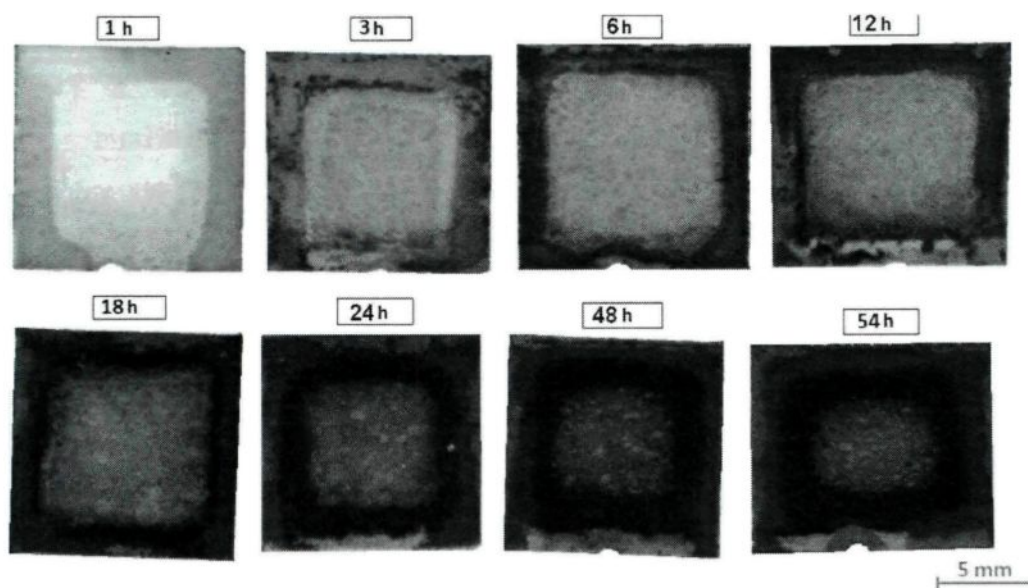
Figure 5-62: Magnesium Diffusion Through Pores of Tablets Made From Reference Alumina (Alcoa T64, 5%Mg-Al Alloy- Dynamic Experiment with 1.8mm/s Velocity and Temperature of 715°C)

Figure 5-63: Appearance of Reaction Zone on Reference Alumina Tablets with 5%Mg-Al Alloy After 36-hour Contact Time

MgAl₂O₄ crystals (gray discrete areas)

Al₂O₃ grains (white particles)

Element	Atomic%
O K	69.13
Mg K	12.86
Al K	17.73
Si K	0.28
Totals	

Figure 5-64: SEM Analysis Made on Reaction Zone of Sample Shown in Figure 5.63.

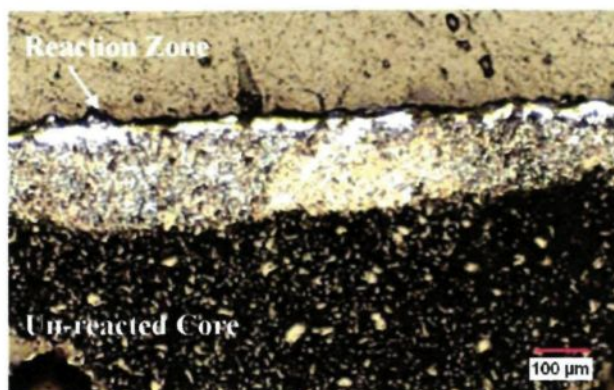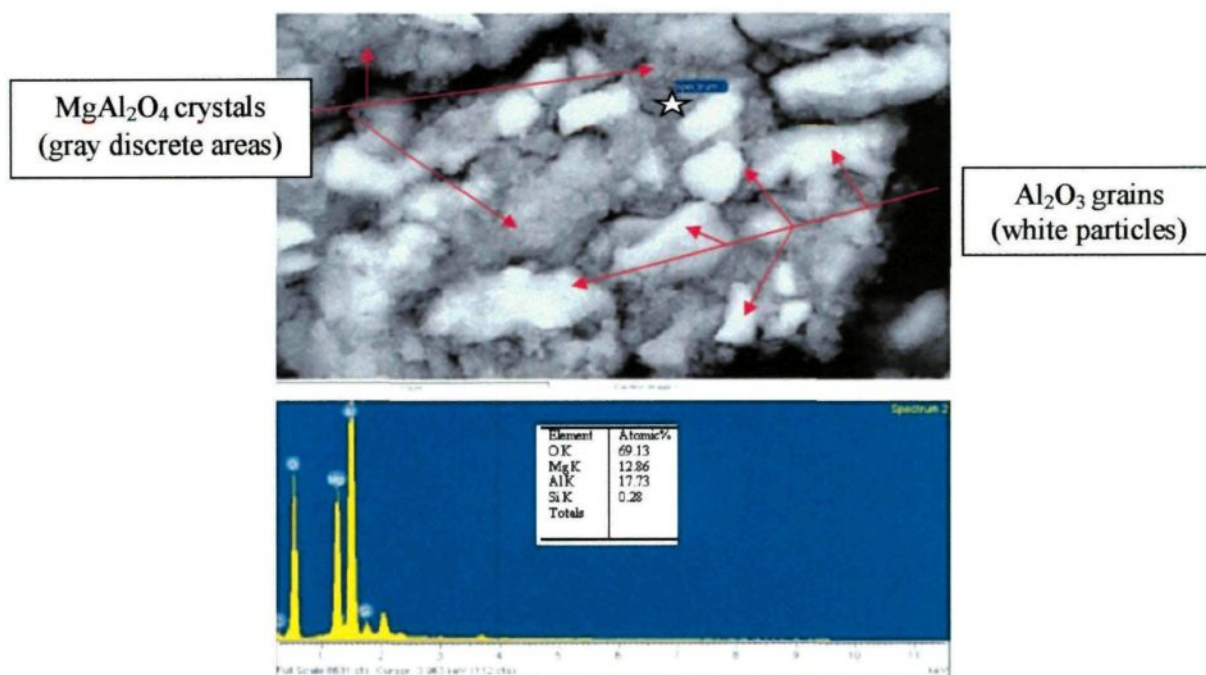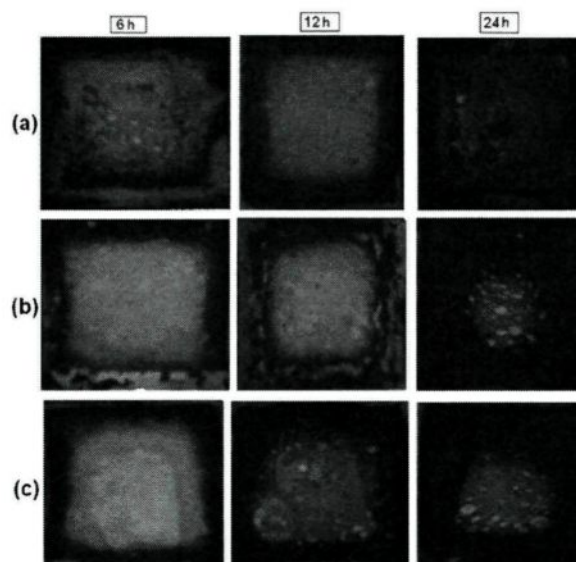Figure 5-65: Magnesium Diffusion Through Pores of an Alumina Tablet with (a)High Soda-0.33% Na$_2$O, (b)High Silica-0.64%SiO$_2$, (c)High Magnesia-0.53% MgO (5%Mg-Al alloy, Dynamic Experiment with 1.8mm/s Velocity, 715°C)

5.4.5.2 Metallographic Examinations of Laboratory-Made Tablets Used in the Study of Inclusions

In the second part, interactions between aluminum tablets made using Alcoa T64 type alumina in the laboratory and possible inclusion sources such as MgO, MgAl$_2$O$_4$ were examined using 5%Mg-Al alloy at 715°C under flow conditions (1.8mm/s).

The Mg-spinel/alumina-tablet/aluminum triple interaction point was investigated using SEM mapping technique and the results are presented in Figure 5-66. This sample was subjected to 5%Mg-Al liquid metal flow for 72 hours at 715°C (The procedure for the preparation of inclusion sources for the experiments was explained in Section 3.2.6 of Chapter 3). EDX point analysis of spinel source can be found in Figure A4-24 in Appendix4.
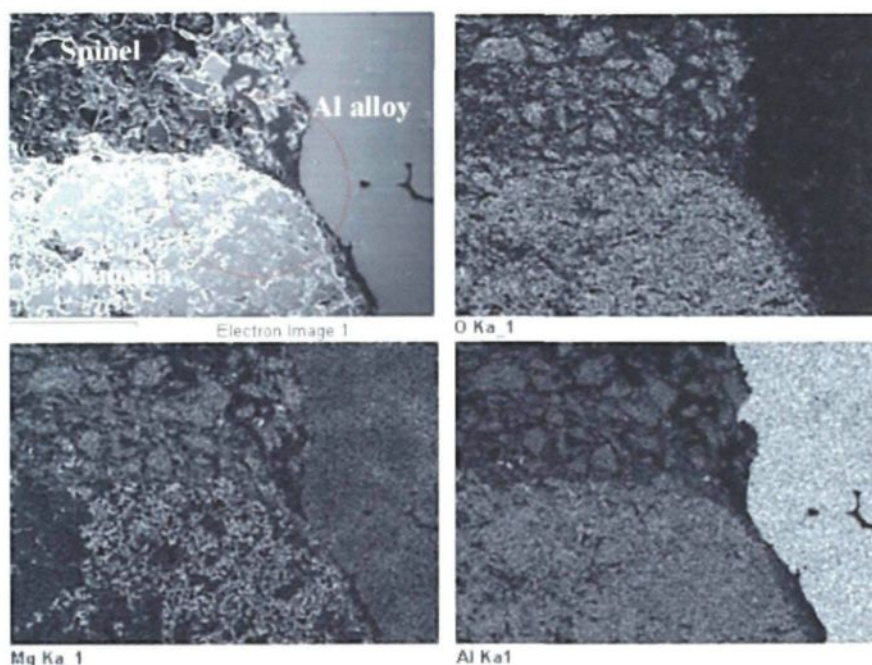
Figure 5-66: Alumina/Aluminum Alloy/MgAl$_2$O$_4$ Triple Point Interaction Zone (72-hour Contact Time, 715°C, Dynamic Experiment- 1.80 m/s)

The mapping study presented in Figure 5-66 shows that an inclusion source does not seem to have any structural change at the triple interaction point. However, the alumina structure looks very rich in magnesium. It appears that alumina was affected by the magnesium diffusion from aluminum alloy. Another mapping study conducted at higher magnifications in the magnesium rich zone of alumina (Figure 5-67) indicates the presence of Mg-spinel and aluminum metal in the reaction zone (similar observations as discussed in 5.4.4.2.2 for commercial alumina). The areas shown with arrows in the images in Figure 5-67 indicate the locations where aluminum metal was found (high Al and Mg concentrations, but no oxygen).
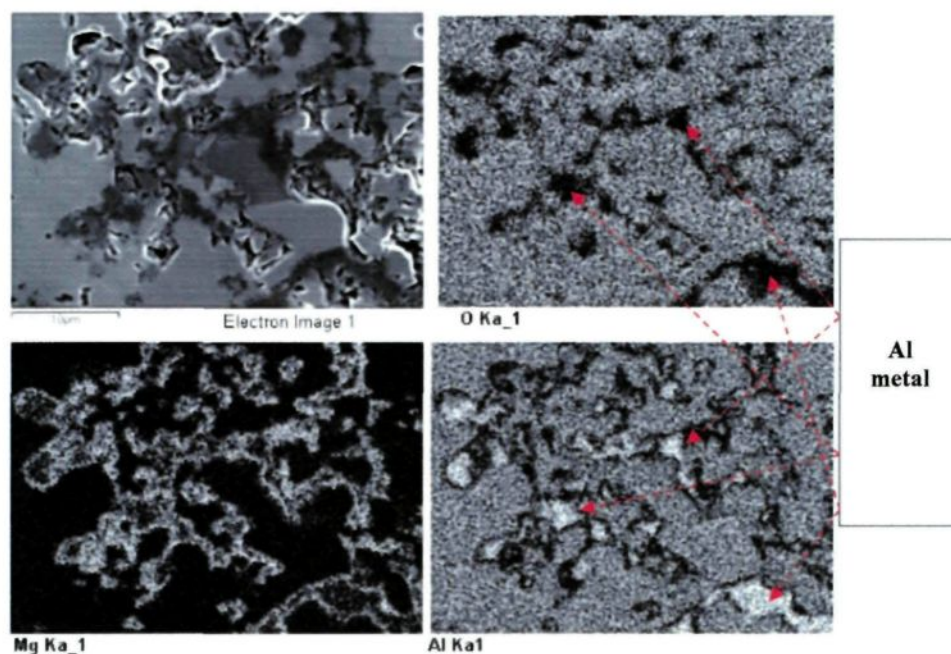
Figure 5-67: Alumina at the Triple Point Interaction Zone (Circled Area in Figure 5-68) (72-hour Contact Time-715°C- Dynamic Experiment with 1.8mm/s)

It was not possible to complete a number of experiments using samples embedded with Mg-spinel powder because the inclusion source placed in a little hole on the alumina tablets were washed away under flow conditions and nothing was left behind on the alumina sample to examine at the end of the experiments. These kinds of experiments definitely require an inclusion source which has higher resistance to drop under flow condition.

In Figure 5-68, one result of MgO inclusion source/Al_2O_3/5%Mg-Al alloy interaction study is shown. The experiment was carried out at 715°C, and the contact time with alloy was 72 hours. Figures 5-68.a and 5-68.b show that the MgO ball had high apparent porosity which facilitated the aluminum metal infiltration through it especially

from the top part where it was subjected to liquid aluminum flow. Liquid aluminum infiltrated between the inclusion source and the alumina as well. EDX analysis shown in Figure 5-69 was conducted on the top part of MgO where aluminum infiltration occurred. This analysis identifies clearly that MgO stays stable and when it is in contact with aluminum alloy. The bottom portion of MgO which stayed in alumina tablet (no fluid flow condition) was not affected as much as the top portion.

The zone shown in dashed lines in Figure 5-68.b is the triple contact point for MgO, Al_2O_3, and aluminum alloy. At this point, a thin oxide film formation was observed. $MgAl_2O_4$ formation shown in Figure 5-68.c was observed at the corner of the alumina.

MgO/alumina interface was investigated using the SEM mapping technique, and the results are shown in Figure 5-70. No magnesium diffusion through alumina from MgO side was observed in this analysis. It is obvious that the two solid phases do not react spontaneously at these temperatures.
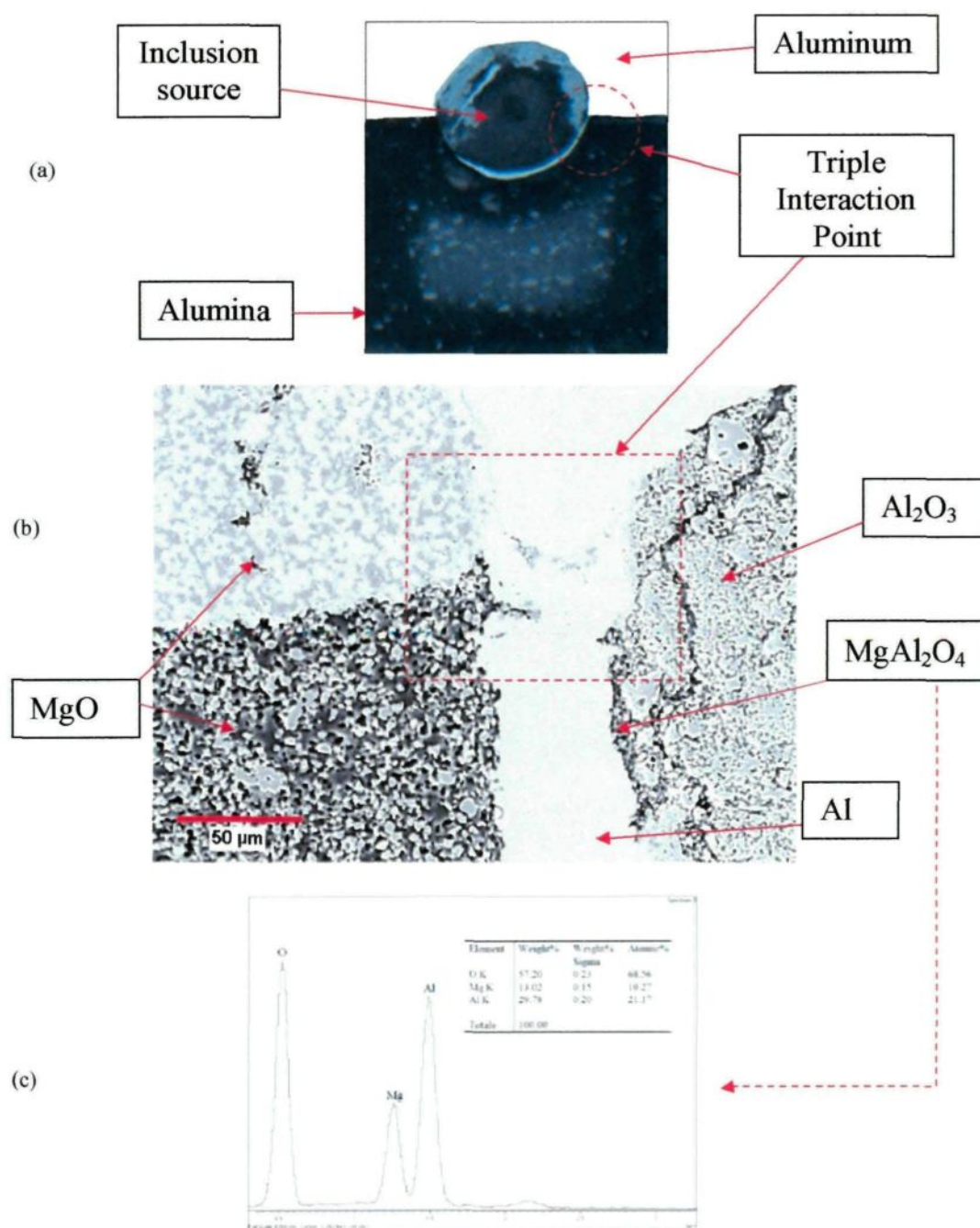
Figure 5-68: Investigation of MgO, Al$_2$O$_3$, and Aluminum Alloy Interactions (a) Appearance of Sample After Experiment, (b) SEM Image of Triple Interaction Point, (c) EDX Analysis Result of MgAl$_2$O$_4$.
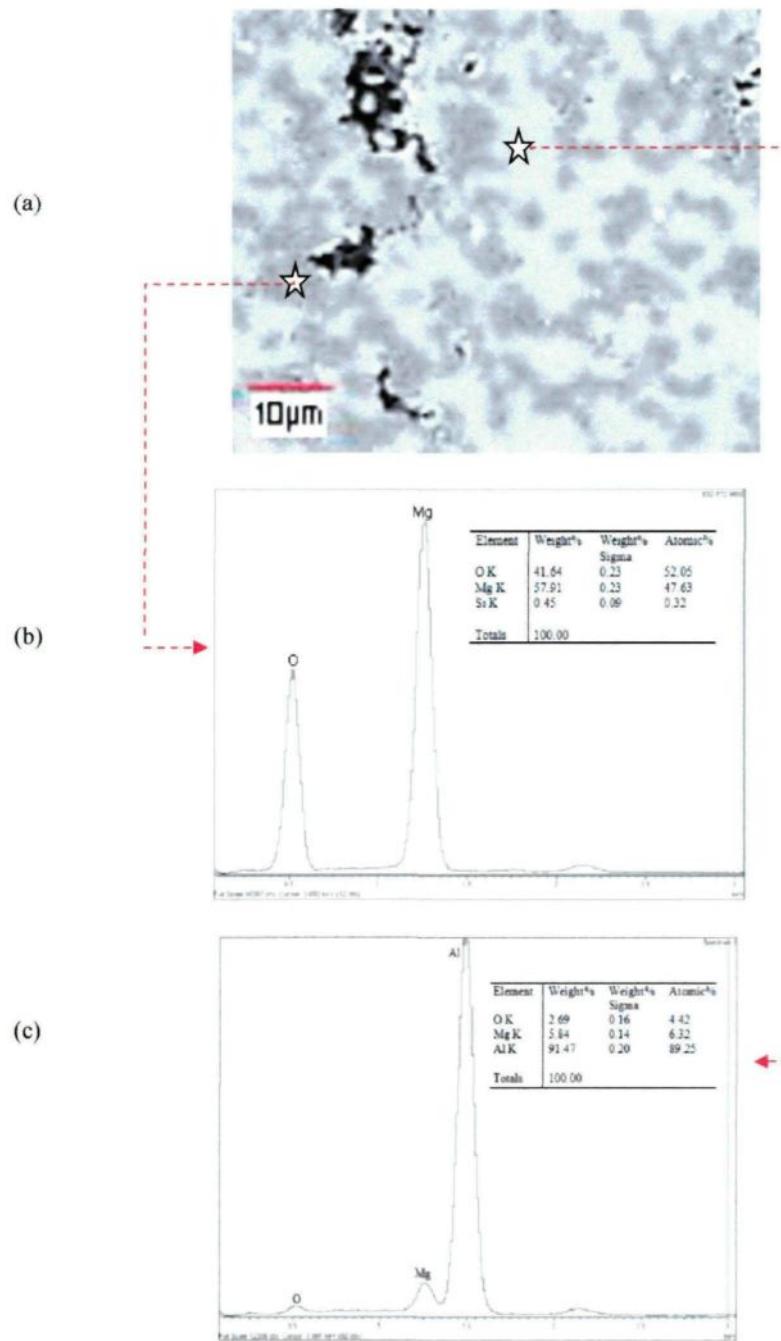
Figure 5-69: (a) SEM Image of Aluminum Infiltrated Part of MgO Shown Figure 5-68, EDX Analysis Result of (b) Dark Phase-MgO, (b) Aluminum Metal Found in Between Dark Phases.

198
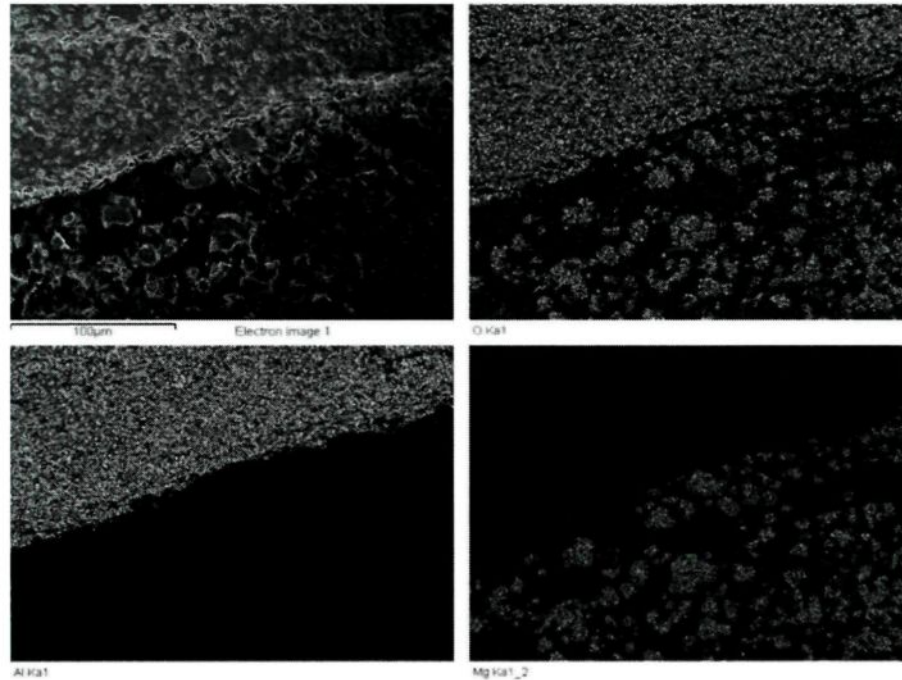
Figure 5-70: Alumina/MgO Interface -Circled Area in Figure 5-68.a (48-hour Contact Time, 715°C, Dynamic Experiment with 1.8mm/s)

5.5   Thermodynamic Considerations

The SEM-EDX analysis results obtained in this study, indicated that reaction product was Mg-spinel and aluminum. A thermodynamic analysis was conducted to determine the possible reactions for magnesium spinel formation. Standard Gibbs free energies of possible reactions are summarized in Table 5-18 [9, 41, 52, 70, 71, 99, 100, 104].

Table 5-18: Standard Gibbs Free Energies of Possible Reactions AT 1000 °K

Reactions	ΔG°_{1000K} [kJ]		Eq. No
	Literature [9, 41, 52, 70, 71]	FACTSAGE [100]	
$2/7NaAl_9O_{14}(s) + Mg(g) = MgAl_2O_4 + 4/7Al(l) + 2/7Na(g)$	-	-89	5.1
$1/14NaAl_9O_{14}(s) + Mg(g) = MgO + 9/14Al(l) + 1/14Na(g)$	-	-82	5.2
$Na_2O(s) + 9Al_2O_3(s) = 2 NaAl_9O_{14}(s)$	-	-253	5.3
$Mg(g) + Na_2O(s) = 2Na(g) + MgO(s)$	-205	-219	5.4
$2/3Al(l) + Na_2O(s) = 2Na(g) + 1/3Al_2O_3(s)$	-96	-144	5.5
$\frac{1}{2} SiO_2(s) + 2/3Al(l) = 1/3 Al_2O_3(s) + 1/2 Si (l)$	-88	-88	5.6
$Mg (l) + 2Al (l) + 2 O_2(g) = MgAl_2O_4 (s)$	-1,898	-1,884	2.3
$Mg (l) + 4/3 Al_2O_3 (s) = MgAl_2O_4 (s) + 2/3 Al (l)$	-88	-104	2.4
$MgO (s) + Al_2O_3 (s) = MgAl_2O_4 (s)$	-47	-29	2.5
$Mg (l) + 1/3Al_2O_3 (s) = MgO (s) + 2/3 Al (l)$	-39	-39	2.6
$2Al (l) + 3/2 O_2(g) = Al_2O_3 (s)$	-1,357	-1,361	2.7
$Mg (l) + \frac{1}{2} O_2 (g) = MgO (s)$	-496	-528	2.8
$\frac{1}{2} SiO_2(s) + Mg(l) = MgO(s) + 1/2 Si (l)$	-128	-128	2.9
$Mg(l) + 2Al(l) + 2SiO_2 = MgAl_2O_4 (s) + 2Si (l)$	-	-384	2.10
$Na_2O (s) + 11Al_2O_3 (s) = Na_2O.11Al_2O_3(s)$	-211	-	2.12
$3Na_2O.11Al_2O_3(s) + 2Al(l) = 6Na(l) + 34Al_2O_3(s)$	344	-	2.13

5.5.1 Reactions between α-Al₂O₃ and Mg-Al Alloy

The reaction shown in Equation 2.4 has the lowest Gibbs free energy value for Mg-Al alloy and alpha-alumina interaction in the absence oxygen in gaseous form. This indicates that Mg-spinel formation (Equation 2.4) has higher possibility compared to that of MgO formation (Equation 2.6). The Mg-spinel can also form via Equation 2.5; however, ΔG of this reaction is less negative compared to those of Equations 2.4 and 2.6. In addition, this reaction takes place between solid state substances; therefore, its kinetics is slow. The

stoichiometric at.% of Mg is ~50% for MgO whereas it is ~15% for Mg-spinel (Table 5-14). The experimental results show that the Mg at.% values in EDX analyses conducted at the reaction zone were 5-25 at.% in almost all samples of this study, which indicates that Mg-spinel is the dominant reaction product. Equation 2.4 seems to be the most probable reaction for the Mg-spinel formation, which is supported by the thermodynamic data.

5.5.2 Reactions between Mg-Al Alloy and Impurities in Alumina

The possible reactions taking place between Na-rich alumina phase (beta-alumina) and Mg-Al alloy was discussed in the Sections 5.4.4.1 and 5.4.4.2. The reaction shown in Equation 5.1 was suggested as the reaction most likely to happen in these discussions. According to the thermodynamic data shown in Table 5-18, it seems possible that the Na-rich alumina phase can be reduced by magnesium vapour.

Experimental study showed that, unlike the reactions taking place between Mg-Al alloys and alpha alumina, the reaction between Mg-Al alloys and beta-alumina seems to be quite spontaneous. The formation of MgO in the presence of Na_2O is thermodynamically possible as shown in Table 5.18 (Equation 5.4). Even in the shortest duration experiments, a reaction in beta-alumina was obvious. This might be due to the presence of Na_2O in the beta alumina structure, and the diffusion of Mg vapour. Magnesium has a high vapour pressure value at the temperatures experiments were conducted. As soon as magnesium diffuses into alumina, an interaction between aluminum and alumina is established since the affinity of magnesium to oxygen is higher than that of sodium as shown in Equation 5.4.

Considering the reactions taking place between Mg-Al alloy and SiO_2, which can be present as an impurity in alumina, Equation 2.9 is more favorable compared to Equation 5.6 as can be seen from their ΔG of reactions. MgO formation was not detected as a reaction product in the experiments. This was possibly due to the small quantity and size of the impurities, and the high apparent porosity level of alumina tablets which makes it hard to detect and distinguish these impurities from alumina matrix. On the other hand, in the presence of Mg in liquid alloy and solid SiO_2, $MgAl_2O_4$ formation was detected in accordance with the reaction shown in Equation 2.10, which is thermodynamically favorable.

5.6   Analysis of the Effect of Flow on the Affected Zone Thickness

As shown in Figures 5-11 - 5-14, increasing contact time increases the thickness of the affected zone on the particles for both dynamic and static experiments. It was observed that the average affected zone (discolored zone) thickness of the dynamic experiment samples is greater than that of the static experiment samples and increases with increasing fluid velocity.

In order to explain this phenomenon, a model based on the diffusion of Mg (in alloy) through the alumina particle (when they are in contact) was developed. In the literature [101], it was reported that the external resistance to mass transfer around a particle is dependent on numerous factors such as relative velocity between particle and fluid, size of particle, and fluid properties. Increasing the relative velocity between particle and fluid decreases this resistance.

When the alumina particle is in contact with molten metal, a component in bulk metal (such as Mg) has to diffuse from the bulk to the surface of the particle through the external liquid film. This is called the external resistance to mass transfer. If this resistance is appreciable, the concentration of the diffusing component will decrease from its bulk value (C_b) to a smaller value at the surface (C_s). Then, the same component has to diffuse through the particle towards its center. At the inner boundary of the affected zone its concentration will be zero ($C_0 = 0$) (see Figure 5-71).
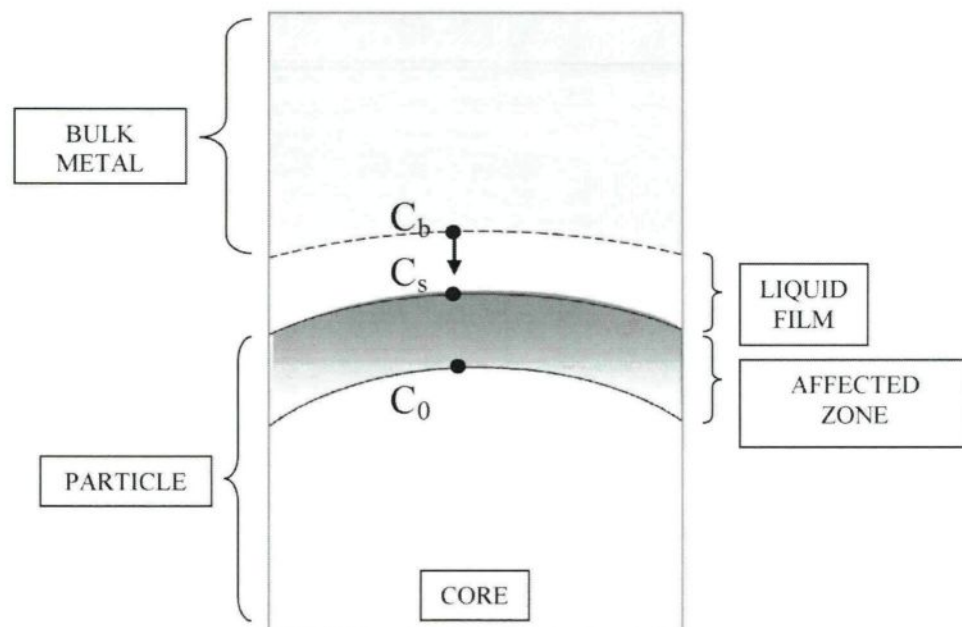

Figure 5-71: Representation of Concentrations of a Diffusing Component Around the Particle with External Mass Transfer Resistance (Static Case and Case with 1.8mm/s Velocity)
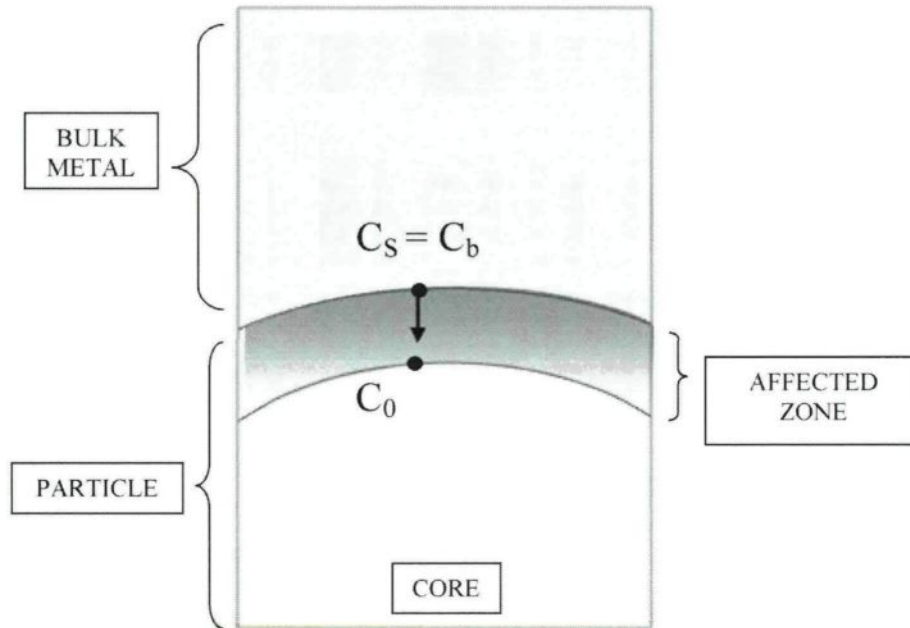
Figure 5-72: Representation of Concentrations of a Diffusing Component around the Particle with Negligible External Mass Transfer Resistance (Case with 3.6mm/s Velocity)

When there is flow, the external resistance to mass transfer is smaller compared to the resistance without the flow (static). For the relative comparison of the static (no flow) and dynamic (with flow) cases, the external mass transfer resistance is taken negligible for the case with flow that had the highest velocity (3.6mm/s as shown in Figure 5-72) in this study. In this case, the concentration at the surface becomes equal to the bulk concentration ($C_s = C_b$). There is only diffusion through the particle. Then, the solution of the diffusion equation with constant surface concentration can be written as [102]:

$$\frac{C(x,t) - C_S}{C_i - C_S} = \text{erf}\left[\frac{x}{2\sqrt{Dt}}\right] \tag{5.17}$$

where C_i is the initial concentration in the particle which is zero. Concentration (C) is a function of time (t) and position (x: distance from the surface towards the center of the particle, x=0 at the surface). During the experiments, the affected zone thickness (L) is measured with time. Since when x = L, C(L, t) = 0. The diffusivity (D) inside the affected zone can be calculated for the flow case using Equation (5.17).

When there is external mass transfer resistance, the equation representing mass transfer through the liquid layer and the particle can be written as [102]:

$$\frac{C(x,t)-C_S}{C_i-C_S} = \text{erf}\left[\frac{x}{2\sqrt{Dt}}\right] - \exp\left[\frac{kx}{D} + \frac{k^2t}{D}\right] \cdot \text{erfc}\left[\frac{x}{2\sqrt{Dt}} + \frac{k\sqrt{DT}}{D}\right] \tag{5.18}$$

with the boundary condition [102]:

$$k(C_b - C_S) = -D\frac{\partial C}{\partial x} \quad (\text{at } x = 0)$$

$$= D\frac{C_S - C(x,t)}{x} \tag{5.19}$$

where k is the mass transfer coefficient in the external liquid layer. The diffusivity is the same as the one for the case with flow, which has already been determined. When x = L, C(L, t) = 0; and when t=0, C_i = 0. Then, the mass transfer coefficient and the ratio of the surface to bulk concentration (C_S/C_b) of the diffusing component can be found from the Equations 5.18 and 5.19.

The diffusion coefficient of magnesium in each commercial alumina was calculated using the experimental data (dynamic case – 3.6mm/s) and Equation 5.17. Then, using this diffusion coefficient and the measured thickness of the affected zone, the mass transfer coefficient and the ratio of surface concentration to bulk concentration were calculated for the case with 1.8mm/s velocity and the static case. The experimental data used in these

calculations are shown in Table 5-19. The calculated diffusivities are presented in Table 5-20.

Table 5-19: Summary of 7 day Experiments with Commercial Alumina Grades

Liquid Aluminum Flow Velocity Around Particles	Contact time, day	Mg content in alloy, %	Commercial Alumina Grades Affected Zone thickness , micron			
			Alcoa T64	Aluchem	Naigai	Alufin
Static - No flow condition			13.4	16.3	56	44
Dynamic - 1.8mm/s	7	5.00	65	59	121	112
Dynamic - 3.6mm/s			77	74	179	207

The results of calculations presented in Table 5.20 showed that diffusivities found for different commercial alumina grades are different from each other. However, those with similar apparent porosities have similar diffusivities. This is an apparent diffusivity which includes the effect of structure. As expected, the diffusivity was found to be nearly one order of magnitude higher for alumina grades with greater apparent porosity as shown in Figure 5-73. These diffusivities were substituted in Equations 5.18 and 5.19. Then, the mass transfer coefficients (k) and the ratios of surface to bulk concentration (C_s/C_b) were determined from these two equations for the case with 1.8mm/s velocity and the static case.

Table 5-20: Summary of Diffusion Model Results based on Dynamic Case (with 3.60 mm/s) Experimental Results

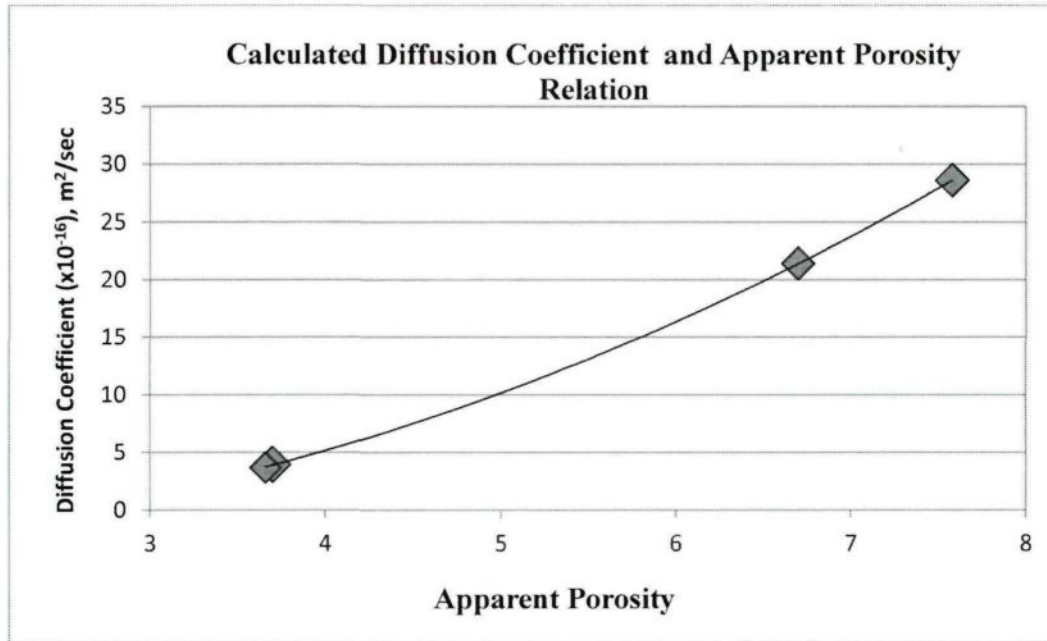| Alumina Grades	D - Diffusion Coefficient, m^2/s
Alcoa	3.95E-16
Aluchem	3.65E-16
Alufin	2.86E-15
Naigai	2.14E-15

Figure 5-73: Calculated Diffusion Coefficient and Apparent Porosity of Commercial Alumina Grades

The mass transfer coefficients and (Cs/Cb) values for dynamic -1.8mm/s and static cases are summarized in Tables 5-21 and 5-22, and Figure 5-74.

(Cs/Cb) values for dynamic-1.8mm/s case shows that external resistance to mass transfer is smaller compared to those of the static case. The calculations indicate that the surface concentration is 13.5-65.0% of the bulk concentration in this case. The results also show that there is a significant external mass transfer resistance when the liquid metal is stagnant (static). The surface concentration varies from 0.10% to 0.92% of the bulk concentration. The mass transfer coefficients are almost two orders of magnitude greater under flow conditions with 1.80 mm/s.

The mass transfer coefficients for the static cases are very similar as expected since the conditions around the particles were kept the same. The same tendency is observed for the 1.8mm/s dynamic cases. The differences could be attributed to the errors that occurred during the experimentation and the measurement of reaction zone thicknesses.

Table 5-21: Summary of Mass Transfer Coefficient Calculations for Dynamic Case (with 1.80 mm/s)

Alumina Grades	k - mass transfer coefficient, m/s	(Cs/Cb) %
Alcoa	1.13E-11	65.0
Aluchem	0.63E-11	50.5
Naigai	0.60E-11	25.5
Alufin	0.39E-11	13.5

Table 5-22: Summary of Mass Transfer Coefficient Calculations for Static Case (Zero Liquid Aluminum Velocity)

Alumina Grades	k - mass transfer coefficient, m/s	(Cs/Cb) %
Alcoa	2.75E-13	0.92
Aluchem	2.05E-13	0.91
Naigai	0.40E-13	0.10
Alufin	1.00E-13	0.15

$$\upsilon = 0 \text{ (static)} \qquad \upsilon = 1.8\text{mm/s} \qquad \upsilon = 3.6\text{mm/s}$$

$$Cb1 = Cb2 = Cb3 = 5\%\text{Mg-Al}$$
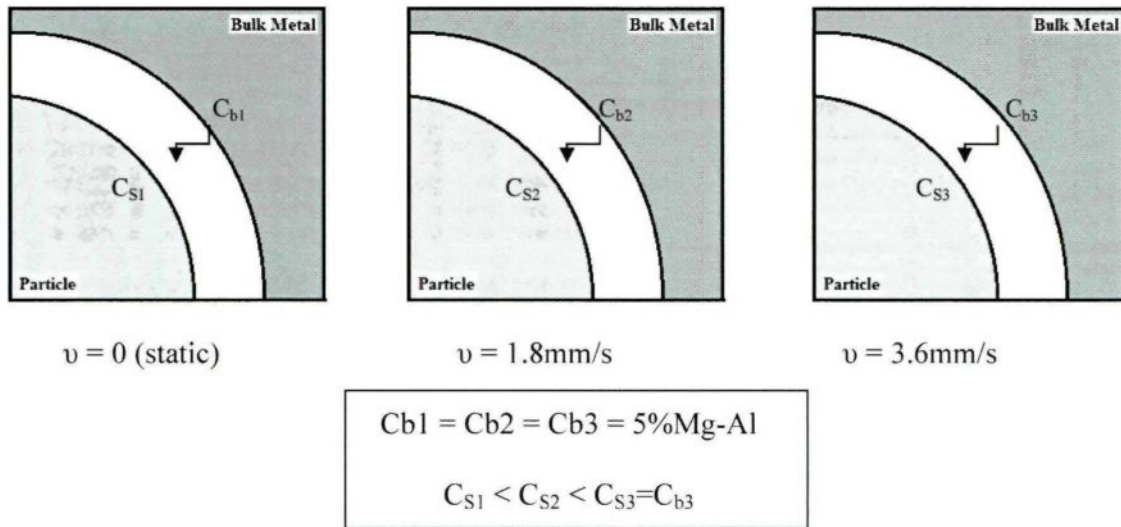
$$C_{S1} < C_{S2} < C_{S3} = C_{b3}$$

Figure 5-74: Effect of Liquid Metal Velocity on Cs (Particle Surface Concentration)

Naigai and Alufin results are somewhat different than those of Alcoa and Aluchem as expected due to the differences in porosity and structure. Even though the model is simple, it represents well the phenomena occurring during filtration. Due to simplifying assumptions, further interpretation of the model results is not possible. The model could be improved by including the type and distribution of porosity. This requires further experimental data.

CHAPTER 6

6. CONCLUSIONS AND RECOMMENDATIONS

6.1 Conclusions

The interactions between molten Mg-Al alloy and alumina were studied with the objective of developing a method to characterize alumina filter bed media (regarding their physical and chemical properties) and to investigate the interactions between alumina, liquid Al-Mg alloys, and its inclusions under both flow (dynamic) and stagnant fluid (static) conditions.

A unique experimental system which can simulate the flow conditions in the filtration process was developed. In the design and building phase of the experimental system, a 3D, one-phase, steady-state mathematical model was modified to simulate the experimental filter system designed for the investigation of interactions between liquid aluminum metal and alumina particles. It is crucial to know the liquid aluminum velocities around the alumina particles for the analysis of experimental results. The simulation results with the mathematical model served to optimize the experimental system to obtain a uniform flow field as well as to calculate the liquid velocities. Measuring the flow in aluminum at high temperatures is a challenge; therefore, a replica of the experimental system was fabricated using Plexiglas and glass. A visualization technique was used to measure the velocity field under different operating conditions for various design parameters of the experimental system. The mathematical model predictions were compared with the water model velocity measurements. The agreement was found

reasonable, especially at low mixer velocities which was the region of interest. The validated model was then used to determine the velocities with aluminum alloy by changing water properties with those of alloy in the model.

Numerous experiments using liquid Mg-Al alloy were conducted for various contact times (from 3 hours to 168 hours). Due to high vapor pressure of magnesium in the molten Mg-Al alloy, excessive oxidation and magnesium loss in the melt created problems. The oxidation issue was solved by replacing Ar with CO_2 gas. Magnesium concentration in the melt was kept within reasonable ranges by small daily additions.

Chemical interactions between alumina and aluminum alloys were investigated under both static and dynamic (flow) conditions. A second experimental system was required to shorten the experimental time. In this investigation, the effects of the followings parameters on the extent of Al/Al_2O_3 interfacial reactions were tested:

- Molten alloy velocity

- Mg content

- Various commercial alumina grades

- Molten alloy temperature

- Physical properties (porosity, grain size, roughness) of alumina

- Presence of impurities in alumina (Na_2O, SiO_2, MgO)

- Presence of inclusions (MgO, $MgAl_2O_4$)

Metallographic studies were conducted to investigate the Al/Al_2O_3 interfacial reactions. The samples obtained from experiments were analyzed by using optical

microscope, scanning electron microscope (SEM-EDX), micro probe, and XRD. According to the results of these tests, the following conclusions were drawn:

- Increasing the molten alloy velocity increases the magnesium diffusion through the alumina particle and affected zone thickness. The size of the samples and molten alloy conditions were varied, and the results obtained using the developed experimental system were reasonable.

- Tabular alumina is not made of only alpha-alumina grains. The presence of impurities such as Na_2O causes Na-beta alumina formation ($Na_2O.11Al_2O_3$). Even at small concentrations of 0.1-0.3% of Na_2O makes the alumina structure weak against chemical attacks. A mechanism was suggested for the reactions taking place between aluminum alloy and Na-beta alumina phase.

- An oxide film was observed in the vicinity of Al/Al_2O_3 interface on some samples. Although this film was not present on every sample, its presence might play an important role on the wetting characteristics of alumina and aluminum alloy.

- Majority of the reaction products was found to be solid $MgAl_2O_4$ and liquid Al, regardless of the duration of experiment, magnesium content, temperature of the melt, alumina type, etc. Thermodynamic analysis indicated the same tendency.

- Increasing magnesium content and temperature increases the affected zone thickness.

- Increasing impurity content in the alumina definitely increases the surface degradation and the affected zone thickness.

- If impurity level is above a certain level in alumina, the filter media starts to degrade and introduces inclusions instead of separating them from the melt.

- Physical properties of alumina play an important role in its degradation.

- Increasing density and grain size of alumina structure decreases the affected zone thickness.

- Roughness did not seem to be an important contributor to the occurrence of interfacial reactions in this study. It is possible that its effect might have been shadowed by other major contributors such as porosity or impurity content.

- $MgAl_2O_3$ as an inclusion source is very stable when it is in contact with Al_2O_3 and 5%Mg-Al alloy.

- MgO inclusion/alumina interface did not show any reaction at 715°C with 72 hours of contact time. Solid/solid reactions require either longer contact times or higher temperatures to take place.

- A diffusion model assuming a semi-infinite medium was used to analyze the static and dynamic condition results. It seems that the difference in affected zone thickness observed in dynamic (with flow) and static (no-flow condition) experiments might be explained by the existence of an external mass transfer resistance when there is no flow and when the velocities are low. Calculated bulk and surface magnesium concentrations for dynamic and static cases follow a reasonable trend.

6.2 Recommendations

- To increase the filter life, filter media should have :

    - As low apparent porosity percentage as possible (~3-4%),

    - homogeneous pore distribution throughout the particle,

    - homogeneous pore size,

    - as low Na_2O content as possible (<0.10 % if possible),

    - as high alpha-alumina purity as possible (> 99% if possible),

    - large alpha-alumina grains (100-150 microns).

- The inclusion study could be repeated using less porous inclusion source in order to have sharp images at the interface which is the site of interest in these types of studies.

- Plant trials followed by inclusion count analyses could be conducted in order to verify the results of the experimental study.

- A more detailed modelling approach could be used to further gain insight into the phenomena taking place during filtration.

REFERENCES

1. M.Torkar, B.Breskvar, M. Tandler,D. Mandrino, M. Dobersek, Study of Inclusions in Technical Aluminum, Cleaner Metals for Industrial Exploitation, International Workshop, Dec.1999, pp.153-162.

2. R. Fuoco, E. R. Correa, A. Bastos, L. S. Escudero, Characterization of Some Types of Oxide Inclusions in Aluminum Alloy Castings, AFS Transactions, 99-85, pp.287-294, 1999.

3. M. J. Lessiter, Understanding Inclusions in Aluminum Castings, Modern Casting, January 1993, pp.29-31.

4. C.J.Simensen, G.Berg, A Survey of Inclusions in Aluminum, 56.Jahrg.1980-5, pp.335-340.

5. Paul N.Crepeau, Molten Aluminum Contamination: Gas, Inclusions and Dross, Modern Casting, July 1997, pp.39-41.

6. S.Shivkumar, L.Wang, D.Apelian, Molten Metal Processing of Advanced Cast Aluminum Alloys, JOM, pp.26-32, January 1991.

7. M. Richard and M. Drouzy, Filtration des alliages d'aluminium, Fondrie-Fondeur d'Aujourd'hui, pp.25-29, Fevrier 1984.

8. F. Frisvold, T. A. Engh, S. T. Johansen and T. Pedersen, Removal of inclusions- A survey and comparison of principles, Light Metals, pp.1125-1132, 1992.

9. G. Ergin,, Wettability of Filter Media by Aluminum Alloys during Aluminum Filtration, Ph.D Thesis, Department of Applied Sciences, University of Quebec at Chicoutimi, 2006.

10. G. Ergin, D. Kocaefe, Y. Kocaefe, D. Emadi and V. Guertsman, Investigation of Interaction Between Al-Mg Alloys and Alumina Particles, Conference of Metallurgist COM, Hamilton, Ontario, Canada, August 2004.

11. G. Clement, The Pechiney Deep Bed Filter: Technology and Performance, Light Metals, pp.1253-1262, 1995.

12. STAS Design-Manufacturing-Marketing web site, www.stas.biz .

13. E. H. Hsu and L. T. Fan, Experimental Study of Deep Bed Filtration: A Stochastic Treatment, AIChE Journal, Vol.30, No.2, pp.267-273, March 1994.

14. C. Choo and C. Tien, Simulation of Hydrosol Deposition in Granular Media, AIChE Journal, Vol.41, No.6, pp.1426-1442, June 1995.

15. R. T. Bui, D. Kocaefe, L. I. Kiss, Modeling the Deep Bed Filtration of Aluminum, The Third Pacific Rim International Conference on Advanced Materials and Processing (PRICM 3), Edited by M. A. Imam, pp.1046-1050, 1998.

16. D. Kocaefe, R. T. Bui and A. Chapdelaine, 1D Mathematical Modeling of Deep Bed Filtration, CIM Conference , pp.203-218, August 22-26 1999.

17. L. Kiss, R.T. Bui, D. Kocaefe, and P. Waite. Flow structure and stability of the deposition layer in deep-bed filters. pages 999-1005, New Orleans, Louisiana, February 11-15 2001. 130e Annual Meeting of the Minerals, Metals and Materials Society (TMS).

18. D. Kocaefe, R.T. Bui, and P. Waite. 2d transient mathematical model of aluminum filtration, pp.817-823, Nashville, Tennessee, Mars 12-16 2000. 129e Annual Meeting of the Minerals, Metals and Materials Society (TMS), Light Metals.

19. D. Kocaefe, L. Kiss, R.T. Bui, C. Painchaud, Y. Fortin, and P. Waite. Mathematical and physical modeling tools for aluminum filtration, CIM Conference, pp. 219-233, Québec, Québec, August 22-26 1999,

20. R.T. Bui, D. Kocaefe, and L. Kiss. Modeling the deep bed filtration of aluminum. volume 1, pp.1045-1050, Honolulu, Hawaii, July 12-16 1998. Third Pacific Rim International Conference on Advance Materials and Processing, TMS.

21. C. Tien, R. M. Turian, and H. Pendse, Simulation of the Dynamic Behavior of Deep Bed Filters, Journal AICE, v. 25, No. 3, p. 385-395, 1979.

22. E. Eckert, R. E. Miller, D. Apelian and R. Mutharasan, Molten aluminum filtration : fundamentals and models, Light Metals, p.1281-1289, 1984.

23. D. Moran, M. Moran, R. S. Cushing and D. F. Lawler, Particle behavior in deep bed filtration: Part1 Ripening and breakthrough / Part 2 - Particle detachment", Journal AWWA. p. 69-93, 1993.

24. J. Desmoulins, Reliability of Molten Metal Filtration, Light Metals, pp.1101-1111, 1992.

25. B. Hubschen, Metal Filtration Modeling, Experiments, and Calculations, Second International Workshop on Aluminum Melt Processing- Aluminum MPT 98, pp.71-80, 1998.

26. P. Netter and C. Conti, Efficiency of industrial filters for molten metal treatment evaluation of a filtration process model, pp.847-860.

27. A. Murray-Chiasson, Étude de la relâche des inclusions lors de la filtration de l'aluminium liquid, Master Thesis, Department of Applied Sciences, University of Quebec at Chicoutimi, 2002.

28. A.Munitz, M.Metzger, R.Mehrabian, The Interface Phase in Al-Mg/Al2O3 Composites, Metallurgical Transactions A, Vol 10A, pp.1491-1497, 1979.

29. C.G.Levi, G.J.Abbaschian, R.Mehrabian, Interface Interactions during fabrication of Aluminum alloy-Alumina Fibre composites, Metallurgical Transactions A, Vol.9A, pp.697-710, 1978.

30. B.F.Quigley, G.J.Abbaschian, R.Wunderlin, R.Mehrabian, A Method for Fabrication of Aluminum-Alumina Composites, Metallurgical Transactions A, Vol.13A, pp.93-100, 1982.

31. I.Jin, D.J.Lloyd, Control of Interfacial Chemical Reaction in Alumina-Reinforced Aluminum MMCs, AFS Transactions, 683-686, 1994.

32. Dickon H.L.Ng, Qing Zhao, Caidong Qin, Man-Wai Ho, Yanrou Hong, Formation of Aluminum/Alumina Ceramic Matrix Composite by Oxidizing an Al-Si-Mg Alloy, Journal of the European Ceramic Society 21(2001) 1049-1053, 2001.

33. A.D.McLeod, C.M.Gabryel, Kinetics of the growth of spinel, MgAl2O4, on Alumina particulate in aluminum alloys containing magnesium, Metallurgical Transactions A, Vol.23A, pp.1279-1283, 1992.

34. P.K.Ghosh, S. Ray, Proc. of fabrication of particulates reinforced metal composites, J.Masounave et.al. (Editor), Montreal, p.23, 1990.

35. M.Fishkis, Journal of Material Sci. 26, p.2651, 1991.

36. B.C.Pai, S.Ray, Material Science and Engineering, Vol.24, p.31, 1976.

37. J.Taft, K.Kristiansen, H.Westengen, Proc.Conf.on Cast Reinforced Metal Matrix Composites, Chicago, Il, Edited by S.G.Fishman, A.K.Dhingra, P.71, 1988.

38. G.R.Cappleman, J.F.Watts, T.W.Clyne, Journal of Mater. Sci. Vol.20, p.2159, 1985.

39. Y.Lepetitcorps, J.M.Quenisset, G.Le Borgne, M.Barthole, Materials Science and Engineering A, Vol.135, p.37, 1991.

40. R. Molins, J.D. Bartout, Y. Bienvenu, Materials Science and Eng. A, Vol.135, p.111, 1991.

41. B.Hallstedt, Z., K. Liu, J. Agren, Materials Science and Eng. A, Vol.129, p.135, 1990.

42. M. Preifer, J.M. Rigsbee, K.K. Chawla, Journal of Materials Science, Vol.25, p.1563, 1990.

43. I.Jin, D.J.Lloyd, 2nd International Conference on Cast Metal Matrix Composites, Tuscaloosa, USA, p.236, 1993.

44. D.O. Karlsen, J.B. Borradaile, J. Gjonnes, J. Taft, Proc. Conf. Riso, Denmark, p.421, 1988.

45. D.A. Weirauch, Jr., Journal of Materials. Res. Vol3, p.729, 1988.

46. W. M. Zhong, Interfaces and deformation behavior of aluminium matrix composites, Ph.D thesis, Ecole Polytechnique de Montreal, 1995.

47. Vaucher and Beffort, Bonding and interface formation in Metal Matrix Composites (MMC), MMC-Assess Consortium, http://mmc-assess.tuwien.ac.at, September 2001.

48. A.Forn, M.T.Baile, E.Ruperez, Spinel effect on the mechanical properties of MMC AA6061/(Al$_2$O$_3$)$_p$, Journal of Materials Processing Technology 143-144, p.58-61, 2003.

49. A.Sangghaleh, M.Halali, Effect of magnesium addition on the wetting of alumina by aluminum, Applied Surface Science 255, pp.8202-8206, 2009.

50. W. M. Zhong, L'Esperance, M. Suery, Effect of current Mg concentration on interfacial reactions during remelting of Al–Mg(5083)/Al$_2$O$_{3p}$ composites, Materials Characterization, Volume 49, Issue 2, p.113-119, 2002.

51. B. C. Pai, S. Ray, K. V. Prabhakar, P. K. Rohatgi, Fabrication of Aluminium-Alumina (Magnesia) Particulate Composites in Foundries Using Magnesium Additions to the Melts, Materials Science and Engineering, Vol. 24, pp. 31-44, 1976.

52. D. Emadi, Study of Oxide Film Formation and Fragmentation at the Liquid-Air Interface in Al and Al-Mg Alloys, Part A: Literature Review on the Melt Oxidation of Pure Al and Al-Mg Alloys, CSMA-95-12, Arvida Research and Development Center, Alcan International Limited, Jonquiere, Quebec, 1995.

53. S.P. Cashion, N.J. Ricketts, M. T. Frost and C. Korn, The Protection of Molten Advanced Technologies, Brisbane, Australia, 2000.

54. C. Allaire, Mechanism of Corundum Growth in Refractories Exposed to Al-Mg Alloys, Aluminum Transactions, Vol.3, pp105-120, 2000.

55. S. Afshar and C. Allaire, The Corrosion of Refractories by Molten Aluminum, JOM, May 1996, pp.23-27.

56. A. M. Wynn, Testing of Castable Refractories for Resistance to Molten Aluminum Alloys, J.Ceramic Transactions, Vol.91, no.5, pp.153-158, 1992.

57. S. Quesnel, C. Allaire and S. Afshar, Criteria for Choosing Refractories in Aluminum Holding and Melting Furnaces, Light Metals, TMS, pp.1391-1402, 1998.

58. Ole-J. Siljan, Gjertrud Rian, Dag T.Pettersen, Arve Solheim, Christian Schoning, Refractories for Molten Aluminum Contact Part I: Thermodynamics and Kinetics, Refractories Applications and News, Vol.7, Number 6, pp.17-25, 2002.

59. V. Gabis, Comportement des réfractaires au contact de l'aluminium et de ses alliages, Fonderie-Fondeur d'aujourd'hui, Vol.131, pp.29-42, 1994.

60. V. Gabis, Refractories in Foundry: Some Recent Progress, Hommes et Fondrie, Juin/Juillet 2000, no. 305, pp. 146-154.

61. T. Richter, T. Vezza, C. Allaire, and S. Afshar, 41. International Colloquium on Refractories-Refractories in Non-Ferrous Metallurgy, pp.86-90, 1998.

62. S. Afshar and C. Allaire, The Corrosion of Refractory Aggregates by Molten Aluminum, JOM, May 2000, pp. 43-46.

63. S. Afshar, C. Allaire, S. Quesnel and M. Allahverdi, Le Magazine de l'aluminum.

64. S. Afshar and C. Allaire, Furnaces: Improving Low Cement Castables by Non-wetting Additives, JOM, August 2001, pp. 24-27.

65. J. Gao, S. Afshar and C. Allaire, Corrosion Kinetics of Refractories by Molten Aluminum, Light Metals, Edited by A. T. Tabereaux, TMS, 2004.

66. D. A. Weirauch and G. E. Graddy, Jr, Wetting and Corrosion in the Al-Mg-Si-O System, Proceeding of the International Symposium on advances in Refractories for the Metallurgical Industries, Edited by M. A. J. Rigaud, Pergamon Press, New York, 1988, pp. 251-266.

67. V. I. Nizhenko and L. I. Floka, Wetting of Al2O3-Based Oxide Ceramics by Molten Aluminum, Powder Metallurgy and Metal Ceramics, Vol.40, No.5-6, pp.271-276, 2001.

68. P. J. Bunyan, Liquid Phase Processing and Interfacial Behaviour of Metal Matrix Composites, Australian Fracture Group Symposium, Sydney, Australia, pp.120-125, 1990.

69. J. S. Moya, H. P. Steier, J. Requena and R. Rezakhanlou, Interfacial Reactions in Mg-Containing Aluminum Alloys/Mullite-Zirconia Reaction Sintered Composites, Acta Materia, Vol. 46, No.7, pp. 2423-2429, 1998.

70. A.L.Yurkov, I.A.Pikhutin, Corrosion of Aluminosilicate Refractories by Molten Aluminum and Melts Based Upon it in Melting and Casting Units, Refractories and Industrial Ceramics,Vol.50, No.3, 2009.

71. C.Allaire, P.Desclaux, Effect of Alkalies and of a Reducing Athmosphere on the Corrosion of Refractories by Molten Aluminum, J.Am.Ceram.Soc, 74 [11]2781-85, 1991.

72. M.S.Baspinar, Optimization of Binder Matrix in Mullite Refractories, Ph.D Thesis, Anadolu University Graduate School of Sciences, Ceramic Engineering Program, 2005

73. M. Fouletier, and D. Gold, "Selective, Accelarated Test for Evaluation of Refractory Lifetime in Contact with Aluminium Alloys", UNITER'91, 1991, 36-38.

74. W. G. Cochran, The Flow due to a Rotating Disk, Proc. Cambridge Phil. Soc. , 30, pp.365-375, 1934.

75. V. G. Levich, Physicochemical Hydrodynamics, Prentice-Hall, Inc., Englewood Cliffs, New Jersey, 1962.

76. K.J. Brondyke, "Effect of molten aluminum on alumina-silica refractories", J. Amer. Ceram. Soc., 36, [5], 171-174, 1953.

77. Luke H. Baumgardner, "World Production and Economics of Alumina Chemicals", Alumina Chemicals Science and Technology Handbook, pp.7-9, The American Ceramic Society, Inc, 1990.

78. K. Wefers, "Nomenclature, Preparation, and Properties of Aluminum Oxides, Oxide Hydroxides, and Trihydroxides", Alumina Chemicals Science and Technology Handbook, pp.13-22, The American Ceramic Society, Inc, 1990.

79. T. J. Carbone, "Production Processes, Properties, and Applications for Calcined and High-Purity Aluminas", Alumina Chemicals Science and Technology Handbook, pp.99-108, The American Ceramic Society, Inc, 1990.

80. Habashi, F. (2005). "A short history of hydrometallurgy". Hydrometallurgy 79: 15–22. doi:10.1016/j.hydromet.2004.01.008.

81. Larry L. Musselman, "Production Processes, Properties, and Applications for Aluminum-Containing Hydroxides", Alumina Chemicals Science and Technology Handbook, pp.75-92, The American Ceramic Society, Inc, 1990.

82. Fathi Habashi, "Alumina Production: A Historical Perspective", Aluminum Transaction, Vol.3, pp.121-131, 2000.

83. Fathi Habashi, " A hundred years of the Bayer Process for alumina production ", CIM Bulletin, January 1988, Vol.81, no.909, pp.70-76.

84. W. E. Lee, W. Mark Rainforth, Ceramic microstructures: property control by processing.

85. Dilip C.Jain, Siva Soora, "Refractories-Fused White vs Tabular Alumina", Ceramic Industry, vol.136, no.5, pp.25-27, 1991.

86. Tom Kendall, "Calcined and Tabular Alumina", Industrial Minerals, April 1995, n.331, pp.21-45.

87. K. A. Evans, "The Manufacture of Alumina and its Use in Ceramics and Related Applications", Key Engineering Materials Vols 122-124 (1996), pp.489-526.

88. George MacZura, "Production Processes, Properties, and Applications for Tabular Alumina Refractory Aggregates", Alumina Chemicals Science and Technology Handbook, pp.109-170, The American Ceramic Society, Inc, 1990.

89. George MacZura, Kenneth J. Moody, Edward M. Anderson, " Annual Mineal Review-Alumina ", American Ceramic Society Bulletin, vol.74, no.6, pp.92-97, June 1995.

90. G.W.Kriechbaum, J.O.Laurich, G.MacZura, Ken Moody, T.Yamamoto, U.Matlos, "Properties and Applications of Tabular Alumina in Refractories", Indian refractories congress (First congress 1994: Jamshedpur –India, 1994), Vol.B, pp.1-6.

91. K.J.I ves, Filtration and Separation, November-December 1970.

92. C.Tien, Granula Filtration of Aerosols and Hydrosols, Butterworth Series in Chemical Engineering, Ed. H. Brenner, 1989.

93. J.P.Herzig, D.M.LeClerc, P.LeGoff, Industrial and Engineering Chemistry, Vol. 62, No. 5, May 1970.

94. F. Hodaj, J. N. Barbier, A. Mortensen, O. Dezellus and N. Eustathopoulos, Modelling Kinetics of Diffusion Controlled Reactive Wetting: The Role of Reaction Behind the 140 Triple Line, Diffusion and Defect Data Part B: Solid State Phenomena, Vol. 72, pp. 91-96,2000.

95. A. Mortensen, B. Drevet and N. Eustathopoulos, Kinetics of Diffusion-Limited Spreading of Sessile Drops in Reactive Wetting, Scripta Materialia, Vol. 36, No. 6, pp.645-651, 1997.

96. N. Eustathopoulos and L. Coudurier, Influence of Alloying Elements on Wettability and Adhesion Energy in Liquid Metal-Ceramic Systems, in Contact Angle. Wettabilitv and Adhesion. Ed. K. L. Mittal, pp. 909-920,1993.

97. Steinke, T.D. and M. A. Stett, Refractories for aluminum melting furnaces, Light Metals, 1977, Vol.2, AIME Proc. , Atlanta, Georgia.

98. P.H. Thanh, "Rev.Hautes Temp. Refractaires", 2, [2], 178, 1965. (Ph.D Thesis, Sci.Faculty Univ. of Lyon, June 3, 1965, p.75.)

99. O.Kubaschewski and C.B.Alcock, Metallurgical Thermo-Chemistry. Revised and Enlarged 5th Edition, Editor: G.V. Raynor, International Series on Materials Science and Technology, Vol.24, Pergamon Press, 1979.

100.D.J.Fray, Determination of Sodium in Molten Aluminum and Aluminum Alloys Using a Beta Alumina Probe, Metallurgical Transactions B, Volume 8B,pp.153-156, March 1977.

101. Octave Levenspiel, "Chemical Reaction Engineering", Third Edition, John Wiley and Sons, pp.566-588, 1999.

102. F.P.Incropera, D.P.DeWitt, Fundamentals of Heat and Mass Transfer-second edition, School of Mechanical Engineering Purdue University, 1985.

103. FACT SAGE (Facility for the Analysis of Chemical Thermodynamics) Thermodynamic Analysis Software Web Site http://www.crct.polymtl.ca/fact/, (Developed by Professors Christopher W. Bale & Arthur D. Pelton of École Polytechnique and Professor William T. Thompson of McGill University, 2001.

104. Turan Tambas, Ph.D Thesis, Determination of Slip Casting Properties of Seydisehir Alumina, Istanbul Technical University, Istanbul-Turkey, 2006.

105. Kocaefe, D. et Bui, R. T., A One-Phase Model of Mixing of Al-SiC Composite Melt, Metallurgical and Materials Transactions B, Volume 27B, 1015-1023, 1996.

106. Kocaefe, D., Bui, R. T., Provencher, R. et Bourgeois, T., Simulating and Optimizing a Composite Mixing Tank , Light Metals TMS, 913-919, 1996.

107. Kocaefe, D., Bui, R. T., A One-Phase Model of Mixing of Al-SiC Composite Melt, Metallurgical and Materials Transactions B, Volume 27B, 1015-1023, 1996.

APPENDIX I

DEVELOPMENT OF AND EXPERIMENTAL SYSTEM WITH LOW VELOCITY

SIMILAR TO THAT OF ALUMINUM FILTRATION

A1.1 Designing an Experimental System

At the beginning of the current study, a number of experimental systems were designed and the experiments were carried out using molten aluminum in order to identify a suitable experimental set-up. In this part, the evolution of the experimental system design and the results of the preliminary experiments are summarized. The problems faced during the utilization of these experimental systems are also discussed. The purpose of this section is to document all the molten aluminum involved activities held during the current study for future reference.

In industrial filters, the metal flows in vertical direction either upward or downward as it was reported in different studies [9, 10]. Thus, the efforts on system design were focused on building/designing a system that is able to create a vertical metal flow in its filter section.

A1.2 Experimental Set-Up with Reciprocal Motion

The first experimental system shown in Figure A1- 1 consisted of two main parts. First part was a cylindrical crucible which had 9 kg of molten aluminum alloy holding capacity. The other part was composed of a sample holder that was submerged into the cylindrical crucible. Sample holder had large number of slots at the bottom and on the top plate. An electrical motor connected to a disc gave a circular motion to the system. The disc

turned with a speed of 10 sec/cycle. A 12-mm diameter steel rod connected to the guide converted the circular motion of the disc to the linear motion just like a crankshaft-piston rod system in automobile engines. Sample holder, submerged into the molten aluminum, moves vertically up and down with a reciprocal motion. Ultimately, alumina particles placed in the sample holder section is being subjected to a vertical molten metal flow.
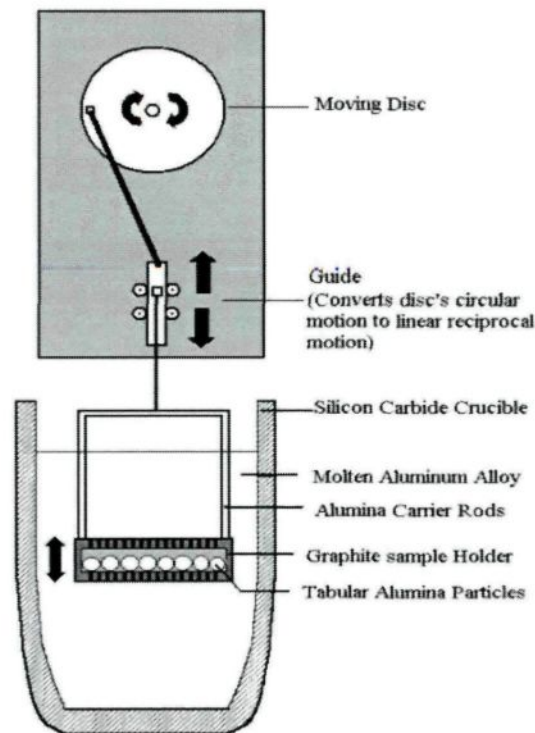
Figure A1- 1: First Experimental System Design (Reciprocal Motion)

A1.2.1 Fabrication - Experimental Set-up with Reciprocal Motion

Sample holder part was fabricated by machining of a graphite block (Pyrotek P-10) which is one of the most common types of graphite used in experiments with molten aluminum. The bottom and top parts of the sample holder was connected to each other using two 6-mm diameter stainless steel rods and bolts. The rods were covered with 10 mm

inner diameter high density alumina hollow tubes. The bolts were isolated using boron nitride paste.

A1.2.2 Preliminary Trial Results and Discussion

The preliminary trials were carried out with 6 mm diameter Naigai type tabular alumina particles and 5%wt Mg-Al alloy at 715°C.

The purpose of the preliminary trials was to find out how the system works at elevated temperatures and to determine the failure mode of the system. The test results showed that the oxidation of Al-Mg alloy was the major limitation of this system, although argon gas was used to reduce the oxidation rate of alloy. The reciprocal motion of the system was creating a violent metal circulation in the crucible, and each motion of sample holder was breaking the protective oxide layer of liquid metal and promoting the oxide formation. Argon gas was not sufficient to prevent oxidation of molten metal.

It is difficult to determine the metal velocity at high temperatures. A transparent water model of the experimental set-up was also fabricated using plexi-glass and stainless steel rods in order to determine the fluid flow pattern of the system. Tests with water and molten aluminum were conducted simultaneously. The preliminary tests showed that the flow pattern in the sample holder section was not easy to determine due to the reciprocal motion of system. Observations indicated that the alternating direction of molten metal in sample holder section cannot represent the actual filtering process. These results were not found promising to pursue any other work with this system.

A1.2.3 Conclusions – Experimental Set-up with Reciprocal Motion

This experimental system design was abandoned due to the following reasons:

- System was not representing the filtration process flow pattern because of its alternating motion,

- Oxidation of metal due to violent metal circulation in the SiC-crucible was not tolerable. It was not possible to conduct experiments longer than 12 hours using this system due to high rate of metal oxidation.

- Sample collection was difficult after experiments.

A1.3 Experimental Set-up with Mixer Motion - System Design I

The second experimental system shown in FigureA1-2 was made of two parts. First part was the cylindrical crucible which had approximately 9 kg of liquid aluminum holding capacity. Second part was composed of a mixer and a sample holder which were being submerged into the cylindrical crucible. The bottom part of the sample holder had a compartment in which the alumina particles were placed. This part represented the filter section. The filter section had a large number of holes both at the bottom and on the top plates. These holes allowed the liquid metal to circulate within the crucible and kept the alumina particles inside at all times. The top plate also acted as a distributor which helped to create a uniform flow pattern. The mixer had 4 blades tilted 37.5°. It pushed the flow downward. The mixer diameter was 63 mm. Alumina particles fill one third of the height of sample holder part. Figure A1-2 shows the experimental set-up schematically. Later on, an

additional diffuser plate was added to the system to regulate the flow in the filter section, and the top part of cylindrical wall was closed leaving enough space for the flow (see Figure A1-3).
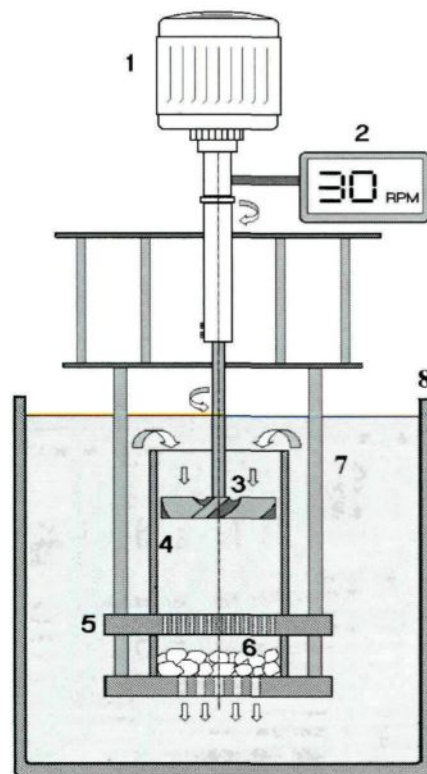
Parts of experimental system:

9. Electrical motor
10. Rotational speed indicator
11. Mixer
12. Cylinder wall
13. Top plate
14. Filter
15. Molten aluminum
16. Crucible

Figure A1- 2: A Schematical Description of the Experimental System-I (First Version)

Before starting to the construction of the experimental system-I for tests with molten aluminum , a 3D, one-phase steady-state mathematical model described in Chapter 4 was modified and adopted to the experimental set-up geometry using CFX4^{TM} to test the effect of experimental design parameters on the flow pattern. The major purpose of studying these parameters was to find out the conditions that could provide a homogenous vertical velocity field in vicinity of the alumina samples in the filter section. A water model

of the system was also fabricated using glass and plexi-glass. The results of the tests carried out using this system were used for comparing the measured velocities with the predicted ones to validate the mathematical model. The water experiments and mathematical modelling study were carried out simultaneously to develop the experimental system-I.
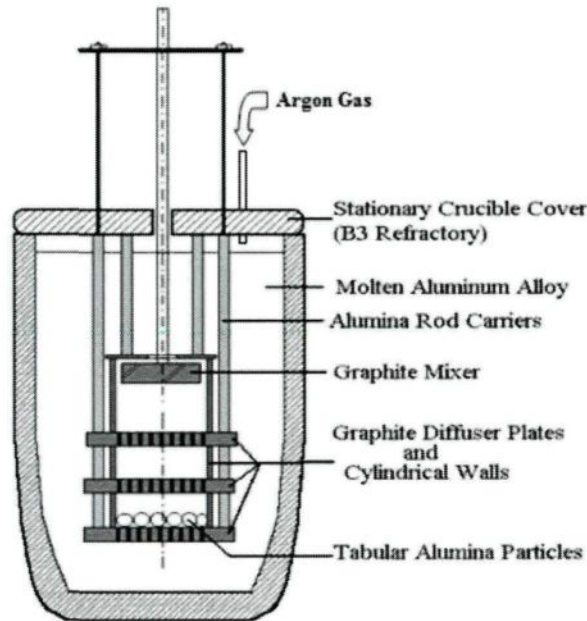
Figure A1- 3: Second Experimental System Design-I with an Additional Diffuser Plate (Version 2)

A1.3.1 Results of Preliminary Experiments and Discussion

The preliminary experiments with molten aluminum were commenced using 5%Mg-Al alloy. The mixer speed used in the tests was 20 rpm which corresponded to about 1.8mm/s vertical molten metal velocity in the sample holder section. The molten metal temperature was kept at 715°C. The depth of the mixer in the molten metal was kept 5 cm below the metal surface in order to prevent vortex formation due to mixer motion and to avoid any dross/surface oxide entrainment into filter section.

Magnesium metal has great affinity to create oxides at the surface of molten aluminum in the presence of oxygen. Although argon gas was blown into the SiC-crucible to prevent the surface oxidation of metal, high rate of metal oxide formation was observed during the first 12-hour experiment.

Another 12-hour experiment was conducted under stationary conditions without using the mixer. It was observed that under this condition the oxide formation was negligible in the system. This observation showed that the mixer movement in the system provoked the surface oxidation, and argon gas did not prevent the formation of thick, dense, and sticky oxide layer during long experiments. This oxide layer blocked the mixer motion after the oxide layer reached the crucible cover and solidified. The metal circulation in the system was interrupted as a result of excessive oxide formation (see Figure A1-4).

Figure A1- 4: Excessive Oxide Formation Causes Filter Motion Blocked.

In the following section, the design modifications made in order to reduce oxidation are summarized.

A1.3.2 Additional Cover Installation on Crucible to Avoid Excessive Oxidation

It was proposed that if the empty space on the top of the metal line is minimized by filling this space with a piece of refractory underneath the crucible cover, the magnesium evaporation and/or oxidation could be limited. An additional refractory (Pyrotek™ B-3) was placed on the top of the crucible on the metal surface as shown in Figure A1-6 schematically.
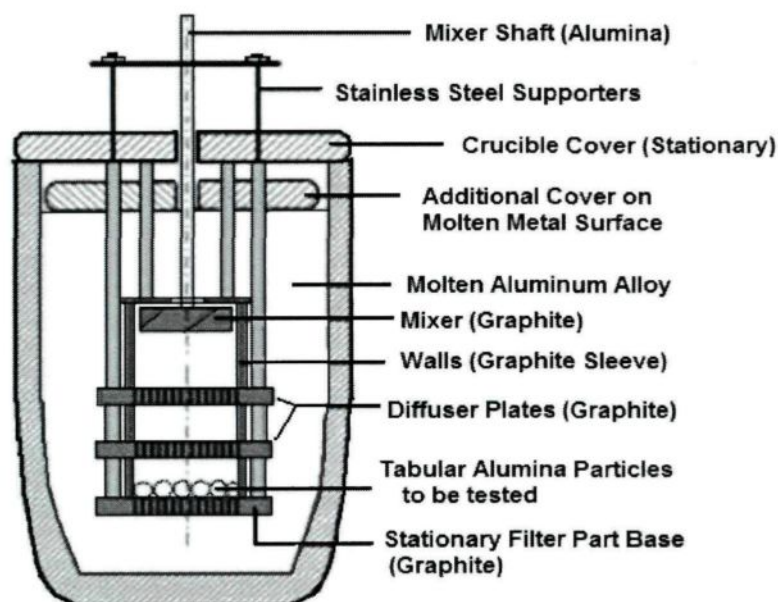
Figure A1- 5: Experimental System-I with Additional Refractory Piece at Metal Line (Version 3)

A number of trials using 5%Mg-Al alloy at 715°C were conducted to determine the effect of this modification on oxidation rate. Research grade Ar gas with 100 cm³/min flow rate was blown into the system during entire trial. Mixer speed was set to 20 rpm. After 12 hours, it was observed that a sticky oxide was formed in the hole on the crucible lid where

the mixer shaft rotated. The volume of the oxide increased with time. Finally, it reached the top of the crucible cover by clinging to the rotating mixer shaft. Then, it was solidified since the temperature at this position was lower compared to that of the interior. Eventually, the oxide built up between two refractory layers completely blocked the mixer motion (see Figure A1-6).

Table A1- 1: Summary of impurities in Argon Gas Reported by the Supplier-Praxair

	O_2 (ppm)	H_2O (ppm)	CO (ppm)	THC (ppm)	N_2 (ppm)	H_2 (ppm)	CO_2 (ppm)
Research Grade Argon	<0.2	<1	<0.1	<0.1	<1	<1	<0.1
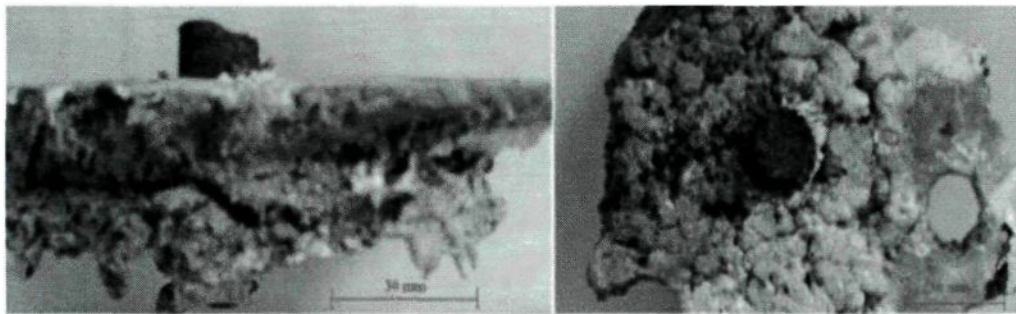
Figure A1- 6: Mixer Shaft Broken due to Oxide Formation on Metal Surface

The effect of rotational speed of the mixer on the rate of surface oxidation was also studied using both experimental system and the mathematical modelling, which is explained in Chapter 4 in detail.

A1.3.2.1 Conclusions

- Argon gas was not sufficient to protect the molten metal against oxidation taking place due to mixer motion.

- The additional refractory underneath the crucible cover was useless in terms of reducing oxidation rate. Instead of using a piece of refractory, the metal level was increased a couple of centimetres by increasing the weight of the alloy by 15-20%. This change provided higher mixer depth to decrease oxide entrainment possibilities into filter section due to mixer motion.

- Sample collection was not easy. Graphite section was easily cracked which was expensive to replace. Fragility of the experimental assembly appeared to be a critical point. It needed to be strengthened.

A1.3.3 Carbon Dioxide (CO_2) Use to Avoid Excessive Oxidation

It was reported in the literature that using SF_6 and CO_2 gasses in the foundry has beneficial effects on decreasing the oxidation rate of Mg or Mg-Al alloys [48, 49]. Densities of SF_6 and CO_2 are 5 and 1.6 times higher than the density of air, respectively. They basically stay on the molten metal surface and isolate the melt from air. According to the Intergovernmental Panel on Climate Change held in 1988, SF_6 is very toxic and the most potent greenhouse gas which has a global warming potential of 22,200 times that of CO_2 over a 100 year period. Therefore, CO_2 gas was chosen for use in experiments.

A 12-hour trial was conducted using 99% pure Praxair CO_2 gas to reduce the oxidation of 5% Mg-Al alloy. The CO_2 flow rate was kept at 10-15 cm^3/min levels during test. Carbon dioxide gas was found to be very effective compared to argon gas in terms of

its ability to slow down the dross formation rate. It was decided to conduct long trials (>3 days) to verify the stability of the system in terms of oxide formation, fluid flow dynamics, magnesium loss in the melt, etc. These trials showed that the oxidation rate is very low compared to experiments with Ar even after 3 days. The magnesium loss was about 10% (decreased from 5%wt to 4.5%wt after 72h), which can be compensated by adding small amount of magnesium into molten metal intermittently. The use of CO_2 gas in the experiments was optimized and 3 cm^3/min gas flow rate was used in the experiments as a standard procedure.

A1.3.3.1 Conclusion – CO_2 use to Avoid Excessive Oxidation

- The molten alloy oxidation problem was solved by using carbon monoxide gas.

- CO_2 gas was chosen as the cover gas for the experimental study.

- The system described above (System-I) was very fragile. After each test, 30-40% of the system parts needed to be replaced with new materials for restarting a new experiment. Especially, the labour needed for machining of some assembly parts was excessive. A more robust experimental set-up design was required.

A1.3.4 Modifications of Experimental Set-up with Mixer Motion to Reduce Operational Difficulties

In the present system, there are two diffuser plates and a filter base made of graphite discs which are all connected to each other by cylindrical graphite sleeves. The whole system is supported and carried by three stainless steel rods isolated by using alumina tubes

(CoorsTek, 99.8%pure alumina, AD-998 Labware). The whole set-up has to be dismantled from top to bottom for sample collection after each experiment, consequently, a number of parts were broken each time due to high fragility of the materials used in the system.

A new experimental set-up (cylindrical body) shown in Figure A1-7 was designed to facilitate the sample collection from the Experimental System-I. The new set-up was divided into 3 parts; mixer chamber, central chamber, and filter sections. In this new design, the diffuser plate and the cylindrical sleeve (graphite sleeves in old system design) of each section were one piece, fabricated by machining a 80-mm diameter graphite block. The filter section base was designed to be assembled to the filter section of the set-up so that dismantling the whole assembly was not required for sample collection after each experiment. Sample holder base was simply released from the body by detaching two pins from each side.

Some tests with hot metal confirmed the stability and solidity of the new system. The width and the volume of the new cylindrical body was much higher than that of the previous one due to thicker walls; therefore, it was decided to use wider and taller SiC-C crucible with 15 kg molten aluminum holding capacity for the following experiments. Also, only one layer of alumina particles instead of a closely packed bed of particles (which was used in previous experiments) was placed in the sample holder in order to facilitate the alumina sample collection and the sample preparations for further metallographic study. This practice also allowed testing all particles under the same flow conditions and avoiding the channeling of molten aluminum in the closely packed bed.
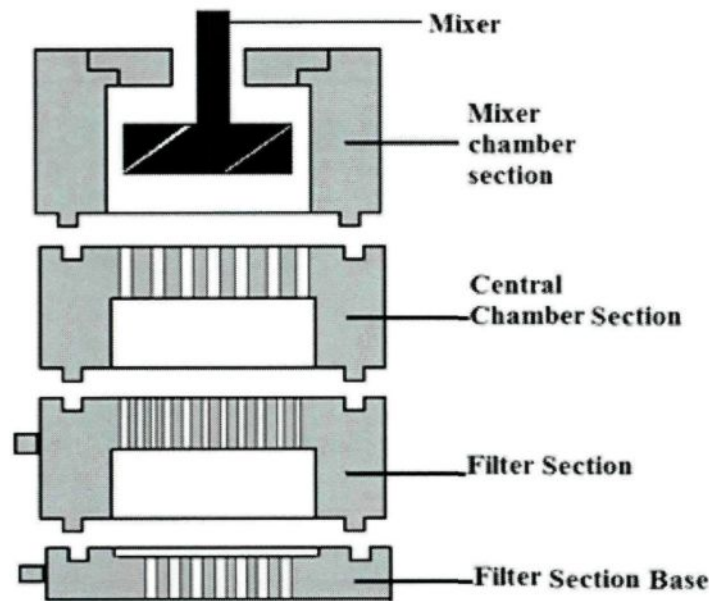
Figure A1- 7: Different Sections of the New Experimental Set-up Cylindrical Body

After determining the operating conditions of the experimental set-up to create a uniform flow field in the filter section, series of experiments were conducted using the setup shown in Figure A1-8. First six experiments were carried out with 6-9 mm diameter Naigai type alumina particles from 1 to 3 days using 7%Mg-Al alloy. The following five experiments were conducted using Aluchem type alumina particles keeping every parameter of the experiments same as those of the experiments conducted with Naigai type alumina particles.

The results of preliminary experiments indicated that:

- Oxides formed on the molten metal surface are needed to be removed from the SiC-crucible at least twice in 72-hour experiments,

- A small daily addition of pure magnesium into molten metal is needed to compensate the magnesium loss due to oxidation.
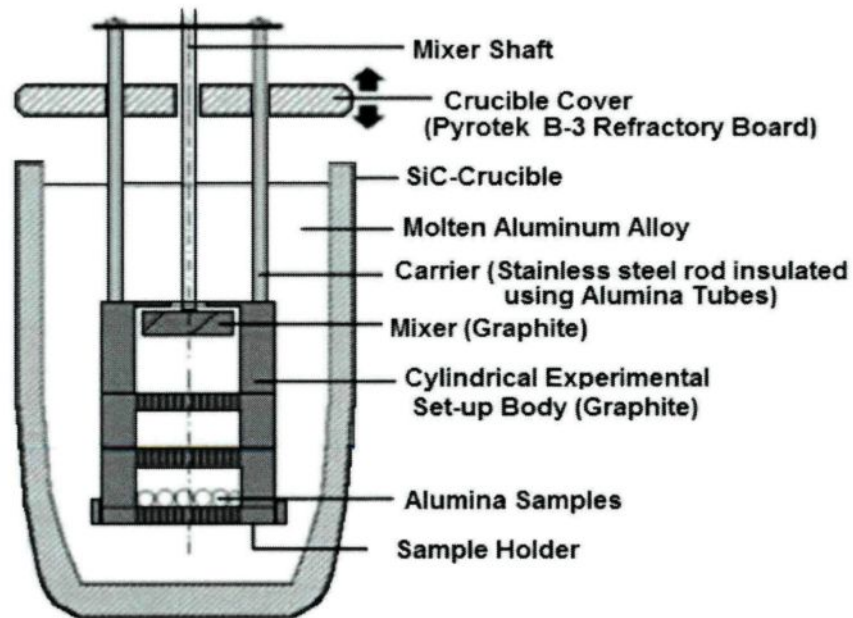
Figure A1- 8: Assembled Experimental System-I (Version 4)

A1.3.4.1 Conclusions – Experimental Set-up with Mixer Motion

- Experimental System-I shown in Figure A1-8 is the most mechanically stable system for the current experimental study.

- System assembly seems to be the most stable and robust set-up among the different versions presented above.

- Spare assemblies or critical parts of the system had to be fabricated to prevent delays in experiments due to any assembly part breakage or loss.

A1.3.5 Modifications of System-I to Avoid Contamination of Alumina Samples

The experimental system-I shown in Figure A1-9 above was used in early experiments. After each experiment, the assembly was cleaned and prepared for the next experiment. The certain graphite parts such as mixer, diffuser plate sections of the chambers, etc. were still easily damageable while cleaning and preparation; therefore, two spare assemblies were fabricated for the following experiments. The same type of graphite (Pyrotek P10) which was used in the fabrication of the first assembly, was not available neither at University work shop nor at the supplier's inventory (Pyrotek). Based on discussions with SGL Carbon technical service, one block of 6 inches diameter SGL Carbon-graphite was purchased and new experimental assemblies were fabricated using this graphite. Although, this graphite was advised by specialist especially for our experimental conditions, brownish-yellow residue was formed on graphite parts and alumina samples. It was observed that the residue formed when new graphite was in contact with Mg-Al alloy. The graphite production steps were questioned in detail and it was found that aluminum phosphate treatment was applied to the graphite to avoid oxidation of graphite at high temperatures. The presence of magnesium in the molten metal caused the formation of magnesium phosphate (brownish yellow residue), when the graphite was in contact with the molten Mg-Al alloy. The supplier suggested using a boron nitride coating (Pyrotek-Hardcoat) to avoid contamination of alumina samples from magnesium phosphate, and to protect graphite from oxidation as well. Starting from experiment #24, all graphite parts were coated using boron nitride Hardcoat (see Figure A1-9).

(a) **(b)**
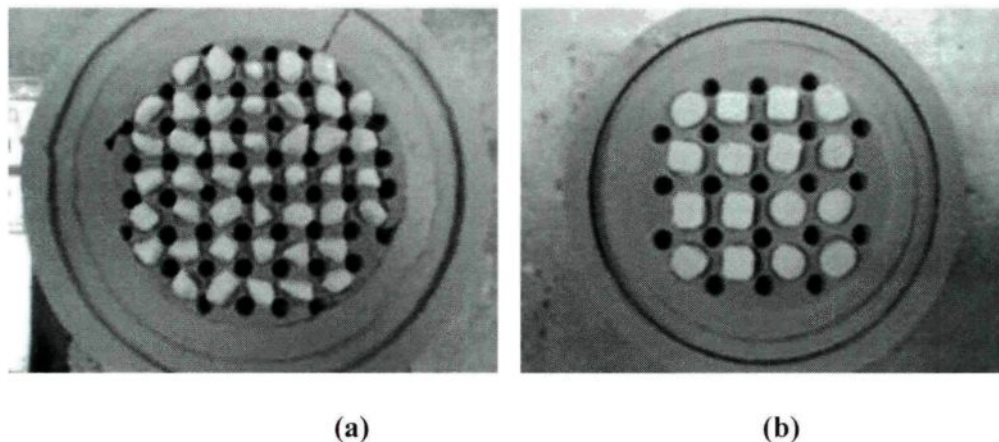
Figure A1- 9: Sample Holder Base Coated Using boron nitride Hardcoat used for
(a) Testing of Tabular Alumina Particles), (b) for Testing of Synthetic Tablets

It was visually observed that the extent of the formation of brownish-yellow residue significantly decreased with the use of coating. Several experiments (25-71) were conducted with this system using different tabular alumina particles and laboratory made alumina tablets, different time periods (1-10 days), and different Mg-Al alloys (2, 5, and 7% Mg). There was no operational problem observed during this series of experiments. The system seemed to run properly.
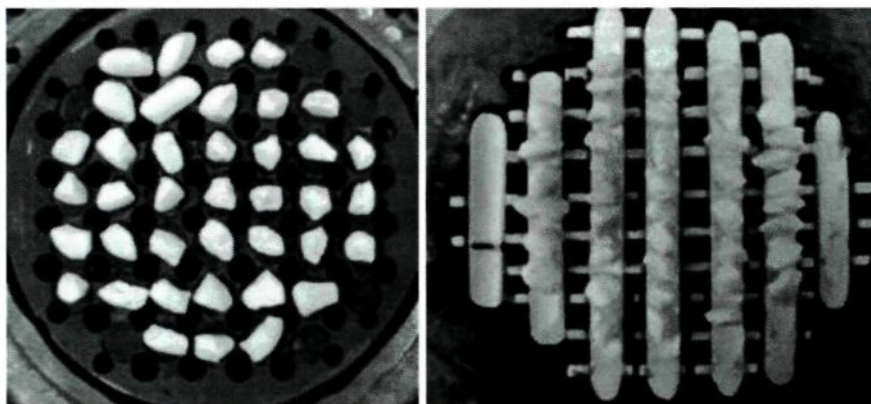
Figure A1- 10: Sample Holder Base with No Coating used for Testing of Tabular Alumina Particles, (a) Graphite Base, (b) Alumina Base (CoorsTek-99.8%Pure Alumina, AD-998 Labware)

While tests were going on using the current experimental set-up, it was noticed that the number of tests remained to be completed was numerous. Using the current system, once an experiment started, the only way of collecting alumina samples at a given time was taking the whole experimental set-up out of the molten metal and restarting the experiment from the beginning. There was no other means of collecting samples intermittently using this system. Another experimental system design which allowed the sample collection without interrupting the ongoing experiment was needed due to time and resource restrictions.

A1.4 Experimental System with Rotating Disc

The above problem was solved using a sample holder disc which was connected to a central shaft (a rotating disc).

This system was composed of two parts. The first part was a crucible which was filled with molten aluminum alloy, and the second part was a rotating disc which was connected to an electrical motor that had a controller for adjusting the rotational speed. The alumina samples were placed on this disc at a certain distance from disc center. It was then submerged into molten metal, and the rotated with a desired velocity.
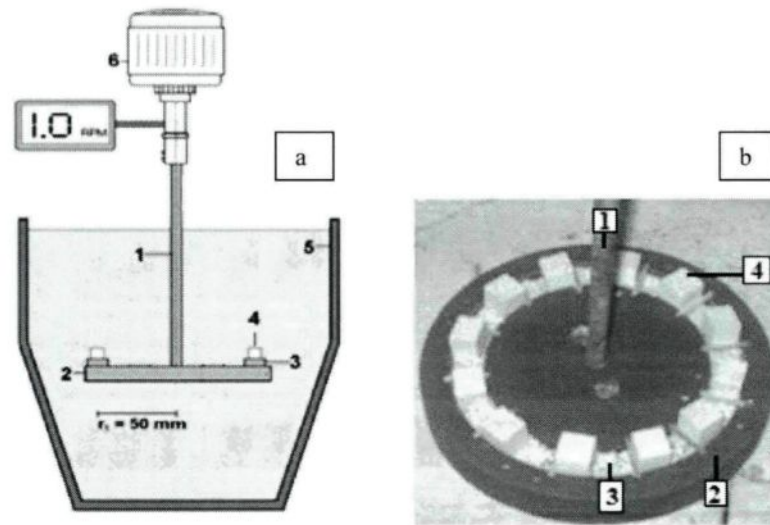
Components of set-up:

1. Alumina shaft
2. High Density Graphite Disc
3. Sample holder-Alumina or high density graphite
4. Alumina samples
5. SiC cylindrical crucible

Figure A1- 11: Rotating Disc Type Experimental System: (a) a Schematic View, (b) a Image of a Disc used in the Experiments.

The advantages of the system:

- Sample collection was possible without interrupting the experiment.

- The velocity of the metal around alumina samples were the line velocity of the disc. No other calculations were required to determine this speed.

- The time and material needed to run experiments were much shorter than the all other systems used in this study.

- Oxide formation on molten metal surface was minimal since the rotation of the shaft was less than 1 rpm. There was no violent molten metal movement in the system.

APPENDIX II

RESULTS OF PHYSICAL AND MATHEMATICAL MODELING OF

EXPERIMENTAL SYSTEM-I USING WATER

CASE 1 15 RPM ROTATIONAL SPEED

Zoomed view of filter section

(a)

CASE 1 30 RPM ROTATIONAL SPEED

Zoomed view of filter section

(b)
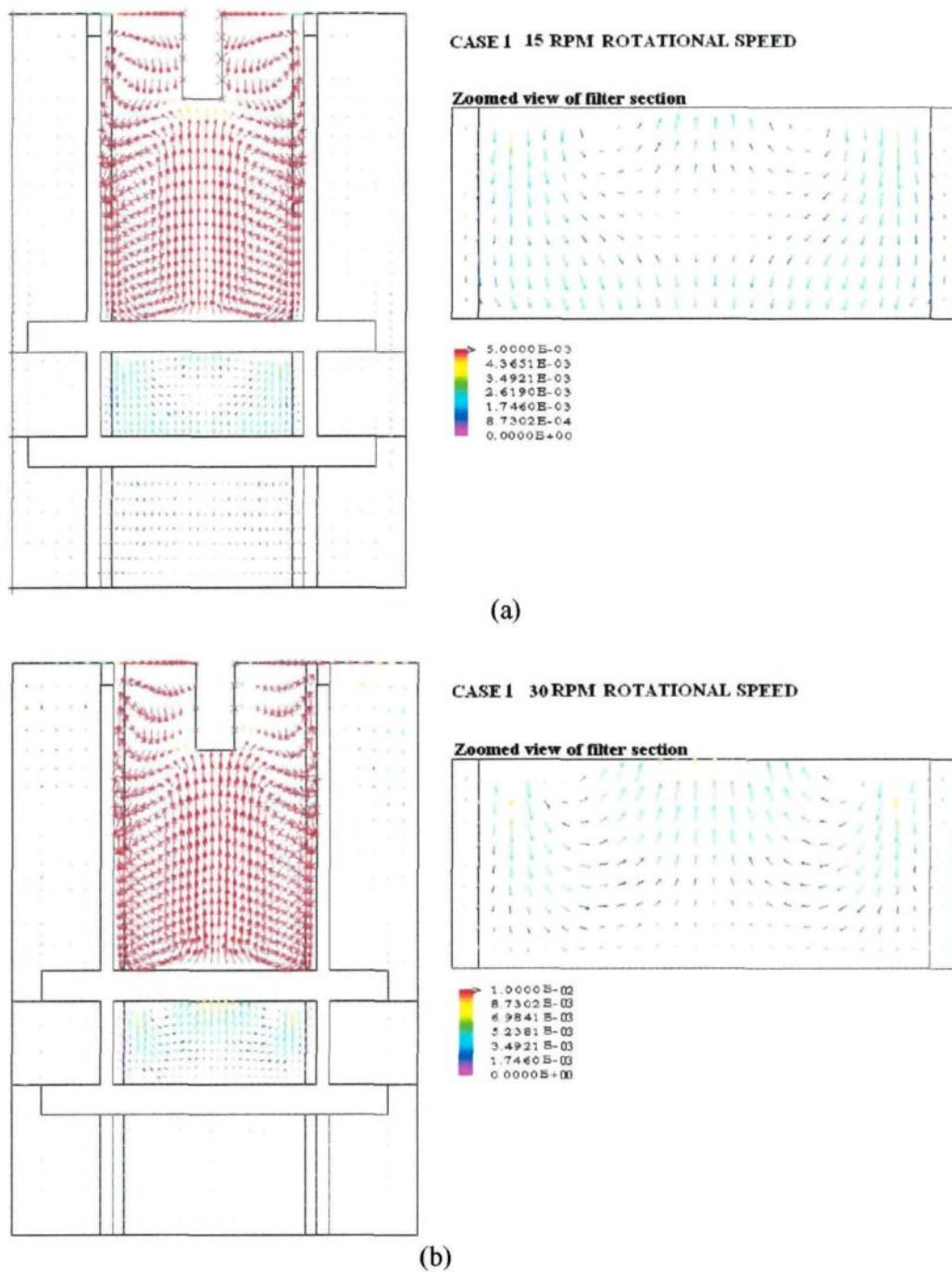
Figure A2-1: Effect of Rotational Speed on the Flow Field for, (a) Rotational Speed:15rpm, (b) Rotational Speed:30rpm.

CASE 2 15 RPM ROTATIONAL SPEED

Zoomed view of filter section

5.0000E-03
4.3651E-03
3.4921E-03
2.6190E-03
1.7460E-03
8.7302E-04
0.0000E+00

(a)

CASE 2 30 RPM ROTATIONAL SPEED

Zoomed view of filter section

1.0000E-02
8.7302E-03
6.9841E-03
5.2381E-03
3.4921E-03
1.7460E-03
0.0000E+00

(b)
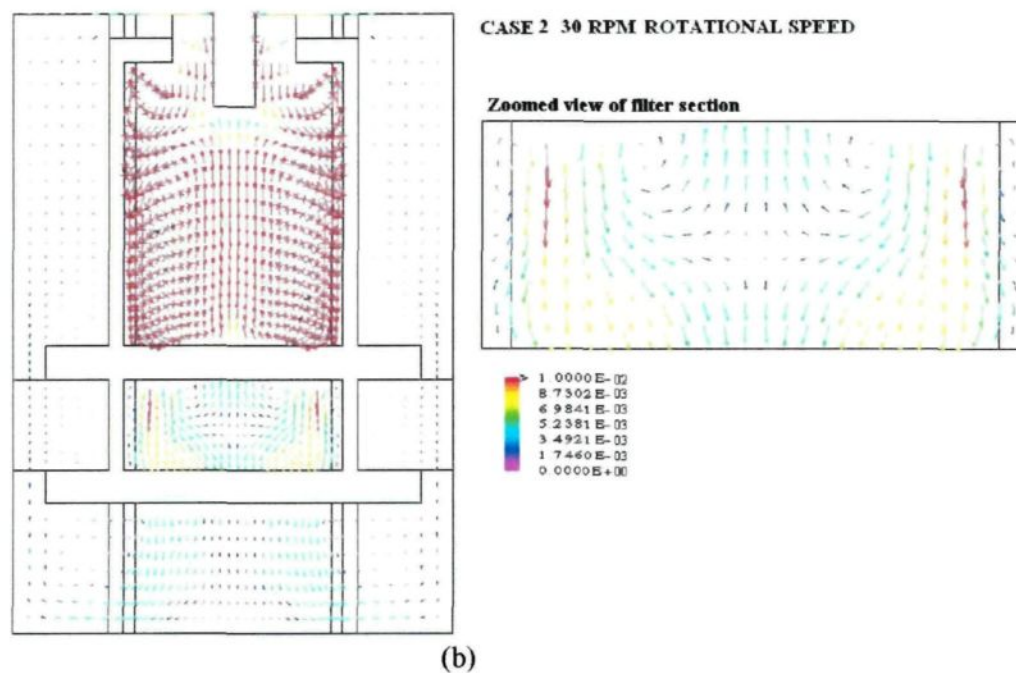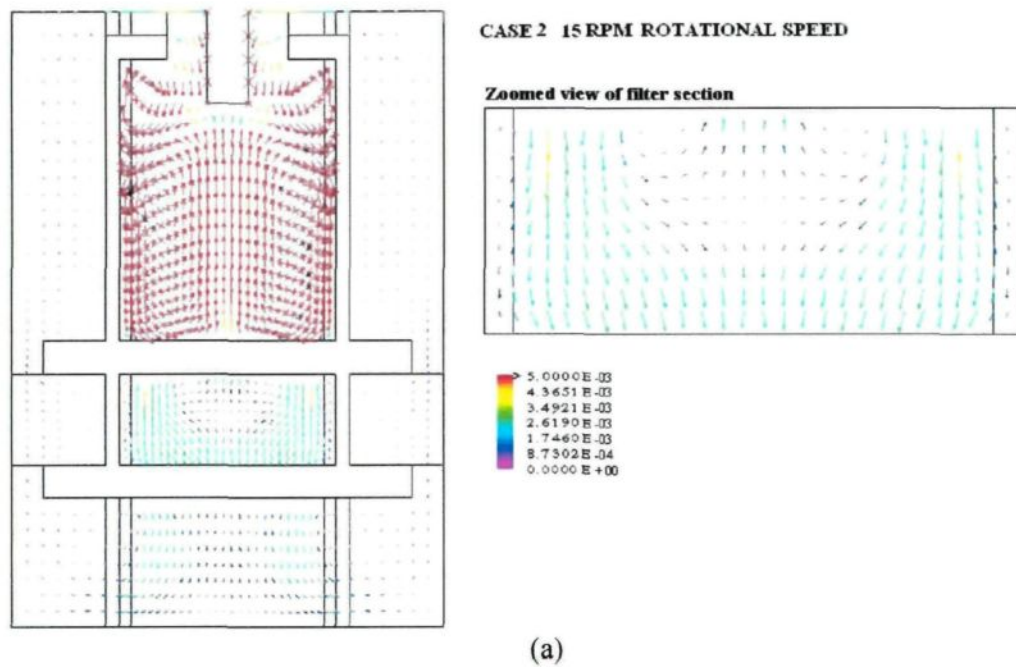
Figure A2-2: Effect of Rotational Speed for Case 2, (a) 15rpm, (b) 30rpm .

(a)

(b)
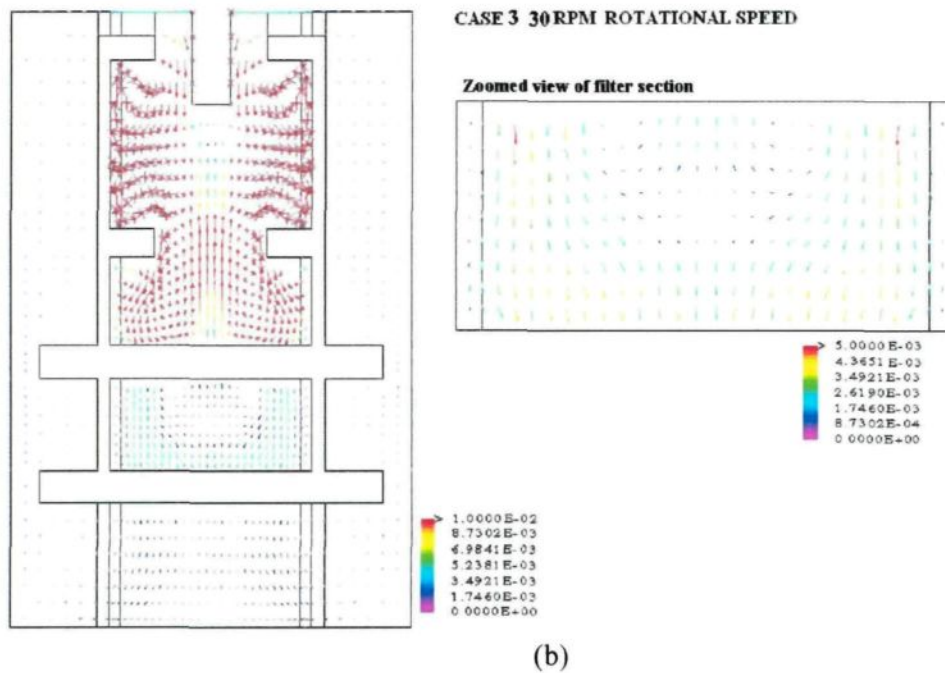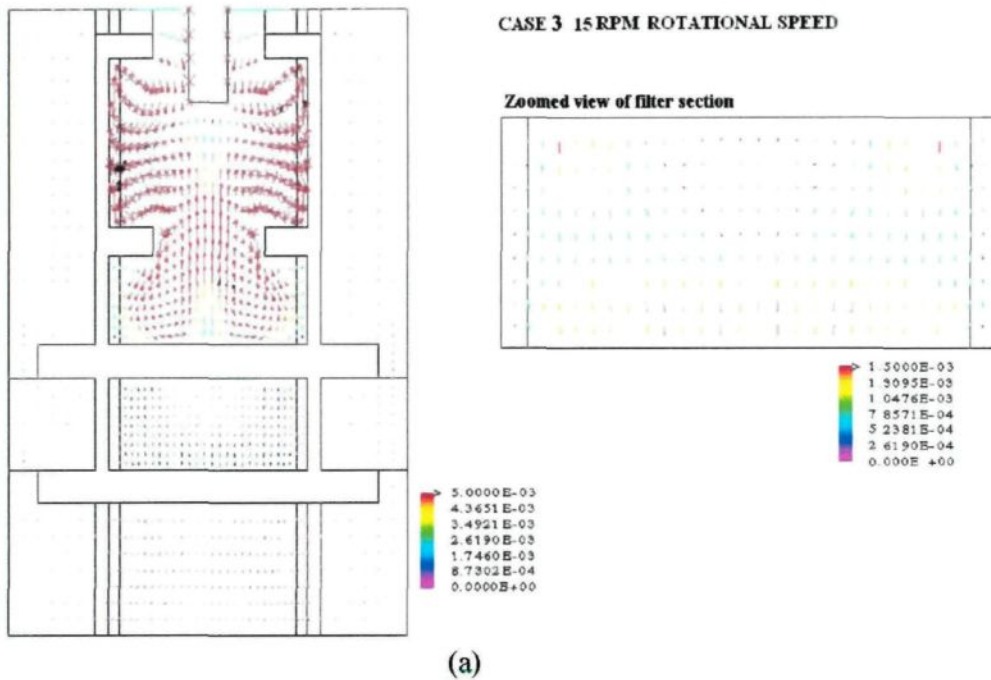
Figure A2-3: Effect of Rotational Speed for Case 3, (a) 15rpm, (b) 30rpm.

CASE 4 15 RPM ROTATIONAL SPEED

Zoomed view of filter section

1.8000E-03
1.5714E-03
1.2571E-03
9.4286E-04
6.2857E-04
3.1429E-04
0.0000E+00

5.0000E-03
4.3651E-03
3.4921E-03
2.6190E-03
1.7460E-03
8.7302E-04
0.0000E+00

(a)

CASE 4 30 RPM ROTATIONAL SPEED

Zoomed view of filter section

5.0000E-03
4.3651E-03
3.4921E-03
2.6190E-03
1.7460E-03
8.7302E-04
0.0000E+00

1.0000E-02
8.7302E-03
6.9841E-03
5.2381E-03
3.4921E-03
1.7460E-03
0.0000E+00

(b)

Figure A2-4: Effect of Rotational Speed for Case 4, (a) 15rpm, (b) 30rpm.

(a)

➤	4.0000E-03
	3.4921E-03
	2.7937E-03
	2.0952E-03
	1.3968E-03
	6.9841E-04
	0.0000E+00
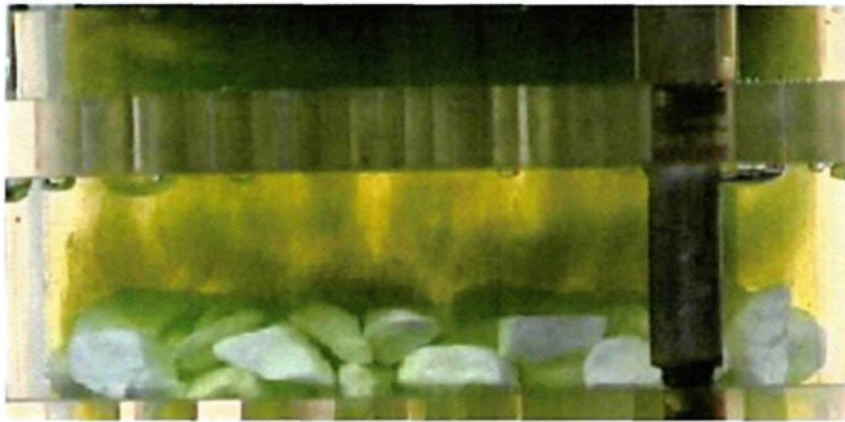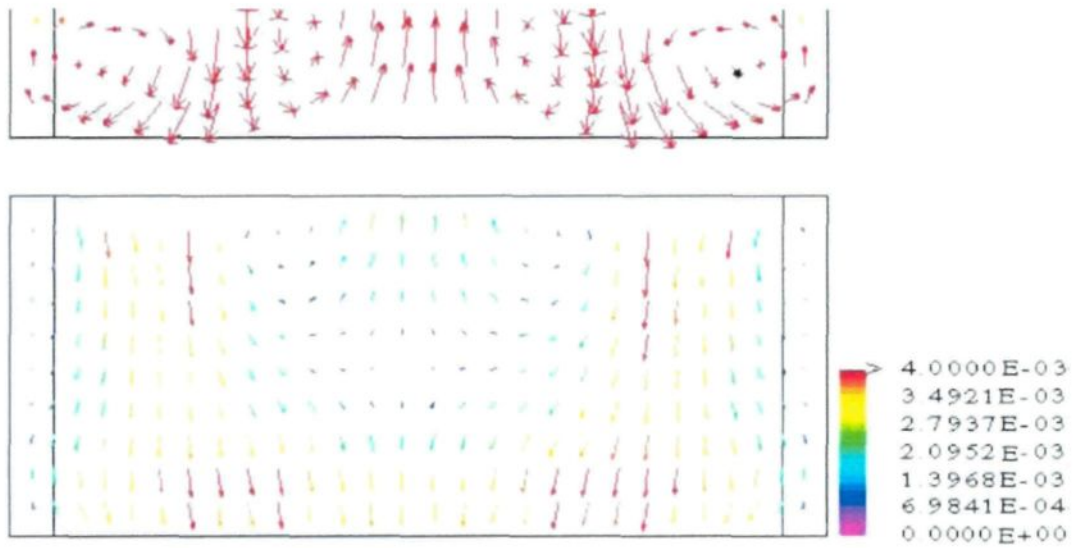
(b)

Figure A2-5: Comparisons of Flow Fields Between Experimental and Mathematical Model
Results for Case4-30rpm., (a) Experimental Result, (b) Mathematical Model Result.

CASE 5   15RPM ROTATIONAL SPEED

Zoomed view of filter section

3.0000E-03
2.6190E-03
2.0952E-03
1.5714E-03
1.0476E-03
5.2381E-04
0.0000E+00

5.0000E-03
4.3651E-03
3.4921E-03
2.6190E-03
1.7460E-03
8.7302E-04
0.0000E+00
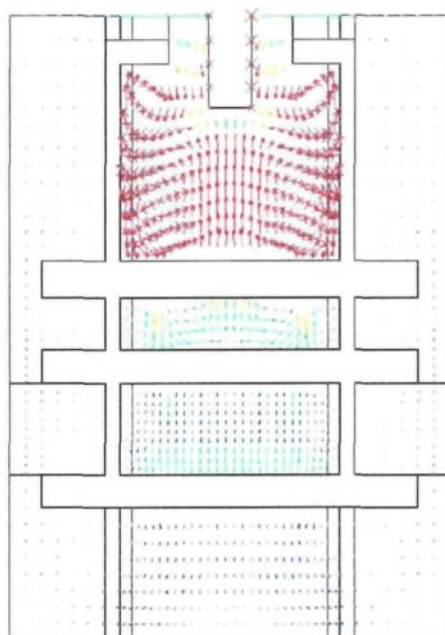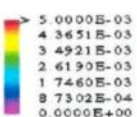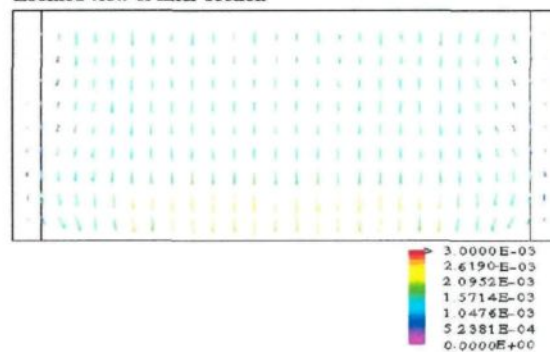
(a)

CASE 5   20RPM ROTATIONAL SPEED

Zoomed view of filter section

3.0000E-03
2.6190E-03
2.0952E-03
1.5714E-03
1.0476E-03
5.2381E-04
0.0000E+00

5.0000E-03
4.3651E-03
3.4921E-03
2.6190E-03
1.7460E-03
8.7302E-04
0.0000E+00

(b)

CASE 5 25RPM ROTATIONAL SPEED

Zoomed view of filter section

(c)

CASE 5 30RPM ROTATIONAL SPEED

Zoomed view of filter section

(d)
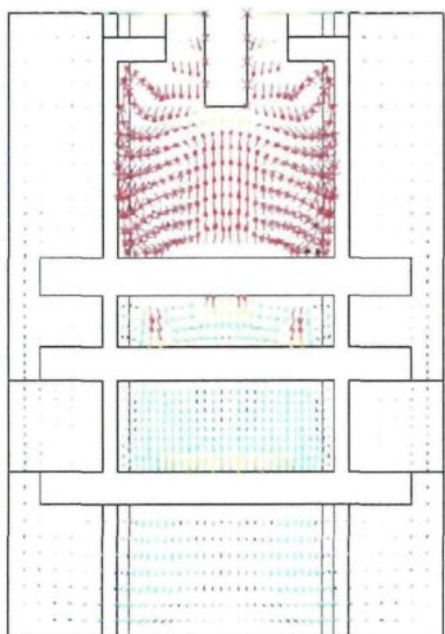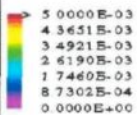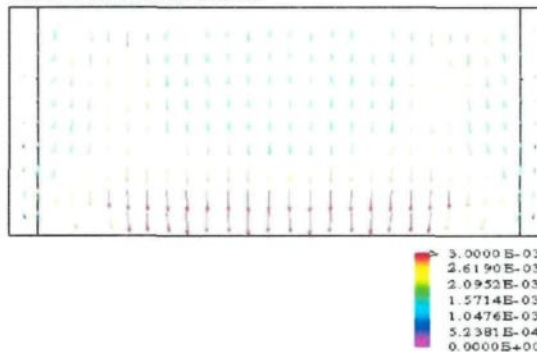
Figure A2-6: Effect of Rotational Speed for Case 5, (a) 15rpm, (b) 20rpm, (c) 25 rpm, (d) 30rpm.

(a)

	5.0000E-03
	4.3651E-03
	3.4921E-03
	2.6190E-03
	1.7460E-03
	8.7302E-04
	0.0000E+00
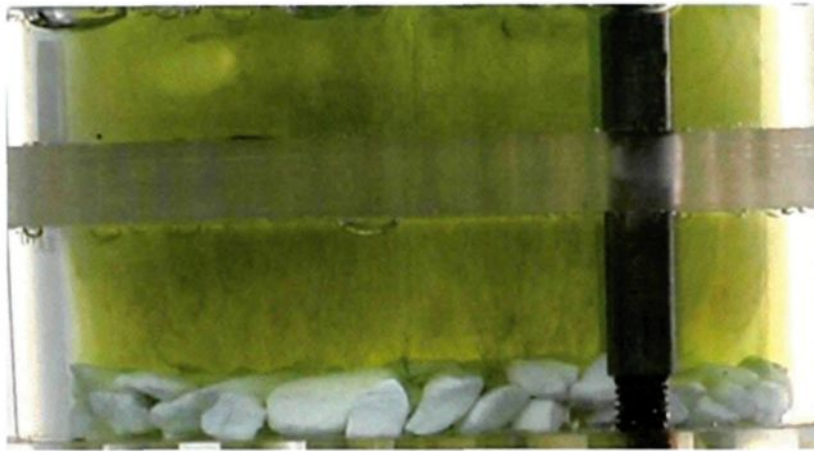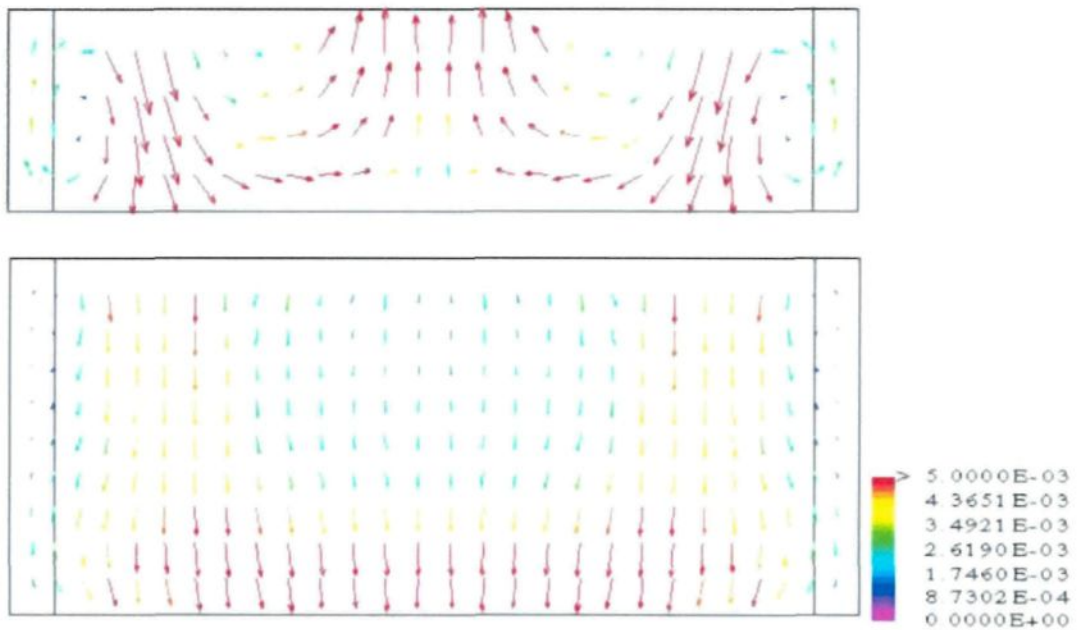
(b)

Figure A2-7: Comparisons of Flow Fields between Experimental and Mathematical Model Results for Case5-30rpm., (a) Experimental Result, (b) Mathematical Model Result.

CASE 6 15 RPM ROTATIONAL SPEED

Zoomed view of filter section

> 2.0000E-03
1.7460E-03
1.3968E-03
1.0476E-03
6.9841E-04
3.4921E-04
0.0000E+00

> 5.0000E-03
4.3651E-03
3.4921E-03
2.6190E-03
1.7460E-03
8.7302E-04
0.0000E+00

(a)

CASE 6 20 RPM ROTATIONAL SPEED

Zoomed view of filter section

> 5.0000E-03
4.3651E-03
3.4921E-03
2.6190E-03
1.7460E-03
8.7302E-04
0.0000E+00

(b)

(c)

CASE 6 30 RPM ROTATIONAL SPEED

Zoomed view of filter section
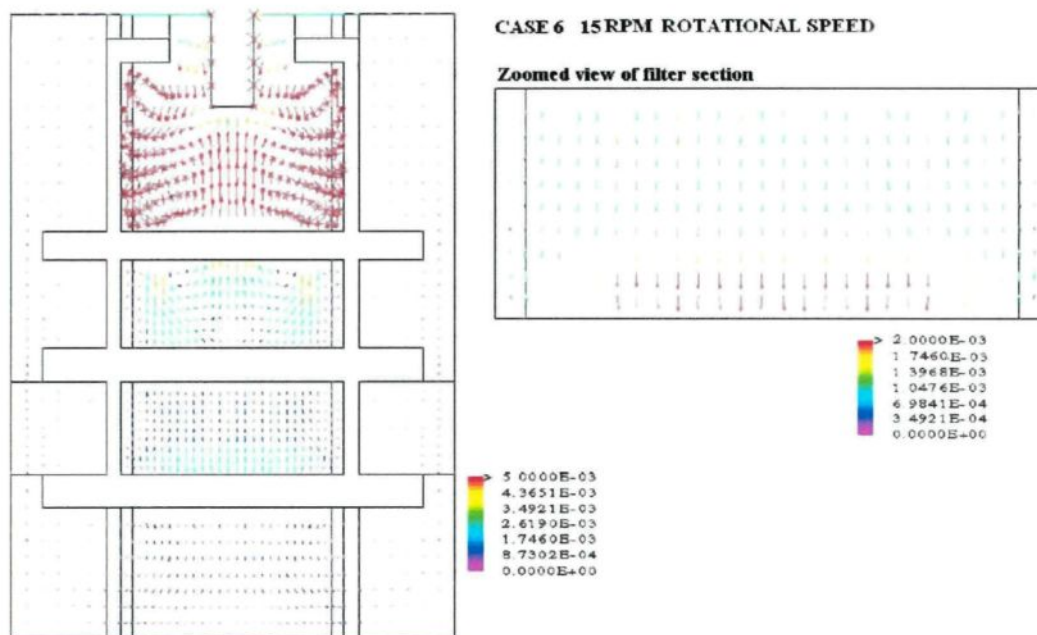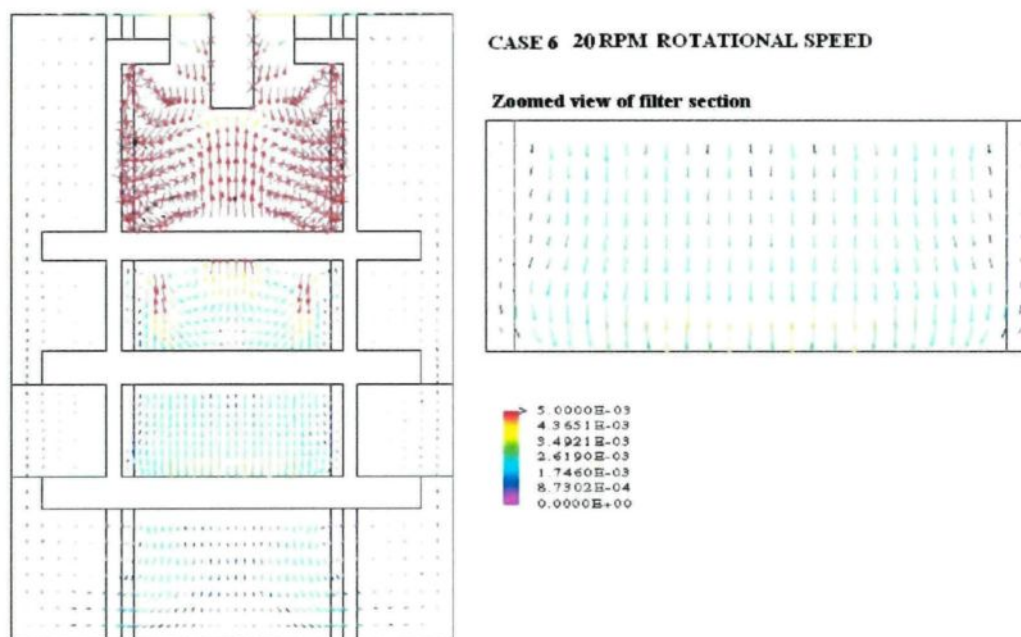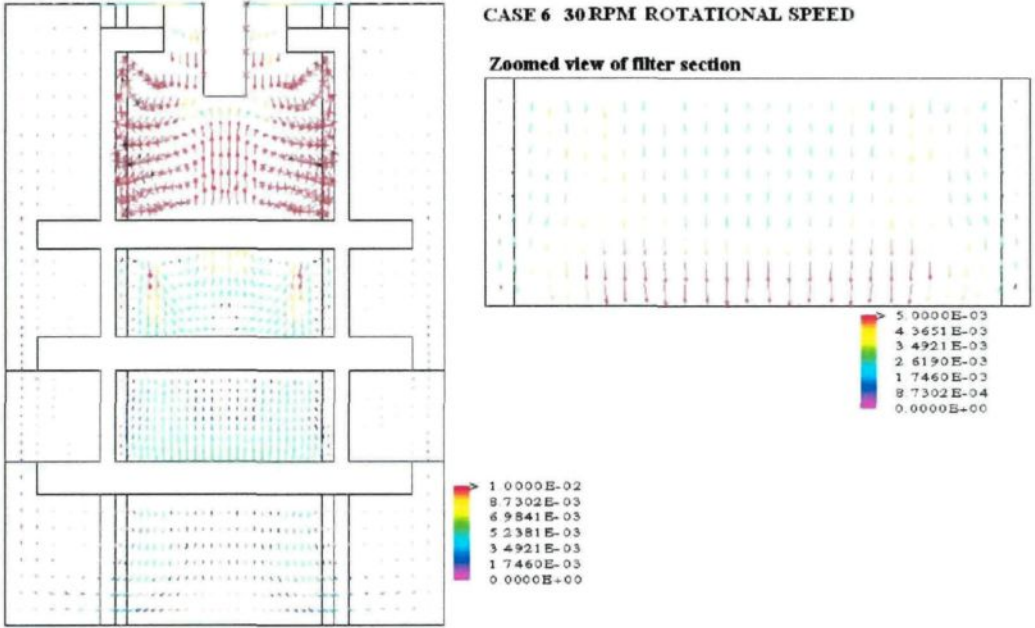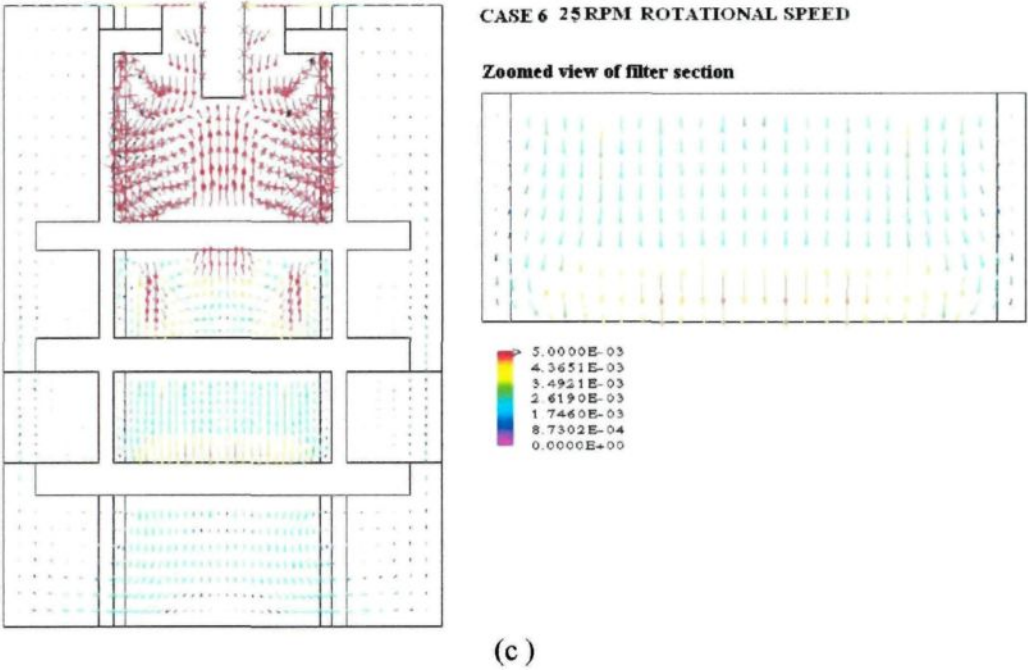
Figure A2-8: Effect of Rotational Speed for Case 6, (a) 15rpm, (b) 20rpm, (c) 25 rpm, (d) 30rpm.
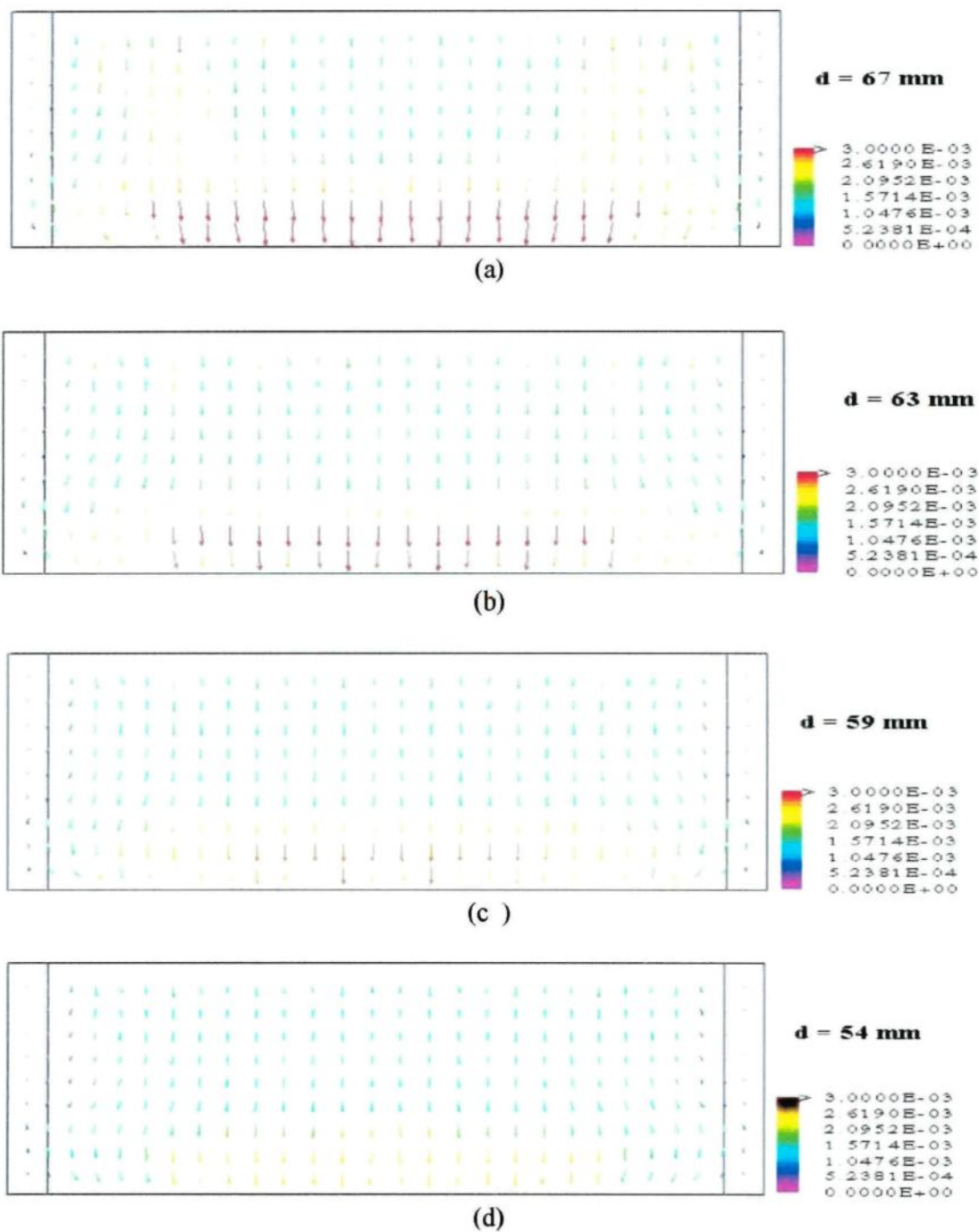
Figure A2-9: Effect of Mixer Diameter (Case 7) on Flow (a) 67mm , (b) 63mm , (c)59mm, (d)54 mm.
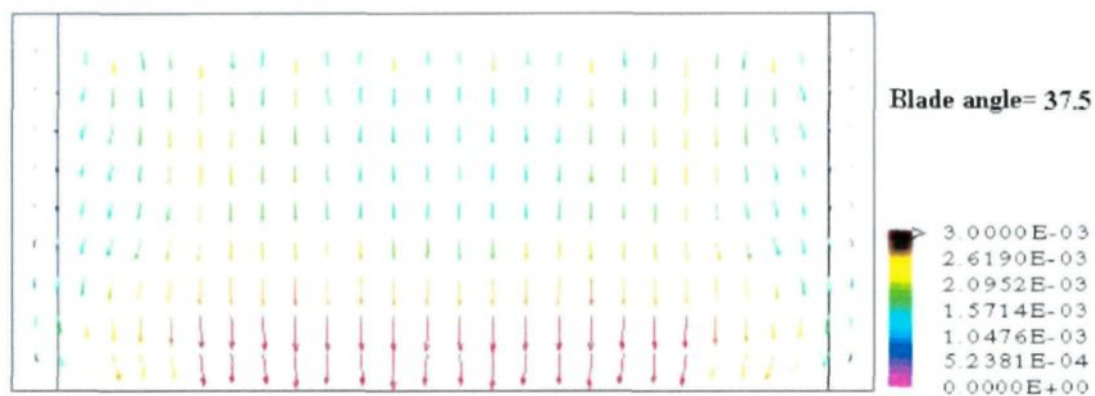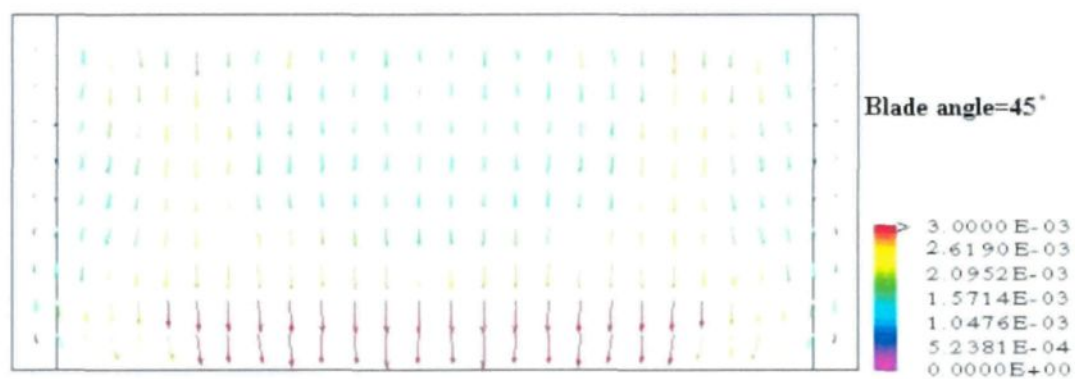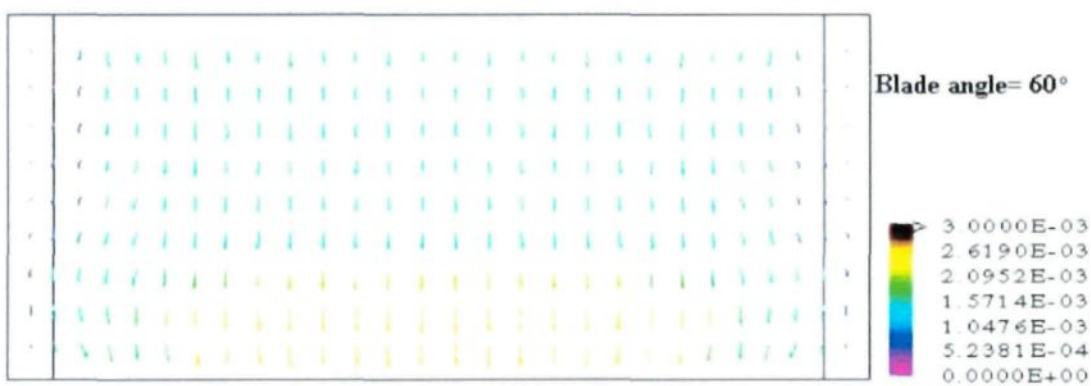
Figure A2-10: Effect of Mixer Angle (Case 8) on Flow (a) 37.5°, (b) 45°, (c) 60 °.

254
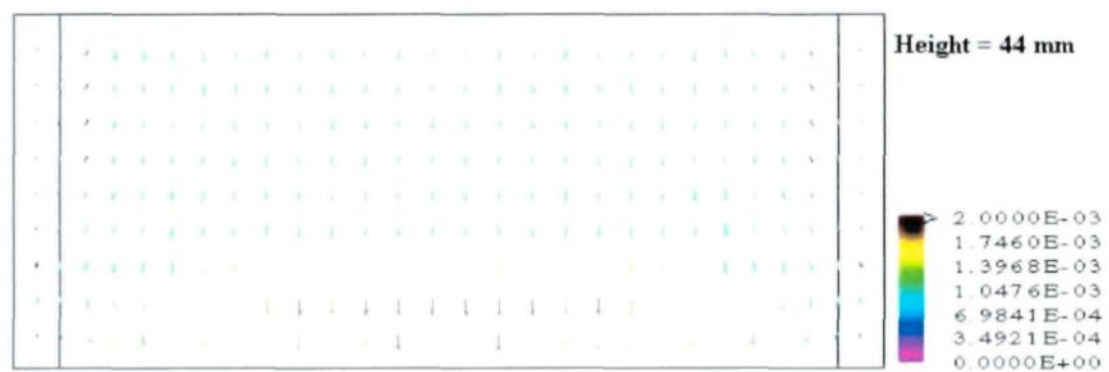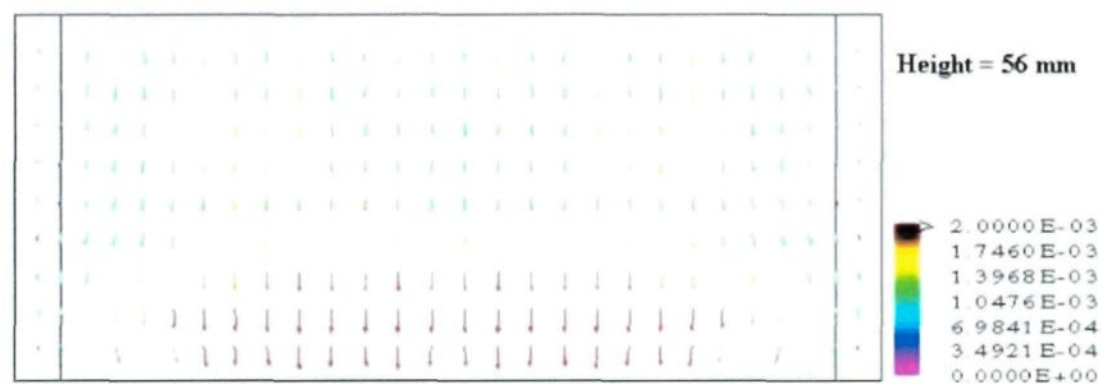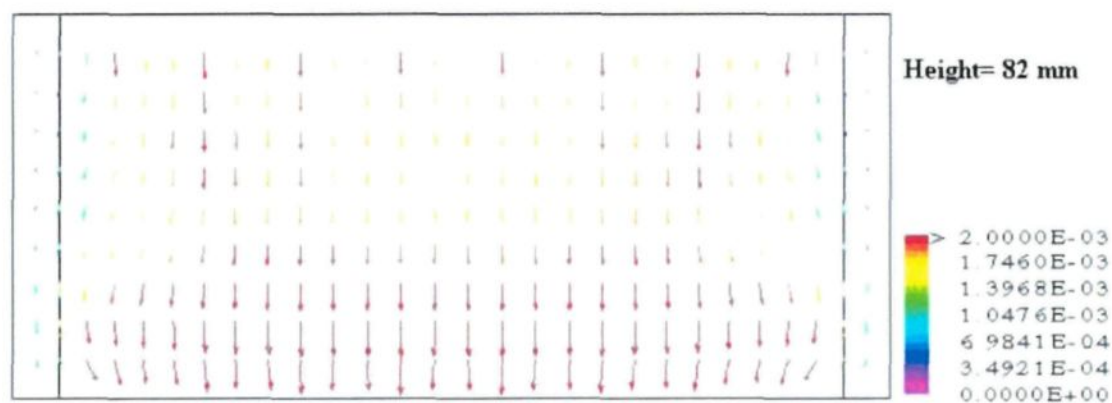
Figure A2-11: Effect of Distance between Mixer and Top Plate (Case 9) on Flow (a) 44 mm, (b) 56 mm, (c) 82mm.

(a)

(b)

(c)
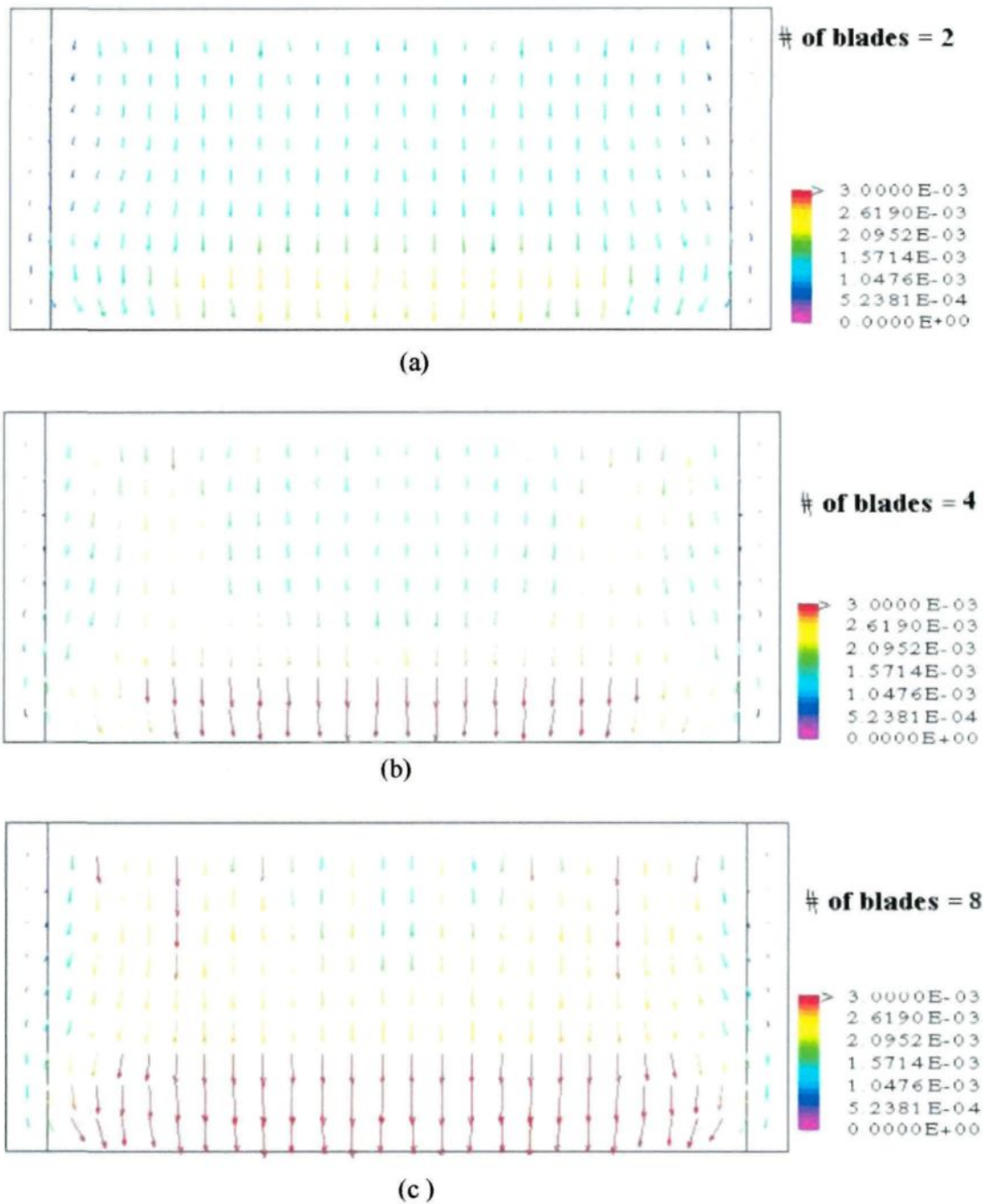
Figure A2-12: Effect of Mixer Blades (Case 10) on Flow (a) 2, (b) 4, (c) 8.

(a)

(b)

(c)

(d)
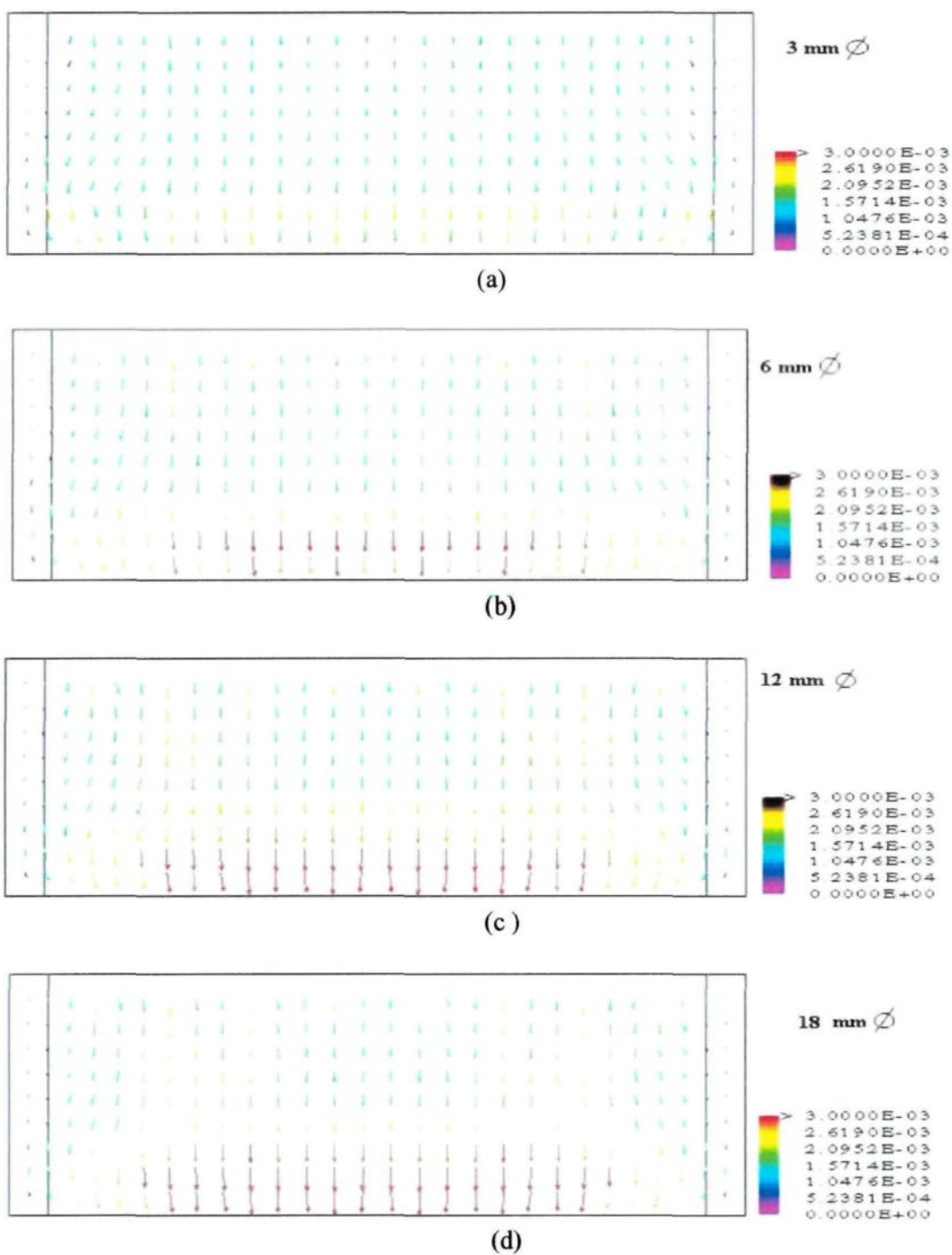
Figure A2-13: Effect of Particle Size (Case 11) on Flow (a)3mm, (b) 6 mm, (c)12 mm, (d)18 mm.
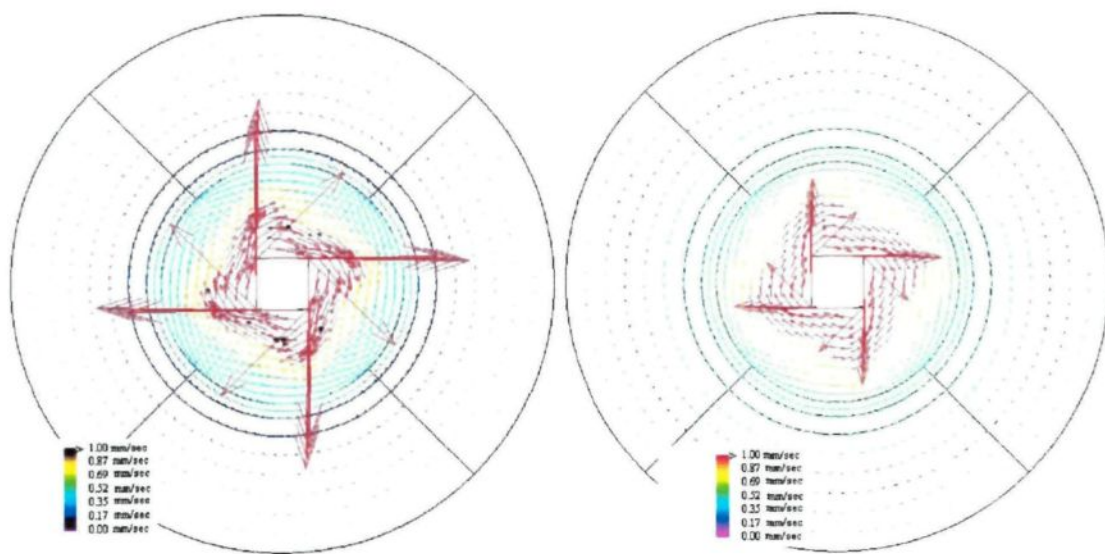
Figure A2-14: Effect of Mixer Rotational Velocity on Surface Flow in the Crucible, (a) 20 rpm, (b) 3 rpm.

APPENDIX III

AFFECTED ZONE THICKNESS MEASUREMENT RESULTS

1. Static Experiments
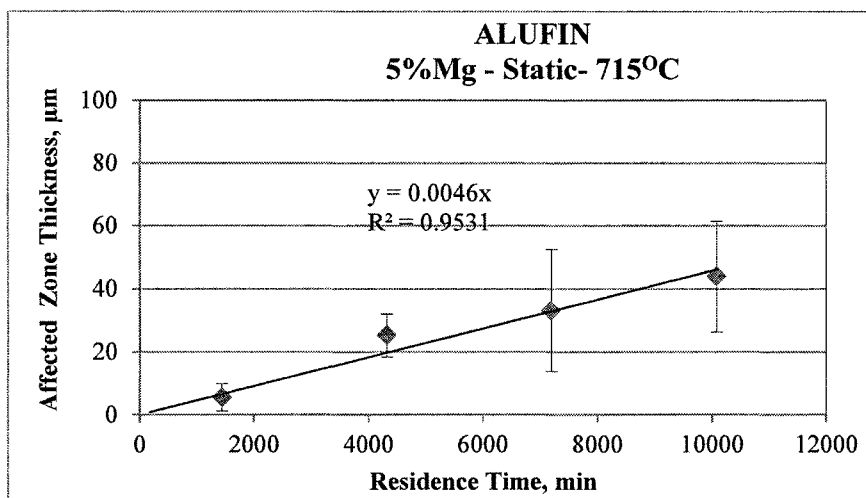
Figure A3- 1: Alufin Static Experiment Results
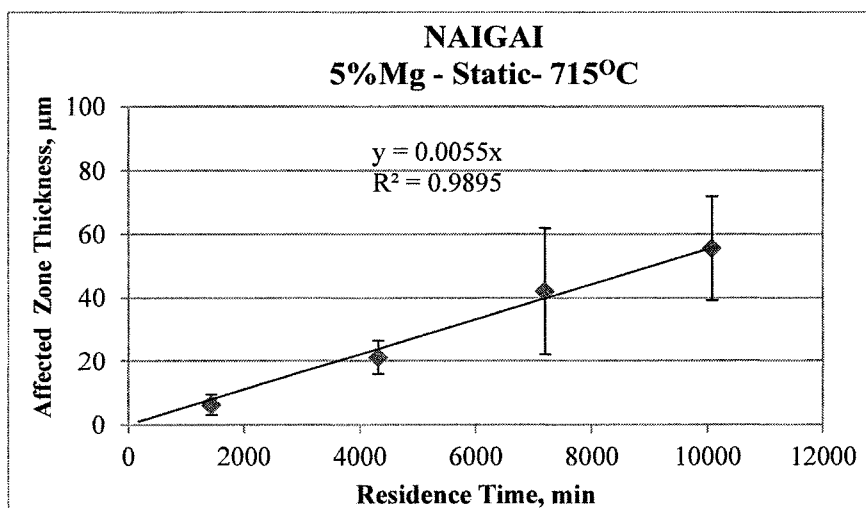
Figure A3- 2: Naigai Static Experiment Results
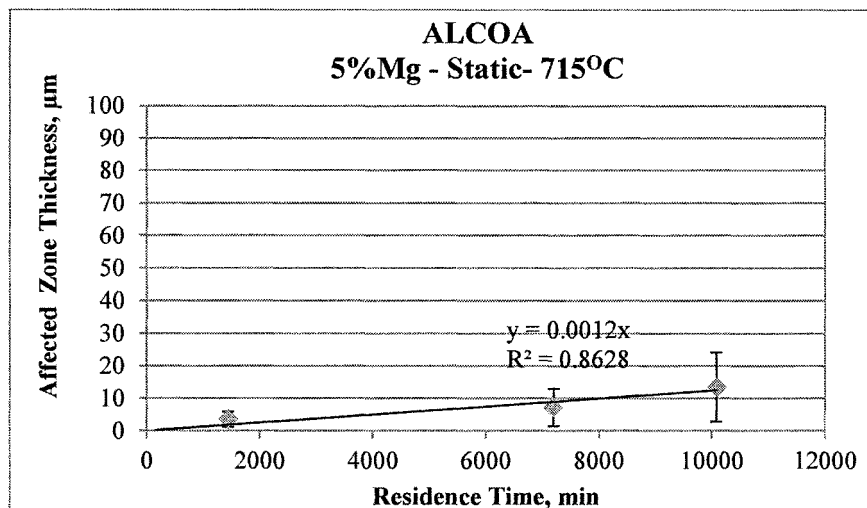
Figure A3- 3: Alcoa Static Experiment Results
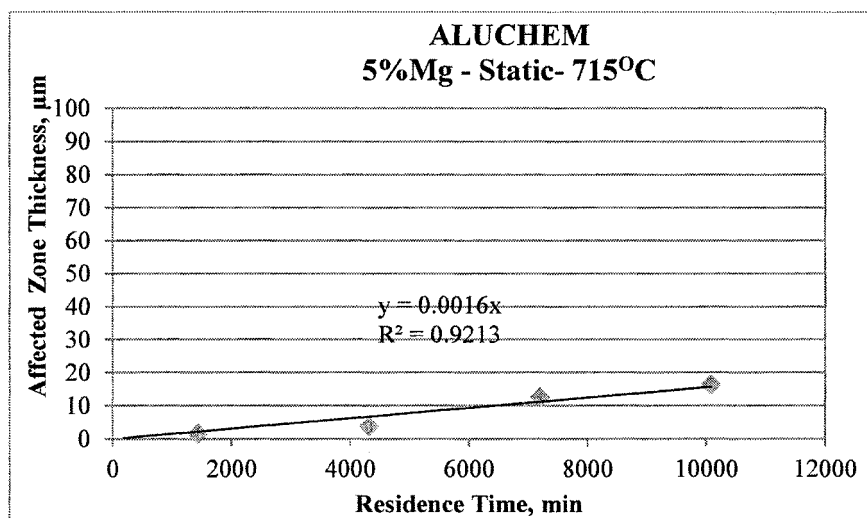
Figure A3- 4: Aluchem Static Experiment Results

2. Dynamic Experiments with 2%Mg-Al Alloy
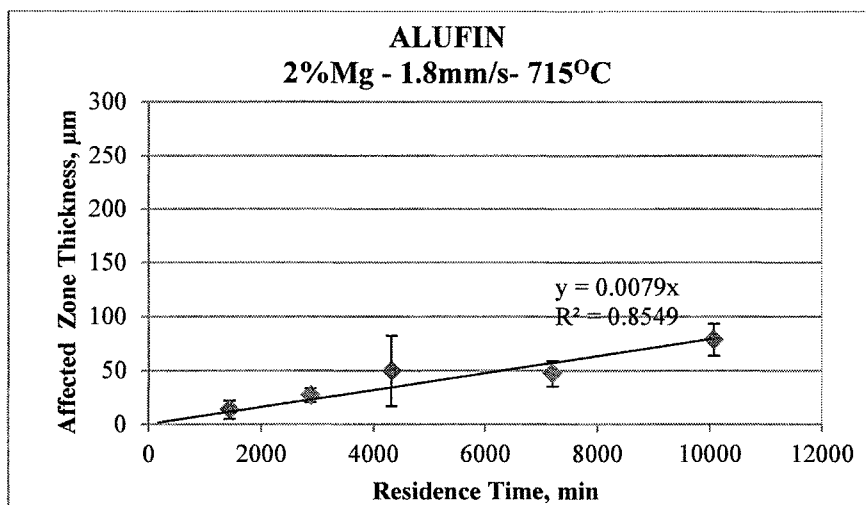
Figure A3- 5: Alufin Dynamic Experiment Results
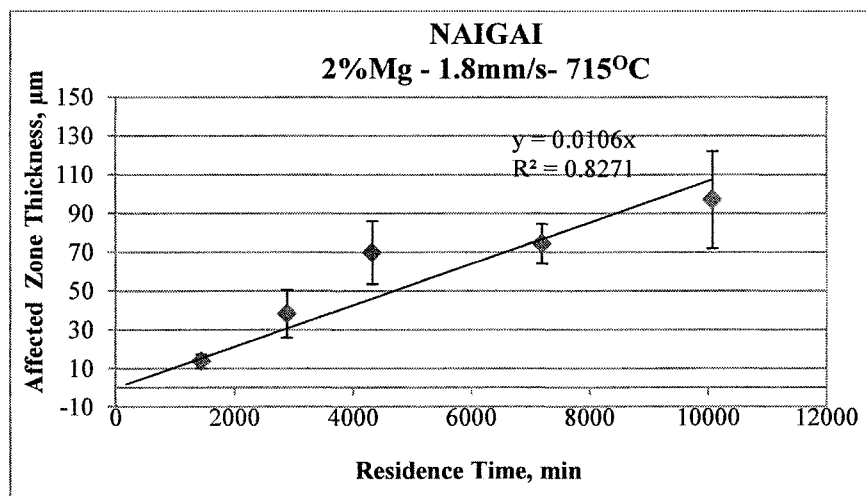
Figure A3- 6: Naigai Dynamic Experiment with 2%Mg-Al Alloy Results
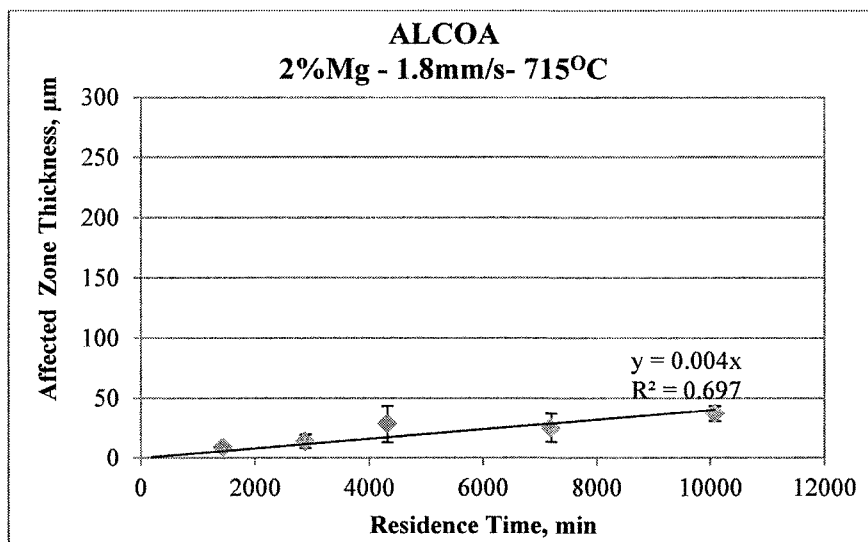
Figure A3- 7: Alcoa Dynamic Experiment with 2%Mg-Al Alloy Results
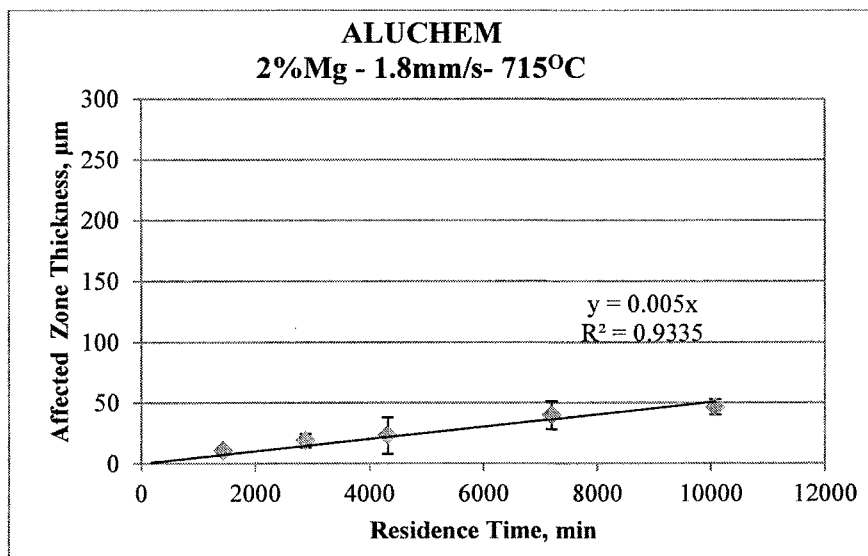
Figure A3- 8: Aluchem Dynamic Experiment with 2%Mg-Al Alloy Results

3. Dynamic Experiments with 5%Mg-Al Alloy

ALUFIN
5%Mg - 1.8mm/s- 715°C

$y = 0.0116x$
$R^2 = 0.9789$
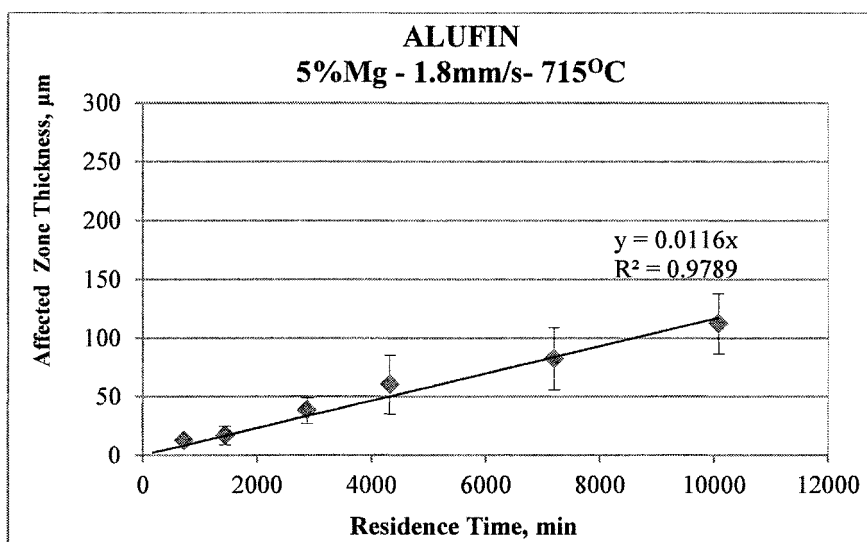
Figure A3- 9: Alufin Dynamic Experiment with 5%Mg-Al Alloy Results

NAIGAI
5%Mg - 1.8mm/s- 715°C

$y = 0.0137x$
$R^2 = 0.8377$
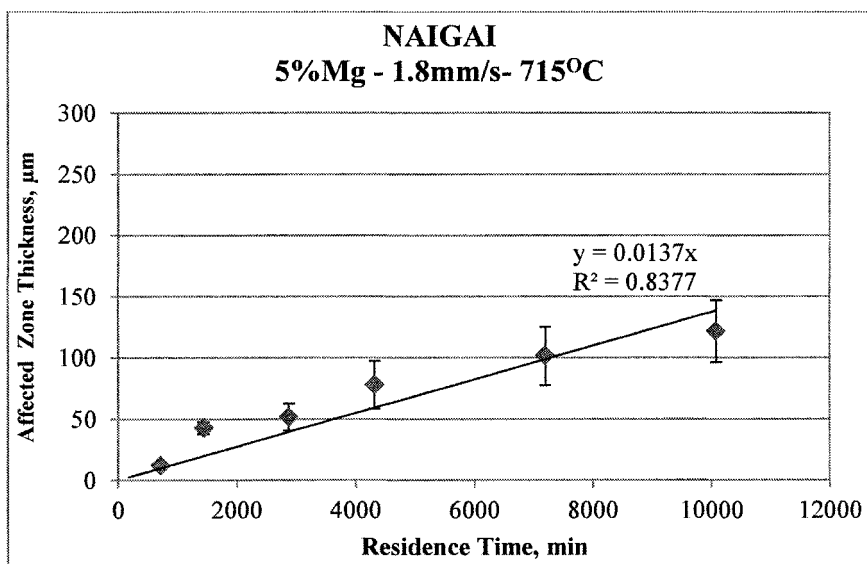
Figure A3- 10: Naigai Dynamic Experiment with 5%Mg-Al Alloy Results

ALCOA
5%Mg - 1.8mm/s- 715°C

$y = 0.0064x$
$R^2 = 0.9094$
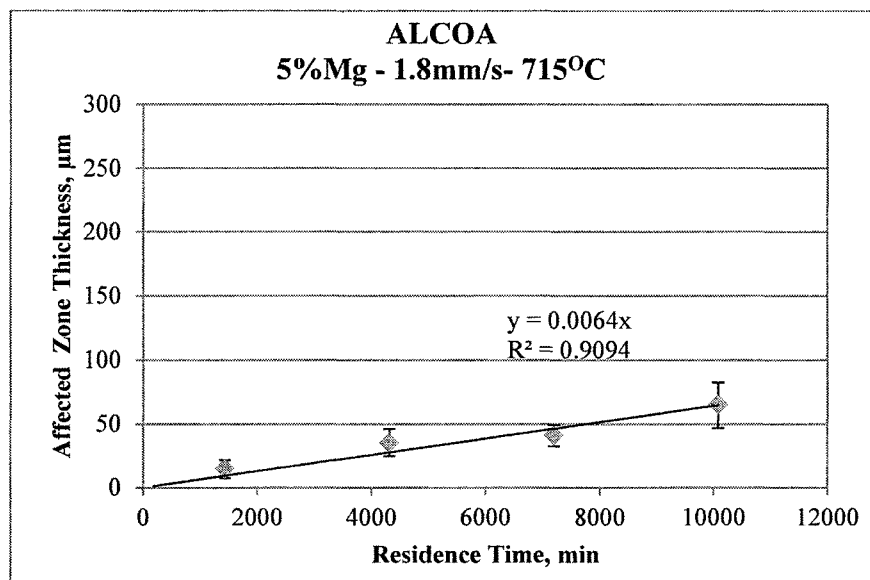
Figure A3- 11: Alcoa Dynamic Experiment with 5%Mg-Al Alloy Results

ALUCHEM
5%Mg - 1.8mm/s- 715°C

$y = 0.0066x$
$R^2 = 0.7929$
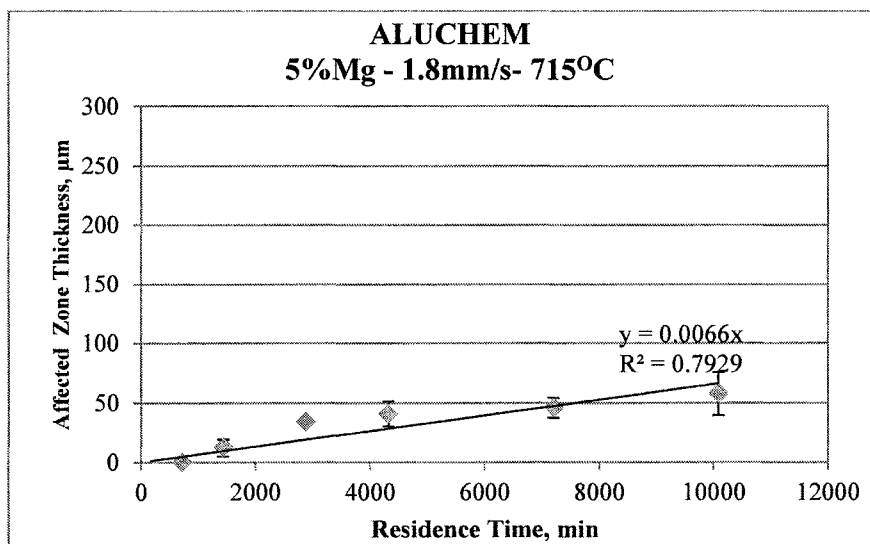
Figure A3- 12: Aluchem Dynamic Experiment with 5%Mg-Al Alloy Results

4. Dynamic Experiments with 7%Mg-Al Alloy
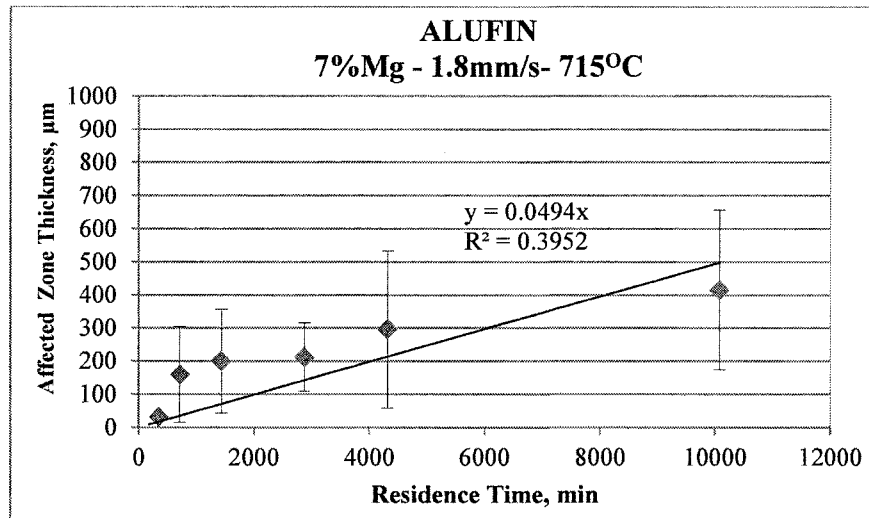
Figure A3- 13: Alufin Dynamic Experiment with 7%Mg-Al Alloy Results
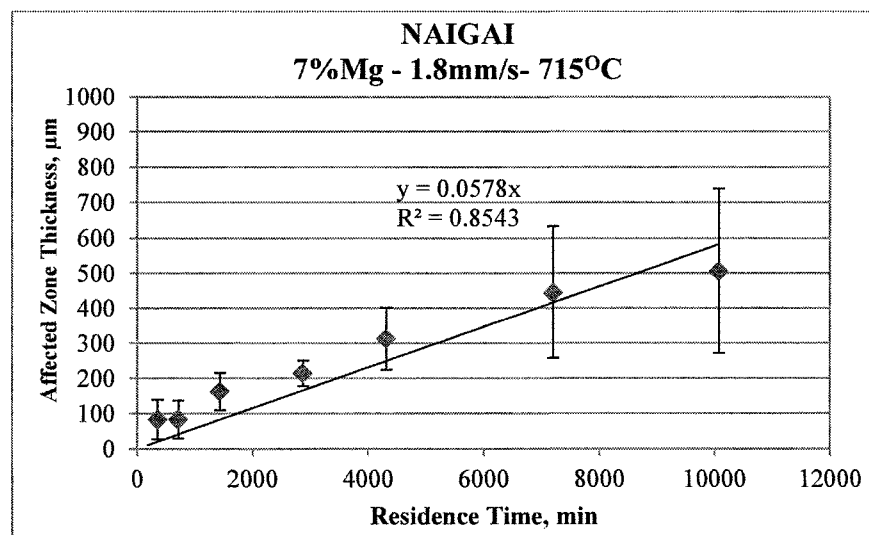
Figure A3- 14: Naigai Dynamic Experiment with 7%Mg-Al Alloy Results
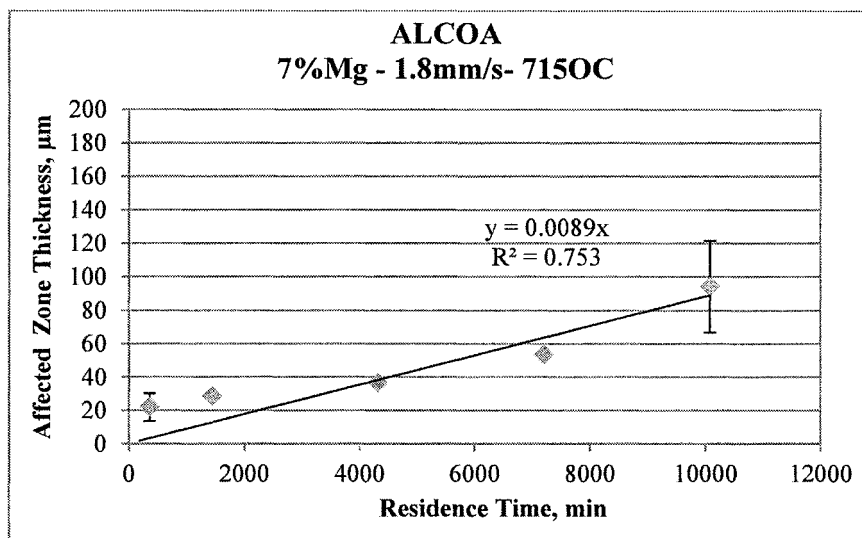
Figure A3- 15: Alcoa Dynamic Experiment with 7%Mg-Al Alloy Results
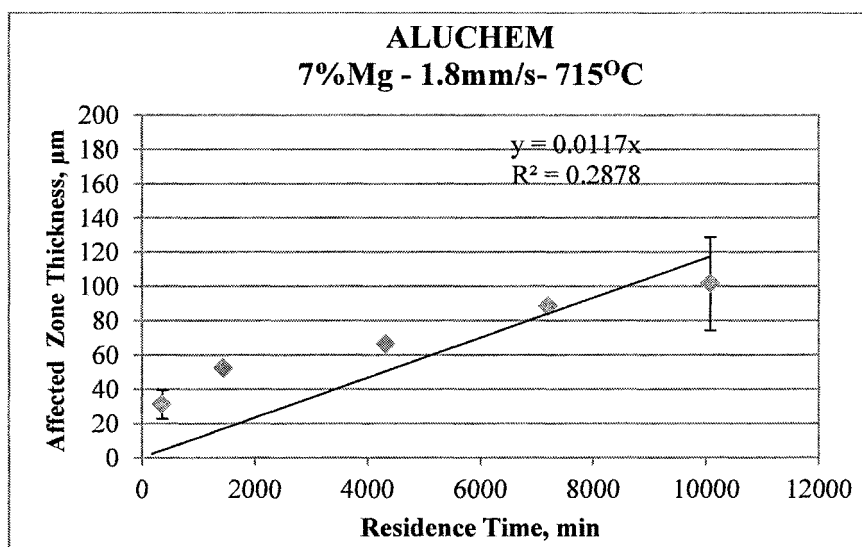
Figure A3- 16: Alcoa Dynamic Experiment with 7%Mg-Al Alloy Results

5. Dynamic Experiments with 3.6mm/s Flow Velocity using 5%Mg-Al Alloy
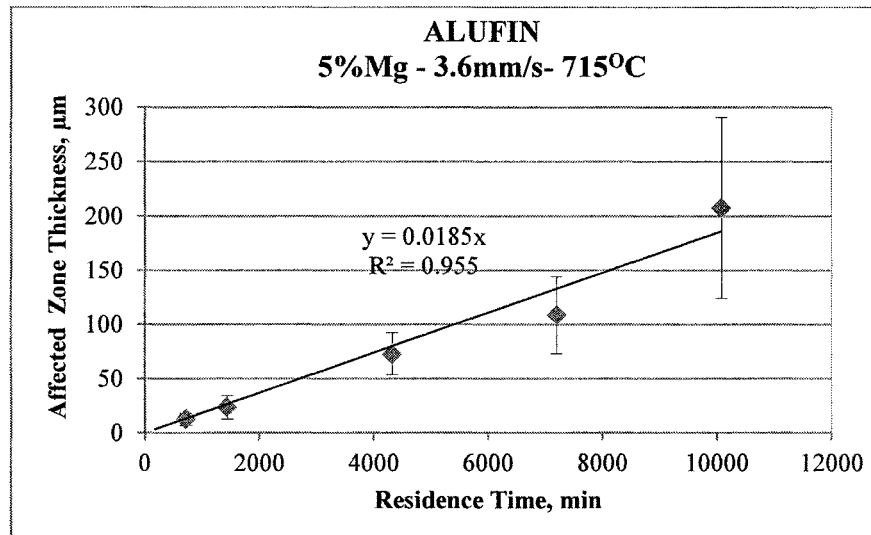
Figure A3- 17: Alufin Dynamic Experiment Results - 3.6mm/s Flow Velocity
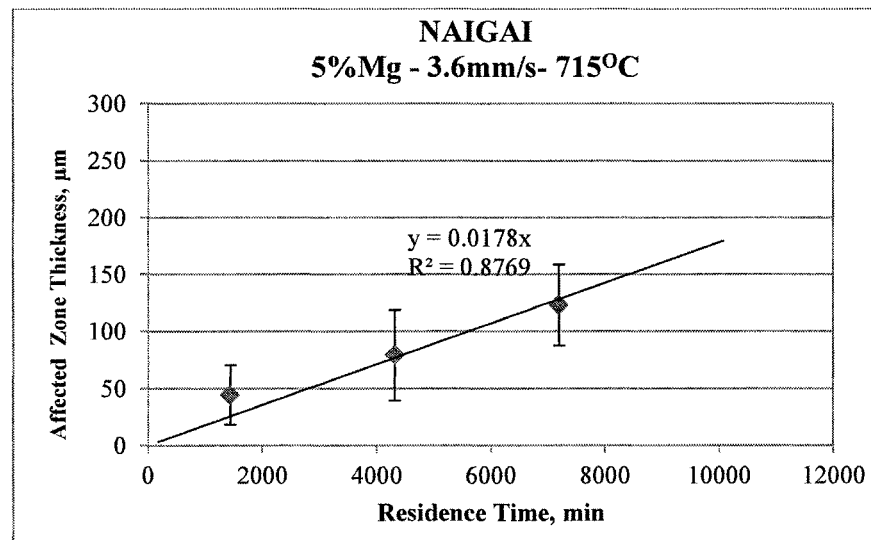
Figure A3- 18: Naigai Dynamic Experiment Results - 3.6mm/s Flow Velocity
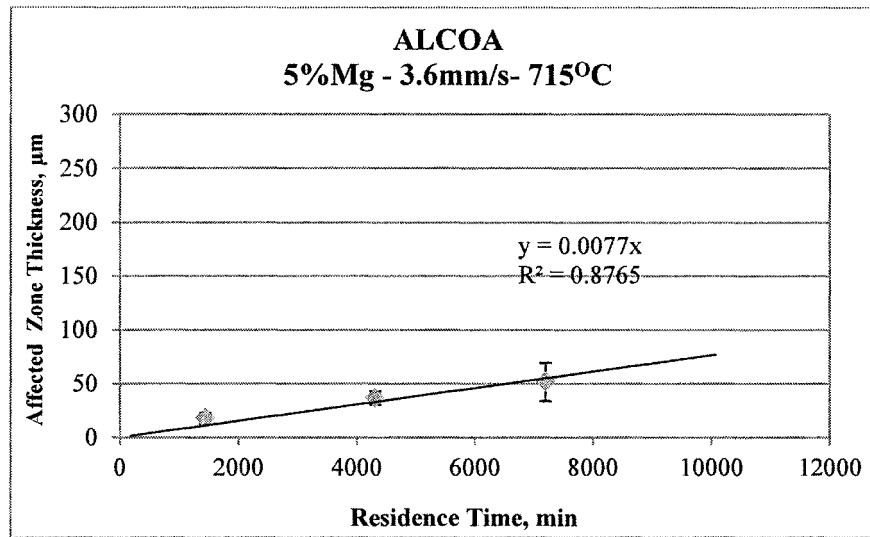
Figure A3- 19: Alcoa Dynamic Experiment Results - 3.6mm/s Flow Velocity
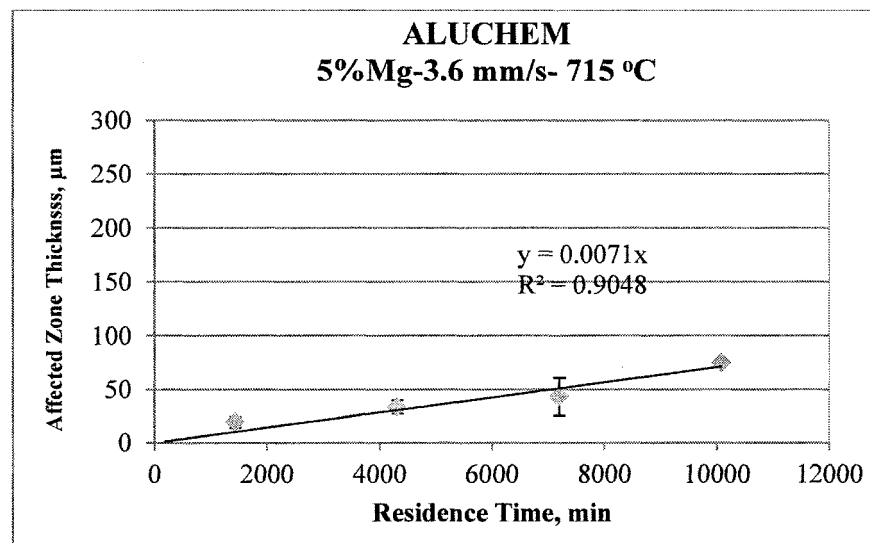
Figure A3- 20: Aluchem Dynamic Experiment Results - 3.6mm/s Flow Velocity

6. Dynamic Experiments using 5%Mg-Al Alloy at 750°C
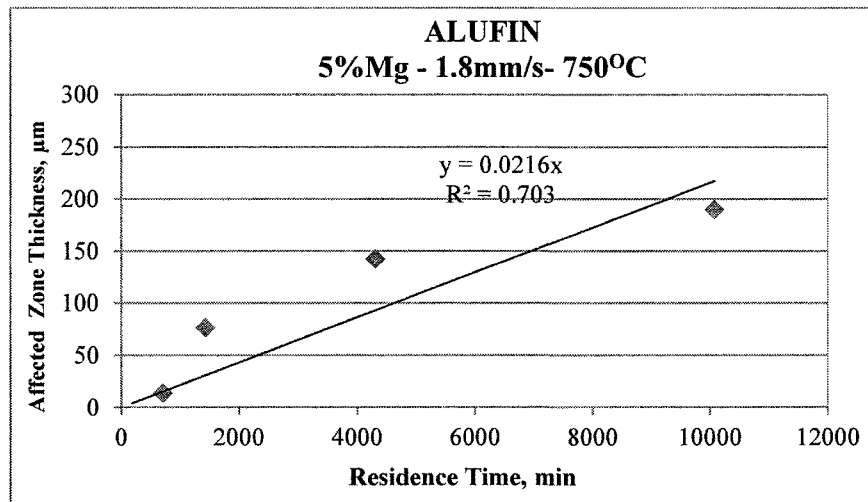
Figure A3- 21: Alufin Dynamic Experiments at 750°C
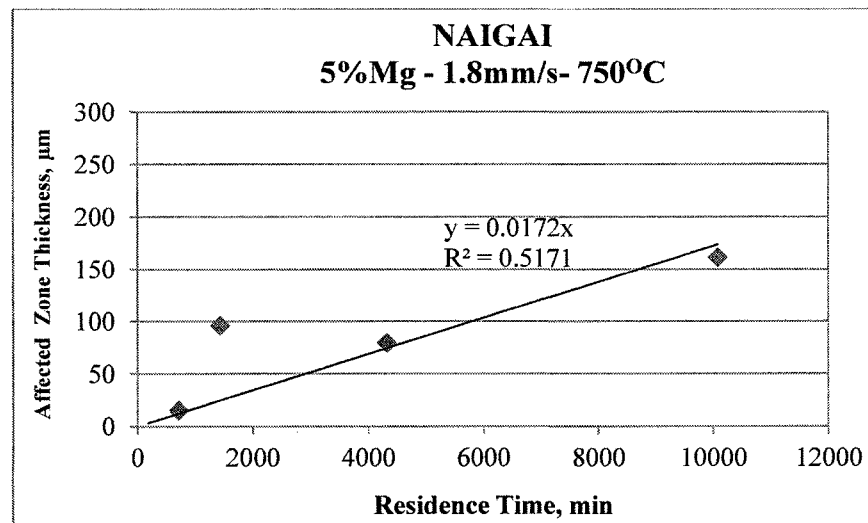
Figure A3- 22: Naigai Dynamic Experiments at 750°C
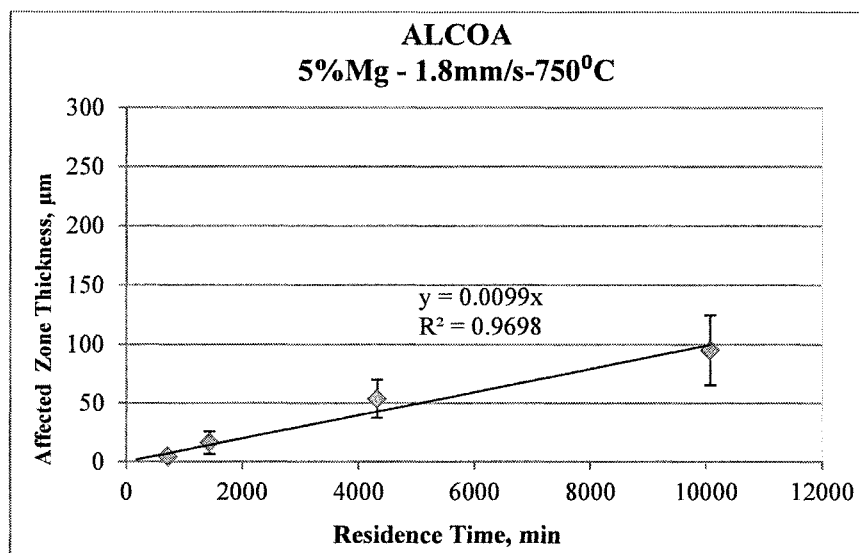
Figure A3- 23: Alcoa Dynamic Experiments at 750°C
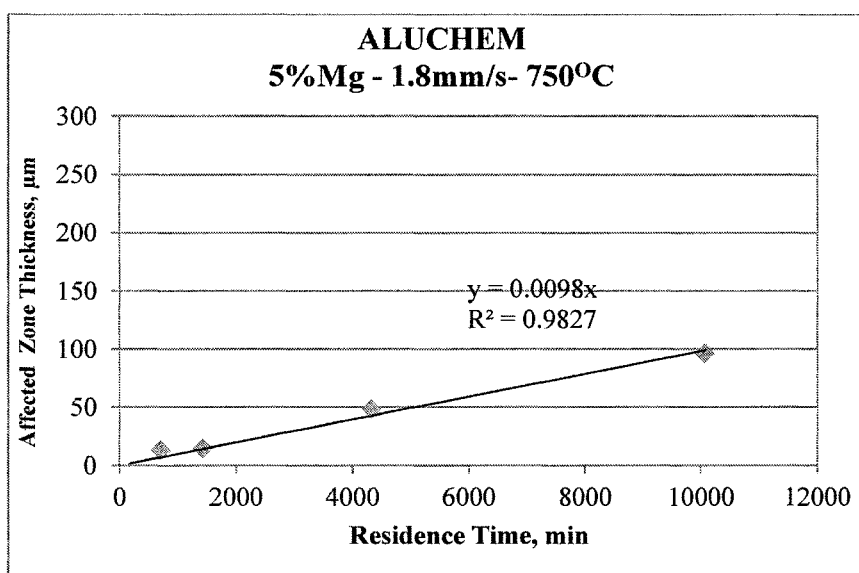
Figure A3- 24: Aluchem Dynamic Experiments at 750°C

APPENDIX IV

METALLOGRAPHIC INVESTIGATION ANALYSIS AND SEM RESULTS
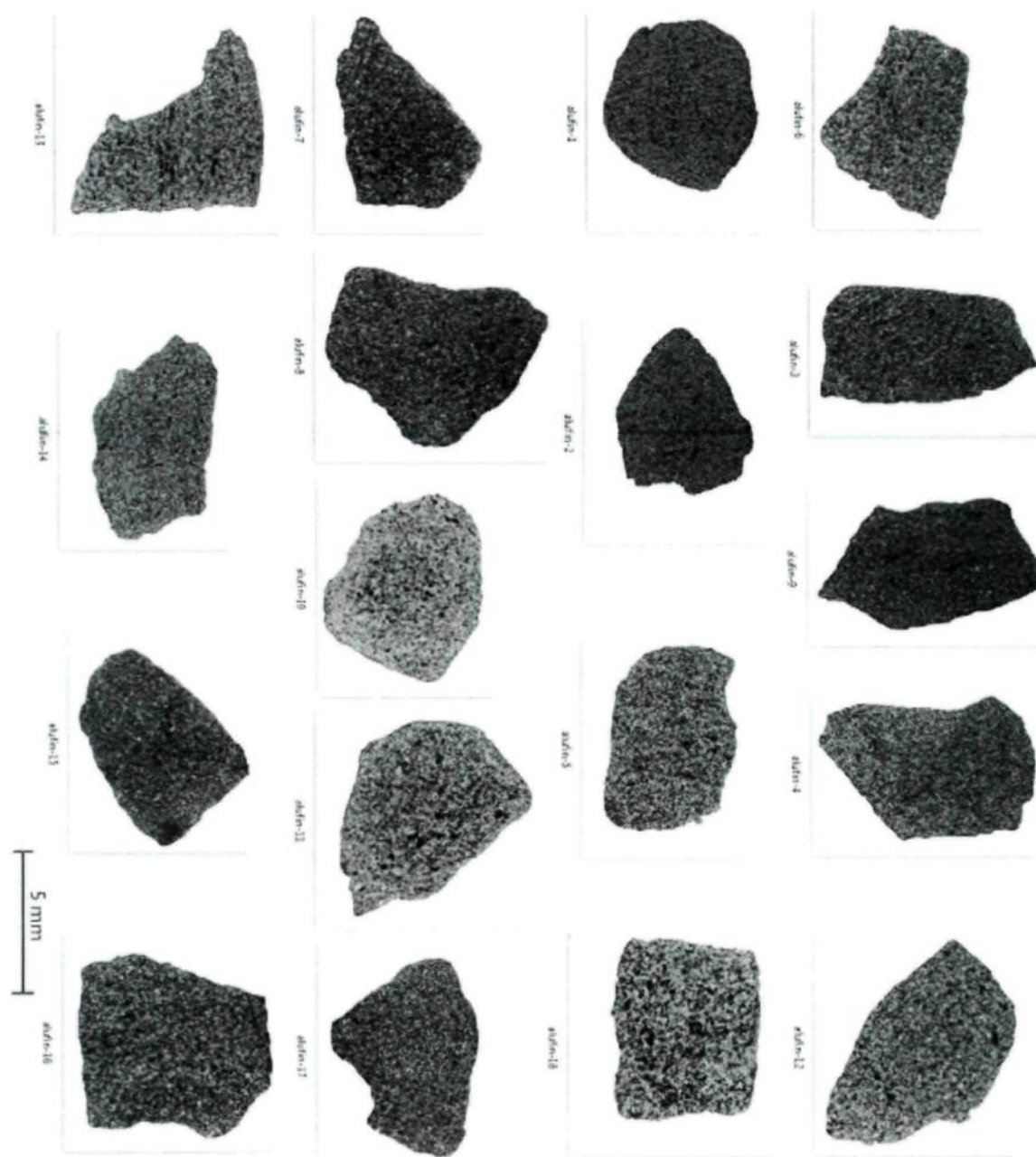
Figure A4- 1: Metallographic Investigation of Alufin – Raw state

Figure A4- 2: Metallographic Investigation of Naigai – Raw state
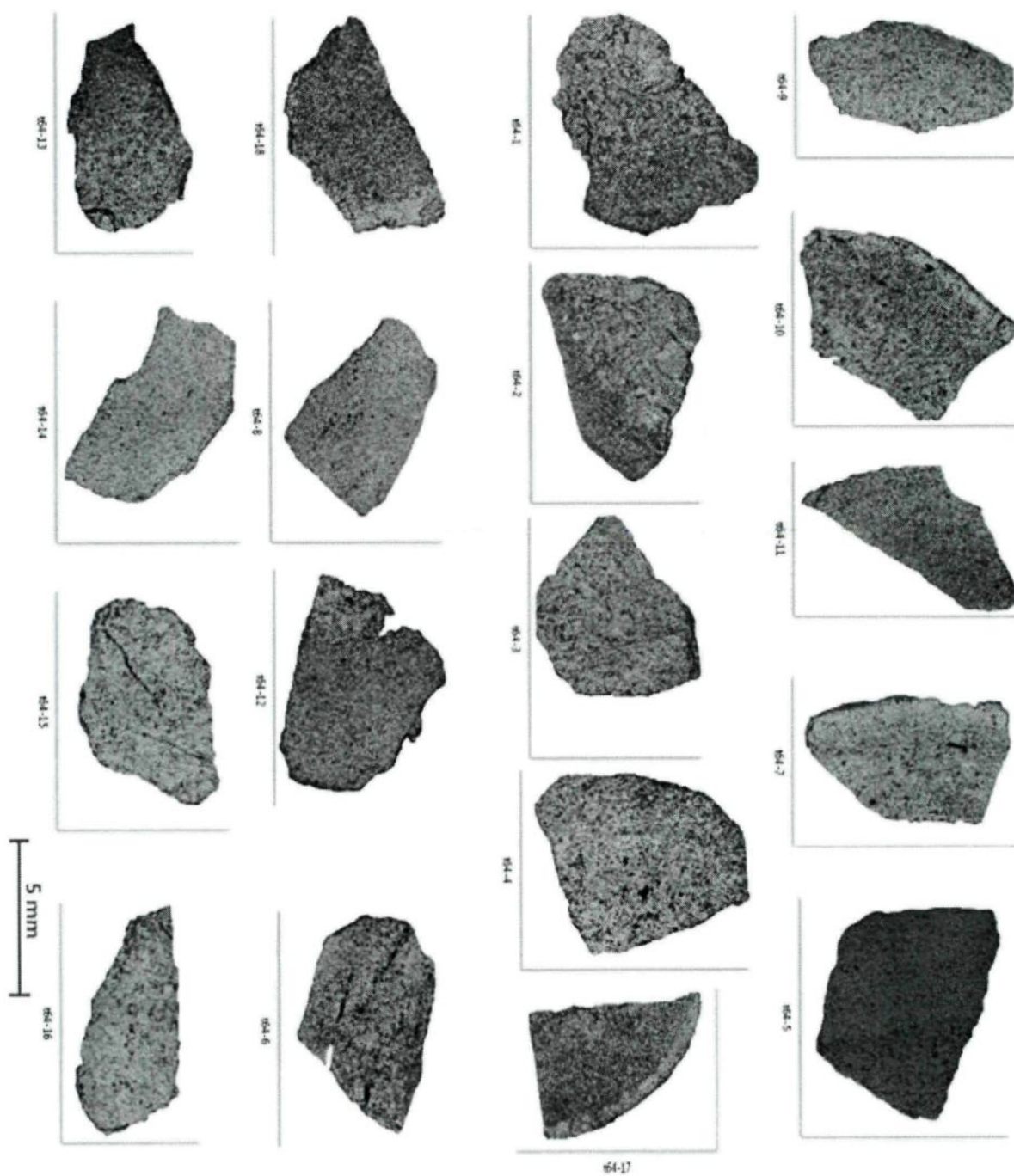
Figure A4- 3: Metallographic Investigation of Alcoa T64 – Raw state
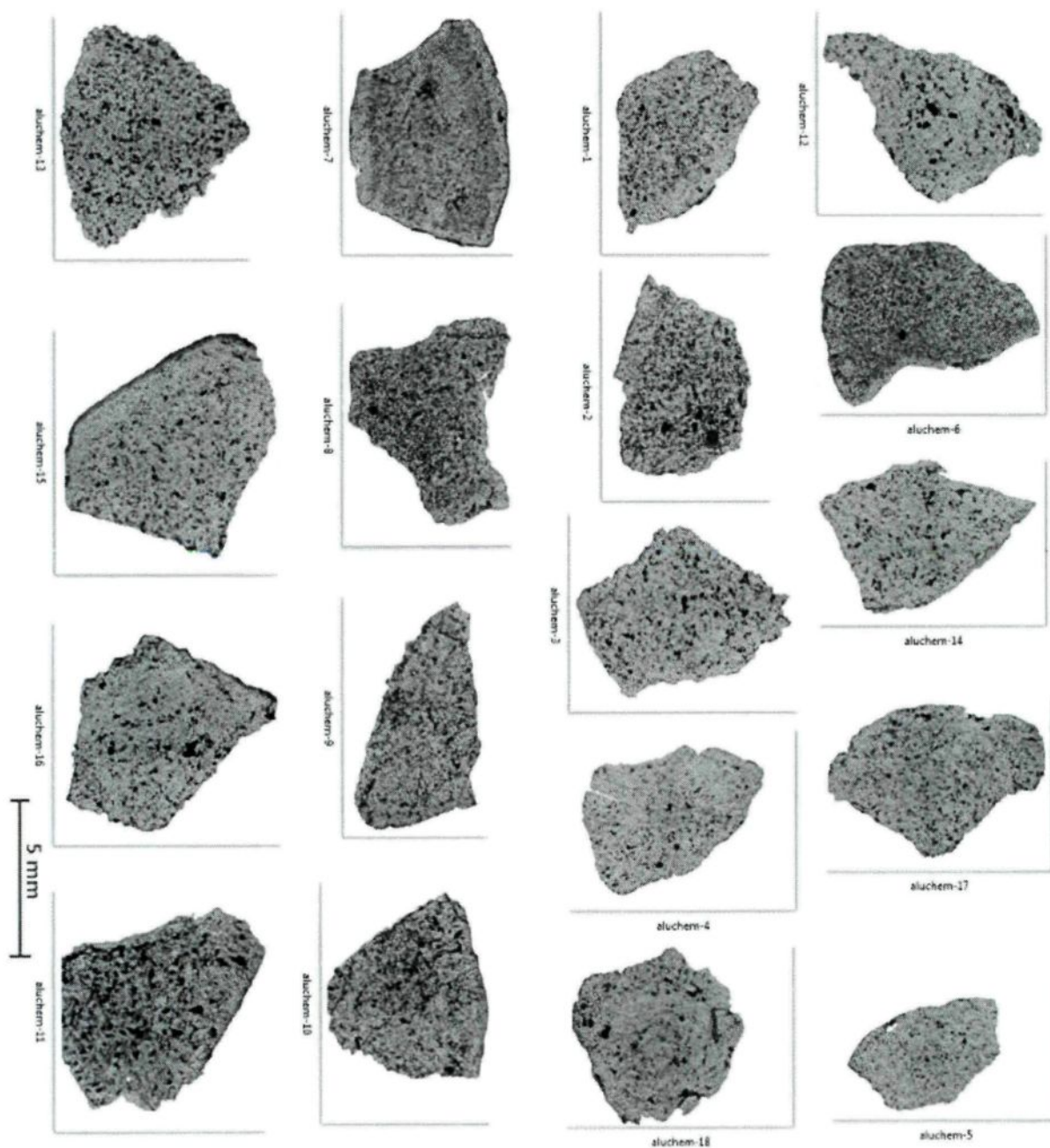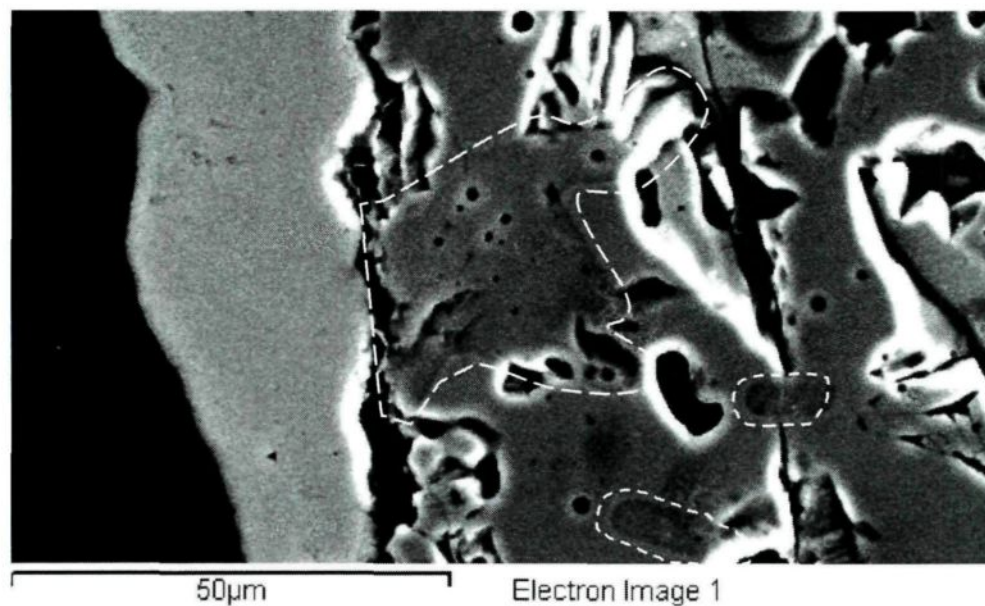
Figure A4- 4: Metallographic Investigation of Aluchem – Raw state
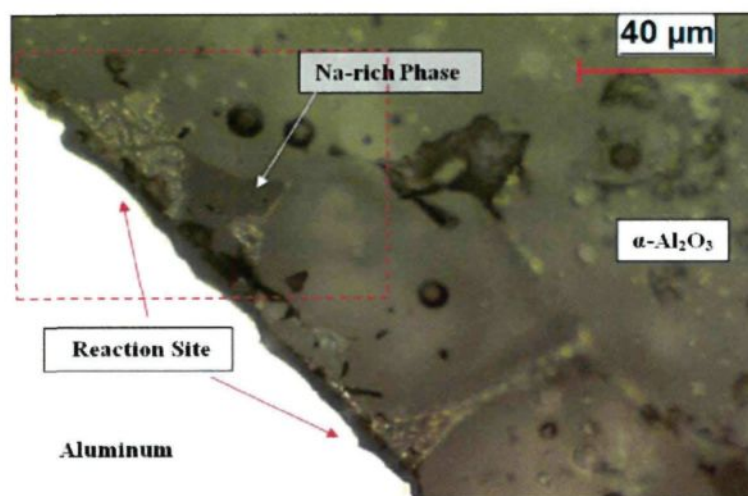
Figure A4- 5: Metallographic Investigation of Aluchem – E7- 2%Mg-Al Alloy- Grain boundary and Na-rich zone reaction
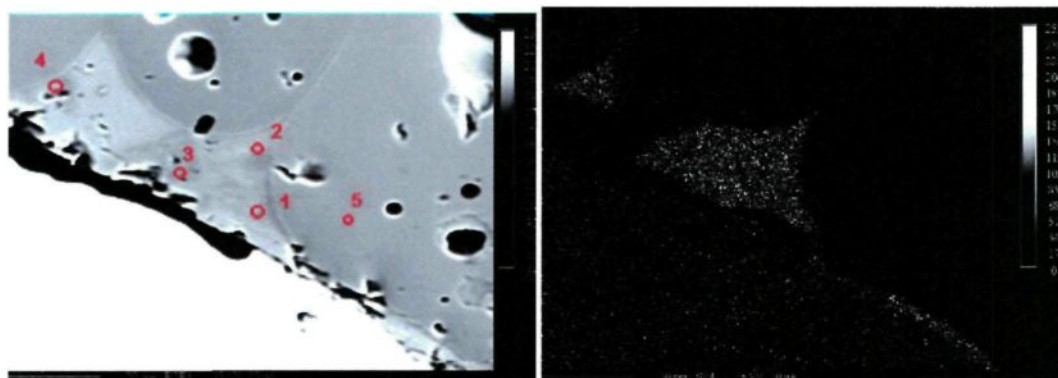
Figure A4- 6: Metallographic Investigation of Aluchem – E7-D1- 5%Mg-Al Alloy Surface reaction zone

Table A4- 1: SEM micro probe point analyses results for the spots shown in Figure A4-6

Analysis#	%Weight				% Atomic			
	O	Mg	Al	Total	O	Mg	Al	Total
E7-D1 p1	37.36	17.17	41.11	95.64	51.15	15.48	33.37	100.00
E7-D1 p2	38.85	16.80	41.37	97.02	52.19	14.86	32.96	100.00
E7-D1 p3	38.59	17.00	41.39	96.98	51.92	15.05	33.03	100.00
E7-D1 p4	36.84	15.51	41.66	94.01	51.35	14.23	34.43	100.00
E7-D1 p5	41.50	0.00	53.47	94.97	56.69	0.00	43.31	100.00
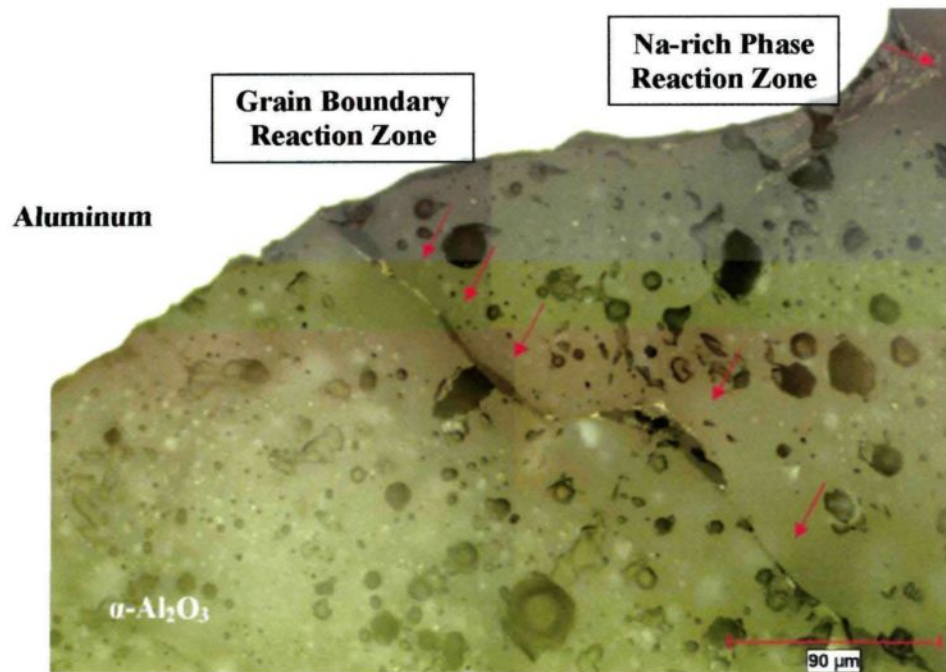
Figure A4- 7: Metallographic Investigation of Aluchem – E7- 2%Mg-Al Alloy
Grain boundary and Na-rich zone reaction
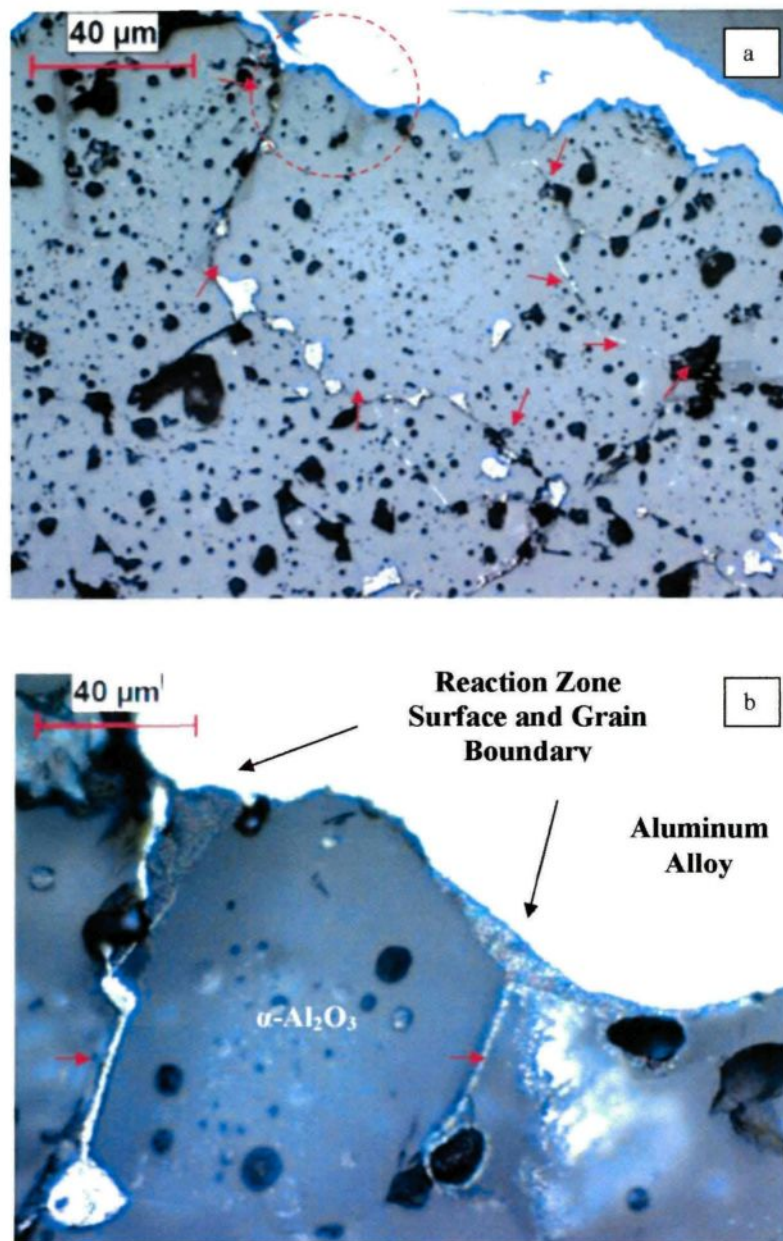
Figure A4- 8: Metallographic Investigation of Naigai – E9- 3d- 5%Mg-Al Alloy
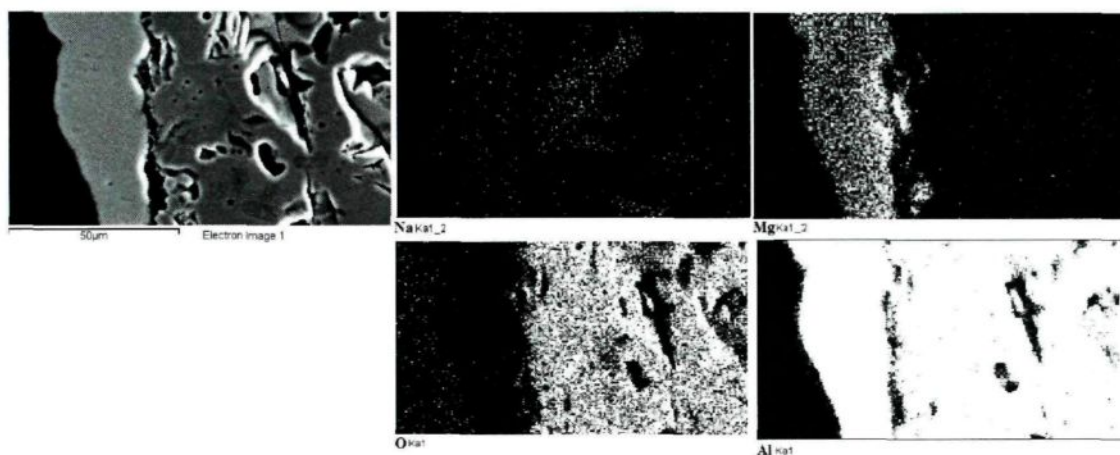
Grain boundary and Na-rich zone reaction
(a) Wider view of reactions and aluminum infiltration through grain boundaries,
(b) circled area in "a" showing the details of reaction zone and grain boundary
aluminum infiltration

Figure A4- 9: Metallographic Investigation of Naigai – E9- 3d- 5%Mg-Al Alloy
Grain boundary and Na-rich zone reaction

Figure A4- 10: SEM Mapping Study on Sample shown in Figure A4.9
(Naigai – E9- 3d- 5%Mg-Al Alloy - Na-rich zone reaction)
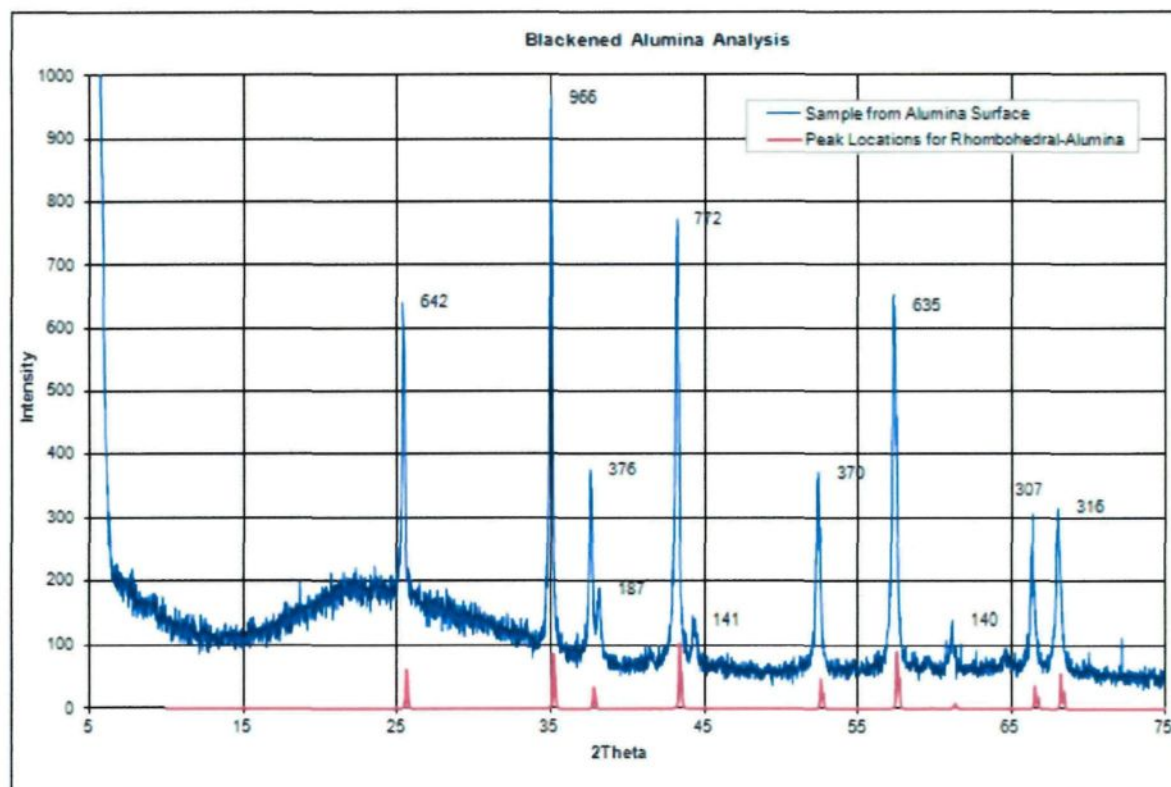
Figure A4- 11: XRD Analysis of Scraped Black Alumina Surface Shown in Figure A4.
(715°C, 5%Mg-Al Alloy, 72-hour contact time, 1.8mm/s liquid metal velocity)

Element	Weight%	Weight% Sigma	Atomic%
O K	24.95	0.32	33.73
Na K	38.73	0.31	36.43
Mg K	9.63	0.20	8.57
Al K	26.30	0.26	21.06
Ca K	0.39	0.08	0.21
Totals	100.00		
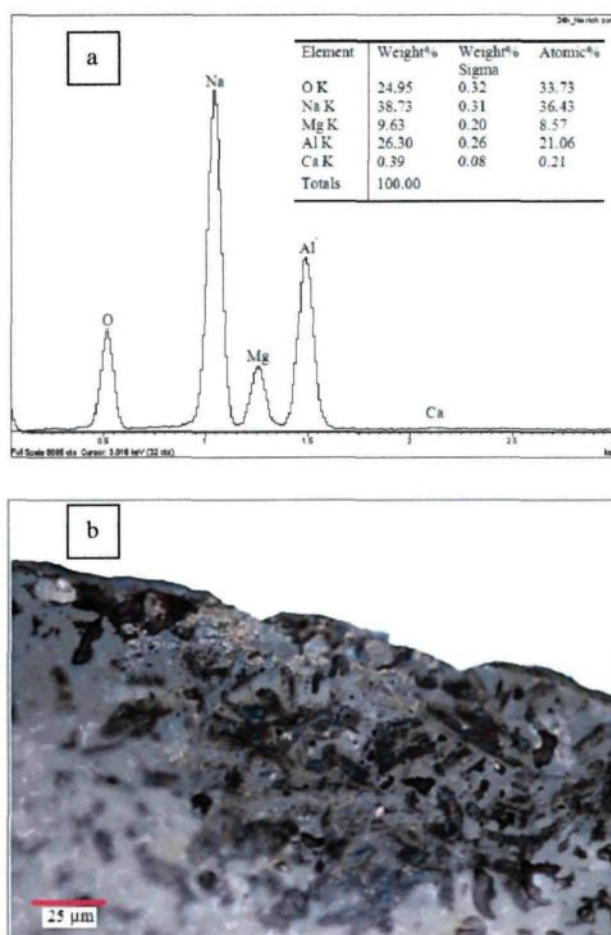
Figure A4- 12: Na rich Alumina Surface (a) EDX Analysis of the spot shown in Figure 6.40.c, (b) optical microscope image of a similar structure found on a different alumina (crossection)
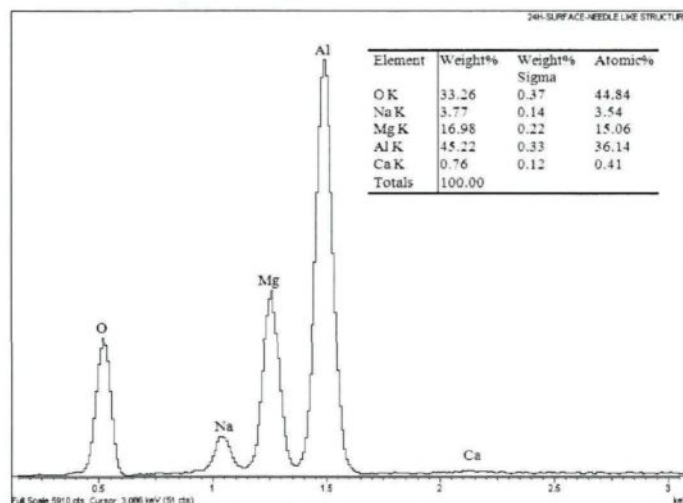
Figure A4- 13: EDX Analysis of Na rich Needles shown in Figure 5.43.f in a circled area
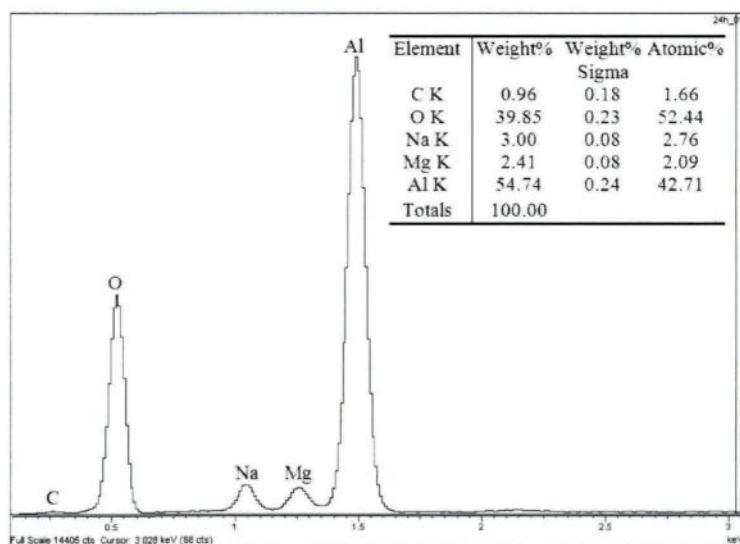
Figure A4- 14: EDX Analysis of Mg-spinel crystal and Na-rich needles shown in Figure 5.44.b
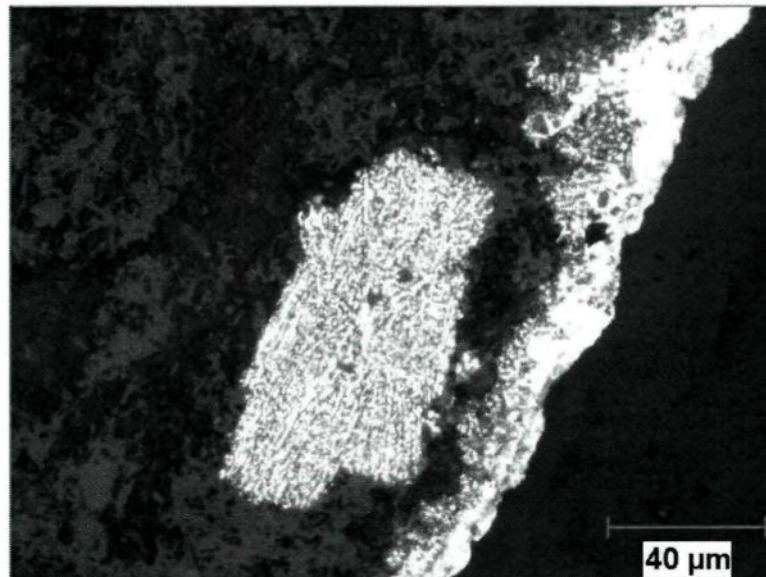
Figure A4- 15: Surface and Sub-surface Degradation observed on Alufin Alumina after 1 day (5%Mg-Al Alloy-Dynamic Experiment at 715°C)
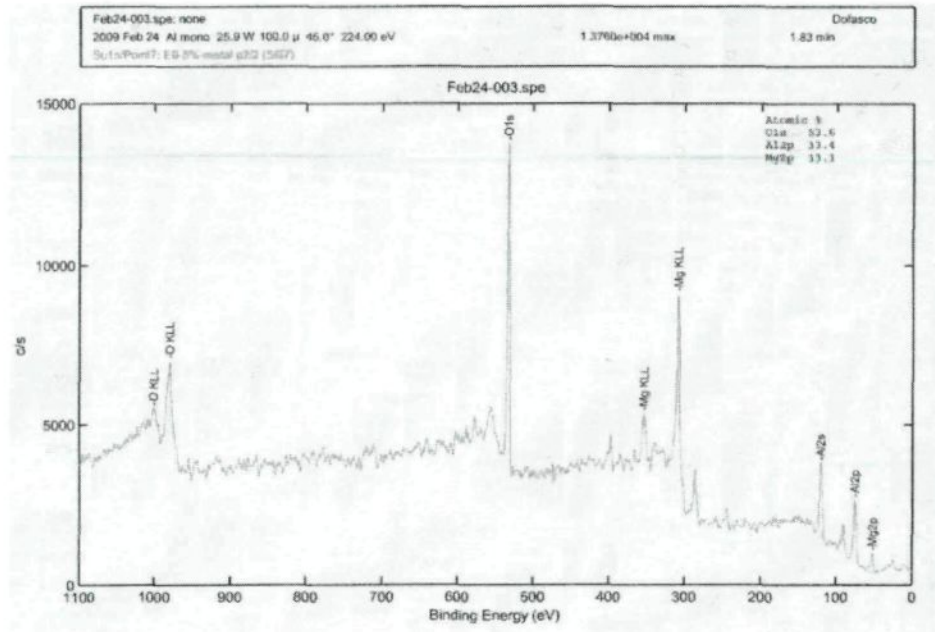
Figure A4- 16: XPS Analysis Results #1 – 5%Mg-Al Alloy, Alcoa, Static Experiment, 715°C
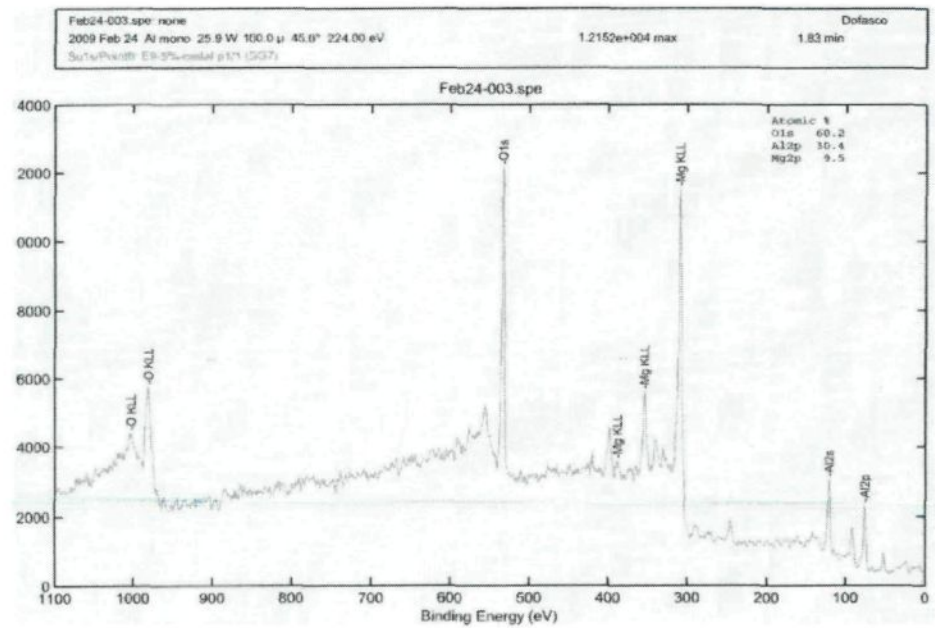

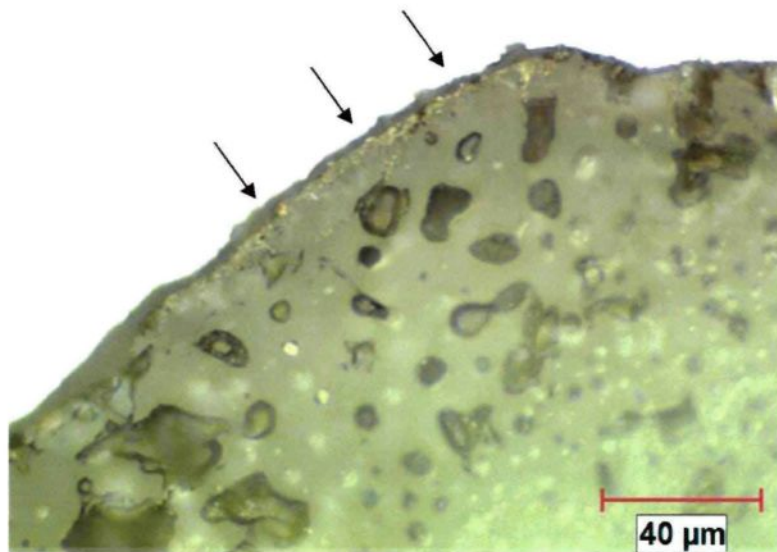Figure A4- 17: XPS Analysis Results #2 – 5%Mg-Al Alloy, Alcoa, Static Experiment, 715°C

Figure A4- 18: Appearance of Reaction Zone at Aluchem/5%Mg-Al Alloy Interface – 3 day long dynamic experiment (EDX microprobe results are shown in Figure A4.12 and Table A4.2)
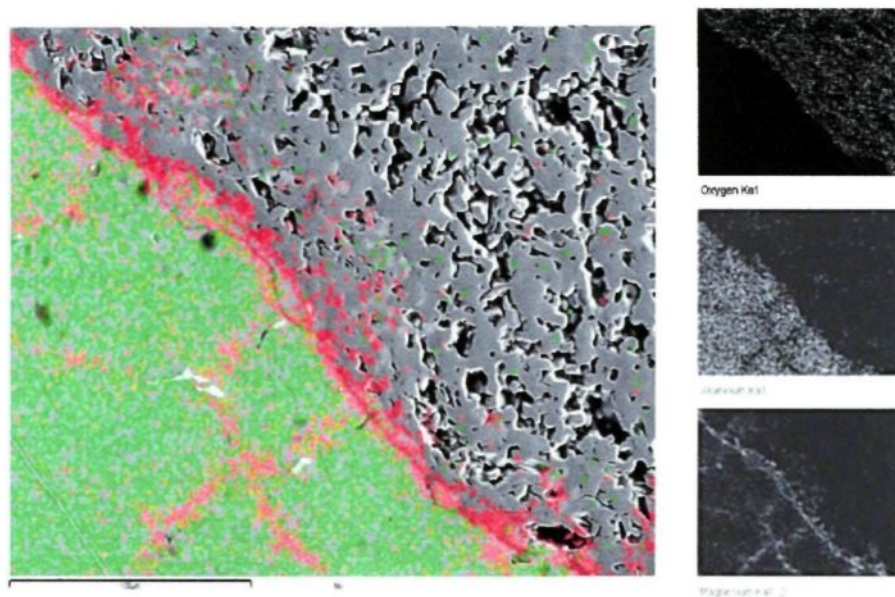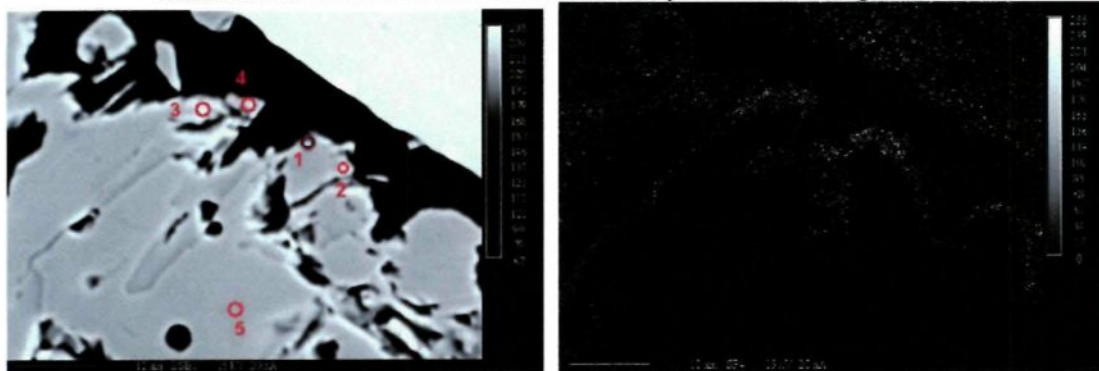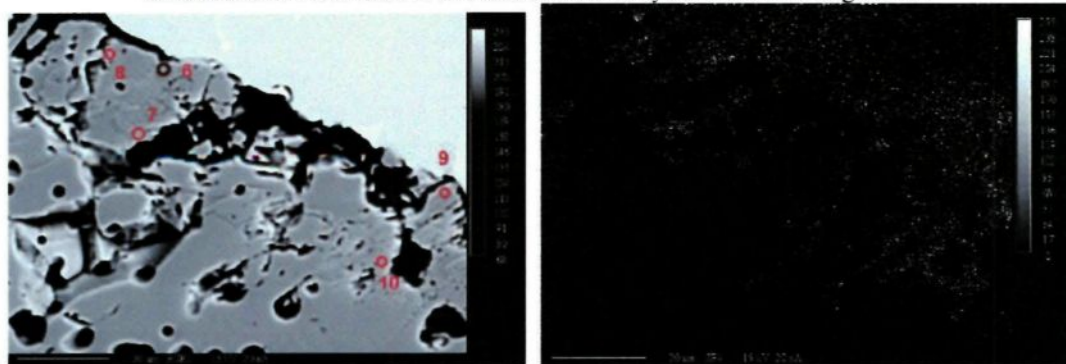
Figure A4- 19: Mapping study of Alcoa T64 Alumina/Aluminum Interface after 3 day Dynamic Experiment with 5%Mg-Al Alloy (Red Color: Magnesium, Yellow: Aluminum metal)

Échantillon E11-D3. Zone 1. Localisation des analyses et carte du magnésium.

Échantillon E11-D3. Zone 2. Localisation des analyses et carte du magnésium.

Échantillon E11-D3. Zone 3. Localisation des analyses et carte du magnésium.
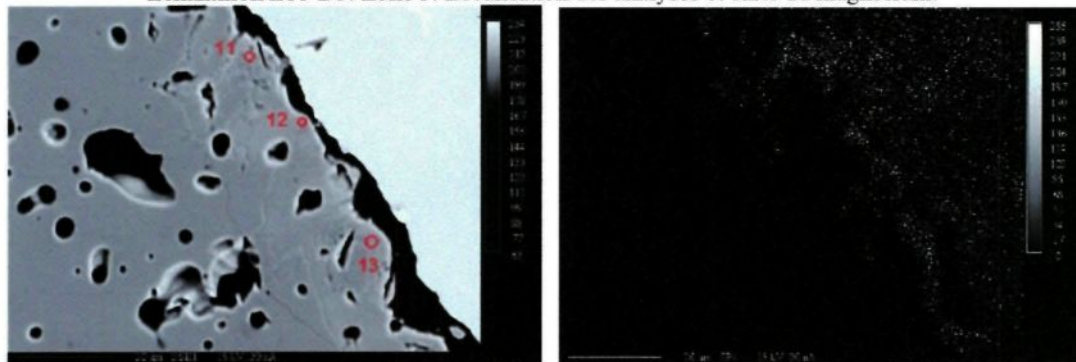

Figure A4- 20: 5% Aluchem, Interface Reactions Investigation-3 Day- 1.8mm/s- SEM EDX Analyses

Table A4- 2:SEM micro probe point analyses results for the spots shown in Figure A4-14

| Échantillon/Analyse	% Wt				% Atomic		
	O	Mg	Al	Total	O	Mg	Al
p1	37.568	8.376	46.610	92.554	53.121	7.796	39.082
p2	35.173	8.582	45.479	89.234	51.884	8.333	39.783
p3	48.036	13.773	34.987	96.796	61.703	11.646	26.650
p4	35.977	11.444	41.079	88.500	53.008	11.100	35.892
p5	43.969	0.008	52.287	96.264	58.641	0.007	41.353
p6	39.799	15.040	43.233	98.072	52.828	13.142	34.030
p7	33.607	14.847	43.146	91.600	48.730	14.172	37.098
p8	40.304	12.399	42.680	95.383	54.631	11.064	34.306
p9	39.856	11.777	42.775	94.408	54.617	10.624	34.759
p10	38.994	11.631	43.824	94.449	53.683	10.541	35.776
p11	40.026	12.136	43.987	96.149	54.017	10.782	35.202
p12	40.802	18.047	36.421	95.270	54.930	15.994	29.076
p13	37.626	13.453	42.677	93.756	52.412	12.336	35.252
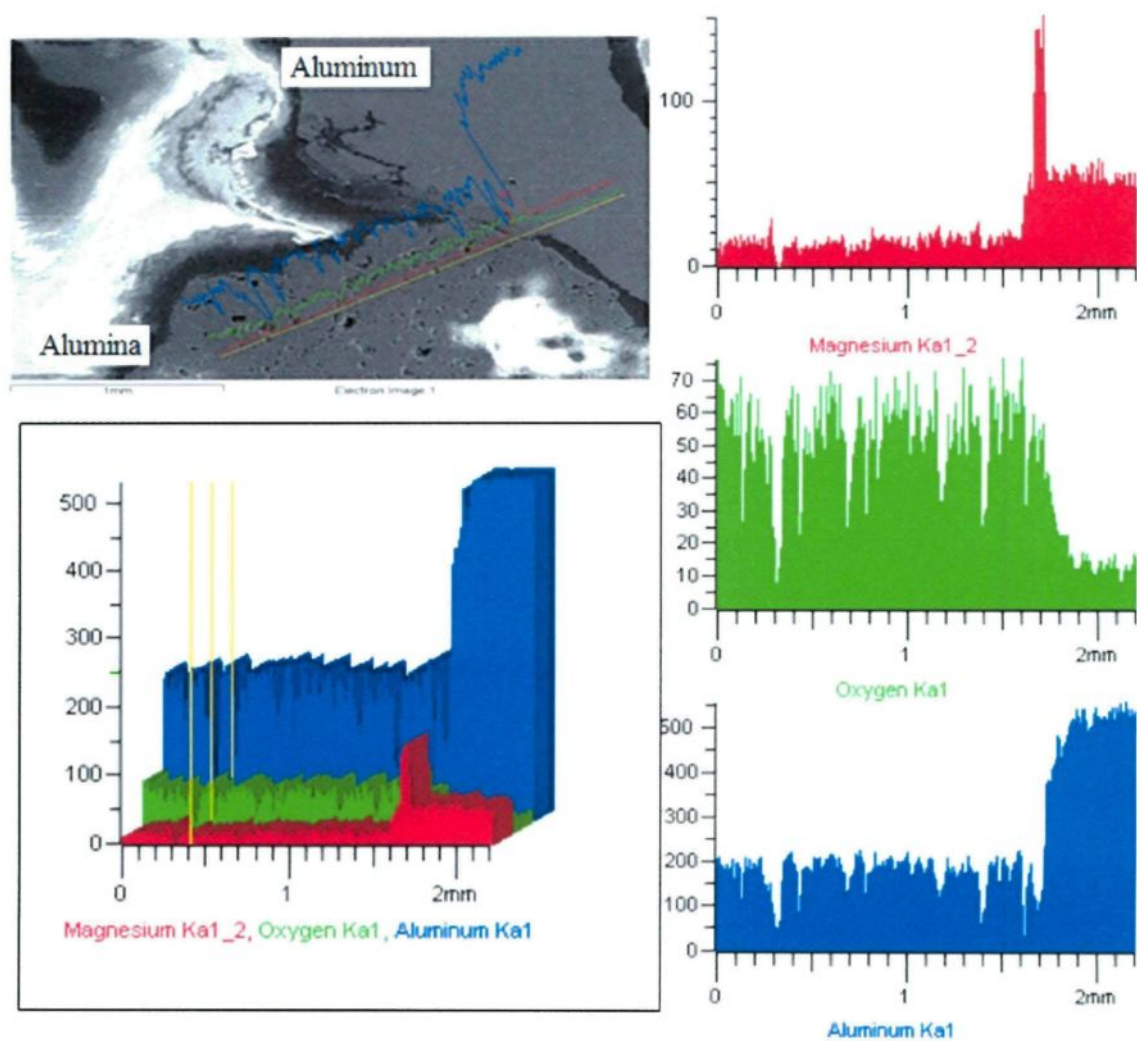
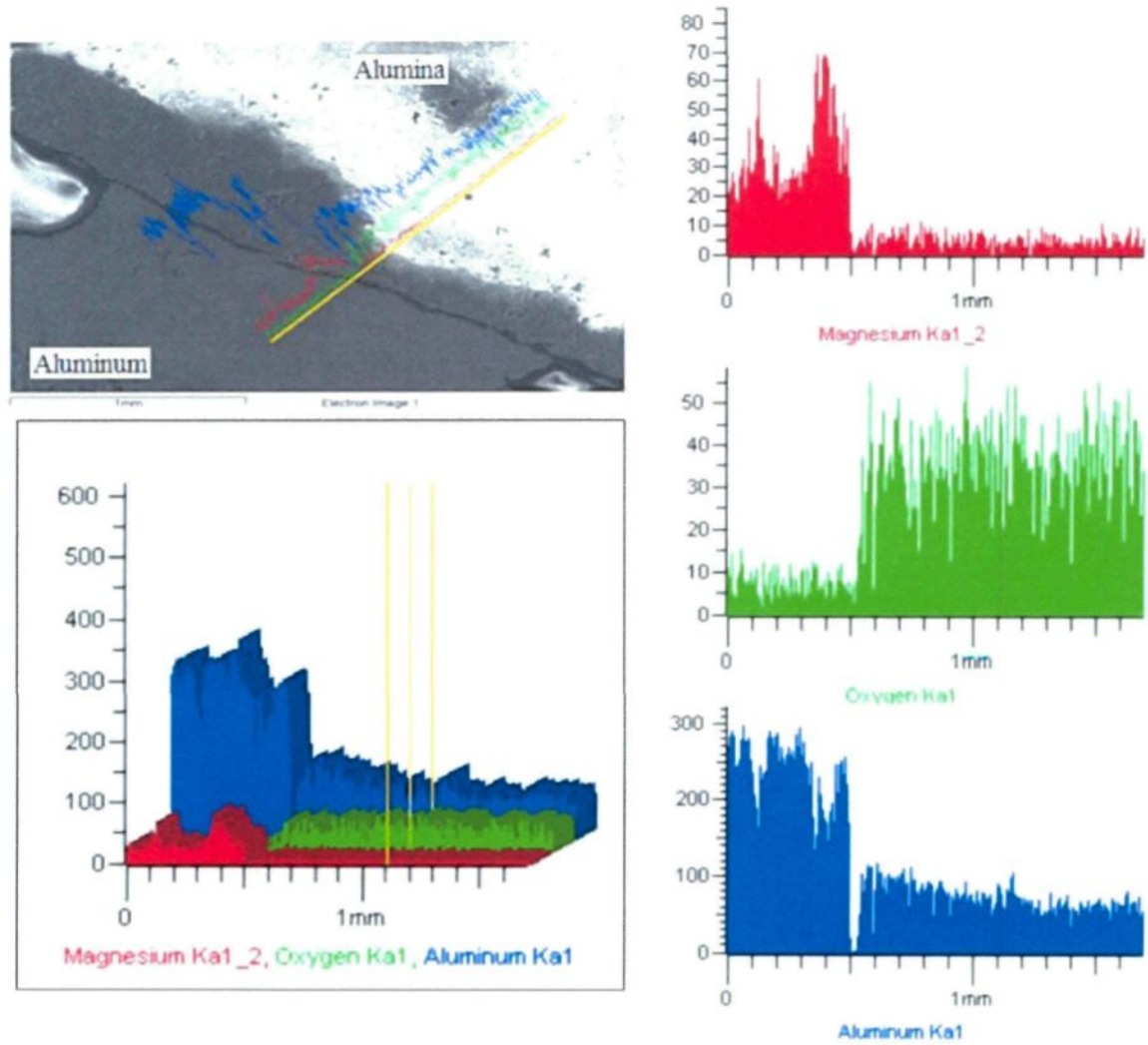Figure A4- 21: Alcoa Interface- Line Scan- 2%Mg Al Alloy- 1.8mm/s- 3 days

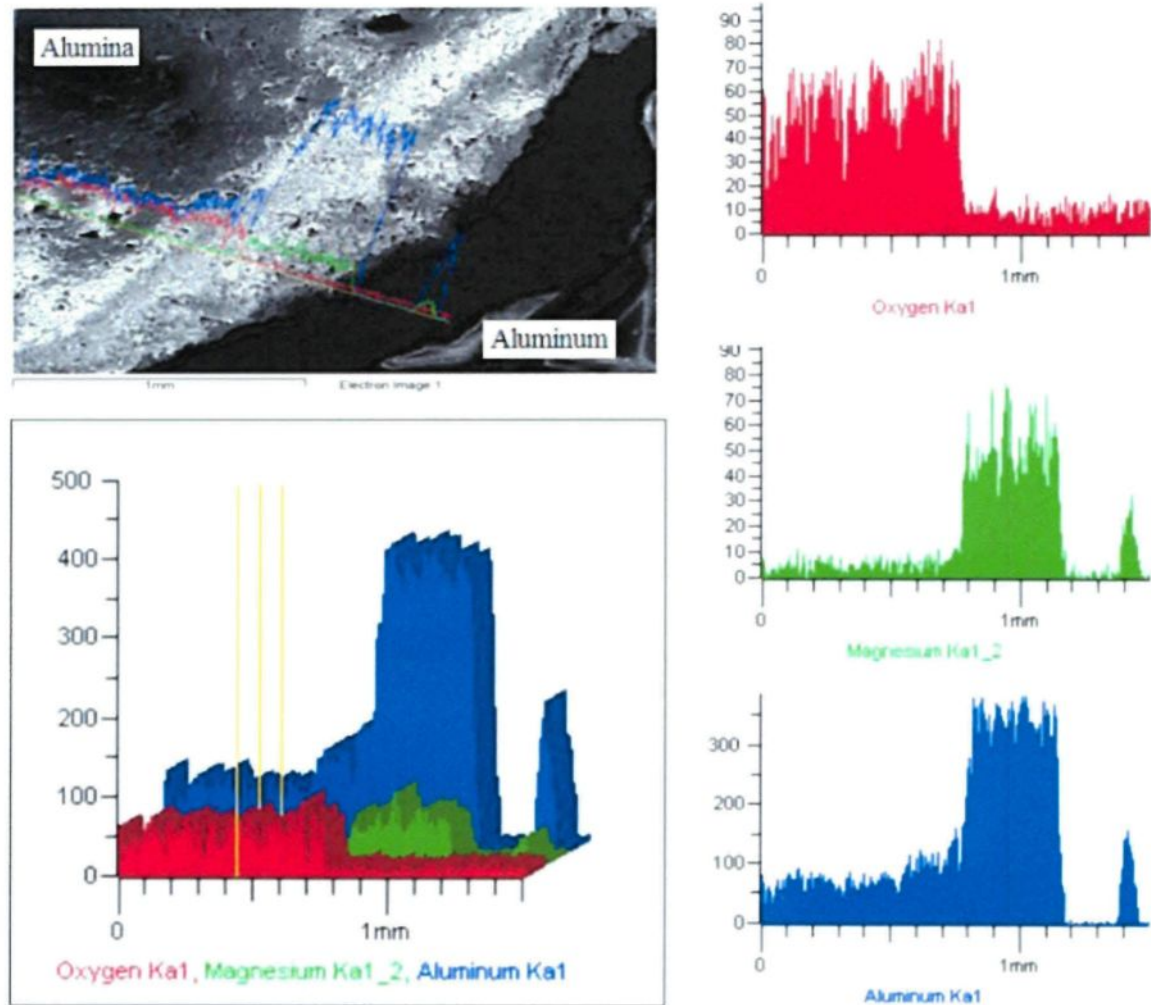Figure A4- 22: Alcoa Interface- Line Scan- 5%Mg Al Alloy- 1.8mm/s- 3 days

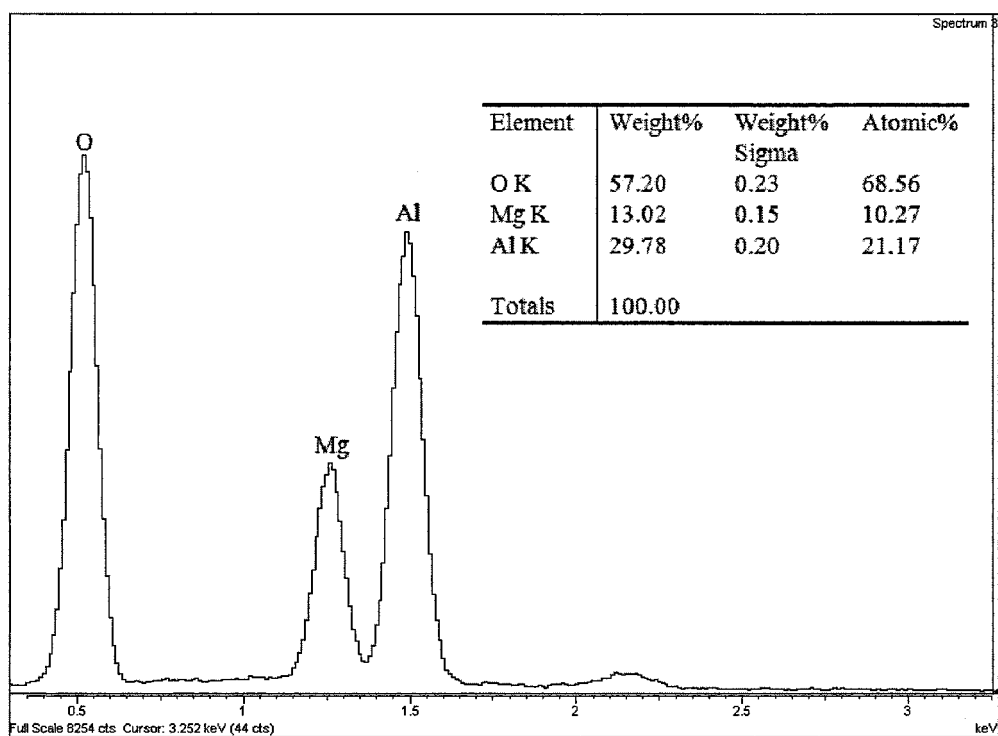Figure A4- 23: Alcoa Interface- Line Scan- 7%Mg Al Alloy- 1.8mm/s- 3 days

Element	Weight%	Weight% Sigma	Atomic%
O K	57.20	0.23	68.56
Mg K	13.02	0.15	10.27
Al K	29.78	0.20	21.17
Totals	100.00		

Figure A4- 24: MgAl2O4 powder EDX Point Analysis – Inclusion study